The Effect of Ground-State Spin on Fission and Quasi-Fission Anisotropies

by

Rachel Deborah Butt

A thesis submitted for the degree of
Doctor of Philosophy
of the Australian National University

February 6, 2003

[This page intentionally left blank.]

Preface

This thesis describes the measurement, analysis, and interpretation of fusion cross-sections and fission fragment anisotropies for the four reactions ^{31}P+^{175}Lu, ^{31}P+^{176}Lu, ^{28}Si+^{178}Hf and ^{29}Si+^{178}Hf, and fission-like cross-sections and anisotropies for the reaction ^{16}O+^{235}U, with some overlap of previous measurements for the reaction ^{16}O+^{238}U. The project was suggested by Drs David Hinde and Nanda Dasgupta.

All experiments were carried out using heavy-ion beams from the 14UD Pelletron accelerator operated by the Department of Nuclear Physics at the Australian National University. All measurements documented in this work were made with the Fusion-Fission research group, with assistance from the academic and technical staff.

The fission measurements were carried out using the existing "CUBE" detector array, comprising mainly two large Multi-Wire Proportional Counters, built and operated by Dr Hinde. The analyses of these data were carried out by myself using a variety of programs, some already written, some written by myself, some adapted by myself or others, as described in Appendix A.

The evaporation residue measurements were carried out using a silicon surface barrier detector mounted in the CUBE detector array. I carried out the analysis of these data using existing programs.

The theory and computer model development to simulate the effect of ground-state spin on fission anisotropies and quasi-fission anisotropies were carried out by myself.

I have written two research papers, directly related to the work described in this thesis, which were published in Physical Review C:

- R. D. Butt, M. Dasgupta, I. Gontchar, D. J. Hinde, A. Mukherjee, A. C. Berriman, C. R. Morton, J. O. Newton, A. E. Stuchbery, J. P. Lestone, *Effects of finite ground-state spin on fission fragment angular distributions following collisions with spherical or deformed nuclei*, Phys. Rev. C, **65** 044606 (2002)

- R. D. Butt, D. J. Hinde, M. Dasgupta, A. C. Berriman, A. Mukherjee, C. R. Morton, J. O. Newton, *Measurement of the effect of large deformation-aligned ground-state spin on fission fragment anisotropies*, Phys. Rev. C, **66** 044601 (2002)

No part of this thesis has been submitted for a degree at any other university.

Rachel Butt
February 6, 2003

Acknowledgements

I'd like to thank my supervisor, David Hinde, for being right about so many things related to my project, and wrong about enough to be good for my self esteem. For giving me something interesting to start on; for getting me unstuck time after time; for being patient with countless drafts; for being friendly and always having the door open, thank you.

I'd like to thank Nanda Dasgupta, my other supervisor, for being such a pleasure to work with, and for all the understanding she shared about coupled-channels calculations in general and CCMOD in particular. Thanks also to Annette Berriman, Igor Gontchar, Clyde Morton, Anjali Mukherjee, and John Newton, who contributed to my experiments and offered critical commentary on my papers, and to my advisor Aidan Byrne.

Thanks also to Kouichi Hagino, for assistance with various theoretical issues; to George Dracoulis and Andrew Stuchbery, for discussions on the alignment of nuclear spin with the nuclear deformation axis; and to John Lestone, for his work, which was a very useful starting point for my work.

Many thanks to the technical staff of the Nuclear Physics Department, who look after the 14UD accelerator that is such an integral part of our research, and especially to Bob Turkentine, who spent much time on my lutetium targets.

And to my partner Peter, who listened, encouraged, and taught me so much about getting the computers to do all the boring work; for whom I could write reams of appreciation; I love you.

Abstract

In heavy-ion induced fusion-fission reactions, the angular distribution of fission fragments is sensitive to the mean square angular momentum brought in by the fusion process, and the nuclear shape and temperature at the fission saddle point. Experimental fission fragment angular distributions are often used to infer one or more of these properties. Historically the analysis of these distributions has relied on the alignment of the total angular momentum $\vec{J}$ of the compound nucleus, perpendicular to the projectile velocity.

A full theoretical approach, written into a computer code for the first time, allows the effect of ground-state spin of the projectile and target nuclei to be correctly treated. This approach takes into account the change in alignment of $\vec{J}$ due to the inclusion of this spin, an effect which is shown to be markedly stronger if the nucleus with appreciable spin also has a strong quadrupole deformation. This change in alignment of $\vec{J}$ results in a much reduced fission fragment anisotropy. In extreme cases, the anisotropy may be below unity, and it ceases to be sufficient to characterise the fission fragment angular distribution.

The calculations have been tested experimentally, by measuring fission and survival cross-sections and fission fragment angular distributions for the four reactions ^{31}P+^{175,176}Lu and ^{28,29}Si+^{178}Hf, where ^{176}Lu is a strongly-deformed nucleus with an intrinsic spin of 7 units, and ^{178}Hf has very similar deformation, but zero spin. The reactions form the compound nuclei ^{206,207}Rn. The total fusion excitation functions are well-reproduced by calculations, but the fission fragment anisotropies are reproduced only when the nuclear spin and deformation are taken into account, confirming the theory and supporting the recent understanding of the role of nuclear deformation in the fusion process and of compound nucleus angular momentum in the fission process.

Having established the effect in the well-understood fusion-fission reactions, the effect of nuclear spin is examined for the less well understood quasi-fission reaction. Experiments were performed to measure fission cross-sections and fission fragment angular distributions for the reactions ^{16}O+^{235,238}U, where ^{235}U has a spin of 7/2 and ^{238}U has a spin of zero. Both nuclei are quadrupole-deformed, and ^{16}O+^{238}U was already known to exhibit evidence for quasi-fission. Theoretical calculations indicate that the fitted anisotropy is sensitive to the range of angles over which the angular distribution is measured, showing that where quasi-fission is present, the anisotropy is not sufficient to entirely characterise the fission fragment angular distribution. Comparison of the measured anisotropies with fusion-fission calculations shows clearly that the reaction is quasi-fission dominated. However, although existing quasi-fission models predict a strong effect from the spin of ^{235}U, it is shown that the observed effect is appreciably stronger still in the experimental angular range. This should be an important tool in evaluating future models of the quasi-fission process.

Contents

Appendices

CHAPTER 1

Introduction

1.1 Overview

Nuclear fission, the separation of a nucleus into two fragments, is a complex process, and significant research effort is devoted to developing an understanding of the dynamics of the fission process. Much of this work is done by studying fusion-fission reactions, where a rapidly-moving projectile nucleus strikes and fuses with a target nucleus, and the resulting compound nucleus subsequently fissions. A wide range of compound nuclear masses, excitation energies, and angular momenta are involved. The associated heavy ion fusion reactions have applications in the areas of super-heavy nucleus formation and gamma-ray spectroscopy.

The defining characteristic of fusion is the formation of a compound nucleus. It was suggested by Bohr [BOH36], in the context of neutron absorption, that once the compound nucleus is formed, the details of its formation can be ignored when considering subsequent evolution. Thus, parameters such as the initial mass asymmetry and the structure of the fusing nuclei affect only the probability of fusion, and are irrelevant thereafter. The proton and neutron numbers are unchanged, and the total angular momentum and excitation energy remain constant under conservation laws; all these influence the fission process. This means that developing a full understanding of the fission process requires an understanding of the fusion process. Conversely, by observing fission following a fusion reaction, even a partial understanding of the fission process may allow us to deduce partial information about the fusion process.

During recent years, methods have been developed that have proved useful in modelling these processes and predicting the outcomes of fusion-fission and fusion-evaporation reactions. In particular, both theoretical and experimental developments have led to an improved understanding of the subtleties of the fusion process [DAS97]. From this has come the belief that the angular momentum distribution may now be accurately predicted for the fusion process, and that its influence on the fission process is well understood. The next step is to test that understanding.

Most calculations to date assume that the angular momentum brought in by the projectile during the fusion process is the only angular momentum that needs to be considered. However, where one or both of the reacting nuclei has significant ground-state spin, this assumption will not be adequate. This thesis presents fusion-fission measurements made on several heavy-ion reactions, one of which involves a nucleus with significant ground-state spin. In attempting to predict fusion-fission anisotropies while including the effects of ground-state spin, it is vital to understand the influence of the fusion angular momentum distribution on the subsequent fission process, including subtle interplays of ground-state spin and static deformation during the fusion process.

The present understanding of fusion indicates that the fusion process is not affected by the ground-state spin of the reacting nuclei. However, for statically deformed nuclei, the orientation of the ground-state spin is affected by the orientation of the reacting nucleus. In turn, the orientation of the reacting nucleus affects the fusion process [STO80]; therefore we can only predict the total fusion angular momentum distribution correctly if we fully understand the role of nuclear deformation and nuclear orientation in the fusion process.

The present understanding of the fission process indicates that it is directly and strongly affected by the total angular momentum $\vec{J}$ of the compound nucleus. This differs from the collision induced angular momentum $\vec{l}$ by the ground-state spins I_0, I_1 of the target and projectile nuclei respectively; they lead to a slight increase in the average $\langle J^2 \rangle$, but more importantly they may introduce components of J along the beam direction. These can have a significant effect on the fission fragment angular distribution, measured with respect to the beam direction, and it should be possible to observe the effect of these ground-state spins experimentally, providing a valuable test of fusion and fission models.

A process closely related to fusion-fission is quasi-fission [BJO81, TOK84], in which the projectile and target form an elongated di-nucleus, as opposed to a fully

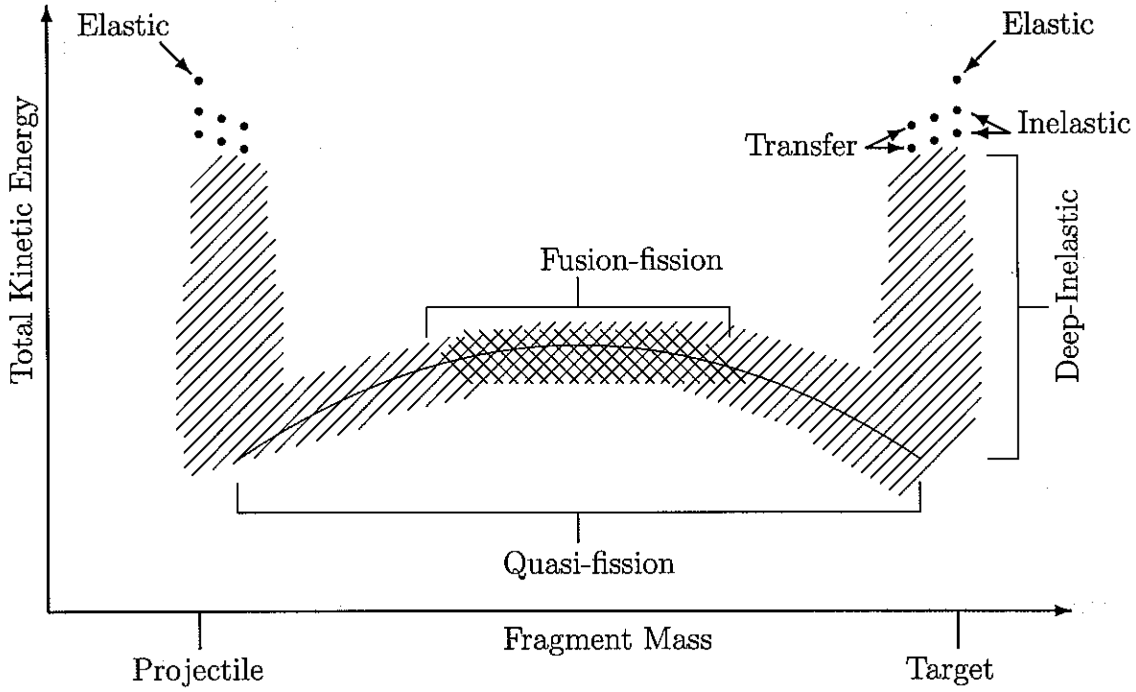

Figure 1.1: Schematic illustration of heavy-ion reactions, characterised by mass split against total kinetic energy.

equilibrated, compact compound nucleus. This di-nucleus subsequently fissions into two fragments after incomplete mass-equilibration. Quasi-fission is not yet as well understood as fusion-fission. By measuring quasi-fission in reactions on nuclei with ground-state spin, and comparing the results to similar reactions with nuclei without ground-state spin, we aim to investigate whether or not quasi-fission is strongly affected by angular momentum, and the extent to which the probability of quasi-fission reactions is affected by nuclear deformation, as has been proposed [HIN96].

1.2 Heavy Ion Reactions

Fusion-fission events are one of several possible outcomes of a heavy ion reaction. Experimentally, a thin foil of target nuclei is bombarded with high-speed projectiles. If fusion-fission is to occur, the projectile must have enough energy to overcome the electrostatic repulsion between it and the target nucleus; that is, energy of the order of 5 MeV per nucleon (depending on the target). The variety of possible heavy-ion reactions may for the most part be distinguished in terms of the total kinetic energy of the detected fragments and mass asymmetry, as illustrated in Figure 1.1. For any given projectile nucleus, one of the following may occur:

Elastic Scattering Only the velocities of the nuclei change. The projectile and target nuclei are unaltered by the interaction, and their identities are preserved. This is not a reaction as such, but a purely electrostatic interaction between two nuclei. In practice, at projectile energies and collision angles where other interactions become possible, the observed differential cross-section of elastically scattered beam particles is reduced. If this does *not* occur, then the two nuclei may be treated as point masses and point charges, and the differential cross-sections may be described by the Rutherford scattering formula.

Inelastic Scattering One or both of the reacting nuclei is excited during the collision, and the velocities of the nuclei are changed. If the excitation is due solely to the electrostatic (Coulomb) field of one nucleus acting on the other nucleus, this is referred to as Coulomb excitation. However, the nuclei may also get close enough for excitation to occur via the nuclear potential.

Transfer Reaction One or more nucleons are transferred between the target and projectile nuclei. This is observed in peripheral interactions.

Deep Inelastic Reaction This occurs predominantly where the inter-nuclear potential is repulsive, but the kinetic energy allows strong interactions. Many nucleons may be exchanged between the nuclei, giving substantial kinetic energy loss, although there is little mass change on average.

Quasi-fission The target and projectile nuclei form a di-nucleus, which fissions into two fragments after a very short period of time ($\sim 5 \times 10^{-21}$ s). The relative kinetic energy between the colliding nuclei is, in general, completely damped. There is a significant degree of mass equilibration.

Fusion Reactions The target and projectile nuclei fuse, to form a compact, equilibrated compound nucleus.

Following a fusion reaction, the system may follow one of several paths, as illustrated in Figure 1.2:

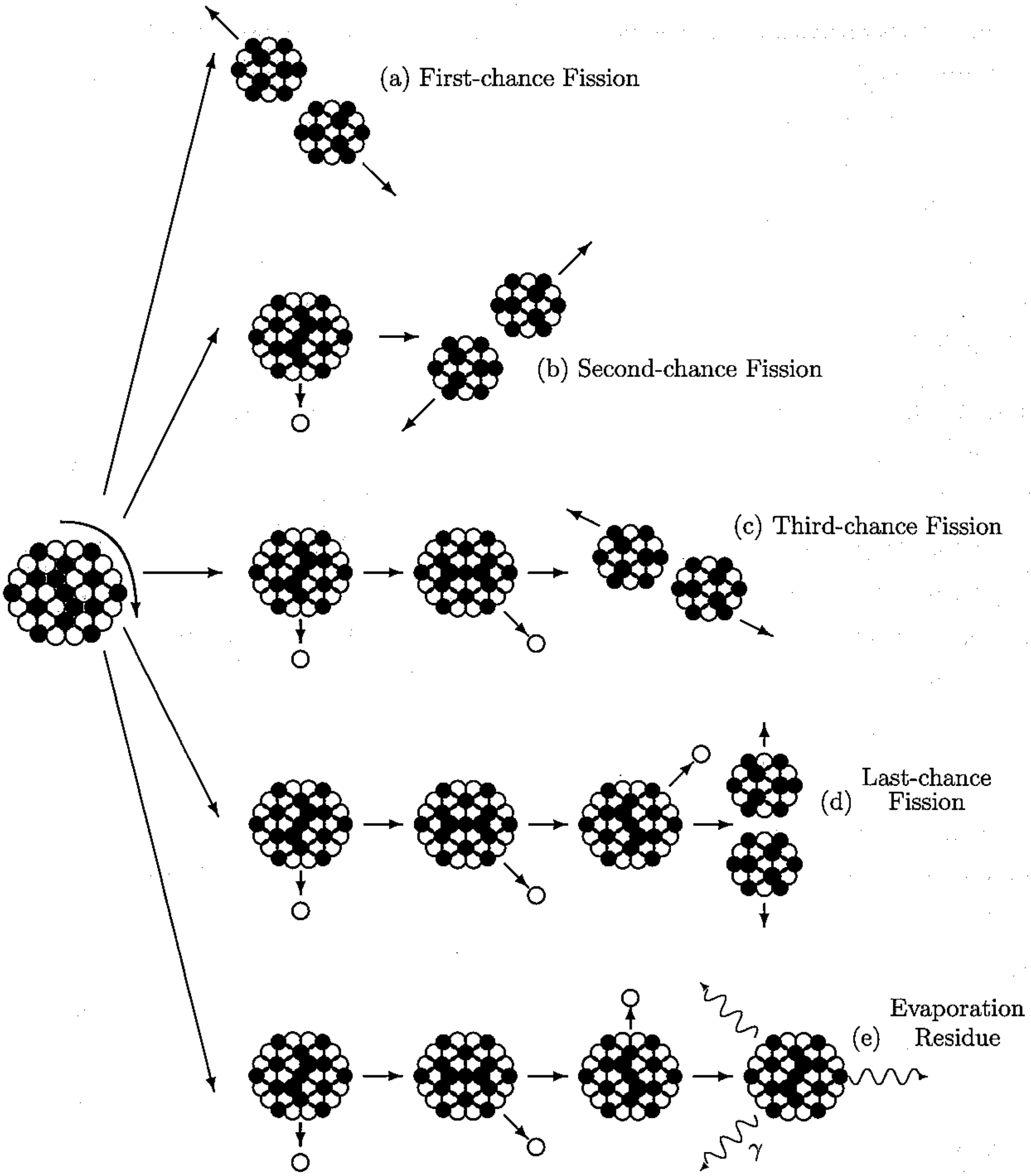

Figure 1.2: A hot, spinning compound nucleus has several available decay paths, proceeding ultimately to fission or formation of an evaporation residue.

- **Particle Evaporation.** The compound nucleus emits one or more particles; for heavy nuclei, these are mostly neutrons. Each particle carries away considerable excitation energy (~8 MeV or more for a neutron). When there is no longer enough excitation energy available to emit another particle, the resulting nucleus is called an "evaporation residue", and the probability of the compound nucleus forming an evaporation residue is called the "survival probability". The nucleus sheds its remaining energy by emitting gamma rays, as indicated in Figure 1.2(e).

- **Fission** The compound nucleus separates into two large fragments. Fission may occur immediately, as in Figure 1.2(a) (this is called "first-chance fission"); or it may follow the emission of one (Figure 1.2(b); "second chance fission") or more (Figure 1.2(c)) particles from the compound nucleus. The nuclear temperature drops significantly with every particle evaporation, affecting both subsequent fission and evaporation processes. Where the compound nucleus excitation energy is too low to allow fission after further particle emission (and possibly too low to allow further particle emission) and still the nucleus fissions (Figure 1.2(d)), then this is the "last-chance" fission.

There are two major areas of research which make extensive use of heavy-ion fusion reactions. One is the quest to create super-heavy elements [OGA99] (elements stabilised only by shell effects, often identified as elements with proton numbers higher than 110). These nuclei can only be formed via heavy-ion fusion-evaporation reactions—and because the compound nucleus is extremely highly charged, the fission probability following the fusion reaction is very high. Experiments attempting to produce these elements are difficult, take a long time, and are expensive. It is thus practically impossible to make systematic studies of reactions forming these nuclei to understand the reaction processes better. However, if we develop a good enough understanding of the fusion and fission processes, we should be able to predict which reactions will produce the super-heavy elements most readily.

In nuclear spectroscopy, heavy-ion fusion-evaporation reactions are used to create nuclei in excited states. The experimenters may then observe the gamma rays emitted by the nucleus as it cools, and make deductions about the structure of the nucleus under observation. For these purposes it is useful to be able to predict the probabilities of forming the various possible evaporation residues as against the probability of fission, and the range of angular momenta with which each evaporation residue may be formed (which is also limited by competition with fission processes).

1.3 The Fission Process

According to the transition state model [VAN73], the fission process is governed by a critical state called the "saddle point". Classically, the compound nucleus is committed to fission once it elongates beyond the saddle point. This is the compound nuclear state for which which the potential energy of the system is a maximum in terms of the system's elongation, but a minimum in terms of all other parameters, such as mass asymmetry. In other words, it is a saddle-point on the potential-energy surface. We cannot detect directly how elongated the compound nucleus is at the saddle point, but theoretical calculations show that a compound nucleus with high atomic number and high angular momentum has a smaller elongation at the saddle-point than one with lower Z or lower angular momentum.

It is necessary, therefore, to use theoretical models to relate concepts such as saddle-point shape to quantities we can observe experimentally, such as the total fission cross-section and the fission fragment anisotropy.

1.3.1 The Fission Fragment Anisotropy

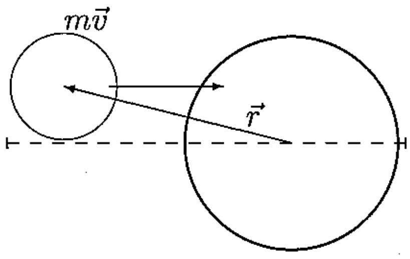

Figure 1.3: A projectile, colliding with a target nucleus, brings in some angular momentum.

In the case of fusion-fission experiments, the projectile nucleus always travels in the same direction (the beam direction); the velocity vector $\vec{v}$ is the same for all projectile nuclei. The angular momentum $\vec{l}$ brought in by the projectile is given by $\vec{l} = m\vec{v} \times \vec{r}$; it is perpendicular to $\vec{v}$.

(Where we denote angular momenta with a vector, eg $\vec{l}$, this is shorthand for the angular momentum vector specified by a set of angular momentum quantum numbers, multiplied by $\hbar$. Where angular momenta are used in calculations, it is the quantum number that should be used, and if $\hbar$ is needed it is included

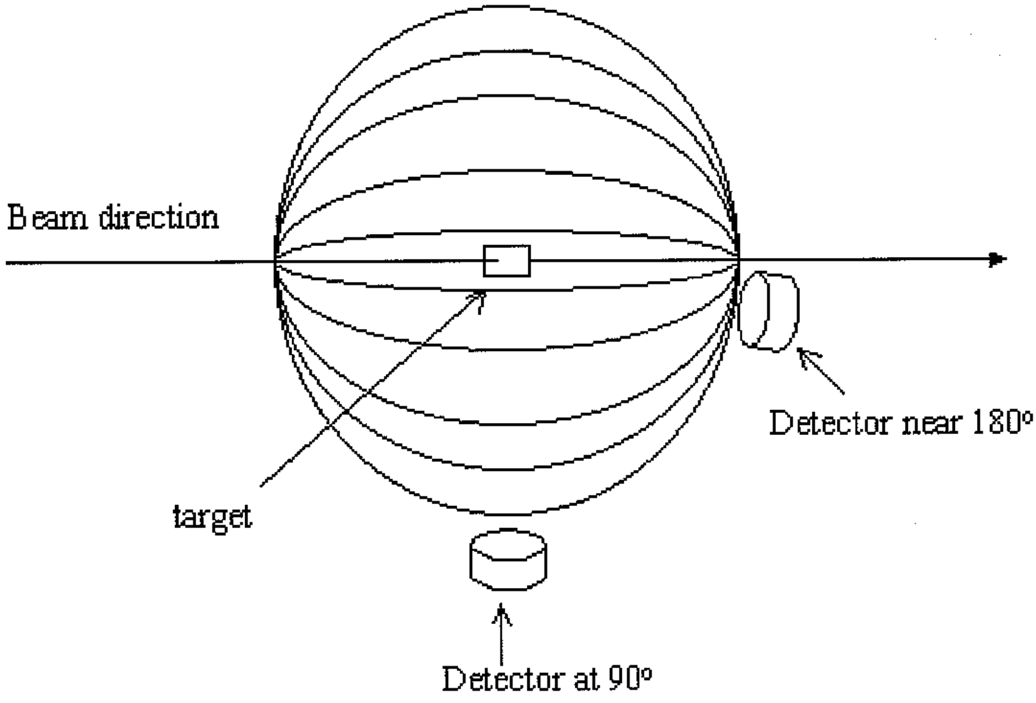

Figure 1.4: Each disk in this figure represents the range of probable trajectories for the fission fragments for one value of the azimuthal collision angle ϕ. Note how all the disks meet at 0° and 180°; more fission fragments are detected at these forward and backward angles than at 90°.

explicitly.)

This is important because when the compound nucleus fissions, the energy required is minimized when the fragments separate perpendicular to the total angular momentum. If all the angular momentum of the compound nucleus comes from the collision with the projectile, then a small detector placed at 0° or 180° to the beam direction will detect fission fragments from every possible azimuthal angle; whereas a detector placed at 90° to the beam direction will detect fission fragments from only a small range of azimuthal angles, as shown in Figure 1.4. Thus we observe an anisotropy in the fission fragment angular distribution.

In experiments, we look at the fission fragment differential cross-section as a function of the angle θ relative to the beam direction: $W(\theta) = \frac{d\sigma(\theta)}{d\Omega}$. The anisotropy A is defined as the ratio of this fission fragment differential cross-section at 0° or

180° to the differential cross-section at 90° to the beam direction:

$$A = \frac{W(0^\circ, 180^\circ)}{W(90^\circ)} \tag{1.1}$$

1.3.2 Relating the Anisotropy to other quantities.

The experimental fission fragment anisotropy depends on the distribution of total angular momentum $\vec{J}$, the nuclear temperature T, and the effective moment of inertia of the nucleus at the saddle point I_{eff}, approximately as [HAL58]:

$$A \approx 1 + \frac{\langle J^2 \rangle \hbar^2}{4\mathcal{I}_{eff} T} \tag{1.2}$$

More precise expressions will be given in Section 2.2.2 and Chapter 3.

In order to use the anisotropy to infer any of the quantities on which it depends, it is necessary to determine or model each of the other quantities; and then the inference of the desired quantity is only as good as the models the other quantities came from. $\mathcal{I}_{eff}$ is unavoidably model-dependent. T can be determined from the excitation energy of the compound nucleus, although this requires the level density a which is also model-dependent. In fission studies, $\vec{J}$ is often taken to be the same as the orbital angular momentum $\vec{l}$. $|\vec{l}|$ may be experimentally determined using the following variety of methods:

γ-ray multiplicities The number of γ-rays emitted by an evaporation residue is roughly proportional to the angular momentum l with which that evaporation residue was formed.

Isomer Ratios Some isotopes have isomeric states with higher spin, which may decay via γ-ray de-excitation or via α or β emission. The isomeric state may be identified according to the energy of the detected particle or γ-ray. The relative cross-sections are related to the proportion of the angular momentum distribution $\sigma(l)$ above the spin of the higher state.

Fusion Cross-section Models show that the angular momentum distribution $\sigma(l)$ is related to the fusion excitation function $\sigma(E_{CM})$. A reliable method has been developed for calculating the distribution $\sigma(l)$ and is described in Section 2.1.2.3.

1.4 How does J depend on the fusion process?

The total angular momentum $\vec{J}$ of the compound nucleus is the sum of the angular momentum $\vec{l}$ brought in by the projectile, and the ground-state spins $\vec{I_0}$ and $\vec{I_1}$ of the target and projectile nuclei respectively. $\vec{l}$ is always perpendicular to the beam direction, and increases with projectile velocity.

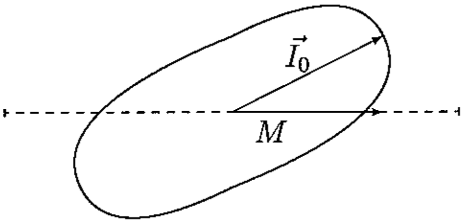

Figure 1.5: The projection of the nuclear elongation axis on the beam direction.

If the reaction involves a spherical target nucleus with significant spin $\vec{I_0}$, then the projection $M\hbar$ of $\vec{J}$ on the beam axis is no longer zero; M will range uniformly from $-I_0$ to $+I_0$. If instead we have a prolate-deformed (football-shaped) target nucleus with significant spin I_0, at energies below the average fusion barrier the projectile will be more likely to fuse with the tips of the target [STO80] rather than the equator. This is important because I_0 will be closely aligned with the nuclear deformation axis, as shown in Figure 1.5. At beam energies slightly below the average fusion barrier, fusion with the tips means the target nucleus lies with its deformation axis on or close to the beam axis. This means $\vec{I_0}$ is aligned with the beam axis, and hence M will preferentially take the values $\pm I_0$.

1.5 How does J influence the fission process?

$\vec{J}$ is significant when it comes to fission for two reasons. For larger $|\vec{J}|$, fission is more probable. And when fission does occur, the resulting fission fragments separate preferentially in directions nearly perpendicular to $\vec{J}$, so that in most circumstances the anisotropy of fission fragments varies as shown in equation 1.2.

However, equation 1.2 is approximately correct only if $\vec{J}$ is perpendicular to the beam direction. This is not always the case, as discussed in Section 1.4. When $\vec{J}$ makes an angle $90° + \alpha$ with the beam axis, the fission fragments will be distributed about α relative to the beam axis, as shown in Figure 1.6, and the observed anisotropy is reduced. This reduction can be stronger if the reacting nucleus with ground-state spin is strongly prolate-deformed than if it were spherical, because in

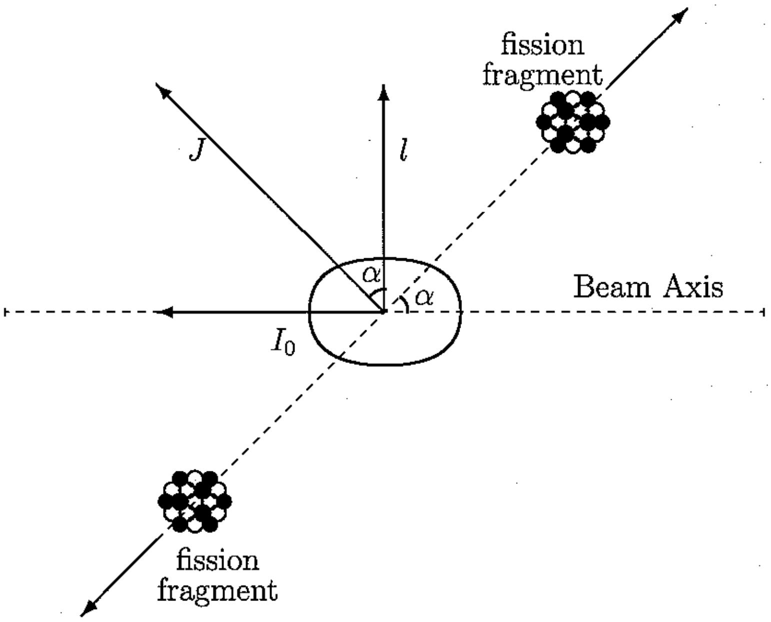

Figure 1.6: If $\vec{J}$ is not perpendicular to the beam axis, then the observed fission fragments are most likely to separate in a plane at an angle to the beam axis, rather than in a plane including the beam axis.

the deformed case a higher proportion of events have larger α.

1.6 Quasi-fission

Quasi-fission events occur when the projectile and target do not form a compact compound nucleus, but form an elongated di-nucleus which then undergoes fission. The fission fragments emerge with a higher anisotropy compared to fragments from fusion-fission events. However, the reason for this is unclear. Is it because the elongated di-nucleus, with its high moment of inertia, is more strongly affected by the angular momentum of the combined system? Or does the di-nucleus not have time to respond to the angular momentum of the system, and does it simply "remember" the direction the projectile came from? In the first case, one would predict that quasi-fission anisotropies would be very strongly affected by ground-state nuclear spins. In the second case, ground-state nuclear spins might have little effect. In this work we examine the effect of nuclear ground-state spin on quasi-fission anisotropies, theoretically and experimentally.

1.7 Present work

In the present work, we seek to test our understanding of the fusion and fission processes by varying the total angular momentum distribution $\sigma(J)$, and the projection M of $\vec{J}$ on the beam axis, by comparing two (or more) very similar reactions, one of which involves a nucleus with significant ground-state spin.

The structure of the rest of this thesis is as follows:

Chapter 2: Standard Theory The basic theory of heavy-ion fusion fission reactions is outlined, with emphasis on the calculation of angular momentum distributions and the probability of fission.

Chapter 3: Extended Theory This chapter covers the inclusion of ground-state nuclear spin in calculations by examining the results of applying established theory, and by extending the existing theory to incorporate the effects associated with nuclear deformation.

Chapter 4: Experiment and Analysis Techniques The experimental methods and associated analysis procedures used in this thesis are described.

Chapter 5: Experimental Anisotropies from a High-spin Target The results of measurements on the reactions ^{31}P+^{175,176}Lu and ^{28,29}Si+^{178}Hf are examined and compared to model calculations.

Chapter 6: Quasi-fission and Target Spin Possible theoretical models for quasi-fission are discussed, along with how ground-state spin might be incorporated, before comparing the results of such models with experimental measurements on the reactions ^{16}O+^{235,238}U.

Chapter 7: Conclusion This chapter summarizes the material presented in this work, and highlights its most important findings.

Appendix A: Simulations This appendix covers the applicability and use of the various programs written for and used in this project.

Appendix B: Data Files This appendix provides input data files for some of the programs described in Appendix A, as used for calculations in this thesis.

CHAPTER 2

Standard Theory

The major goal of this work is to predict and observe the effect of ground-state nuclear spin on fusion-fission reactions. This constitutes a sensitive test of our understanding of the role of angular momentum in both the fusion and fission processes.

In this chapter, we examine the fusion process, setting out the present understanding, and showing that this permits us to reliably obtain the fusion angular momentum distribution or l-distribution. We then examine the fission process, calculating the total fission angular momentum distribution from the fusion angular momentum distribution according to the competition with evaporation residues, and relating the fission angular momentum distribution to the fission fragment anisotropy.

2.1 The Fusion Process

Fusion is the process whereby two nuclei merge to form a single equilibrated compound nucleus. The existence of such a state, with multiple competing decay paths, as opposed to a set of different states each with different decay paths, was proposed by Bohr [BOH36]. Bohr's independence hypothesis states that once a compound nucleus is formed it has a particular mass, charge, excitation energy and angular momentum (all conserved quantities), and its decay is independent of its formation. The failure of certain nuclear reactions to conform with this hypothesis (e.g. quasi-fission) is discussed in Chapter 6.

In the simplest picture of fusion, both projectile and target nuclei may be treated as inert, positively charged spheres. They interact according to the repulsive electrostatic force between them, unless they get close enough to touch; in which case they fuse, due to attraction of the nuclear surfaces. This simple model involves most of the important concepts and is quite effective in many cases. However, there are other effects that have significant consequences, which we will also describe in this section.

2.1.1 The Basics

2.1.1.1 Nuclear Potential

In the absence of nuclear structure effects, the potential between two nuclei may be described in terms of a single degree of freedom: the distance r between the centres of the two nuclei. The total potential between two interacting nuclei is then made up of three parts: nuclear, Coulomb, and centrifugal.

The precise form of the nuclear potential is not wholly determined; there are various algebraic forms often used in calculations. The general features are well established; the force is strong and attractive when two nuclei touch, but small or zero when the nuclei are widely separated. The following "Woods-Saxon" form of the nuclear potential is widely used, and will be used throughout this work:

$$V_n(r) = \frac{-V_0}{1 + \exp[(r - R_N)/a_0]} \tag{2.1}$$

where V_0 is the potential depth, a_0 the surface diffuseness, and R_N is related to the potential radius parameter r_0 according to $R_N = r_0(A_0^{1/3} + A_1^{1/3})$. Z and A are the proton and nucleon numbers for the target and projectile nuclei (denoted by subscripts of 0 and 1 respectively).

The electrostatic component of the nuclear potential is the well-known Coulomb potential energy:

$$\begin{aligned} V_c(r) &= \tfrac{Z_0 Z_1 e^2}{4\pi\epsilon_0 r} && \text{for } r \geq R_C \\ &= \tfrac{Z_0 Z_1 e^2 (3R_C^2 - r^2)}{8\pi\epsilon_0 R_C^3} && \text{for } r < R_C \end{aligned} \tag{2.2}$$

where $R_C = 1.2(A_0^{1/3} + A_1^{1/3})$.

The third component of the nuclear potential comes from conservation of angular momentum, and comprises the component of kinetic energy of the system required to conserve the angular momentum l:

$$V_l(r) = \frac{l(l+1)\hbar^2}{2\mu r^2} \tag{2.3}$$

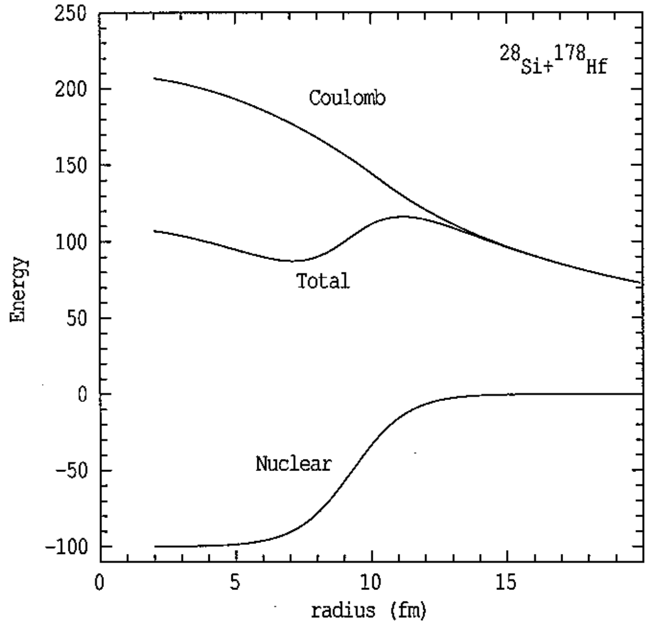

Figure 2.1: The Coulomb barrier.

where μ is the reduced mass of the system. It results in a projectile approaching the target with high angular momentum (i.e. high impact parameter b, as illustrated in Figure 2.3(b)) being deflected away from its initial direction.

The total is simply given by:

$$V(r) = V_n(r) + V_c(r) + V_l(r) \tag{2.4}$$

2.1.1.2 The Coulomb Barrier

In order for two nuclei to fuse, the nuclei must get sufficiently close together that the nuclear force overcomes the repulsive "Coulomb" (electrostatic) force between the charged nuclei. Because the energy tied up in conserving angular momentum, $V_l(r)$, is positive or zero, fusion will be easiest when the angular momentum is zero (i.e. a head-on collision). Figure 2.1 shows the individual Coulomb and nuclear potentials, and the total potential for $l = 0$.

Classically, the projectile will fuse with the target if it comes in with enough energy to pass over the local maximum into the potential pocket. The local maximum is called the Coulomb Barrier; it has a height B_0 and a barrier radius R_0. For $l > 0$ the barrier is at a higher energy, and a slightly smaller radius, as shown in Figure 2.2 for four nuclear potentials for different angular momenta, calculated

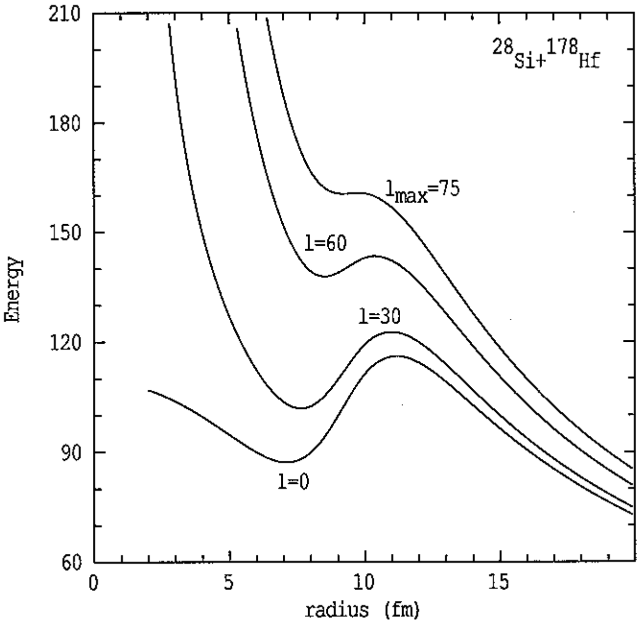

Figure 2.2: l-dependent fusion barriers for a spherical system.

according to Equation 2.4. But at sufficiently high angular momentum ($l > l_{max}$), the fusion pocket disappears, and even if the projectile has sufficient energy, fusion doesn't occur.

Quantum-mechanically, there is a probability that the projectile may tunnel through the barrier even if its energy is too low, or be reflected from the barrier even though its energy is high enough to pass over it.

2.1.1.3 Angular momentum

The angular momentum l brought in by the projectile has a strong influence on the probability of fusion, as is obvious from Figure 2.2. For a given beam energy, the projectile velocity $\vec{v}$ is fixed, and we would like to know the distribution $\sigma(l)$ of angular momenta $\vec{l} = m\vec{v} \times \vec{r}$ for fused systems; where $\vec{r}$ is the vector between the centres of the two nuclei, as shown in Figure 2.3(c). The impact parameter b is defined as the perpendicular distance between the velocity vector at infinity and a parallel line through the centre of the nucleus, as illustrated in Figure 2.3(b); then we obtain the simplified equation $|\vec{l}| = mvb$.

For small b we get small l as illustrated in Figure 2.3(a), but there is a larger area associated with larger b and hence larger l (Figure 2.3(b)). When b gets too large

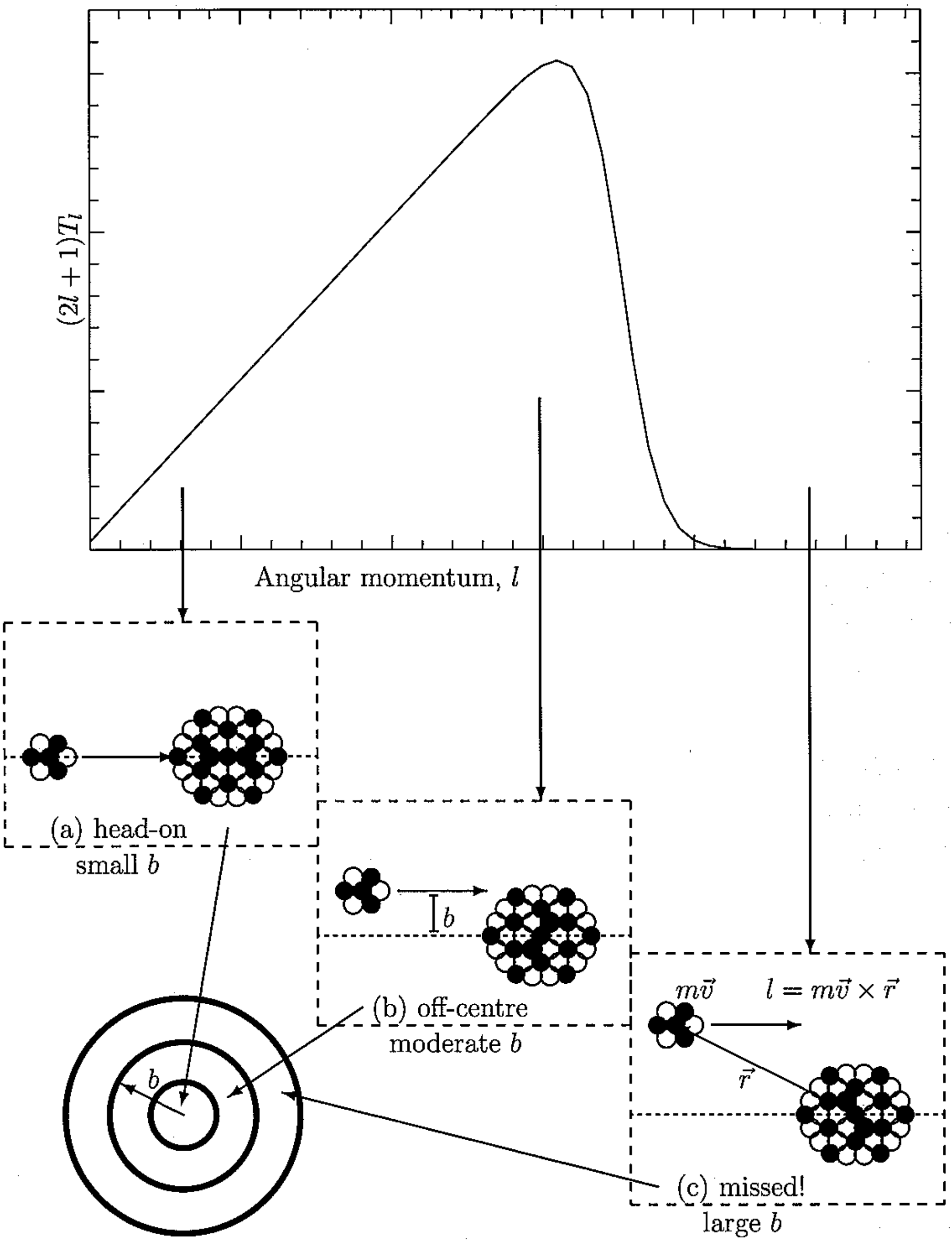

Figure 2.3: Angular Momentum Distributions for a reaction involving spherical, inert nuclei.

the projectile does not get close enough to the target to fuse with it (Figure 2.3(c)). This gives us a roughly triangular distribution, with a cut-off at high l, as shown in the upper part of Figure 2.3. (The distribution would be precisely triangular if the classical description applied, meaning that there was neither below-barrier tunnelling nor above-barrier reflection.)

2.1.1.4 Cross-section

The cross-section σ is a measure of the probability of a reaction occurring. From the experimenter's perspective, it is related to the number N of times that reaction occurs by:

$$N = \sigma N_{projectiles} N_{targets} / A_{beam} \tag{2.5}$$

where $N_{projectiles}$ is the number of incident particles in the beam, and $N_{targets}$ is the number of nuclei in the target in the area A_{beam} illuminated by the beam. However, in practice (a) not all events are detected, simply because available detectors rarely have 4π steradian coverage; and (b) detectable particles may emerge with some angular distribution, so that the same detector may see different numbers of particles for the same reaction rate, depending on the angle at which it is placed. It is therefore often desirable to work with the *differential cross-section* $\frac{d\sigma(\theta,\phi)}{d\Omega}$.

The differential cross-section is simply the cross-section per unit solid angle. Most heavy ion experiments involving a beam of projectiles striking a target have cylindrical symmetry. Detector areas are defined in terms of solid angle, so the quantity $\frac{d\sigma(\theta)}{d\Omega}$ is readily measured. Rutherford scattering is an example of a reaction where $\frac{d\sigma(\theta)}{d\Omega}$ does vary with θ; most incident projectiles are scattered through very small angles, with only a few particles being scattered into backward angles. Fusion-fission events also exhibit a strong variation in the differential cross-section with θ.

One type of cross-section important in this work is the fusion cross-section. Once two nuclei touch, collisions between individual nucleons rapidly convert kinetic energy into internal excitation energy. This is why, the two nuclei do generally fuse rather than re-separating (or are at least "captured"; see Chapter 6), once inside the Coulomb barrier. This justifies the assumption, in the one-dimensional barrier penetration model and some other models, that the nuclei will fuse with unit probability if the projectile penetrates inside the barrier.

The fusion cross-section is given by:

$$\sigma(E) = \frac{\pi\hbar^2}{2\mu E}\sum_{l=0}^{\infty}(2l+1)T_l(E) \tag{2.6}$$

where μ is the reduced mass of the system, E is the centre of mass energy, and T_l is the barrier transmission probability for a given angular momentum l.

For many purposes what is required is not the fusion cross-section at a single energy, but the fusion cross-section as a function of energy; this is called the "excitation function". The energy used is generally not the "lab" energy E_{lab} (measured in the reference frame where the target nucleus is stationary, which is usually the laboratory reference frame) but is the centre of mass energy $E_{c.m.}$ (measured, of course, in the centre of mass reference frame). The two are related simply by $E_{c.m.} = \frac{E_{lab}A_{tgt}}{A_{tgt}+A_{prj}}$.

2.1.1.5 Reduced Cross-section

For certain applications, the reduced cross-section may be defined. The reduced cross-section has a reduced dependence on the projectile and target combination used, and is related to the total cross-section according to:

$$\tilde{\sigma}(E) = \sigma(E)\frac{2\mu E}{\pi\hbar^2} = \sum_{l=0}^{\infty}(2l+1)T_l(E) \tag{2.7}$$

and retains dependence only on $T_l(E)$. $T_l(E)$ is bounded in the range $0 < T_l(E) < 1$, and should saturate at 1 when l is small and E is large.

The reduced cross-section is most applicable when considering formation of evaporation residues, which only appear at low l in fairly fissile systems. (See Section 2.2.1.3.) Because Bohr's independence hypothesis states that the decay of a compound nucleus is independent of its formation, at high beam energies where the relevant $T_l(E)$ should approach unity, the reduced cross-section for evaporation residue formation should be independent of the reaction used to form the compound nucleus.

2.1.2 Coupled Channels model of Fusion

The one-dimensional barrier penetration model, where $T_l(E)$ depends only on l and E, may be appropriate in situations where the probability of fusion occurring

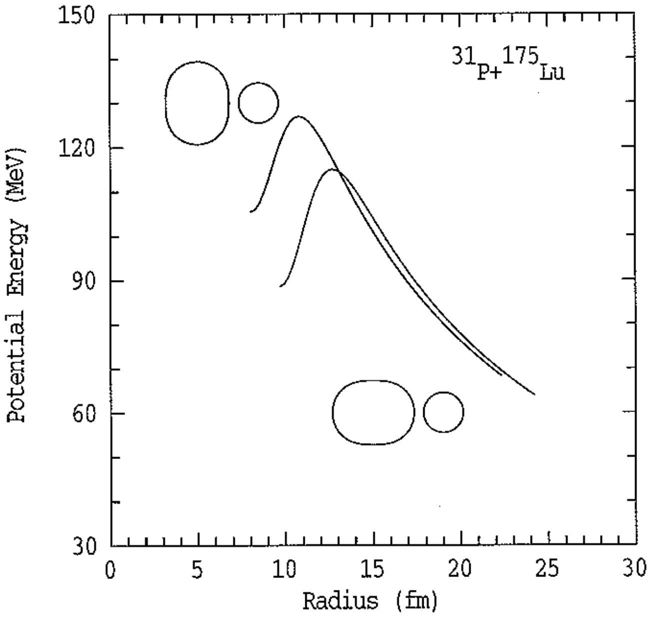

Figure 2.4: The calculated fusion barriers for ^{31}P+^{175}Lu, corresponding to two extreme orientations of the prolate deformed target nucleus. Collisions with the tip of the deformed nucleus results in a lower fusion barrier (green line) than collisions with the sides (black line).

depends on only one degree of freedom (the relative separation r of the target and projectile). However, this is not always the case. Where other degrees of freedom are significant, sub-barrier fusion cross-sections are typically increased by a few orders of magnitude.

2.1.2.1 Nuclear Deformation

Consider a reaction in which one of the nuclei has a prolate deformation. Assuming that the nuclei are not excessively heavy, fusion will occur when the nuclei get close enough to touch. Classically, the nucleus can be described as having an arbitrarily well-defined shape, and in this picture we can easily see that there is less Coulomb repulsion when the nuclei touch at the tip of the deformed nucleus, as illustrated in green in Figure 2.4, as the centres of charge are separated by a larger distance than when the projectile strikes the target at its narrower equator (Figure 2.4, black line) where the Coulomb repulsion is higher. Thus there are different fusion barriers for these different nuclear orientations. In a collision the target and projectile can be oriented at any angle between these two extremes, giving rise to barriers which lie between the two barriers described above.

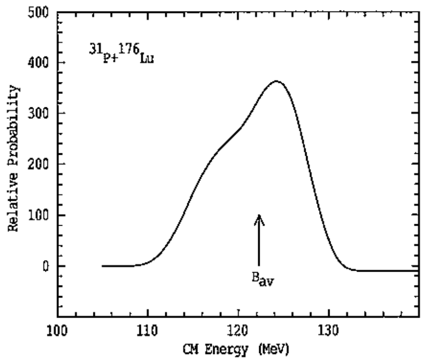

Figure 2.5: The effective fusion barrier distribution, corresponding to all different orientations of a deformed target nucleus, and including quantum-mechanical tunnelling effects.

In the language of quantum physics, there is a coupling to a series of rotational excited states of the deformed nucleus. The distribution of barrier heights encountered in the collision is centered about the average barrier B_{av}, as illustrated in Figure 2.5. In this case B_{av} is equal to the barrier that would be encountered if both target and projectile nuclei were spherical. Thus, at an energy $E < B_{av}$, classically no fusion will occur for a spherical target and projectile. However, for a deformed target, there exist barriers lower than B_{av}.

Because the tunnelling probability depends exponentially on the difference between the barrier height and the projectile energy, the fraction of projectiles encountering the lower barrier result in significantly more tunnelling than would be observed if all particles encountered the average barrier. The sub-barrier fusion cross-sections are therefore dramatically increased.

Similarly, couplings to vibrational excited states or to nucleon transfer channels also enhance the probability of fusion at low energies.

2.1.2.2 Mathematics of coupled-channels calculations

The coupled-channels equations may be written [DAS98]:

$$(T_i + V(r) - (E - \epsilon_i))\psi_i(r) = \sum_j V_{ij}(r)\psi_j(r) \tag{2.8}$$

where r is the target-projectile separation, and T is the kinetic energy operator. The label i enumerates all possible combinations of states of the target and the projectile, and ϵ_i is the total excitation energy above the ground states, while the state $\psi_i(r)$ describes the relative motion of the two nuclei. $V(r)$ is the internuclear potential $(V_C(r) + V_N(r)$, usually evaluated according to Equations 2.2 and 2.1) and the matrix elements $V_{ij}(r)$ specify elements of the coupling Hamiltonian between the states i, j.

In theory, then, there are an infinite number of channels to consider. In practice only a limited number n of channels have significant strength, and the rest may be neglected, truncating the problem. This strength consideration has the effect of excluding all single-particle inelastic channels, selecting only collective excitations (rotation and vibration) and certain nucleon transfer channels.

For the purposes of practical calculations, several simplifying assumptions are often used [HAG97]. The purpose of these assumptions is to reduce the problem by either reducing the number of coupled channels to be considered, and/or finding a way to decouple the equations into several single-channel equations, thereby drastically reducing the complexity of the calculations. These assumptions are:

zero excitation energies. The excitation energies ϵ_i are treated as zero. This means, effectively, that the reaction occurs much faster than the nuclei can respond, so this approximation is also called "sudden" or "sudden tunnelling". (The opposite assumption applies where the excitation energy ϵ_i associated with a channel is large, and therefore the target and projectile nuclei can be thought of as continuously rearranging themselves into the lowest energy configuration. This is called the **adiabatic limit.**)

no-Coriolis. The kinetic energy operator T_i depends on the channel i through the centrifugal term $l_i(l_i+1)/2\mu r^2$, where the total angular momentum $J = l_i + I_i$ is the same for all channels. If the channel spin I_i is not too large, we make the no-Coriolis approximation $l_i(l_i+1)/2\mu r^2 \approx J(J+1)/2\mu r^2$ [KRU93], or, equivalently, $T_i \approx T_0$. This is also called the iso-centrifugal approximation or orbital sudden approximation.

linear coupling. The nuclear coupling potential $V_{ij}(r)$ is assumed to be linear with respect to the coordinate β of the nuclear vibrational excitation. (In the simplified calculations employing this assumption, the calculations for rotational nuclei are usually done in the classical limit.) This assumption is applied when determining $V_{ij}(r)$ from β from existing nuclear data; it affects both the input strength and the radial dependence of $V_{ij}(r)$. This assumption has no impact on the decoupling of the coupled channels (see the next two points), although it reduces computational complexity. The importance and limitations of this assumption are discussed in [HAG97B].

constant coupling. The coupling potential $V_{ij}(r)$ is assumed to be constant over the interaction range. It is usually taken to be the value at the barrier radius r_B.

CCMOD, a simplified coupled-channels code. The CCMOD program used in this work to generate coupled-channels cross-sections and angular momentum distributions uses the no-Coriolis approximation, and the linear coupling approximation for vibrational excitations. Rotational excitations are handled by using a statically deformed potential, evaluating cross-sections in one degree steps in target and projectile orientations. This use of a statically deformed potential amounts to coupling to all orders of rotational excitation (the linear coupling approximation is *not* used), and to all states in the rotational band, using the zero excitation energy approximation. This treatment has been shown to closely correspond to the exact quantum-mechanical calculations as long as the excitation energy of the first rotational state is low [MOR01]. In contrast, for vibrational excitations, coupling is only done to first order in β. The transfer channels are treated in an approximate way by using the 1-nucleon transfer form factor as given in [POL83]. CCMOD uses an approximate treatment of excitation energies as described below.

We define a matrix:

$$M_{ij}(r) = -\epsilon_i \delta_{ij} + V_{ij}(r) \tag{2.9}$$

as this, together with the no-Coriolis approximation (which is generally reasonable [ESB87]), allows us to rewrite Equation 2.8 as:

$$(T_0 + V(r) - E)\psi_i(r) = \sum_j M_{ij}(r)\psi_j(r), \tag{2.10}$$

Decoupling the coupled channels usually amounts to finding a unitary matrix $\Lambda(r)$ that diagonalizes $M_{ij}(r)$. If each excited channel couples only to the ground state, and not to other coupled channels, then $M_{ij}(r)$ is mostly zero:

$$M = \begin{pmatrix} 0 & V_{0,1}(r) & V_{0,2}(r) & \dots & V_{0,n}(r) \\ V_{1,0}(r) & \epsilon_1 & 0 & \dots & 0 \\ \vdots & \vdots & \vdots & \ddots & \vdots \\ V_{n,0}(r) & 0 & 0 & \dots & \epsilon_n \end{pmatrix} \tag{2.11}$$

Once $\Lambda(r)$ is calculated, a new set of basis states may be defined from linear superpositions of the physical channels, according to:

$$\Psi_\alpha = \sum_i \Lambda_{\alpha i}\psi_i \tag{2.12}$$

giving us the de-coupled equations:

$$(T_0 + V(r) - \lambda_\alpha(r) - E)\Psi_\alpha = 0 \tag{2.13}$$

where $\lambda_\alpha(r)$ are the eigenvalues of $M_{ij}(r)$ $(\Lambda^\dagger_{\alpha i}(r)M_{ij}(r)\Lambda_{j\beta}(r) = \lambda_\alpha(r)\delta_{\alpha\beta})$. From these decoupled equations we obtain fusion cross-sections σ_α in the same manner as σ would be obtained from the Hamiltonian in a single-barrier calculation. The fusion cross-section for the physical (ground-state) entrance channel ψ_0 is then obtained according to:

$$\sigma = \sum_\alpha |\Lambda_{0,\alpha}|^2\sigma_\alpha \tag{2.14}$$

This last step gives rise to difficulties when Λ depends on r. At what r should $\Lambda(r)$ be evaluated? If the constant coupling approximation had been used, M_{ij} would be independent of r and therefore so would Λ. If the zero excitation energy (sudden) approximation were used, and also if the elements of M all had the same dependence on r (so that $M_{ij}(r) = \Gamma_{ij}F(r)$ for some form factor $F(r)$), again Λ would be independent of r. However, the approach taken in CCMOD is to determine weighting factors $\Lambda_{0,\alpha}(r)$ at the average barrier radius $r = r_b$, although λ_α is evaluated as a function of r. This works for moderate excitation energies because the coupling strengths $V_{ij}(r)$ vary only slowly near the average barrier position, meaning that the weightings $w_\alpha = |\Lambda_{0,\alpha}|^2$ also vary only slowly (and are very similar to those obtained using the constant coupling approximation). In contrast, the barriers obtained from Equations 2.13 appear at different radii and have slightly different heights to those that would be obtained using the constant coupling approximation. The fusion cross-sections σ_α are very sensitive to this variation in barrier height.

There are known limitations with this procedure and the other approximations used by CCMOD [HAG97]. However, for the purposes of this work we are interested in the angular momentum distribution; and, as shown in Section 2.1.2.3 and Refs. [BAL96, ROW93], if the excitation function is well reproduced, the angular momentum distributions will also be well reproduced, irrespective of whether or not the channel couplings are identified and treated accurately.

2.1.2.3 Relating the angular momentum distribution to the excitation function

With or without coupled channels, fusion excitation functions appear to be relatively smooth and featureless. In contrast, the fusion angular momentum distributions show structure which depends on the coupled channels that are significant in that reaction. We show here how the fusion angular momentum distribution $\sigma_l(E)$ may be related to the first derivative of the excitation function.

At any given energy E the fusion cross-section σ comprises the sum of all the partial waves $\sigma_l(E)$:

$$\sigma(E) = \sum_{l=0}^{\infty} \sigma_l(E) = \frac{\pi\hbar^2}{2\mu E} \sum_{l=0}^{\infty} (2l+1) T_l(E) \tag{2.15}$$

The key step in the reversal of this equation to yield $\sigma_l(E)$ is the reduction of the countably infinite set of functions $T_l(E)$ to a single function $T_0(E)$, by assuming:

$$T_l(E) = T_0(E - l(l+1)\hbar^2/2\mu r^2) \tag{2.16}$$

This assumption will fail for sufficiently high l, because the fusion pocket disappears (as shown in Section 2.1.1.2), so $T_l(E)$ becomes zero irrespective of E. This is important at energies well above the Coulomb barrier. It also fails at low energies, where quantum-mechanical tunnelling effects dominate. However, it does hold near the Coulomb barrier. In that case we are dealing with the transformation between $T_0(E)$ and $\sigma(E)$:

$$\sigma(E) = \frac{\pi\hbar^2}{2\mu E} \sum_{l=0}^{\infty} (2l+1) T_0(E - l(l+1)\hbar^2/2\mu r^2) \tag{2.17}$$

This transformation exists, is continuous, and has no pathological behaviours preventing it being "one-to-one" and "onto", which allows the existence of a continuous inverse to be demonstrated mathematically. Thus, if the excitation function is reproduced sufficiently well, the angular momentum distribution σ_l is also correct within a corresponding uncertainty.

Pragmatically, obtaining such an inverse transformation is non-trivial without making approximations like the following:

$$\begin{aligned} \sigma(E) &= \frac{\pi\hbar^2}{2\mu E} \sum_{l=0}^{\infty} (2l+1) T_0(E - l(l+1)\hbar^2/2\mu r^2) \\ &\approx \frac{\pi\hbar^2}{2\mu E} \int_{l=0}^{\infty} (2l+1) T_0(E - l(l+1)\hbar^2/2\mu r^2) dl \end{aligned} \tag{2.18}$$

Given this approximation (which is good if $T_0(E)$ is slowly varying on the scale of $\Delta l = 1$, which is reasonable around the Coulomb barrier), we can use the dummy variable $E' = E - l(l+1)\hbar^2/2\mu r^2$, obtaining:

$$\begin{aligned}\sigma(E) &= \frac{\pi\hbar^2}{2\mu E}\int_{E'=E}^{E'=0}\frac{(2l+1)T_0(E')dE'}{-(2l+1)\hbar^2/2\mu r^2} \\ &= \frac{\pi r^2}{E}\int_{E'=0}^{E'=E} T_0(E')dE' \qquad (2.19)\end{aligned}$$

And in this case the inverse that obtains $T_0(E)$ from $\sigma(E)$ becomes obvious:

$$T_0(E) = \frac{1}{\pi r^2}\frac{d(E\sigma)}{dE} \qquad (2.20)$$

where r takes its value at the fusion barrier radius.

One detail that has been neglected in this derivation is the fact that the fusion barrier radius r may vary for each fusion channel α. As all these operations are linear, we may independently relate $T_{0,\alpha}(E)$ to $\sigma_\alpha(E)$ for each channel α, encountering difficulties only when relating the total cross-section to the total transmission probability using Equation 2.20, as r_α takes slightly different values for the different channels.

2.1.2.4 The Barrier Distribution

It has been shown that the transmission probability $T_0(E)$ is related to the first derivative of the fusion excitation function $\sigma(E)$. The derivative of the transmission probability in turn gives us the barrier distribution. It has been shown that the barrier distribution is a sensitive and useful method for examining structure associated with coupled channels [DAS98, and references therein]. We examine here the applicability of the barrier distribution.

The effect of coupled-channels have already been discussed in terms of fusion barriers, and it has been established that a useful "barrier distribution" may be obtained from experimental data, according to [ROW91, DAS98]:

$$D_{exp}(E) = \frac{d^2(E\sigma)}{dE^2} \qquad (2.21)$$

Let us first establish the validity of this expression in the case of classical or quantum-mechanical single barrier systems. By taking the derivative of Equation 2.20 with respect to E we observe that:

$$\frac{1}{\pi r^2}\frac{d^2(E\sigma)}{dE^2} = \frac{d(T_0(E))}{dE} \qquad (2.22)$$

Classically, for a single barrier at energy B:

$$\begin{aligned} T_0(E) &= 0; E < B \\ T_0(E) &= 1; E \geq B \end{aligned} \tag{2.23}$$

and the first derivative of $T_0(E)$ is a delta-function $\delta(E-B)$. This may be interpreted as one barrier of height exactly B, encountered with unit probability.

Quantum-mechanically, consider a single parabolic potential barrier of height B and width characterised by $\hbar w$, where w is the oscillator frequency of the inverted barrier. The transmission coefficient $T_0(E)$ is [DAS98]:

$$T_0(E) = \frac{1}{1 + \exp(\frac{2\pi(B-E)}{\hbar w})} = \frac{1}{1+e^x} \tag{2.24}$$

where we define x to simplify the algebra. Then we obtain:

$$\frac{d(T_0(E))}{dE} = \frac{2\pi}{\hbar w}\frac{e^x}{(1+e^x)^2} \equiv G(E-B) \tag{2.25}$$

To compare the quantum mechanical result to the classical result, we consider $G(E-B)$ in the limit as $\hbar \to 0$. The integral under this probability distribution remains unity independent of $\hbar$; $\int_{-\infty}^{+\infty} G(E-B)dE = 1$. The distribution gets arbitrarily narrow as $\hbar \to 0$; this is one of the definitions of $\delta(E-B)$. In other words, as $\hbar \to 0$, $G(E-B) \to \delta(E-B)$ and the classical result is returned correctly.

If coupled channels are significant, the projectile nucleus may encounter one of a range of barriers, with some probability $D(B)$. The total cross-section is given according to:

$$\sigma(E) = \int \sigma(E,B)D(B)dB \tag{2.26}$$

and if we approximate all the barriers as parabolic barriers, we then have:

$$\frac{1}{\pi r^2}\frac{d^2(E\sigma)}{dE^2} = \int G(E-B)D(B)dB \tag{2.27}$$

which in the classical limit returns:

$$\frac{1}{\pi r^2}\frac{d^2(E\sigma)}{dE^2} = \int \delta(E-B)D(B)dB = D(E) \tag{2.28}$$

This is where the strength of the barrier distribution approach becomes evident. It is extremely useful for reactions where coupled channels have a significant effect.

The calculated (or measured) barrier distribution will extend over a larger range than the corresponding single barrier. It also has a particular shape which is characteristic of the energies and types of coupled channels which are important in that reaction [DAS98].

So far in this section we have discussed the barrier distribution in terms of the transmission coefficients. However, what are available in practice are cross-sections, so what is used is Equation 2.21, where $D_{exp}(E)$ differs from $D(E)$ by a constant factor πr^2 and the quantum-mechanical smoothing $G(E-B)$. Henceforth we refer only to $D_{exp}(E)$. Experimentally, the cross-section is measured with only finite accuracy at a finite number of energies. The barrier distribution is therefore evaluated numerically. At the energy $(E_1+2E_2+E_3)/4$ it is given by:

$$\frac{d^2(E\sigma)}{dE^2} = 2\left(\frac{(E\sigma)_3-(E\sigma)_2}{E_3-E_2} - \frac{E\sigma)_2-(E\sigma)_1}{E_2-E_1}\right)\left(\frac{1}{E_3-E_1}\right) \tag{2.29}$$

This introduces some further smoothing, as shown in Figure 2.6, so for the purposes of comparing experimental and theoretical barrier distributions, we calculate theoretical cross-sections and use the above equation to generate the theoretical barrier distribution.

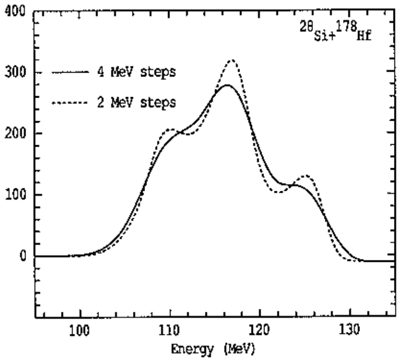

Figure 2.6: Barrier distributions calculated from the same theoretical cross-section with different energy steps.

If the energy steps are equal ($E_3-E_2 = E_2-E_1$) then the calculation simplifies to:

$$\frac{d^2(E\sigma)}{dE^2} = 2\left(\frac{(E\sigma)_3-2(E\sigma)_2+(E\sigma)_1}{\Delta E^2}\right) \tag{2.30}$$

and the associated statistical error δ is approximately:

$$\delta \simeq \left(\frac{E}{\Delta E^2}\right)\left[(\delta\sigma)_1^2+4(\delta\sigma)_2^2+(\delta\sigma)_3^2\right]^{1/2} \tag{2.31}$$

This equation, describing the propagation of uncertainties, has the following practical consequences: At high cross-sections, where the slope becomes almost constant, a 1% error in cross-section gives rise to a large error in barrier distribution. Larger energy steps result in smaller error bars. However, less of the barrier structure may be apparent, as shown in Figure 2.6. Quantum tunnelling effects mean that the true underlying barrier distribution is already smoothed over the 2–3 MeV scale. Therefore, when studying the barrier distribution in detail, it is common practice to measure the fusion cross-section to high precision in steps of approximately 1 MeV, and calculate the barrier distribution using 2 MeV steps. (Thus alternate points in the barrier distribution are entirely independent of one another.)

2.1.2.5 Relating the Barrier Distribution to the Angular momentum distribution

The structure of the barrier distribution and the angular momentum distribution are closely related, as described above. For the simple case of a single barrier, the angular momentum distribution will be a smooth, rounded-triangle shape, as shown in Figure 2.3.

If there are significant couplings, the angular momentum distribution may show more structure. Figure 2.7 illustrates this for the case of a two-peaked barrier distribution. In this case, the system sees two barriers at separate energies, and the total l-distribution is simply the sum of the l-distributions for each barrier. This linearity applies for all barrier distributions.

This then leads to one of the other major consequences of channel coupling interactions. In the presence of a barrier at lower than average energy, we have already observed that the fusion cross-section is greatly enhanced at sub-barrier energies. At above-barrier energies the cross-section is not so greatly enhanced—but because much of the cross-section comes from the lower barrier, the average angular momentum l is significantly increased.

2.2 The Fission Process

Once fusion has occurred, a compound nucleus is formed. Such compound nuclear systems, when formed by heavy ion reactions, tend to have a significant excess of energy, and often significant angular momentum. In the previous section the calculation of the fusion angular momentum distribution has been covered. The next step is to examine the subsequent evolution of the compound nucleus.

There are two main decay modes of the compound nucleus. It can emit a light

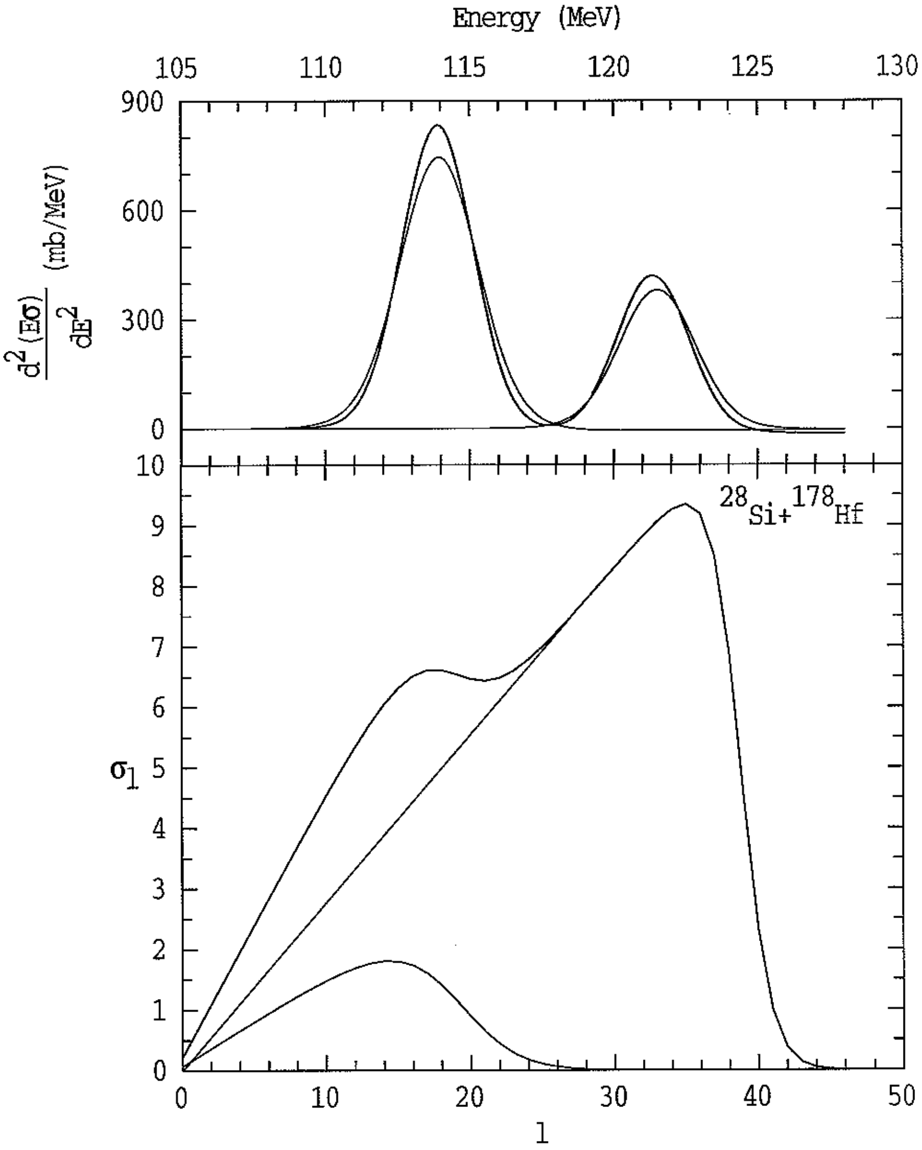

Figure 2.7: Angular Momentum Distributions from a structured distribution. Each barrier effectively contributes as if it were a single barrier, with the higher-energy barrier giving rise to the lower l-distribution; the total l-distribution is then the sum of these components.

particle (neutron, proton, or α-particle, or a γ-ray), or it can fission into two fragments. In this section we examine the angular-momentum dependent competition between these processes, and the subsequent evolution of the fissioning events.

2.2.1 Statistical Fission Decay

All calculations in this work involving fission probabilities and particle evaporation were performed using JOANNE, as developed by Lestone [LES90B] and extended by Berriman [BER01C]. In this work JOANNE has been modified to track additional information, but the probability of fission occurring is unaltered.

2.2.1.1 The Fission Barrier

Consider a spherical compound nucleus. The potential energy of the nucleus may be well described by the liquid drop model. There are two terms in this model which are sensitive to the shape of the nucleus; one describing the increase in potential energy with surface area, and one describing the Coulomb repulsion between the protons, which decreases as the nucleus elongates. For small deformations, the surface area dominates; as the elongation increases, the potential energy increases. For larger deformations, the Coulomb repulsion is more important, and the potential energy decreases with elongation, favouring fission. In between, there is an elongation where the potential energy reaches its maximum; this is called the saddle point, and the maximum energy is called the fission barrier. Once a nucleus has evolved over the saddle point, it is very likely to proceed to fission.

In this work we use the transition state model [VAN73], which assumes that fission is governed by the saddle-point properties. In particular, the fission width, the fission fragment angular distribution and the fragment mass distribution may all be determined from conditions at the saddle point.

Fission Width According to the statistical model [STO85] the probability of fission is dependent primarily on the level density at the saddle point. This is schematically illustrated in Figure 2.8. The fission width used in this work is [BER01C]:

$$\Gamma_{fis} = \frac{U_i^2}{2\pi \exp(2\sqrt{a_{eq} U_i})} \sqrt{\frac{a_f}{a_{eq}}} \int_0^{E_i - k_f B_f} \frac{\exp(2\sqrt{a_f U_{sp}})}{U_{sp}^2} d\epsilon_{sp} \qquad (2.32)$$

where:

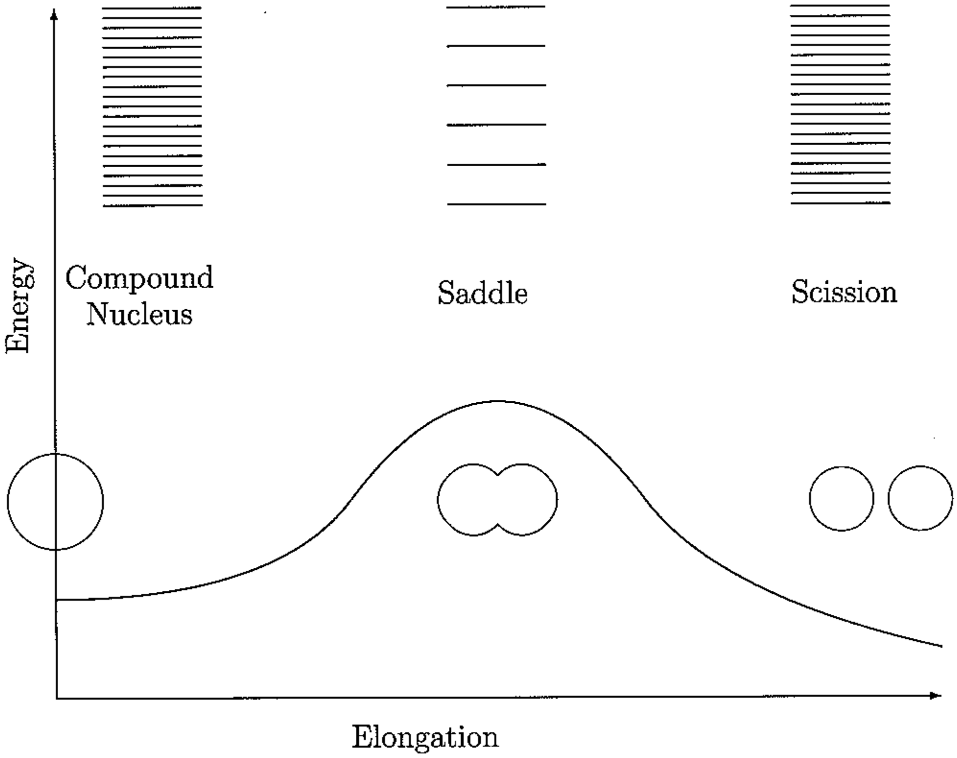

Figure 2.8: A schematic illustration of the fission barrier as a function of nuclear elongation. The compound system is sketched at three points; the spherical, equilibrated compound nucleus, where the level density (illustrated above) is quite high; the saddle point, where the potential energy is highest, and the level density lowest; and the scission point, where the compound system has split into two fragments.

B_f is the fission barrier height,

ϵ_{sp} is the kinetic energy of separation at the saddle point,

k_f is the fission barrier scaling factor,

E_i is the excitation energy of the parent nucleus,

U_i is the *thermal* energy of the parent nucleus: $U_i = E_i - E_{rot}(J_i)$, where J_i is the angular momentum of the parent nucleus,

U_{sp} is the thermal energy at the saddle point: $U_{sp} = E_i - \epsilon_{sp} - k_f B_f$,

a_f is the level density at the fission saddle point, and

a_{eq} is the level density of the parent compound nucleus at the equilibrium deformation.

The fission barrier B_f depends on the proton number Z and the nucleon number N of the compound nucleus; it is lower in the case of high Z, low N nuclei.

Angular momentum and rotational energy The fission barrier also decreases as the total angular momentum J increases. Consider a prolate-deformed compound nucleus. The moment of inertia $\mathcal{I}_{\|}$ measured about an axis parallel to the axis of symmetry, through the centre of mass, decreases as the deformation β increases. The moment of inertia $\mathcal{I}_{\perp}$ measured perpendicular to the axis of symmetry increases as β increases. For $\beta = 0$ (a spherical nucleus) the two moments are equal.

The rotational energy $E_{rot}(J)$ of the compound nucleus is given by:

$$\begin{aligned} E_{rot}(J) &= (\hbar^2/2\mathcal{I}_{\perp})(J^2 - K^2) + (\hbar^2/2\mathcal{I}_{\|})K^2 && (2.33) \\ &= (\hbar^2/2\mathcal{I}_{\perp})J^2 + (\hbar^2/2\mathcal{I}_{eff})K^2 && (2.34) \end{aligned}$$

where K is the projection of $\vec{J}$ on the nuclear symmetry axis, and the effective moment of inertia I_{eff} is defined according to:

$$1/\mathcal{I}_{eff} = 1/\mathcal{I}_{\|} - 1/\mathcal{I}_{\perp}. \qquad (2.35)$$

$\mathcal{I}_{eff}$ is non-negative; it is infinite when the elongation is zero. Therefore, tilting the nucleus relative to $\vec{J}$ requires no energy for a spherical nucleus (where the tilt is meaningless), but at a non-zero elongation, if the nuclear deformation axis is not orthogonal to $\vec{J}$, more energy is tied up in rotation.

If $K = 0$, when the nucleus elongates, $\mathcal{I}_\perp$ increases and therefore $E_{rot}(J)$ decreases; this leads to a reduced fission barrier height and more fission. For $K = |\vec{J}|$, $E_{rot}(J)$ increases with elongation. This variation in barrier heights gives rise to a distribution of fissioning fragments about $K = 0$, described further in Section 2.2.2.2.

2.2.1.2 Particle evaporation decay width

The particle evaporation widths for neutrons, protons, and α-particles are determined according to [BER01C]:

$$\begin{aligned}\Gamma_{n,p,\alpha} &= \sum_{l=0}^{\infty} \sum_{J_f=|J_i-l|}^{J_i+l} \frac{U_i^2(2s+1)(2J_f+1)}{2\pi(2J_i+1)\exp(2\sqrt{a_{eq}U_i})} \sqrt{\frac{a_{n,p,\alpha}}{a_{eq}}} \\ &\quad \int_0^{E_i-E_{rot}(J_f)-B_{n,p,\alpha}} T_l(\epsilon) \frac{\exp(2\sqrt{a_{n,p,\alpha}U_f})}{U_f^2} d\epsilon \end{aligned} \tag{2.36}$$

where:

$B_{n,p,\alpha}$ is the binding energy of the particle,

J_i is the angular momentum of the parent nucleus,

J_f is the angular momentum of the daughter nucleus,

l is the orbital angular momentum carried off by the particle,

s is the intrinsic angular momentum of the particle,

$E_{rot}(J_f)$ is the rotational energy of the daughter nucleus,

$a_{n,p,\alpha}$ is the level density of the daughter nucleus,

U_f is the thermal energy of the daughter nucleus, and

$T_l(E)$ is the particle emission probability for the angular momentum l.

Because of their charge, the binding energies of protons and α-particles are less than those of neutrons; however, the charged particles must overcome a Coulomb barrier in order to escape, which means that for the reactions of interest in this work, neutron emission is dominant. When the charged particles *do* escape, they carry off more kinetic energy than the neutrons do.

2.2.1.3 Competition between fission and evaporation

The competition between fission and particle emission depends on the relative heights of the barriers for each process. As particle emission barriers don't change with compound nucleus angular momentum, and fission barriers do reduce as angular momentum increases, fission is more probable than survival at higher angular momenta. This is schematically illustrated in Figure 2.9. This results in a "spin fractionation" effect; the angular momentum distribution of the events leading to fission is not the same as the fusion angular momentum distribution.

Fission and particle emission are not mutually exclusive processes. Fission may follow particle emission. As each evaporated particle carries away significant excitation energy, both the fission and particle evaporation widths are changed for the daughter nucleus compared to the parent. Further, the angular distribution of fission fragments is affected by the change in excitation energy. This effect and the effect of the angular momentum carried away by the evaporated particles are both included in all calculations in this thesis, except as indicated.

2.2.2 The Fission Fragment Angular Distribution

The fission fragment angular distribution is an experimentally accessible quantity which depends on several parameters which are interesting theoretically. Its dependence on the ground-state spin of the target and projectile nuclei is the main focus of this thesis, and will be discussed in Chapter 3. Here, we describe the fission fragment angular distribution in the absence of nuclear spin.

Quantitative calculations of the fission fragment anisotropy depend on two assumptions. Firstly, that the fission fragments separate along the line of the nuclear elongation axis. Secondly, that the projection K of the total angular momentum $\vec{J}$ on the nuclear elongation axis (later the fission axis) does not change as the system evolves from the saddle-point to the scission point and beyond. (Minor corrections to this assumption will be discussed in Chapter 3.)

For the purposes of these calculations we rely on the transition state model, deriving all information from the conditions at the saddle point.

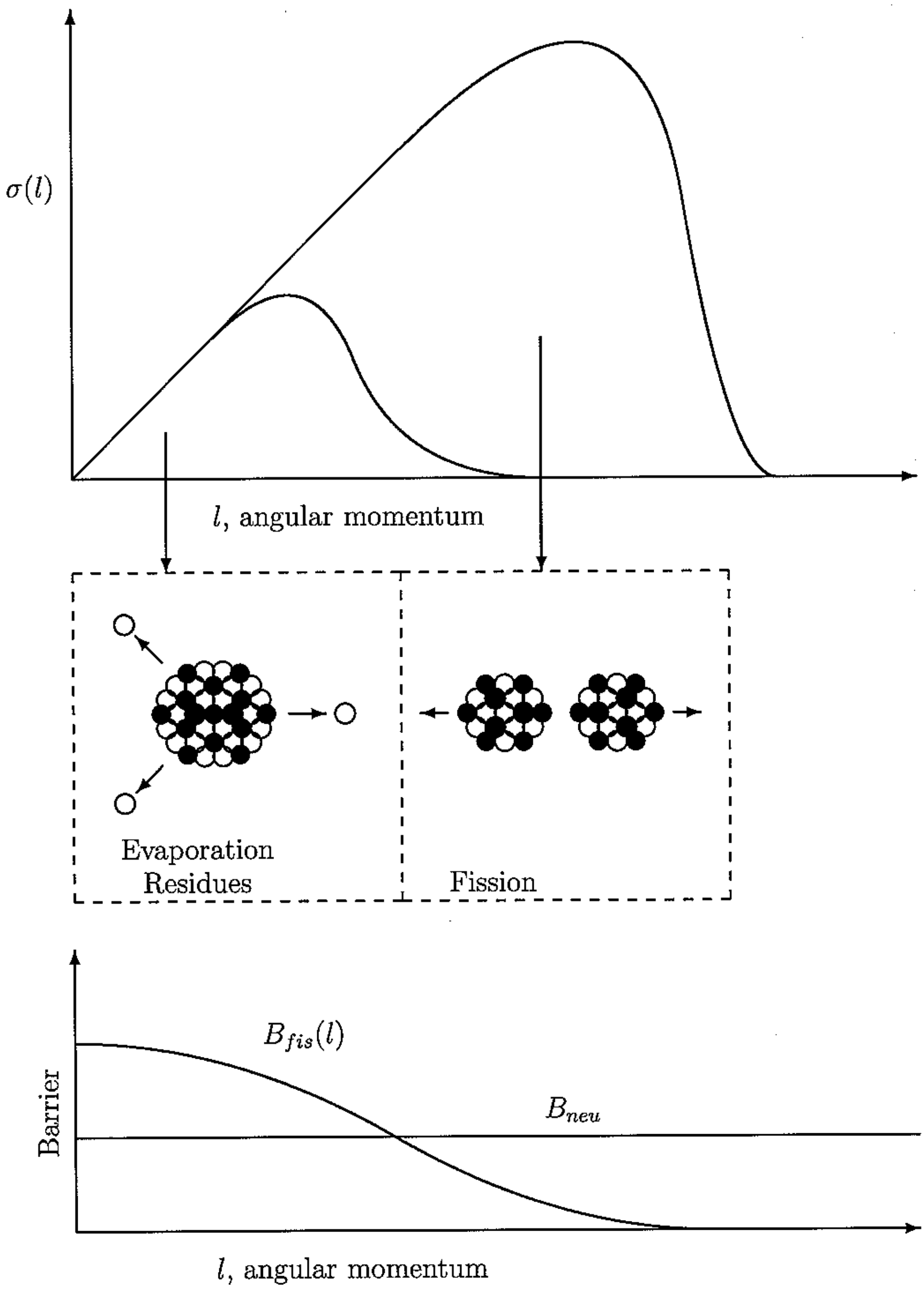

Figure 2.9: The fusion angular momentum distribution schematically illustrated in the top half of this figure is partitioned between fission and survival, with the low-l component being more likely to survive, as indicated in the graph at the bottom of this figure.

2.2.2.1 Angular momentum dependence

In the absence of ground-state nuclear spin of the reacting nuclei, the total angular momentum $\vec{J}$ differs from the fusion induced angular momentum $\vec{l}$, calculated as per Section 2.1.2.3, according to (a) spin fractionation effects, and (b) angular momentum carried away by evaporated particles, for fission events following particle emission. Both effects, as mentioned in Section 2.2.1.3, are taken into account in the computer code JOANNE. For the purpose of this discussion we assume that calculations such as JOANNE have provided us with a nuclear temperature T and either an associated angular momentum distribution $\sigma(J)$, or equivalently a set of transmission coefficients T_J.

For a given $\vec{J}$ we define projections as illustrated in Figure 2.10. $\vec{J}$ is invariant, so M, the projection of $\vec{J}$ on the beam axis, is also constant. In contrast, K, the projection of $\vec{J}$ on the nuclear elongation axis, may change, by way of the orientation of the nuclear elongation axis changing. K is therefore a measure of the tilting of the nucleus relative to $\vec{J}$.

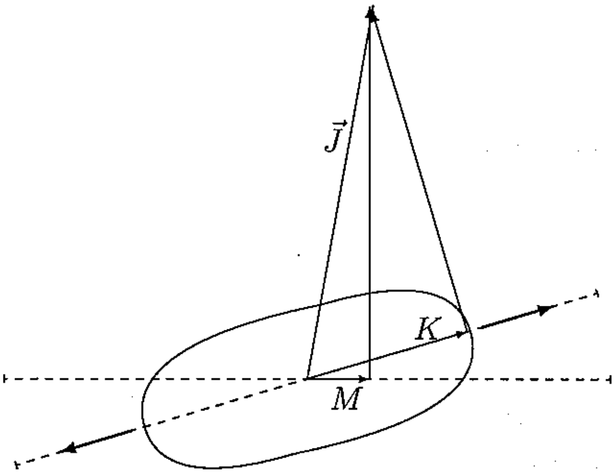

Figure 2.10: A nucleus at the saddle-point elongation. The nucleus is tilted with respect to J, so that J has a projection K on the nuclear elongation axis.

2.2.2.2 Nuclear Tilt

Since fission fragments separate along the line of the nuclear elongation axis, it is important to determine the distribution of angles the nuclear elongation axis can take, relative to the beam axis. We assume that all possible saddle-point states are equally likely; this is the statistical approach, and is equivalent to assuming that the distribution of parameters at the saddle-point corresponds to a thermal equilibrium.

The density of states is governed by the amount of thermal energy available:

$$\rho \propto \exp[(E - E_{rot}(J, K))/T] \tag{2.37}$$

where T is the nuclear temperature and E is the total energy. The rotational energy $E_{rot}(J,K)$ depends on the total spin $\vec{J}$, and its projection K on the nuclear symmetry axis, according to Equation 2.34:

$$E_{rot}(J) = (\hbar^2/2\mathcal{I}_\perp)J^2 + (\hbar^2/2\mathcal{I}_{eff})K^2$$

For fixed J, then, the density of K states is:

$$\rho(K) \propto \exp\left[\frac{-\hbar^2 K^2 \mathcal{I}_{eff}}{2T}\right] \tag{2.38}$$

We assume that $\mathcal{I}_{eff}$ depends only on $|\vec{J}|$. Then $\rho(K)$ takes a pure Gaussian form:

$$\begin{aligned} \rho(K) &\propto \exp(-K^2/2K_0^2), \quad K \leq J \\ &= 0, \qquad\qquad\qquad K > J \end{aligned} \tag{2.39}$$

where [HAL58]:

$$K_0^2 = T\mathcal{I}_{eff}/\hbar^2 \tag{2.40}$$

(In fact, $\mathcal{I}_{eff}$ should depend on both J and K, because according to the potential energy surfaces, the elongation of the saddle-point should increase with K for a given J. However, this would make subsequent calculations far more complex, and is outside the scope of this thesis. In any case the additional increase in E_{rot} at the saddle-point for high-K states simply leads to a narrower K-distribution for higher J, which we can approximate by using a smaller K_0 overall.)

Note that these conditions at the saddle-point may have arisen from or been fixed before the saddle-point is reached. It is not that the compound nucleus hovers on the saddle-point while everything equilibrates. Rather, the probability of a nucleus reaching the saddle-point in any assault on the barrier depends on parameters that hold for that oscillation. So, for example, a spherical compound nucleus may start an oscillation with the elongation axis developing in any direction with uniform probability, but when the elongation axis is well defined, if $K = 0$ the nucleus is far more likely to elongate all the way to the saddle-point than if $K = J$. These probabilities are dependent on the energies involved; an elongated nucleus with $K = J$ has more energy tied up in rotation than a nucleus with the same elongation and $K = 0$. This is why we *can* talk about things in terms of conditions at the saddle-point, rather than trajectories through phase-space that pass through the saddle-point.

From the known orientation of $\vec{J}$ (as specified by its projection M on the beam axis) and the distribution of projections K onto the nuclear orientation axis, we deduce the distribution $\rho(J,M,\theta)$ of the angle between the fission axis and the beam axis according to:

$$\begin{aligned}\rho(J,M,\theta) &= \sum_{K=-J}^{J} \frac{(2J+1)|d^J_{M,K}(\theta)|^2 \rho(J,K)}{\sum_{K=-J}^{J} \rho(J,K)} \\ &= \sum_{K=-J}^{J} \frac{(2J+1)|d^J_{M,K}(\theta)|^2 \exp(-K^2/2K_0^2)}{\sum_{K=-J}^{J} \exp(-K^2/2K_0^2)} \qquad (2.41)\end{aligned}$$

where $d^J_{M,K}(\theta)$ is the well known "little d-function" [VAN73, ROS61]:

$$\begin{aligned}d^J_{M,K}(\theta) &= \{(J+M)!(J-M)!(J+K)!(J-K)!\}^{1/2} \\ &\quad \times \sum_X \frac{(-1)^X [\sin(\theta/2)]^{K-M+2X} [\cos(\theta/2)]^{2J-K+M-2X}}{(J-K-X)!(J+M-X)!(X+K-M)!X!} \qquad (2.42)\end{aligned}$$

where the summation is performed over all integer values of X where all factorial arguments are non-negative.

Since we have assumed that the fission fragments separate along the nuclear elongation axis, $\rho(J,M,\theta)$ also specifies the angular distribution of fission fragments from an initial compound nucleus state $|J,M\rangle$.

2.2.2.3 Fission Fragment Anisotropy

For a given distribution of fissioning compound nuclei $w(J,M)$ the total fission fragment angular distribution $W(\theta)$ may be determined using Equation 2.41 as:

$$\begin{aligned}W(\theta) &\propto \sum_{J=0}^{\infty} \sum_{M=-J}^{J} w(J,M)\rho(J,M,\theta) \\ &= \sum_{J=0}^{\infty} \sum_{M=-J}^{J} w(J,M) \sum_{K=-J}^{J} \frac{(2J+1)|d^J_{M,K}(\theta)|^2 \exp(-K^2/2K_0^2)}{\sum_{K=-J}^{J} \exp(-K^2/2K_0^2)} \qquad (2.43)\end{aligned}$$

In most cases it is assumed that M is always zero; in other words, $w(J,M)$ is zero unless M is zero, simplifying the calculations considerably. Situations where M is significant are discussed in Chapter 3. $W(\theta)$ is symmetric about 90°.

In general it is convenient to characterise $W(\theta)$ by the anisotropy, defined as:

$$A = \frac{W(0^\circ, 180^\circ)}{W(90^\circ)} \qquad (2.44)$$

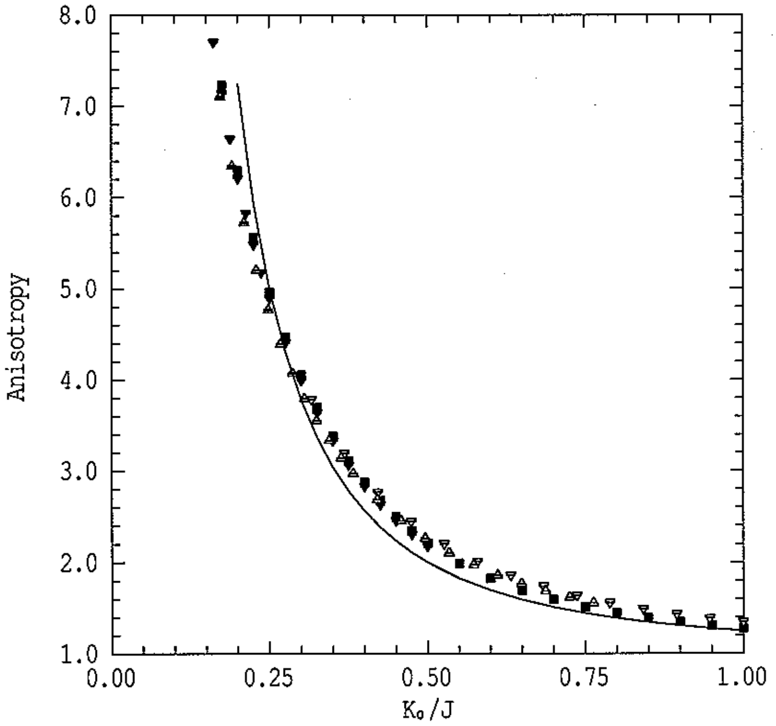

Figure 2.11: Testing the primitive anisotropy approximation; the solid line shows $A = 1 + \frac{\langle J^2 \rangle}{4K_0^2}$. The points show anisotropies calculated using Equation 2.43 for various single values of J and two J-distributions.

Experimental anisotropies may be determined by fitting measured fission fragment angular distributions, and compared with theoretical anisotropies.

The importance of the parameter K_0^2, which is commonly used in the interpretation and discussion of fission angular distributions, is made clear from the approximate expression [HAL58] for the anisotropy A:

$$A \approx 1 + \langle J^2 \rangle / 4K_0^2 \tag{2.45}$$

We use Eq. 3.1 to assess the accuracy of the above approximation; Figure 2.11 shows the difference between this approximation and calculations performed using Equation 2.43 as a function of K_0/J, for single J values and two J-distributions. This shows that the approximation is only good to about 0.3 over the range where most anisotropies arise.†

---

†Kailas & Singh use only Eq. 2.45, rather than more exact calculations, in an investigation of fission anisotropies [KAI94].

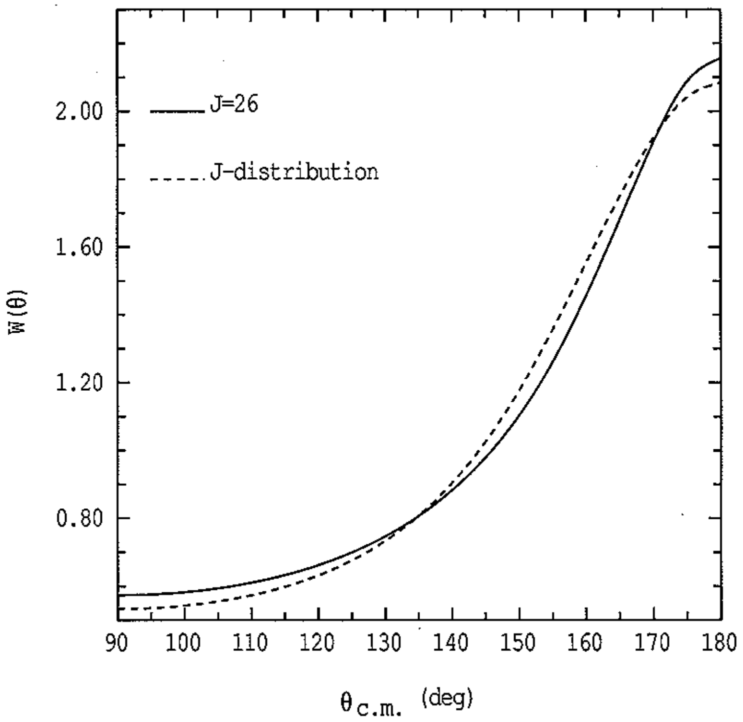

Figure 2.12: Fission fragment angular distributions calculated for $\overline{J}$=26. The solid line shows a curve generated from a realistic J-distribution; the dashed line shows a curve with the same K_0, generated using only $J = 26$.

2.2.2.4 Examples of angular distributions

Figure 2.12 illustrates two fission fragment angular distributions calculated using Equation 2.43. The general shape of these distributions is characteristic of fission fragment angular distributions in general; the anisotropy varies, but all the distributions follow the same kind of monotonic curve as shown in Figure 2.12. If the angular momentum J took a single value, as per the dashed curve in Figure 2.12, the range of possible curves would be confined to a family parameterized by the ratio K_0/J, and approaching the limit $\frac{1}{\sin(\theta)}$ as $K_0/J \to 0$. However, in practice J comes from a distribution, and the corresponding fission fragment angular distribution has a slightly different shape (solid line in Figure 2.12). If data points selected along this curve were fitted using distributions generated with a single J-value, it would introduce some systematic error in the resulting anisotropy. The shape of the FFAD is not very sensitive to variations in the shape of the angular momentum distribution, if only because the shape of the angular momentum distribution doesn't vary much; it is generally roughly triangular.

The practical consequence of this observation is that experimental fission fragment angular distributions should be fitted using distributions generated with as accurate an angular momentum distribution as is available.

2.3 Other Heavy Ion Reaction Processes

2.3.1 Transfer-Fission

Some naturally abundant nuclei (especially the actinides) are fairly fissile in themselves, and fission may be induced by heavy-ion reactions that simply transfer sufficient excitation energy to the heavy nucleus. So, for example, if a heavy projectile transfers a nucleon to a target nucleus like ^{238}U, the target nucleus may fission. This fission event should be distinguished from true fusion-fission events, where the projectile has been fully captured.

2.3.1.1 Experimental signature

There are several differences between a transfer-fission event and a fusion-fission event. A transfer-fission event involves a smaller fissioning nucleus, and the rest of the projectile nucleus must still go somewhere. In this work it is the linear momentum of the projectile remnant that is used to distinguish the transfer fission events from fusion-fission events.

In the laboratory reference frame, the total momentum of the projectile+target system is known; initially the momentum is all carried by the projectile. Following the detection of two fission fragments, their masses and velocities are deduced from experimental data. The velocity of the fissioning nucleus is reconstructed, and compared to the centre of mass velocity. Where there is a significant difference, the event can be recognized as a transfer-fission event. Where the two velocities are in agreement, the event may be described as "Full Momentum Transfer" Fission.

2.3.2 Quasi-fission

Full Momentum Transfer (FMT) Fission does not necessarily constitute fusion-fission. The other process that produces FMT events is Quasi-fission, in which the target and projectile nuclei meet and form a di-nucleus, undergoing significant mass equilibration without forming a fully equilibrated compound nucleus. (This is not expected to be significant for the reactions of P+Lu and Si+Hf, as these reactions form compound nuclei only slightly more fissile than lead.)

A detailed discussion of Quasi-fission and related theories is given in Chapter 6.

2.4 Nuclei with Significant Ground-State Spin

Where nuclei have significant ground-state spin, several of the assumptions widely used in calculations of fission fragment angular distributions must be re-examined. When considering the fusion process, the existence of a ground-state spin might influence couplings to rotational states, and couplings to rotational states may influence the orientation of the ground-state spin. When considering the fission process, the changes to the total angular momentum due to the ground-state spin of reacting nuclei may affect both the fission probability and the angular distribution of the fission fragments.

2.4.1 Fusion

2.4.1.1 The effect of ground-state spin on the fusion process

It is conceivable that ground-state spin could affect the fusion process. However, in the classical limit one can show that the fusion cross-section is independent of the ground-state spin, as follows.

The total fusion cross-section in the classical limit is given by:

$$\sigma(E) = \sum_{M=-I_i}^{I_i} \frac{1}{2I_i+1} \int_0^{2\pi} d\phi \int_o^{\pi} \sin\theta d\theta \int_0^{2\pi} d\chi \left|\Psi^{I_i}_{M,K}(\phi,\theta,\chi)\right|^2 \sigma(E,\theta) \qquad (2.46)$$

where $\sigma(E,\theta)$ is the cross-section at a given energy E and nuclear orientation angle θ, calculated using a statically deformed potential, and I_i is the ground-state spin of the target nucleus. $\Psi^{I_i}_{M,K}(\phi,\theta,\chi)$ is the normalised eigenfunction [DES90, (eqn 3.30)] of the zeroth order Hamiltonian [DES90, Equation 3.28] for axially symmetric rotational nuclei:

$$\Psi^{I}_{M,K}(\phi,\theta,\chi) = \Phi_K \sqrt{\frac{2I+1}{8\pi^2}} D^{I}_{M,K}(\phi,\theta,\chi) \qquad (2.47)$$

where ϕ, θ and χ are the Euler angles. Using Equation 2.47 and the following

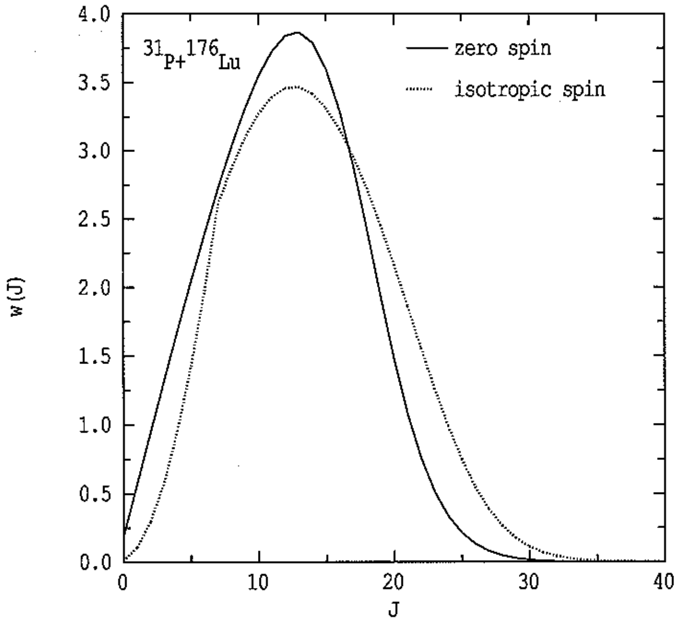

Figure 2.13: The distribution $w(J)$ calculated for ^{31}P+^{176}Lu at $E_{c.m.}$ =123.27 MeV (E/B_0 =1.008).

identity on Wigner's D-matrices $D^I_{M,K}(\phi,\theta,\chi)$:

$$\sum_M \left| D^{I*}_{M,K}(\phi,\theta,\chi) \right|^2 = 1 \tag{2.48}$$

we obtain:

$$\sigma(E) = \frac{1}{8\pi^2} \int_0^{2\pi} d\phi \int_o^{\pi} \sin\theta d\theta \int_0^{2\pi} d\chi\ \sigma(E,\theta) \tag{2.49}$$

which is independent of I_i.

2.4.1.2 Selection of ground-state spin alignment during the fusion process

Spherical nuclei Consider the case where a projectile fuses with a target nucleus, and the target nucleus has ground-state spin. If the target nucleus is spherical, that ground-state spin $\vec{I_0}$ will be randomly oriented—isotropic—and unrelated to $\vec{l}$. The total angular momentum $\vec{J}$ is given by $\vec{J} = \vec{l} + \vec{I_0}$. Since we know how both $\vec{l}$ and $\vec{I_0}$ are distributed, we can calculate how their sum is distributed. A sample calculation for moderate beam energy is shown in Figure 2.13, calculated according to:

$$w(J,M) = \sum_{l=0}^{\infty} \sum_{\mu_0=-I_0}^{+I_0} (2l+1) T_l |C^{I_0,l,J}_{M,0,M}|^2 \tag{2.50}$$

The orbital angular momentum l, together with I_0, determines $\vec{J} = \vec{l} + \vec{I_0}$, the total angular momentum of the fissioning nucleus. M is the projection of J onto the space-fixed axis. $C^{S,l,J}_{M,0,M}$ is a Clebsch-Gordan coefficient. T_l is the fusion transmission coefficient for a given orbital angular momentum l.

For ground-state spins I_0 smaller than $\langle l \rangle$ we observe that the J-distribution has a slightly higher average and slightly greater width than the l-distribution—if $\vec{J}$ were confined to the same plane as $\vec{l}$, this would give rise to a very slightly higher anisotropy. This slightly higher average J may be explained using Figure 2.14; in order to add $\vec{l}$ and $\vec{I_0}$ to give a vector $\vec{J}$ of the same length as (or shorter than) $\vec{l}$, the angle between $\vec{l}$ and $\vec{I_0}$ must be less than 90°, which occurs less than half the time. To put it another way, I_0 is isotropically oriented, so the angle between $\vec{I_0}$ and $\vec{l}$ is equally likely to be above or below 90°; and at 90°, $|\vec{J}| = \sqrt{l^2 + I_0^2} > |\vec{l}|$.

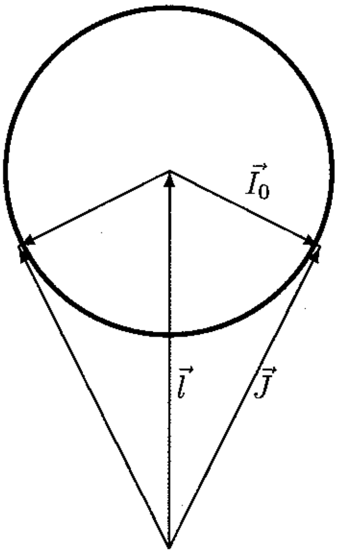

Figure 2.14: When you add one isotropically oriented spin $\vec{I_0}$ to another spin $\vec{l}$, the angle for $\vec{I_0}$ such that $|\vec{J}| = |\vec{l}|$ is at less than 90°; on average, $|\vec{J}| > |\vec{l}|$.

The orientation of $\vec{J}$ is also significant; its projection M on the beam axis varies nearly uniformly from $+I_0$ to $-I_0$, as illustrated in Figure 2.15, where in the absence of nuclear spin M would always be zero.

One nucleus deformed. If a deformed nucleus has non-zero spin in its ground state, that spin is aligned with the nuclear deformation axis. The significance of this alignment in the context of fusion-fission anisotropies is the subject of Chapter 3, however we give a brief overview here. The orientation of the nuclear deformation axis also governs the probability of fusion; in particular, at low beam energies, if fusion occurs, the nuclear deformation axis must have been aligned with the beam axis; and therefore the ground-state spin $\vec{I_0}$ is also aligned with the beam axis, as illustrated in Figure 2.16.

If the beam energy is low enough that fusion would not occur with a spherical

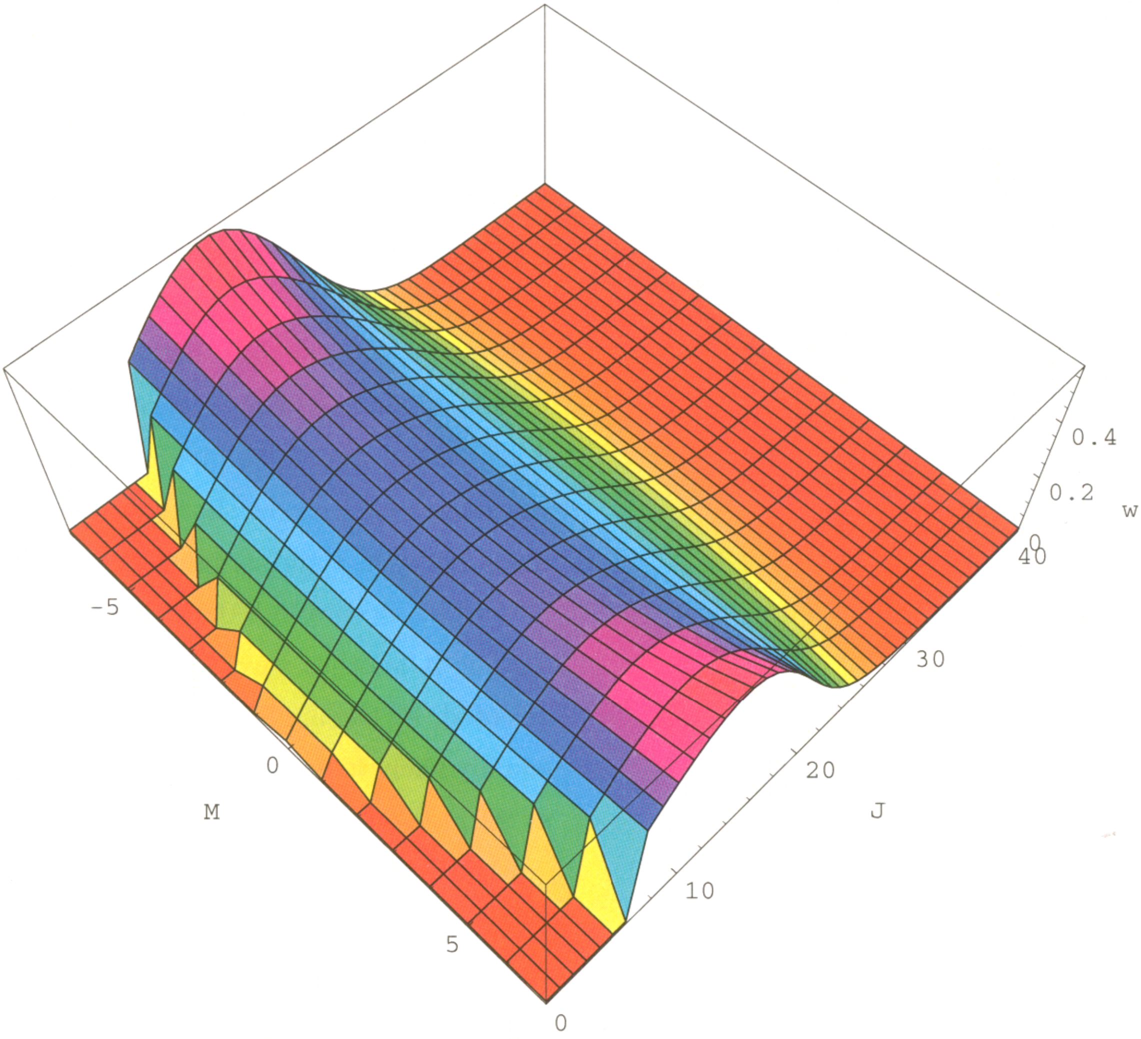

Figure 2.15: The distribution $w(J, M)$ calculated for ^{31}P+^{176}Lu at $E_{c.m.}$ =123.27 MeV (E/B_0 =1.008), assuming that ^{176}Lu is spherical and inert, and ignoring the $\frac{1}{2}$ unit of spin of ^{31}P.

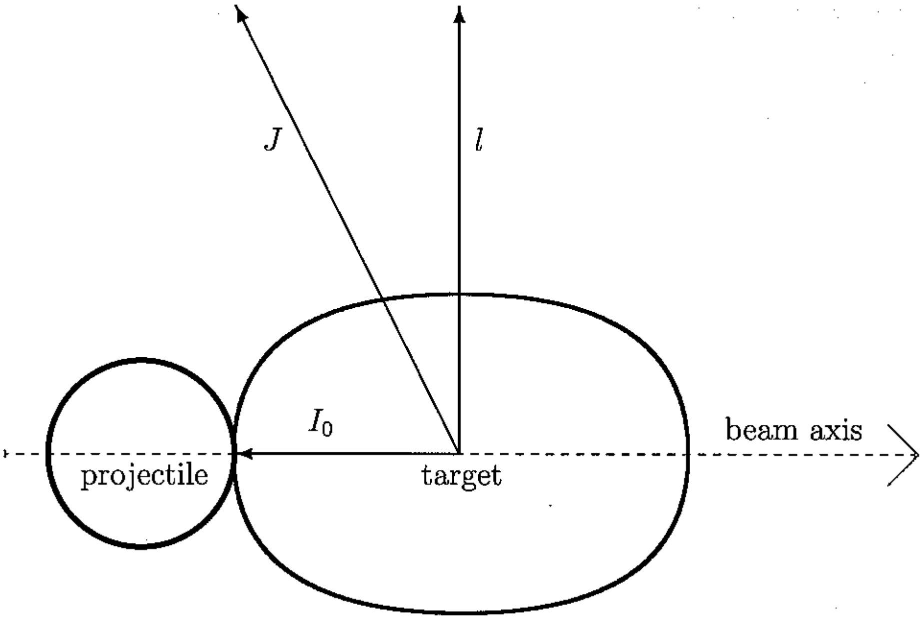

Figure 2.16: Collision of a spherical projectile with the tip of a deformed target nucleus. The ground-state spin I_0 of the target nucleus is aligned with the nuclear deformation axis, and therefore perpendicular to the collision-induced angular momentum l.

nucleus, but does occur with the tip of the deformed nucleus, the projection M of $\vec{J}$ on the beam axis takes mainly the maximum values.

At high beam energies, in contrast, fusion can occur whatever the orientation of the target nucleus, so at low J the distribution of M is uniform or nearly so; but the high-l events correspond only to collisions with the tip of the nucleus, and therefore still correspond to high M.

2.4.2 Fission

The effect of ground-state spin on $\vec{J}$ has two consequences. Firstly, $|\vec{J}|$ is on average slightly larger, reducing the height of the fission barrier and making fission more probable. This is a small effect. Secondly, the fission fragment anisotropy is reduced when $\vec{J}$ is not orthogonal to the beam direction. This topic is discussed in detail in the next chapter, however a brief explanation is given below.

When fission occurs, the resulting fission fragments fly off in directions nearly perpendicular to $\vec{J}$. The distribution of fission fragment angles relative to $\vec{J}$ depends on the nuclear temperature T and the elongation of the nucleus at the saddlepoint, characterised by I_{eff}. In most circumstances the observed anisotropy varies as shown in equation 2.43.

However, equation 2.43 is normally simplified on the assumption that $\vec{J}$ is perpendicular to the beam direction. This is not always the case, as discussed in the previous subsection. When $\vec{J}$ makes an angle $90° + \alpha$ with the beam axis, the fission fragments will be distributed about α relative to the beam axis, and the observed anisotropy is reduced.

CHAPTER 3

Extended Theory of Fission Fragment Angular Distributions

In this chapter the fission fragment angular distribution in the presence of ground-state nuclear spin is discussed. An existing description [VAN73] of fission fragment angular distributions in the presence of nuclear spin (Equation 3.1) is presented and evaluated. The most significant limitation of this formulation is its assumption that the ground-state spins of the reacting nuclei are isotropically oriented. This assumption may be expected to fail in the presence of nuclear deformation, since the nuclear spin should be aligned with the nuclear deformation axis, and the orientation of the nuclear deformation axis in turn affects the fusion barrier energy. This correlation has been pointed out by Lestone et al. [LES97] in a paper on pre-equilibrium fission effects, but their calculations are not appropriate to full fusion-fission reactions.

Development of an effective method for calculating the influence of nuclear spin on fission fragment angular distributions in the presence of nuclear deformation is the major focus of this project. We will detail some methods for accounting for nuclear deformation, in order of increasing complexity and physical accuracy.

3.1 Spherical Nuclei With Spin

To determine the influence of the ground-state spins of nuclei on the fusion angular momentum distribution and the fission process, we need to know both the magnitude and the orientation of the spin. The magnitude is generally available from publications such as Nuclear Data Sheets. If the nuclei with significant ground-state spin are spherical, it should be appropriate to assume that in fusion the spin is isotropically oriented.

3.1.1 Existing Quantum-Mechanical Theory

The influence of nuclear spin on the fission fragment angular distribution has long been recognised.

In quantum mechanical calculations of the angular distribution of fission fragments, it is assumed that fission fragments separate along the nuclear symmetry axis, and that K, the projection of the total angular momentum $\vec{J}$ onto the nuclear symmetry axis, is a good quantum number at and beyond the fission saddle point. For an isotropic distribution of spins I_0 and I_1, the angular distribution of fission fragments is given [HUI69, VAN73] by:

$$\begin{aligned} W(\theta) \;\propto\; & \sum_{J=0}^{\infty} \sum_{M=-(I_0+I_1)}^{+I_0+I_1} \left\{ \sum_{l=0}^{\infty} \sum_{S=|I_0-I_1|}^{I_0+I_1} \sum_{\mu_0=-I_0}^{+I_0} \frac{(2l+1)T_l |C^{S,l,J}_{M,0,M}|^2 |C^{I_0,I_1,S}_{\mu_0,M-\mu_0,M}|^2}{\sum_{l=0}^{\infty}(2l+1)T_l} \right\} \\ & \times \left[\sum_{K=-J}^{J} \frac{(2J+1)|d^J_{M,K}(\theta)|^2 \exp(-K^2/2K_0^2)}{\sum_{K=-J}^{J} \exp(-K^2/2K_0^2)} \right] \end{aligned} \tag{3.1}$$

Here, I_0 is the spin of the target nucleus, and μ_0 its projection upon a space-fixed axis (in experiments, the beam axis). The channel spin S is the vector sum of I_0 and I_1, where I_1 is the spin of the projectile nucleus. The orbital angular momentum l, together with S, determines $\vec{J} = \vec{l} + \vec{S}$, the total angular momentum of the fissioning nucleus. M is the projection of J onto the space-fixed axis. K_0^2 is as defined in Section 2.2.2. $C^{S,l,J}_{M,0,M}$ and $C^{I_0,I_1,S}_{\mu_0,M-\mu_0,M}$ are Clebsch-Gordan coefficients. The function $d^J_{M,K}(\theta)$ is the well known d-function, as defined in Equation 2.42. T_l is the fusion transmission coefficient for a given orbital angular momentum l.

The quantity in curly brackets in Equation 3.1 is $w(J,M)$, the weighting for each possible fission channel (J,M). The quantity in square brackets in Equation 3.1 specifies the fission fragment angular distribution $\rho(J,M,\theta)$ for a given channel (J,M).

Equation 3.1 is rarely, if ever, actually used in full. There are two reasons for this. Firstly, the equation is computationally demanding; while calculations may be performed in reasonable times on modern computers, ten years ago they were much more difficult. Secondly, in practice, nuclear spin is rarely significant, and the equation may be simplified to the $M = 0$ special case, with a substantial reduction in computational requirements. Where nuclear spin has been recognised as significant, an approximate correction has been used [KAI94]. We will evaluate the validity of this approximation, used by Kailas and Singh [KAI94], by comparing it to the exact equation it approximates, in the next subsection.

3.1.2 An existing approximation

Equation 3.1 is appropriate for calculations involving spherical nuclei, whose ground-state spins are expected to be isotropically oriented. To examine the effect of spin on fission fragment angular distributions, we start with the simplest case of a spherical target nucleus with appreciable ground-state spin, and a projectile with no spin. There are a number of reactions that fit this description, e.g. ^{16}O+^{209}Bi.

Kailas and Singh [KAI94] avoided the complexity of exact calculations by using an effective K_0^2 to predict the anisotropies for reactions involving nuclei of non-zero spin. The effect of a ground-state spin I (belonging to either projectile or target) was approximated [KAI94] by replacing K_0 with K_{0eff}, where K_{0eff} is given by the ansatz:

$$K_{0eff}^2 = K_0^2 + I^2/3. \tag{3.2}$$

This ansatz is credited to a private communication from R. Vandenbosch. Although in Ref. [KAI94] the explanation for the factor 1/3 is not given, presumably it arises from the assumption that $\vec{I}$ is isotropically oriented, which gives $\langle I_z^2 \rangle = I^2/3$. Changes in $\langle J^2 \rangle$ (Equation 2.45) due to the presence of finite ground-state spin are small, and in any case $\langle J^2 \rangle$ is rather bigger than K_0^2, so changes in $\langle J^2 \rangle$ are therefore expected to have a much smaller effect on the anisotropy than the effect of I_z^2 on K_0^2.

Here we examine the accuracy and the range of validity of the approximation in Equation 3.2. This approximation was used [KAI94] when calculating anisotropies for the reaction ^{16}O+^{209}Bi ($I_0 = 9/2$). The anisotropies were in the range 1.3 to 3.0; K_0 was in the range 9 to 13, and $\langle l^2 \rangle^{1/2}$ was in the range 7 to 30. Figure 3.1(a) shows fission fragment angular distributions calculated using Equation 3.1 at a near-barrier and an above-barrier energy, with and without target spin. Figure 3.1(b) and 3.1(c) show the ratio R of $W(\theta)$ calculated with spin to that calculated without. The distributions obtained using the $I = 0$ limit of Equation 3.1, but replacing K_0 with

K_{0eff} as given by Equation 3.2, are drawn with a short-dashed-line; for this case the accuracy of the approximation far exceeds that required for most experiments.

To assess the general accuracy of Equation 3.2, its predictions were compared with those obtained using Equation 3.1. Fission fragment angular distributions were calculated using Equation 3.1 for single values of l, I_0, and K_0. A value of K_{0eff}, to be compared with that from Equation 3.2, was then obtained by fitting the distribution in the spin-zero limit of Equation 3.1, using K_{0eff} as a free parameter in place of K_0.

A comparison of the two methods is presented in Figure 3.2 by plotting $y = (K_{0eff}^2 - K_0^2)/I_0^2$ against K_0/l for representative values of I_0. If Equation 3.2 were in close agreement with the exact calculations, the points would all lie on a straight line at $y = 1/3$ (solid line). However, it is clear from the figure that there is some dependence on K_0/l, as well as a dependence on I_0, arising from spin quantization. We conclude that the approximation of Equation 3.2 will not hold good under all circumstances.

More complex normalizations, like $y = (K_{0eff}^2 - K_0^2)/(I_0^2 + I_0)$, or $y = (K_{0eff}^2 - K_0^2)/(I_0(I_0 + 0.5))$, or plotting against $K_0/\sqrt{\langle l^2 \rangle + I_0^2}$, improve the appearance of the graph, but are least accurate where the effect is most important, at low K_0/l. The complex dependence on l and I_0 appears to prohibit a simple parameterization. Since exact calculations can be performed, a better approximation was not sought.

Experimental situations involve a distribution of angular momenta l, meaning that K_0/l spans a range of values, and the errors in the simple approximation cancel out to some extent. For spherical nuclei it may still be adequate to use Equation 3.2. This depends on the precision required, and upon the relative values of K_0, l, and I_0; the deviations $A_{\text{approx}} - A_{\text{exact}}$ are shown in Figure 3.3, for a realistic fusion T_l distribution with $\langle l \rangle = 26$. A_{approx} is determined using Equation 3.2 and Equation 3.1 with $I_0 = 0$. We have verified that if K_0, l, and I_0 are scaled together, the anisotropy A_{exact} remains unchanged. Figure 3.3 shows that the approximation holds good to $\Delta A = 0.03$ for $K_0/l > 0.3$. However, this approximation does not include the effect of nuclear deformation, which has previously been shown [LES97] to change anisotropies significantly, and is discussed in Section 3.2.

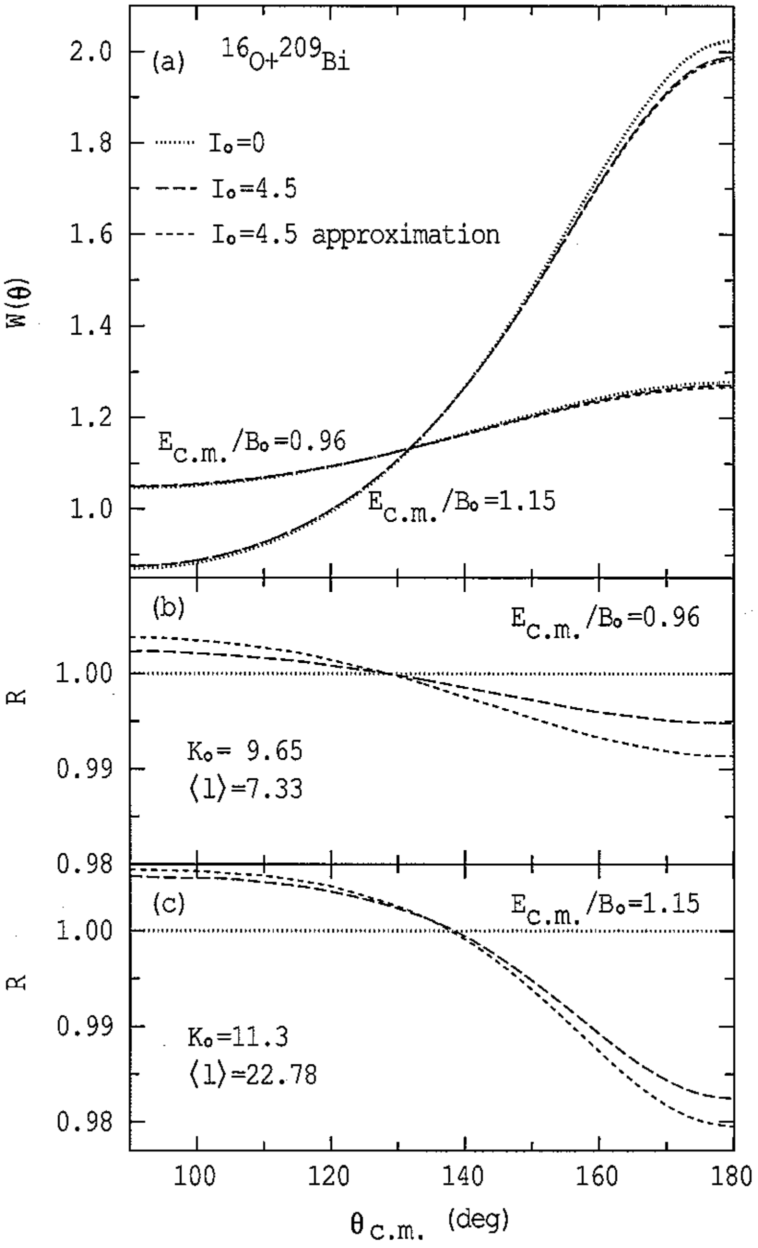

Figure 3.1: The fission fragment angular distribution for ^{16}O+^{209}Bi, calculated for energies above and below the barrier (average barrier height $B_0 = 75.8$ MeV). (a) shows the fission fragment angular distributions, calculated for zero spin (dotted line), $I_0 = 4.5$ (long-dashed line), and the approximation (Equation 3.2) for $I_0 = 4.5$ (short-dashed line). The long-dashed line and the short-dashed line can hardly be distinguished. In (b) and (c) we show the ratio R of the distribution from Equation 3.1 and from Equation 3.2, compared to the zero-spin limit of Equation 3.1, for below and above barrier energies, respectively.

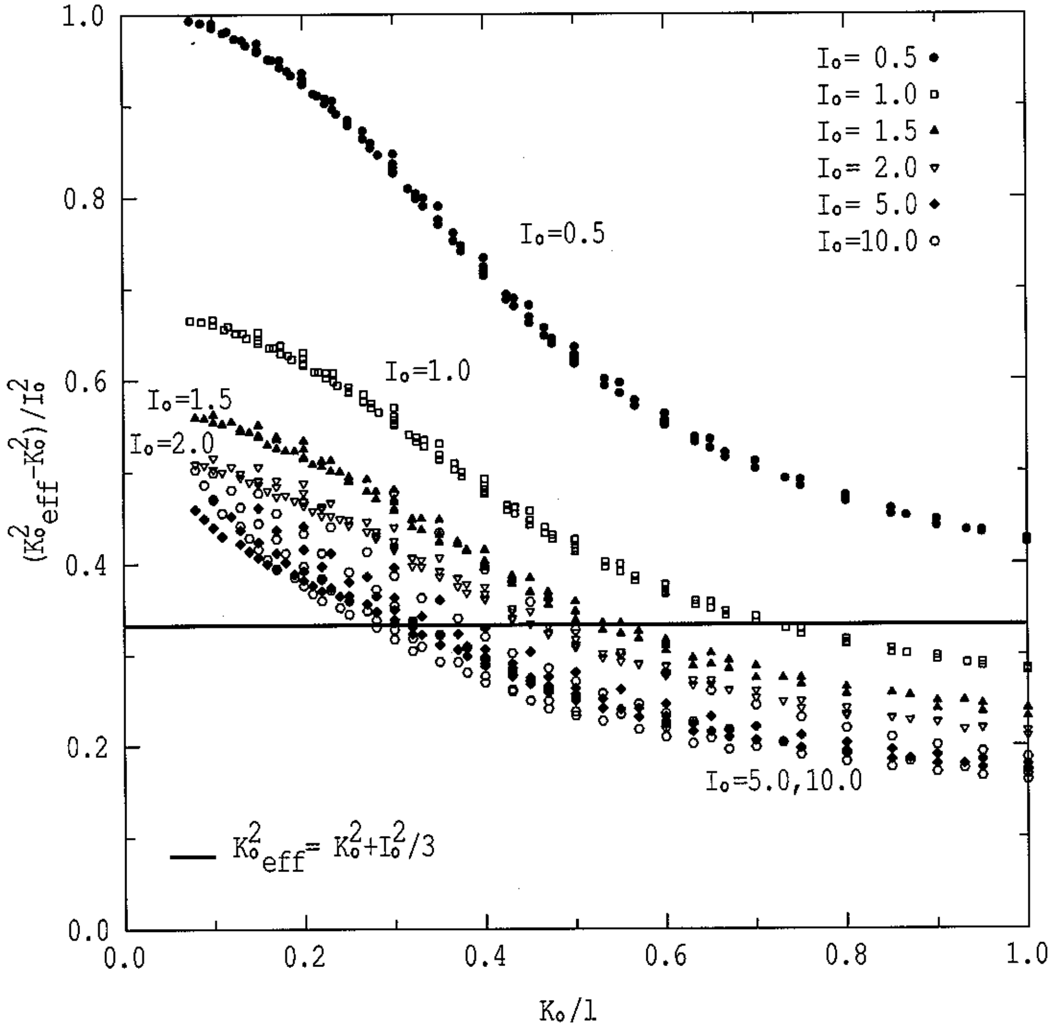

Figure 3.2: The difference between K_{0eff}^2 and K_0^2, normalized by I_0^2, according to exact calculations (Equation 3.1). l takes single values in the range 10–40. We show the points corresponding to $I_0 = 0.5, 1.0, 1.5, 2.0, 5.0$ and 10.0; points corresponding to I_0 in the range 2–10 all fall in the region occupied by $I_0 = 2.0, 5.0, 10.0$, with some scatter due to the complex interaction between I_0 and l. It is clear both that the difference does not behave as predicted by Equation 3.2 (solid line) and that there is some further dependence of the difference upon I_0 and on K_0/l.

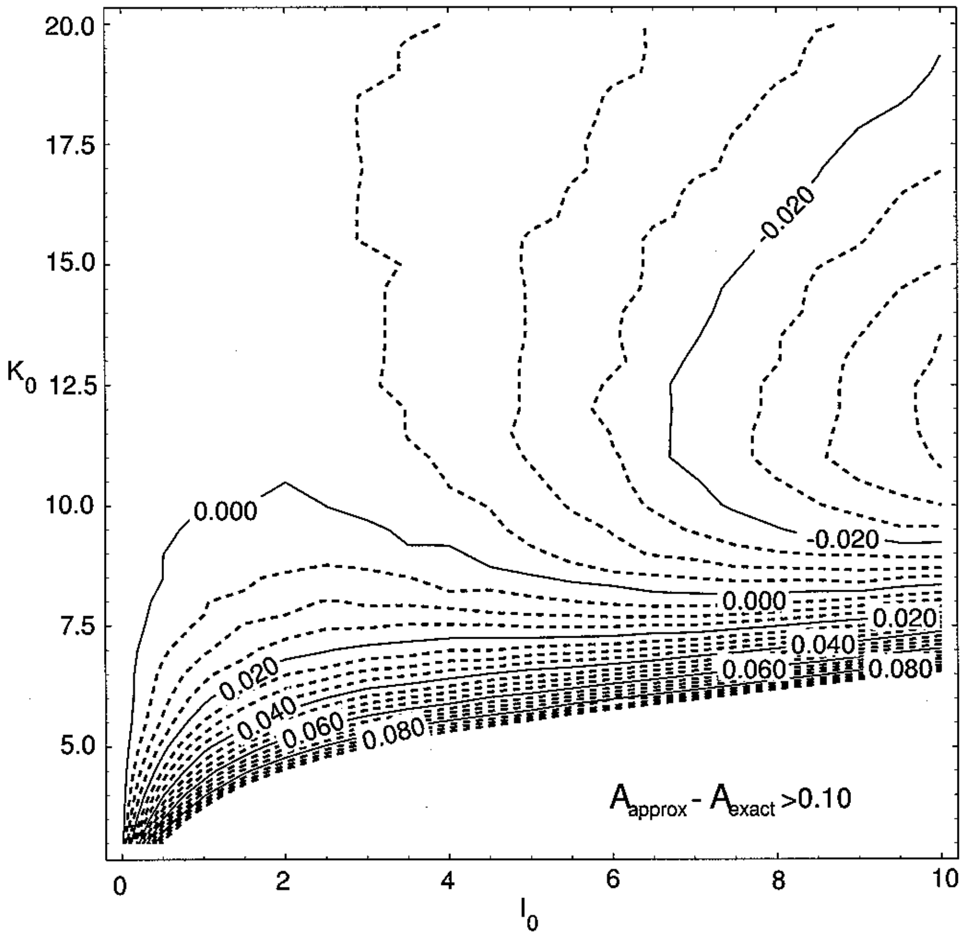

Figure 3.3: A contour graph of the difference between the anisotropy A_{approx} predicted by Equation 3.2 and A_{exact} calculated for the same K_0, I_0, and $\langle l \rangle = 26$, using the exact quantum mechanical expression (Equation 3.1). Contours are at intervals of 0.005.

3.1.3 Limitations of the existing formula

Equation 3.1 is derived using a number of assumptions which are not always appropriate. The assumption that fission fragments separate along the nuclear symmetry axis is not appropriate for large values of compound nucleus angular momentum, which cause the fragments to follow hyperbolic trajectories after scission. Back *et al.* [BAC85] showed that this post-scission reorientation results in a J-dependent reduction in K, and estimated the change based on the assumption that the system may be treated as two touching spheres at the scission point. The apparent variance $K_0'^2$ of the K-distribution after post-scission reorientation is given by [BAC85]:

$$K_0'^2 \simeq K_0^2 \left[1 + 122\frac{J^2}{A^{4/3}Z^2}\right]^{-2} \tag{3.3}$$

where J is the total angular momentum of the compound nucleus, and A and Z are the nucleon and proton numbers of the compound nucleus. This formula will be used in full calculations as described in Section 3.2.7.

It is implicit in Equation 3.1 that all compound nuclei proceed to fission. In practice, the fission probability is less than unity, and depends upon J. T_l should be multiplied by the fission probability $P_f(J)$. The effects of particle evaporation preceding fission must also be considered. An evaporated particle carries away energy and angular momentum, affecting K_0, J, and M. A statistical model code such as JOANNE [LES93] may be used to account for all of these effects. Of these, the changes in M usually have the smallest impact, and are often neglected [MOR95].

It is also implicit in Equation 3.1 that all possible projections of the target or projectile ground-state spin onto the beam axis are equally likely. In the presence of nuclear deformation, this assumption can break down, as described in the next section.

3.2 Deformed Nuclei with spin.

For nuclei with large ground-state spin and deformation, the ground-state spin is aligned with the deformation axis. The fusion barrier energy is correlated with the angle between the deformation axis and the beam axis. At beam energies below the average fusion barrier, fusion only occurs when the nuclear deformation axis is aligned with the beam direction, which in turn means that the ground-state spin is aligned with the beam direction. Thus Equation 3.1 must be generalized for deformed nuclei with finite ground-state spin.

3.2.1 The Effect of Deformation on Fission Anisotropies

Consider the special case of a perfectly aligned target nucleus, with $\vec{I_0}$ pointing along the beam axis as shown in Figure 3.4(a). After fusion with a projectile, when the compound nucleus splits into two fission fragments, the fragments separate in directions close to the plane perpendicular to $\vec{J}$. The larger the ground-state target spin I_0, the further this plane is from the beam axis, and the less probable it is that fission fragments will be detected at 0° or 180° to the beam axis, reducing the anisotropy.

This situation is more likely to arise if the target nucleus is prolate-deformed, as follows. Consider the collision of a spherical projectile with the high spin, strongly deformed prolate target nucleus. At energies below the average fusion barrier, only the lowest barriers will give rise to fusion. These barriers (Figure 2.4) correspond to the nuclear deformation axis being closely aligned with the beam axis, which in turn means that the ground-state spin is closely aligned with the beam axis (and orthogonal to the collision-induced spin, as illustrated in the classical limit in Figure 2.16). Thus the height of the fusion barrier and the orientation of the ground-state spin are both governed by the angle between the nuclear deformation axis and the beam axis. Therefore at beam energies below the average fusion barrier, for a prolate nucleus with ground-state spin, the configuration where the ground-state spin is aligned with the beam axis is strongly favoured over configurations where $\vec{I_0}$ is orthogonal to the beam axis (e.g. Figure 3.4(b)).

At higher beam energies, although collisions are possible for all orientations of the target nucleus, there still remains a correlation between the ground-state spin $\vec{I_0}$ and the angular momentum l brought in by the projectile, since at all energies the highest l introduced can only occur in collisions with the tips of the target nucleus.

The fact that fusion with a deformed target nucleus selectively populates states where the ground-state spin is aligned with the nuclear deformation axis means that the reduction in anisotropy due to ground-state spin is greater if the target

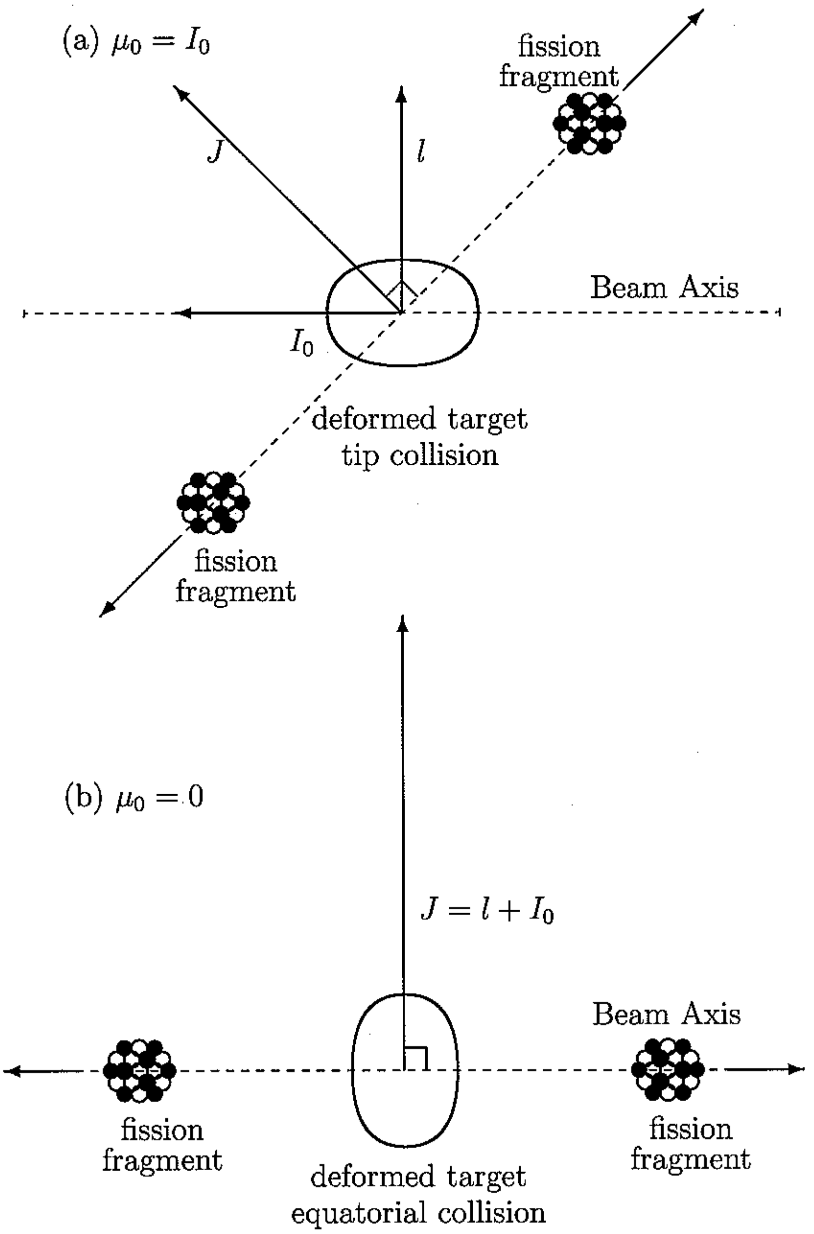

Figure 3.4: (a) At beam energies well below the average fusion barrier, the projectile collides with the tip of the prolate-deformed target nucleus. This results in alignment of the target spin I_0, so that μ_0 takes its maximum values. The total angular momentum J will not lie in the plane perpendicular to the beam direction. Fission fragments will separate in or near the plane at right angles to J; this plane does not include the beam axis. (b) At higher beam energies, collisions with the equator of the prolate-deformed target are also energetically permissible. For these events where I_0 is parallel to l, the larger (or smaller) J results in an angular distribution of fission fragments with a larger (or smaller) anisotropy than if I_0 were zero.

is deformed, rather than spherical. In the spherical case, the spin is isotropically oriented and can actually increase the anisotropy in some configurations, partially compensating for the reduction in anisotropy for other configurations. So, for example, if $\vec{I_0}$ is parallel to $\vec{l}$, this results in a larger J for the same K_0, as illustrated in Figure 3.4(b), and the corresponding contribution to the fission fragment angular distribution will have higher anisotropy, unlike the configuration illustrated in Figure 3.4(a). Thus, in the absence of nuclear deformation, the overall effect of nuclear spin on the anisotropy is not as large as it might be, whereas fusion with a prolate-deformed nucleus selectively populates the states where I_0 is aligned with the beam direction; that is to say, precisely those states where the effect on the anisotropy is maximal.

3.2.2 Modelling the effect of ground-state spin

We have established that the ground-state spin of a strongly deformed, prolate nucleus need not be isotropically oriented; that for fusion-fission events where the beam energy is below the average fusion barrier, the fusion process selects configurations where the ground-state spin is aligned with the beam axis. One possible model of this process involves characterizing this alignment using the distribution $w(M)$ of projections M of the spin I onto the beam axis, as discussed in Section 3.2.3.

However, by using this characterization, we are ignoring potentially important information. In particular, M is correlated with l, the orbital angular momentum brought in by the projectile. Consider collisions at above-barrier energies. At low l, the projectile may fuse with the equator or the tips of the target, and M is distributed fairly evenly, as illustrated in Figure 3.5. However, the highest l populated at this beam energy correspond only to the lowest fusion barriers; which means collisions with the tips of the deformed nucleus, and that in turn means that the spin I is aligned with the beam axis (M takes its extreme values, as shown for high J in Figure 3.5). A second model, taking into account the correlation between l and M, is described in Section 3.2.4.

Both the models mentioned above rely upon a semi-classical method of determining the projection M of the ground-state spin on the beam axis. This semi-classical method assumes that the ground-state nuclear spin is perfectly aligned with the nuclear deformation axis. However, quantum-mechanically, there is an inescapable

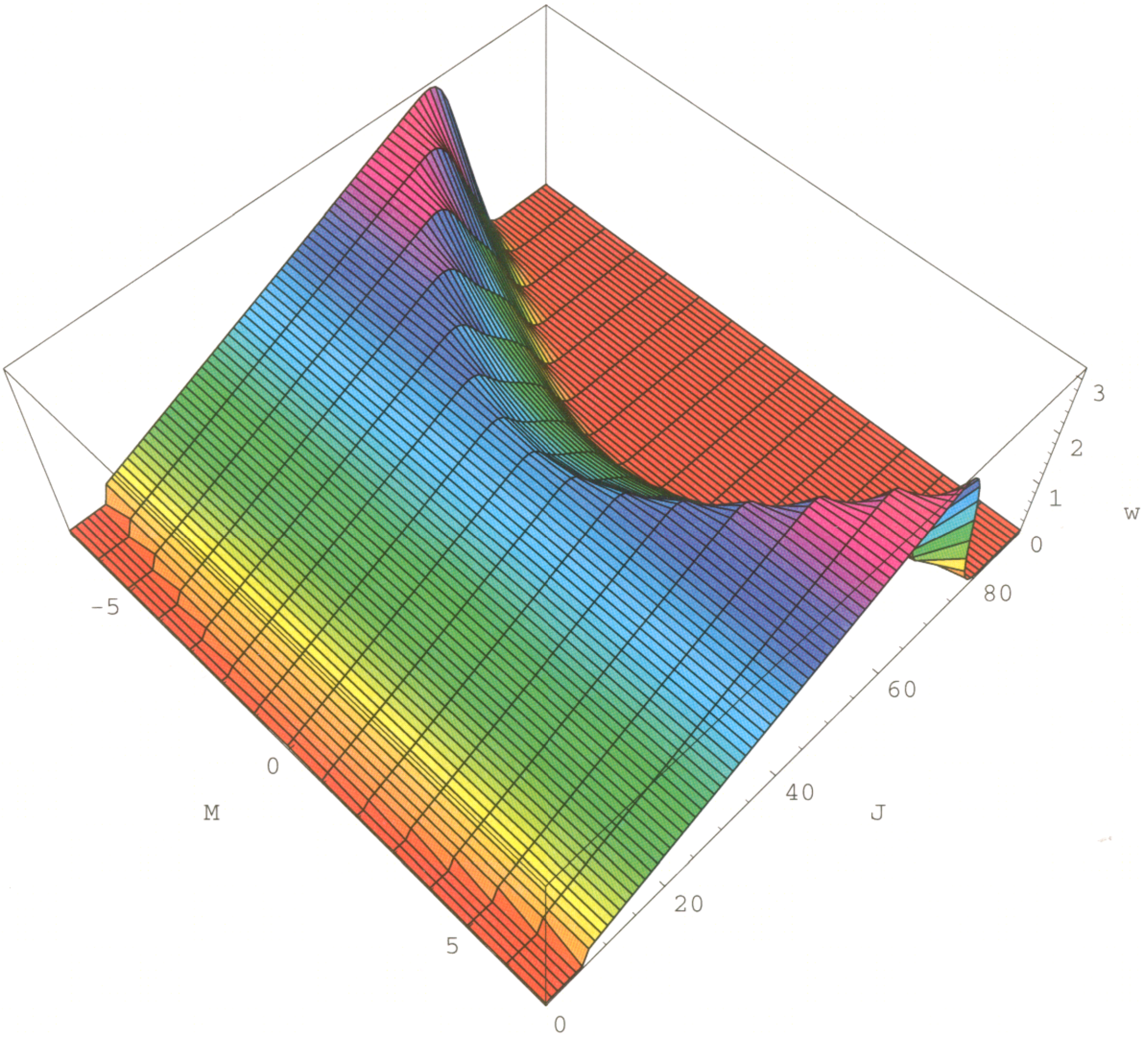

Figure 3.5: The distribution $w(J, M)$ calculated for $^{31}\mathrm{P}+^{176}\mathrm{Lu}$ at $E_{c.m.}$ =144.54 MeV (E/B_0 =1.182), taking into account the deformation of ^{176}Lu, and ignoring the $\frac{1}{2}$ unit of spin of ^{31}P.

degree of uncertainty in the orientation of any angular momentum. A third model, taking this uncertainty into account, is discussed in Section 3.2.5. For completeness, these three formalisms all take into account significant deformations for both target and projectile nuclei, although in the reactions studied, none of the projectiles have either significant deformation or significant spin.

The three models are compared in Section 3.2.6. The agreement between the models is fairly good, so that the choice of which model to use should depend on the trade-off between completeness and the time it takes for calculations to complete.

We then describe a calculation which also addresses the issues of J-dependent fission probabilities, pre-fission particle emission, and post-scission re-orientation.

3.2.3 Semi-classical un-correlated M-distributions

The simplest generalisation of Equation 3.1 to include the effects of aligned nuclear spin is as follows:

$$\begin{aligned} W(\theta) \;\propto\; & \sum_{J=0}^{\infty} \sum_{M=-(I_0+I_1)}^{+I_0+I_1} \left\{ \sum_{l=0}^{\infty} \sum_{S=|I_0-I_1|}^{I_0+I_1} \sum_{\mu_0=-I_0}^{+I_0} \frac{\boldsymbol{\partial\sigma(M)}(2l+1)T_l|C^{S,l,J}_{M,0,M}|^2|C^{I_0,I_1,S}_{\mu_0,M-\mu_0,M}|^2}{\sum_{l=0}^{\infty}(2l+1)T_l\sum_{\boldsymbol{M=-(I_0+I_1)}}^{\boldsymbol{+I_0+I_1}}\boldsymbol{\partial\sigma(M)}} \right\} \\ & \times \left[\sum_{K=-J}^{J} \frac{(2J+1)|d^J_{M,K}(\theta)|^2 \exp(-K^2/2K_0^2)}{\sum_{K=-J}^{J}\exp(-K^2/2K_0^2)} \right] \end{aligned} \tag{3.4}$$

where we have introduced the M-distribution $\partial\sigma(M)$, the weighting of each value of M, assumed to be independent of l. The normalization in the denominator in the curly brackets is constant. It might perhaps have been simpler to introduce two distributions, $\partial\sigma_0(\mu_0)$ and $\partial\sigma_1(\mu_1)$, describing the alignment of target and projectile spins directly; in which case Equation 3.4 would reduce to Equation 3.1 when both $\partial\sigma_0(\mu_0)$ and $\partial\sigma_1(\mu_1)$ are constant. However, since $\partial\sigma(M) = \sum_{\mu_0}\partial\sigma_0(\mu_0)\partial\sigma_1(M-\mu_0)$, this is a largely cosmetic issue.

The next step is to calculate $\partial\sigma(M)$. We perform a coupled-channels cross-section calculation, specifying the static deformation of both target and projectile nuclei. (Naturally the resulting cross-sections should reproduce the observed excitation function, where such experimental information is available.) The deformations are treated classically, assuming that the angles θ_0 and θ_1 between the beam axis and the deformation axes of the target and projectile respectively are well defined within 1° steps. The calculation yields T_l and the cross-section distribution $\partial\sigma(\theta_0, \theta_1)$.

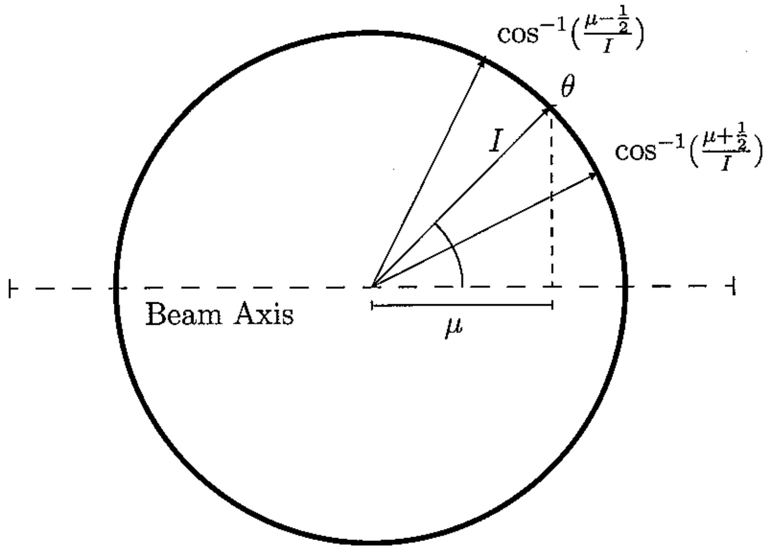

Figure 3.6: If the nuclear spin I makes an angle θ with the beam axis, the classical projection of I on the beam axis is taken as μ if $\mu - \frac{1}{2} < I\cos(\theta) < \mu + \frac{1}{2}$.

We then assign $\partial\sigma(\theta_0, \theta_1)$ to $\partial\sigma(M)$:

$$\partial\sigma(M) = \sum_{\mu_0=\max(-I_0,M-I_1)}^{\min(I_0,M+I_1)} \int_{\theta_0=\cos^{-1}\left(\frac{\mu_0+\frac{1}{2}}{I_0}\right)}^{\cos^{-1}\left(\frac{\mu_0-\frac{1}{2}}{I_0}\right)} \int_{\theta_1=\cos^{-1}\left(\frac{M-\mu_0+\frac{1}{2}}{I_1}\right)}^{\cos^{-1}\left(\frac{M-\mu_0-\frac{1}{2}}{I_1}\right)} \partial\sigma(\theta_0, \theta_1) d\theta_0 d\theta_1 \quad (3.5)$$

where the limits of the integrals are assigned according to the projections of the target and projectile nuclei on the beam axis, as illustrated in Figure 3.6. In practice, the integrals are evaluated numerically in 1° steps, using linear interpolation at the boundaries.

This approach captures the essence of the nuclear deformation effect, and further refinements do not give very different results, as shown in Section 3.2.6. One weakness of this approach is that it assumes that l and M are not correlated. However, as shown in Figure 3.5, l and M *are* correlated. This refinement is taken into account in the next Subsection.

3.2.4 Semi-classical correlated l, M-distributions

If l and M are correlated, then using Equation 3.4 is not completely physical. We could improve our calculation by using the matrix of partial cross-sections

$\partial\sigma(l, \mu_0, \mu_1)$:

$$W(\theta) \propto \sum_{J=0}^{\infty} \sum_{M=-(I_0+I_1)}^{+I_0+I_1} \left\{ \sum_{l=0}^{\infty} \sum_{S=|I_0-I_1|}^{I_0+I_1} \sum_{\mu_0=-I_0}^{+I_0} \frac{\boldsymbol{\partial\sigma(l, \mu_0, M-\mu_0)}|C^{S,l,J}_{M,0,M}|^2 |C^{I_0,I_1,S}_{\mu_0,M-\mu_0,M}|^2}{\boldsymbol{\sum_{l=0}^{\infty} \sum_{\mu_0=-I_0}^{+I_0} \sum_{\mu_1=-I_1}^{I_1} \partial\sigma(l, \mu_0, \mu_1)}} \right\}$$
$$\times \left[\sum_{K=-J}^{J} \frac{(2J+1)|d^J_{M,K}(\theta)|^2 \exp(-K^2/2K_0^2)}{\sum_{K=-J}^{J} \exp(-K^2/2K_0^2)} \right] \tag{3.6}$$

where in the top line we substitute $\mu_1 = M - \mu_0$, and as with Equation 3.4 the denominator in the curly brackets is a constant normalization.

To evaluate $\partial\sigma(l, \mu_0, \mu_1)$ we use a semi-classical coupled-channels calculation as described in Section 3.2.4, extracting the distribution $\partial\sigma(l, \theta_0, \theta_1)$ and calculating $\partial\sigma(l, \mu_0, \mu_1)$ according to:

$$\partial\sigma(l, \mu_0, \mu_1) = \int_{\theta_0=\cos^{-1}\left(\frac{\mu_0+\frac{1}{2}}{I_0}\right)}^{\cos^{-1}\left(\frac{\mu_0-\frac{1}{2}}{I_0}\right)} \int_{\theta_1=\cos^{-1}\left(\frac{\mu_1+\frac{1}{2}}{I_1}\right)}^{\cos^{-1}\left(\frac{\mu_1-\frac{1}{2}}{I_1}\right)} \partial\sigma(l, \theta_0, \theta_1) d\theta_0 d\theta_1 \tag{3.7}$$

using the same classical partitioning of θ into μ as illustrated in Figure 3.6.

We can then perform an angular momentum addition using the three angular momenta $\vec{l}$, $\vec{I_0}$, $\vec{I_1}$:

$$w(J, M) = \left\{ \sum_{l=0}^{\infty} \sum_{S=|I_0-I_1|}^{I_0+I_1} \sum_{\mu_0=-I_0}^{+I_0} \frac{\partial\sigma(l, \mu_0, M-\mu_0)|C^{S,l,J}_{M,0,M}|^2 |C^{I_0,I_1,S}_{\mu_0,M-\mu_0,M}|^2}{\sum_{l=0}^{\infty} \sum_{\mu_0=-I_0}^{+I_0} \sum_{\mu_1=-I_1}^{I_1} \partial\sigma(l, \mu_0, \mu_1)} \right\} \tag{3.8}$$

where $\vec{S} = \vec{I_0} + \vec{I_1}$ and $\vec{J} = \vec{I_0} + \vec{I_1} + \vec{l}$. (We distinguish between various matrices $\partial\sigma$ and the matrices w according to whether or not the angular momentum additions have been performed; in other words, $\partial\sigma$ corresponds to a quantity evaluated before addition using Clebsch-Gordan coefficients, whereas w has been evaluated after an addition using Clebsch-Gordan coefficients. This notation is slightly at variance with that used in [BUT02, BUT02B].)

It is worth examining the effect of nuclear ground-state spin on the angular momentum distribution $w(J, M)$ itself. Figure 3.7 compares $w(J, M)$ at $E_{c.m.} =$ 123.3 MeV (the average fusion barrier energy is $E_{c.m.}$=122.3 MeV) for the reaction ^{31}P+^{176}Lu (I_0=7), assuming zero spin (solid line), isotropic spin (dotted line), and deformation aligned spin (dashed line) respectively. In the presence of ground-state spin I_0, the J-distribution $w(J) = \sum_M w(J, M)$ shown in Figure 3.7(a) is depleted for $J < I_0$ compared to the $I_0 = 0$ case (the cross-section reappearing at higher J). Since the fission probability increases with J, this depletion should slightly reduce

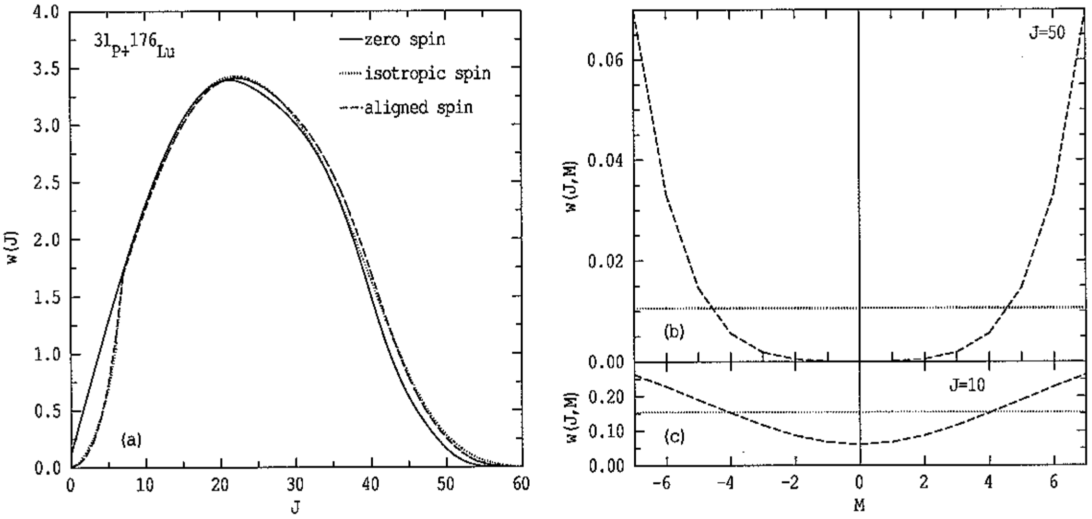

Figure 3.7: (a) The distribution $w(J)$ calculated for ^{31}P+^{176}Lu at $E_{c.m.}$ =123.27 MeV. The distribution $w(J, M)$ for (b) $J = 50$ and (c) $J = 10$.

the total ER cross-section. The J-distributions resulting from isotropic or aligned ground-state spins are almost indistinguishable; however, the M-distribution at any J in the presence of nuclear deformation is far from isotropic, as shown in Figure 3.7(b) and Figure 3.7(c). Differences between isotropic and aligned FFAD calculations are therefore due almost entirely to this distribution of M.

The fission fragment angular distribution $W(\theta)$ may be determined from $w(J, M)$ according to:

$$W(\theta) \propto \sum_{J=0}^{\infty} \sum_{M=-(I_0+I_1)}^{+I_0+I_1} w(J,M) \times \left[\sum_{K=-J}^{J} \frac{(2J+1)|d^J_{M,K}(\theta)|^2 \exp(-K^2/2K_0^2)}{\sum_{K=-J}^{J} \exp(-K^2/2K_0^2)} \right] \quad (3.9)$$

3.2.5 Quantum-Mechanical correlated l, M-distributions

The ground-state spin of a nucleus usually lies in the range 0–9$\hbar$. This spin cannot be perfectly aligned with the nuclear deformation axis, contrary to assumptions made in Subsections 3.2.3 and 3.2.4. Quantum mechanically, if we are dealing with a nuclear spin I, it may have a projection κ on *any* axis of at most κ numerically equal to I—since the length of the vector $\vec{I}$ is $\sqrt{I(I+1)}\hbar$. So, for example, if $I = 7$ and $\kappa = 7$, the classical angle between $\vec{I}$ and the axis along which κ is measured is 22°. The projection μ of I onto the beam axis may then take a range of values, as shown in Figure 3.8.

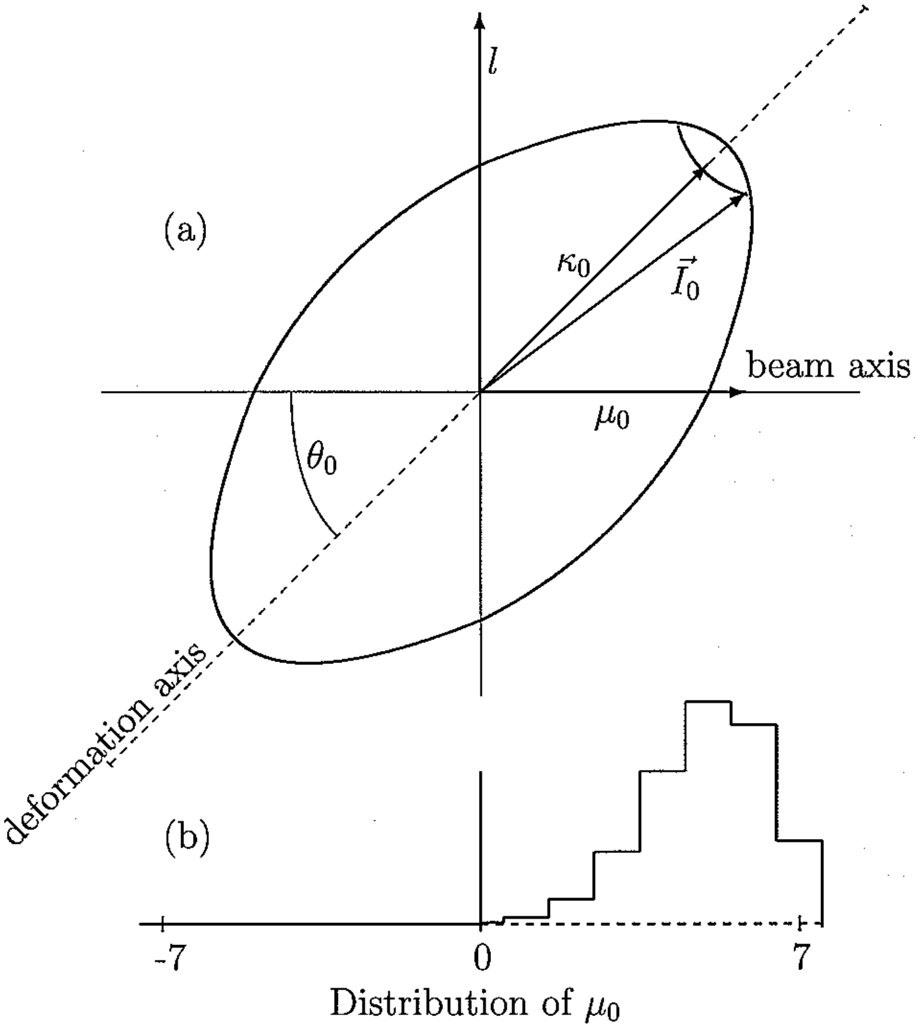

Figure 3.8: (a) A schematic diagram of a deformed nucleus with ground-state spin. Because the ground-state nuclear spin $\vec{I}_0$ cannot be perfectly aligned with the nuclear deformation axis, μ_0 may take a range of values. (b) The calculated distribution of μ_0 is illustrated for the case $I_0 = 7$, $\kappa_0 = 7$, $\theta_0 = 45°$.

This then breaks down into two problems. One is that we need to determine κ, the projection of the nuclear spin along the nuclear deformation axis. In the cases of interest (high deformation, high ground-state spin I) the odd nucleons will be in high-Ω Nilsson orbitals, where Ω is the projection of the particle angular momentum on the nuclear deformation axis, and the strong-coupling (deformation aligned) limit [NIL95] is applicable. In this limit, κ is a good quantum number and has the value $\kappa = I$ (the ground-state spin is aligned with the nuclear deformation axis). During the collision between projectile and target nuclei, the nuclei will be excited up their ground-state rotational bands, which can lead to increased κ-mixing for the excited states. However, the total angular momentum $\vec{J}$ is determined before the nuclei collide. Thus, for nuclei with spin I in their ground state, κ is numerically equal to I.

The second question is, given a spin I with projection κ on the nuclear deformation axis, what projection μ does I have on the beam axis? In other words, how does angular momentum transform under rotation? We assume an angle θ between the two axes. Rose [ROS61] shows that the angular momentum eigenfunction $|I,\kappa\rangle$, expressed in terms of the basis of eigenfunctions $|I,\mu\rangle$ relative to the beam axis, is as follows:

$$|I,\kappa\rangle = \sum_{\mu} d^{I}_{\mu,\kappa}(\theta)|I,\mu\rangle \tag{3.10}$$

Hence, to obtain the partial cross-sections $\partial\sigma(l,\mu_0,\mu_1)$, we must invert the above using the partial cross-sections $\partial\sigma(l,\theta_0,\theta_1)$. CCMOD has calculated this distribution in one-degree steps. The inversion is as follows:

$$\partial\sigma(l,\mu_0,\mu_1) = \sum_{\theta_0,\theta_1} |d^{I_0}_{\kappa_0=I_0,\mu_0}(\theta_0)|^2 |d^{I_1}_{\kappa_1=I_1,\mu_1}(\theta_1)|^2 \partial\sigma(l,\theta_0,\theta_1)\sin\theta_0\sin\theta_1 \tag{3.11}$$

The resulting distributions are compared with the classical projection of I on the nuclear deformation axis, $\sqrt{I_0(I_0+1)}\cos(\theta_0)$, in Figure 3.9. At most angles the average of the QM projections corresponds closely to the classical projection. However, at small angles the reduced alignment of the quantum-mechanical case becomes significant; the average of the QM projections is lower than the classical estimate. The importance of this difference is examined in Section 3.2.6.

From $\partial\sigma(l,\mu_0,\mu_1)$ we determine $w(J,M)$ precisely as given in Equation 3.8; that is to say, we add the three angular momenta from ground-state target spin, ground-state projectile spin, and collision-induced angular momentum, according to the

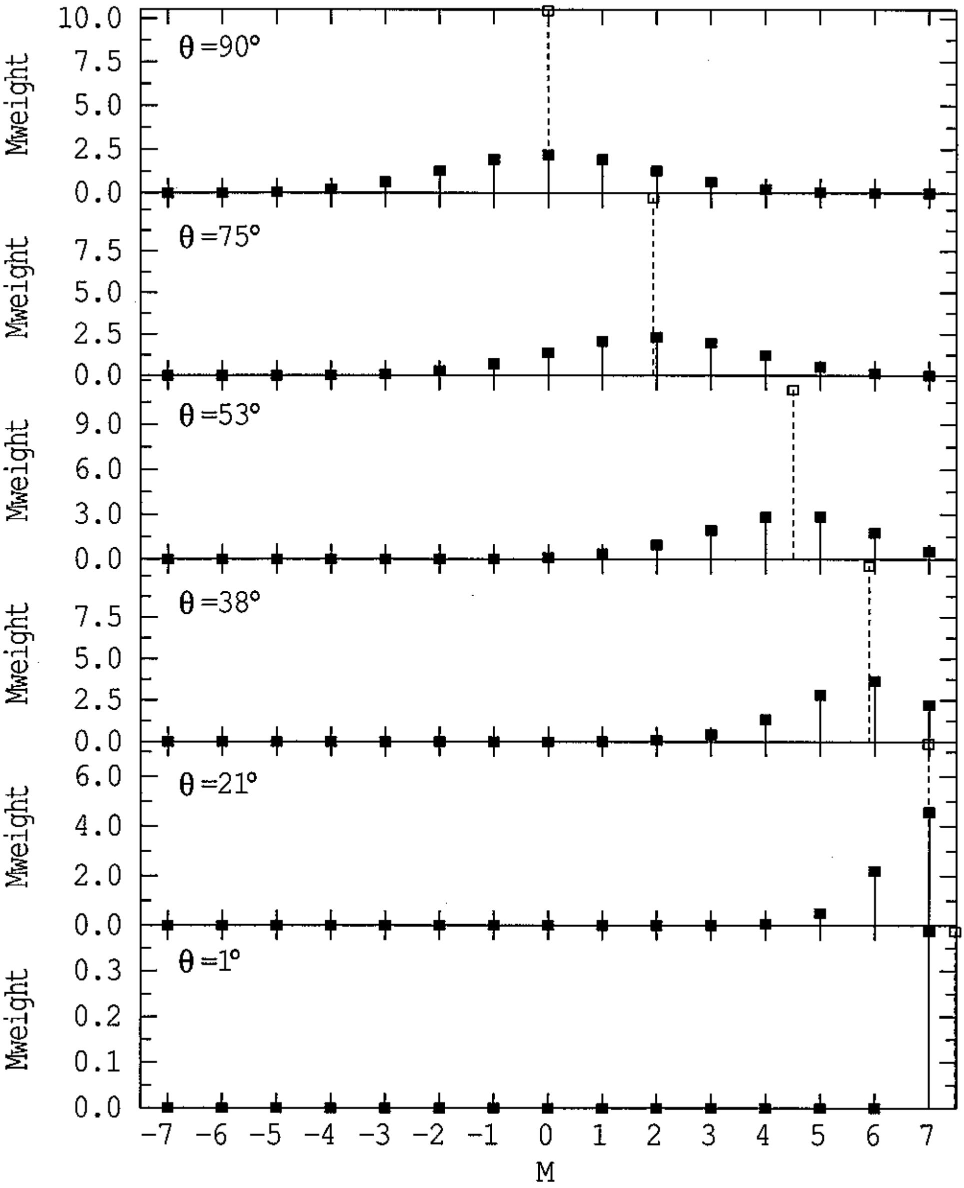

Figure 3.9: For a given state $|I,\kappa\rangle$, where semi-classical calculations assign all the weighting from one angle θ to the nearest M (hollow points), quantum-mechanical calculations spread the weighting between several M (solid points). This distribution is illustrated at various angles θ.

Clebsch-Gordan coefficients.

This quantum-mechanical treatment still uses the semi-classical assumption inherent in CCMOD, namely that the angle θ between the beam axis and the nuclear deformation axis is well defined. This is not expected to introduce significant error for the silicon and phosphorus induced reactions. This is because states in the rotational band built on the ground state are excited with significant probability to angular momenta $>\approx 14\hbar$ above the ground state. The angular uncertainty [NAG86] will thus be considerably smaller than that associated with the projection of the 7 units of spin. Since the latter effect results in only a minor correction to the anisotropies (Section 3.2.6), the classical assumption of an arbitrarily well-defined angle should result in negligible error for these reactions. For much lighter projectiles, however, this need not be the case.

3.2.6 Comparing the calculation methods

So far, in Sections 3.2.3, 3.2.4 and 3.2.5, we have described three increasingly sophisticated methods of handling the interaction between nuclear deformation and the effect of ground-state nuclear spin on the fission fragment angular distribution. The results from these methods should be compared to find out the importance of the refinements to the model.

First we examine the validity of the assumption which distinguishes the correlated and uncorrelated semi-classical models (Sections 3.2.3 and 3.2.4). That is to say, we consider the degree to which $w(J, M)$ differs from a separable distribution (one which could be written as $w(J, M) = f(J)g(M)$, for suitably chosen $f(J)$ and $g(M)$). When we consider the correlation between J and M, we see that, as expected, at higher J-values the ground-state spin is strongly aligned with the beam axis, as shown in Figure 3.7(b), whilst it is weakly aligned for lower J-values, as shown in Figure 3.7(c). The weak alignment at low J explains the similarity of the depletions of $w(J)$ for $J < I_0$ for isotropic and aligned calculations in Figure 3.7(a). The alignment ultimately serves to decrease the fission fragment anisotropy. The effect on the anisotropy is greatest at lower beam energies, because the alignment is stronger and the maximum J is smaller.

The effect of the correlation between J and M on the anisotropies is actually quite small; Figure 3.10 compares anisotropy calculations at a range of energies

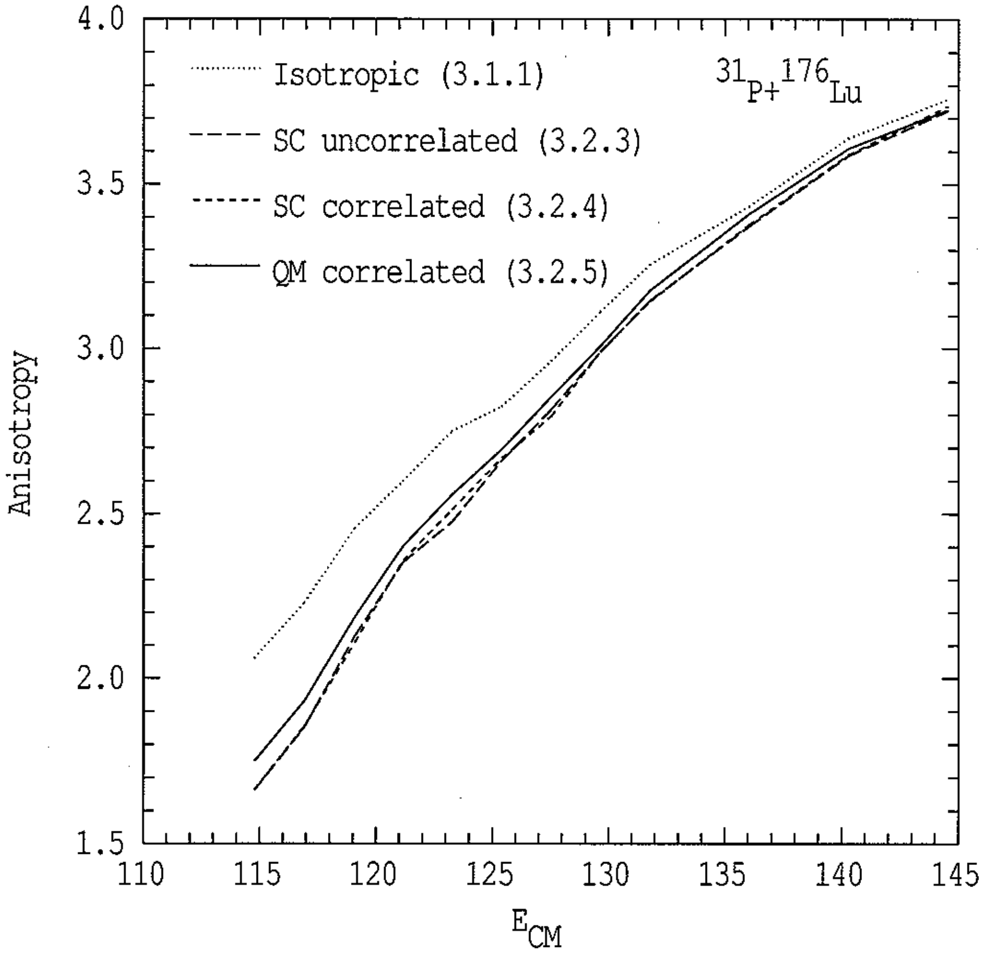

Figure 3.10: Anisotropy calculations using $w(J, M)$ distributions calculated using semi-classical and quantum-mechanical methods. The numbers in brackets specify the sections describing each type of calculation.

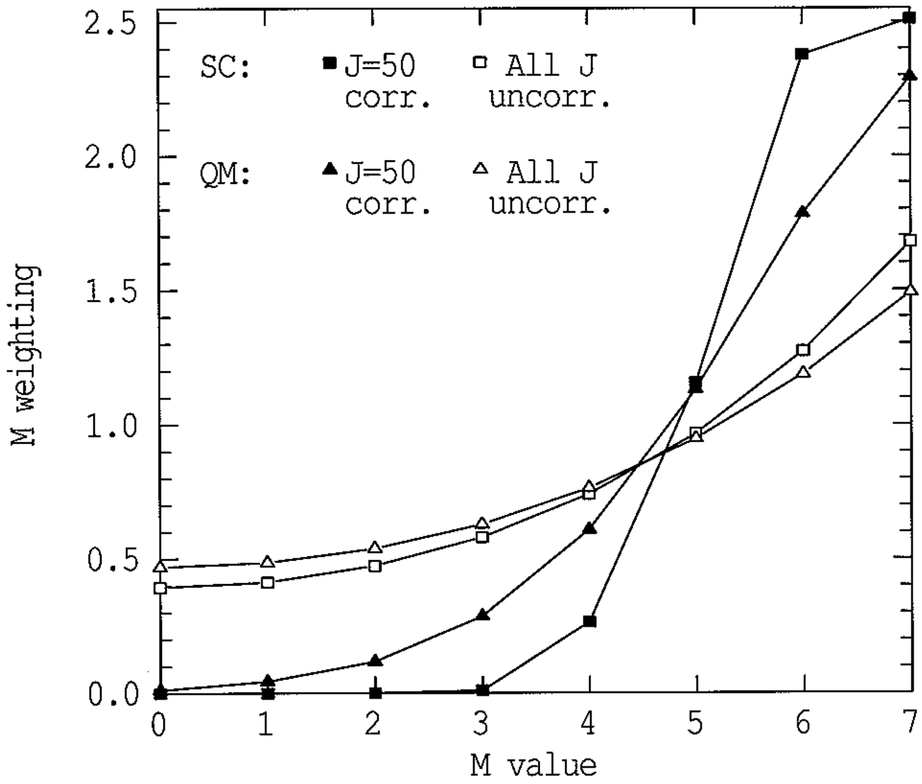

Figure 3.11: The difference between semi-classical and quantum-mechanical calculations is at its greatest when the alignment is at its greatest. M-distributions displayed using solid points are taken from correlated distributions $w(J, M)$ at J=50, whereas hollow points show M-distributions averaged over the whole range of J. All calculations are for the reaction ^{31}P+^{176}Lu at $E_{c.m.}$=114.8 MeV (E/B_0=0.939).

spanning the Coulomb barrier for the system ^{31}P+^{176}Lu. The uncorrelated (long-dashed line) and correlated (short-dashed line) semi-classical calculations are barely distinguishable, observable differences arising largely from statistical fluctuations in the Monte Carlo program used to calculate anisotropies as per Section 3.2.7.

In contrast, the quantum-mechanical calculation has a larger impact on the calculated anisotropy, especially at low energies. Because the ground-state spin of the nucleus is not perfectly aligned with the nuclear deformation axis, the overall alignment of the ground-state spin with the beam axis is also reduced, as illustrated in Figure 3.11. (We examine the overall alignment using $w(M) = \sum_J w(J, M)$.) Figure 3.10 shows the fission fragment anisotropy calculated with the quantum mechanical calculation (solid line); it is slightly higher than semi-classical calculations (dashed line) would yield, although still lower than an isotropic distribution of M

would yield (dotted line).

3.2.7 Incorporating other effects

For the calculations used in the rest of this thesis, we adopt the approach described in Section 3.2.5, determining the partial cross-sections $\partial(l, \mu_0, \mu_1)$ according to Equation 3.11 and the fusion channel weighting $w(J, M)$ according to Equation 3.8.

We are, however, interested in the *fission* channels. Until now we have assumed that all fusion channels proceed immediately to fission. However, Figure 1.2 illustrates a variety of possible outcomes for a given fusion event. In particular, fission probabilities and pre-fission particle emission must be considered.

Fission probabilities are significant because survival is more probable for low angular momenta, changing the shape of the distribution $w(J, M)$ for fission to favour larger angular momenta.

Pre-fission particle emission has a number of effects. The evaporating particle carries away energy (typically about 8 MeV) and angular momentum. The energy is far more important as far as the effect on the anisotropy is concerned; second chance fission, where one particle has evaporated, occurs with significantly lower nuclear temperature (and hence lower K_0) than first chance fission (where no particle emission occurs). This results in an increased anisotropy.

The angular momentum carried away by evaporated particles may change both J and M. In practice the effects are small; changes in M in particular are insignificant, as shown in Figure 3.12. They are, nevertheless, included in our calculations for completeness.

Post-scission reorientation is treated simply as a J-dependent correction to K_0, as given in Equation 3.3.

The J-dependence of $\mathcal{I}_{eff}$ may also be included in calculations. For larger J, the saddle-point appears at smaller elongations, and so $\mathcal{I}_{eff}$ is larger. This gives rise to a gradual increase in K_0 with J. While this effect has been included in the calculations described below, we have *not* included the variation of $\mathcal{I}_{eff}$ with K (Section 2.2.2.2, [LES99]), that narrows the K-distribution. The dependence of the rotational energy E_{rot} on elongation is appreciably different if K is large, so the change in the saddle point position is difficult to determine. However, since J is

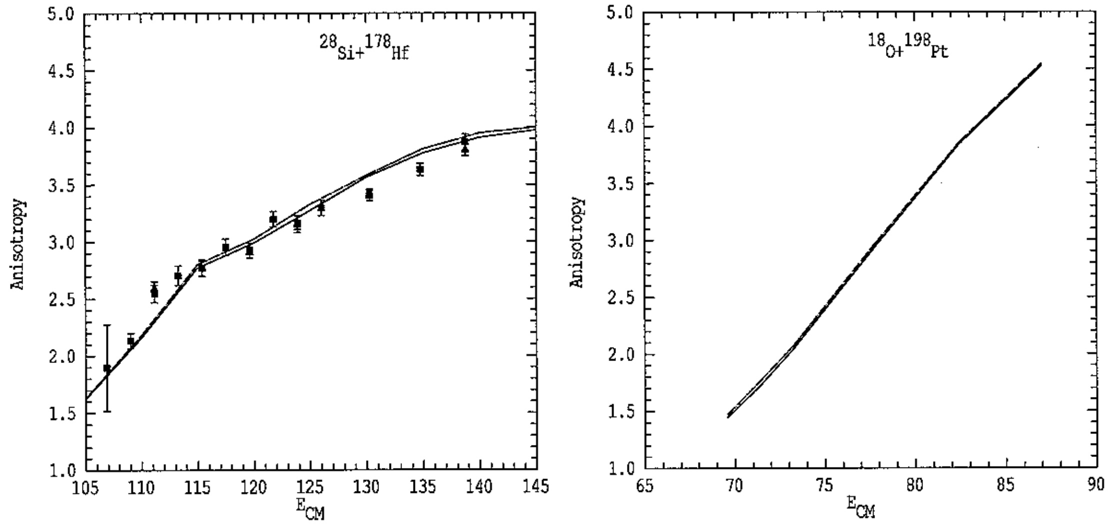

Figure 3.12: Anisotropy calculations with (solid line) and without (dashed line) changes in M due to the angular momentum carried away by evaporated particles. The reaction ^{28}Si+^{78}Hf is fission-dominated, whereas the reaction ^{18}O+^{198}Pt produces mostly evaporation residues, and of those events that do fission, a relatively high fraction are second or later chance fissions.

typically a few times larger than K in the reactions of interest, i.e. $K^2 \ll J^2$, and the effect should be minor. This variation of $\mathcal{I}_{eff}$ with K is generally not mentioned in the literature.

Hereafter we distinguish conditions of the compound nucleus initially formed following fusion from those at the saddle point by denoting all quantities determined at the saddle-point with a prime.

Mathematically we could write all these different effects as a combined operator $\vec{\mathcal{O}}_{K_0}$ applied to $w(J,M)$: $\vec{\mathcal{O}}_{K_0} w(J,M) = w'(J',M',K'_0)$. In practice we have a computer code to do all the number-crunching, using a statistical model code like JOANNE [LES93]. The code JOANNE was extended to include the changes in M due to pre-scission particle emission, and to accept $w(J,M)$ as input rather than $\partial\sigma(l)$, and was renamed JO_EVAP.

The fission fragment angular distribution is then determined as follows:

$$W(\theta) \propto \sum_{J'=0}^{\infty} \sum_{M'=-J'}^{+J'} \int_{K'_0} w'(J',M',K'_0) \sum_{K=-J'}^{J'} \frac{(2J'+1)|d^{J'}_{M',K'}(\theta)|^2 \exp(-K^2/2K_0'^2)dK'_0}{\sum_{K=-J'}^{J'} \exp(-K^2/2K_0'^2)} \tag{3.12}$$

In practice the distribution of K'_0 is handled by fission events being binned into J, T, M bins, K'_0 being evaluated for each bin, depending on $\mathcal{I}_{eff}(J)$ and T. This is the approach taken throughout the remainder of this thesis, except in most of the next section, where a slightly simpler calculation is used for the purposes of focusing on the effect of the nuclear ground-state spin.

3.3 Examples of Deformed Nuclei with Spin

For the purposes of these examples, we are interested in the change in fission fragment angular distributions due to the ground-state nuclear spins I_0 and I_1. So, in most of the calculations presented in this section, particle evaporation and post-scission reorientation effects are neglected; we assume every compound nucleus fissions with the same temperature (and K_0), using the simplified equation:

$$W(\theta) \propto \sum_{J=0}^{\infty} \sum_{M=-(I_0+I_1)}^{+I_0+I_1} w(J,M) \sum_{K=-J}^{J} \frac{(2J+1)|d^J_{M,K}(\theta)|^2 \exp(-K^2/2K_0^2)}{\sum_{K=-J}^{J} \exp(-K^2/2K_0^2)} \quad (3.13)$$

For nuclei with static deformation, the effect of ground-state spin is most significant at energies below the average fusion barrier, and for I_0/K_0 greater than about 0.3; when these conditions hold, the anisotropy $A = W(180°)/W(90°)$ may cease to be sufficient to characterize the fission fragment angular distribution. This will now be illustrated using the reactions ^{31}P+^{176}Lu and ^{28}Si+^{178}Hf^{m2}.

For the purposes of these calculations, and throughout this thesis, the level density parameter a'_f was taken as 8.6 MeV^{-1}. Calculations were performed assuming zero fission transient delay time [LES93], a Kramers factor (correcting for fission width suppression due to Brownian motion of systems at the saddle-point) of 1.0, a fission barrier scaling factor of 0.94, and taking $a'_f/a_n = 1.0$. Taking the transient delay time as zero has a minimal effect at the excitation energies used. These parameters reproduce experimental data well for these or similar reactions, as shown in Chapter 5.

^{176}Lu is a highly deformed nucleus ($Q = 4.92$ b [NDS98], giving $\beta_2 = 0.29$ for $r_0 = 1.2$ fm) with a ground-state spin of 7. Figure 3.13(a) shows calculations of the fission fragment angular distributions for the reaction ^{31}P+^{176}Lu at $E_{\text{c.m.}}/B_0 = 0.97$ ($B_0 = 122.3$ MeV). The dotted line shows a calculation ignoring all ground-state spins; the dashed line shows the calculation assuming that the ground-state spins are isotropically oriented (using Equation 3.1; including the $\frac{1}{2}$ spin of ^{31}P for completeness), and the points show the fission fragment angular distribution from Equation 3.13, including the spin alignment resulting from nuclear deformation of

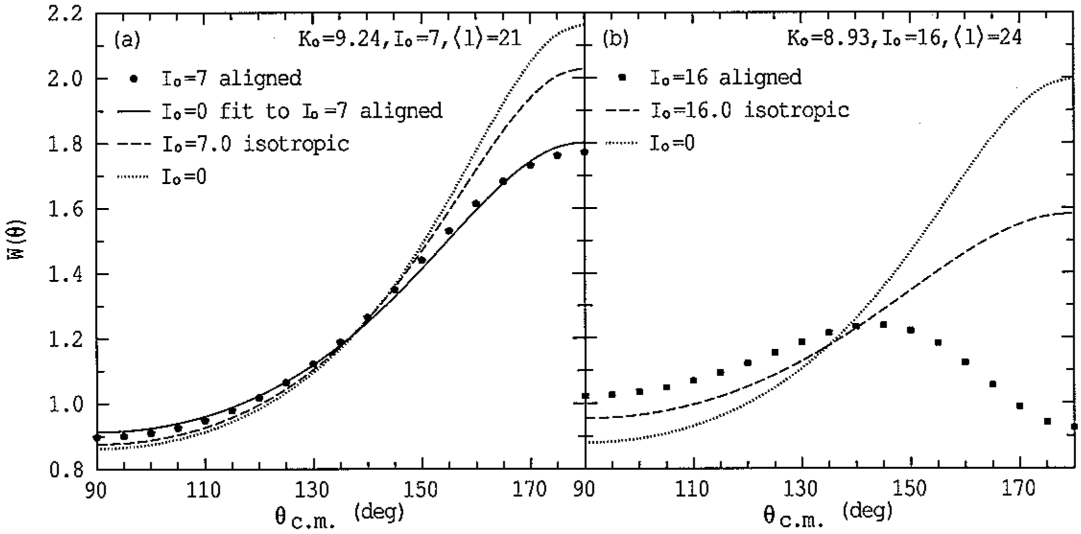

Figure 3.13: Calculated angular distributions for no-spin (dotted line), isotropic-spin (dashed line), and aligned-spin distributions (points) for (a) ^{31}P+^{176}Lu at $E_{\mathrm{c.m.}}/B_0 = 0.97$ and (b) ^{28}Si+^{178}Hf^{m2} at $E_{\mathrm{c.m.}}/B_0 = 0.99$.

the lutetium. The solid line is a least-squares fit to this distribution using the $I_0 = I_1 = 0$ limit of Equation 3.1, with K_0 a free parameter. The anisotropy of the fragment distribution calculated using aligned nuclear spin (solid points) is significantly lower than the anisotropy predicted using only isotropic spins (dashed line). For this reaction, the change in anisotropy due to nuclear spin ($(A_{I=0} - A_{I=7})/A_{I=7} = 29\%$) should be measurable, since targets may be made with relatively high enrichments of ^{176}Lu. It is interesting to note that the aligned distribution (solid points) has a different shape than an $I = 0$ curve with the same anisotropy; the ratio $W(135°)/(W(90°)+W(180°))$ differs by 2% from the $I_0 = 0$ fit, information which would be missed if only anisotropies were to be compared. Alternatively, if experimental measurements were obtained only in the range (for example) 110°–165°, fitting the resulting angular distribution with an $I = 0$ curve would yield too high an anisotropy.

An extreme example of a target nucleus with large spin and deformation is the long-lived isomer ^{178}Hf^{m2}, which has spin 16. At least one target has been made containing a small fraction (~3%) of this isomer [OGA92]. If this could be increased, it might therefore be possible in future to carry out fission fragment angular distribution measurements for a reaction on ^{178}Hf^{m2}.

Calculations using Equation 3.12, for the reaction ^{28}Si+^{178}Hf^{m2}, at $E_{\mathrm{c.m.}}/B_0 =$

0.99 ($B_0 = 116.4$ MeV), are shown in Figure 3.13(b) as solid points. The deformation is taken as $\beta_2 = 0.267, \beta_4 = -0.062$ (calculated from $\epsilon_2 = 0.254, \epsilon_4 = 0.053$, as used in Ref. [MUL97]). The incoming projectile brings in an average of $24.4\hbar$, and K_0 is calculated (using JOANNE [LES97]) to be 8.9. Also plotted, for comparison, is the corresponding calculation assuming zero spin (dotted line), and for a target with isotropically oriented spin (dashed line). Note that the realistic calculation peaks around 140°, and has an anisotropy significantly less than unity; this cannot be predicted by simple approximate treatments of ground-state spin.

Since the spin alignment has such a dramatic effect, further calculations have been made at a range of energies below and above the average barrier. In order that these predictions should be accurate, these calculations were performed using Equation 3.12, including all effects of evaporative competition with fission. These calculated anisotropies are shown in Figure 3.14(a) by the solid line. The anisotropy predicted for the same reaction assuming an isotropic spin distribution is shown with a dashed line, whilst for reference, the anisotropy predicted for the reaction ^{28}Si+^{178}Hf is shown by the dotted line; ^{178}Hf has zero spin in its ground state. As the energy increases above the average barrier, the spin alignment of ^{178}Hf^{m2} decreases, and so the anisotropy approaches that corresponding to the isotropic spin distribution. The anisotropies remain low compared to the reaction on ^{178}Hf, due mainly to the extremely high spin of ^{178}Hf^{m2}. The shape of the fission fragment angular distribution returns to normal as the beam energy increases, with the peak moving from 90° to 180°, as shown in Figure 3.14(b). According to the calculations, using standard parameters, fission is the dominant decay process at all energies, as illustrated in Figure 3.14(c). Even where the effects of spin alignment are approaching maximum, the fission cross-section is still ~ 10 mb, meaning that measurements of anisotropies may in principle be feasible, if a target with a higher fraction of the isomer were made.

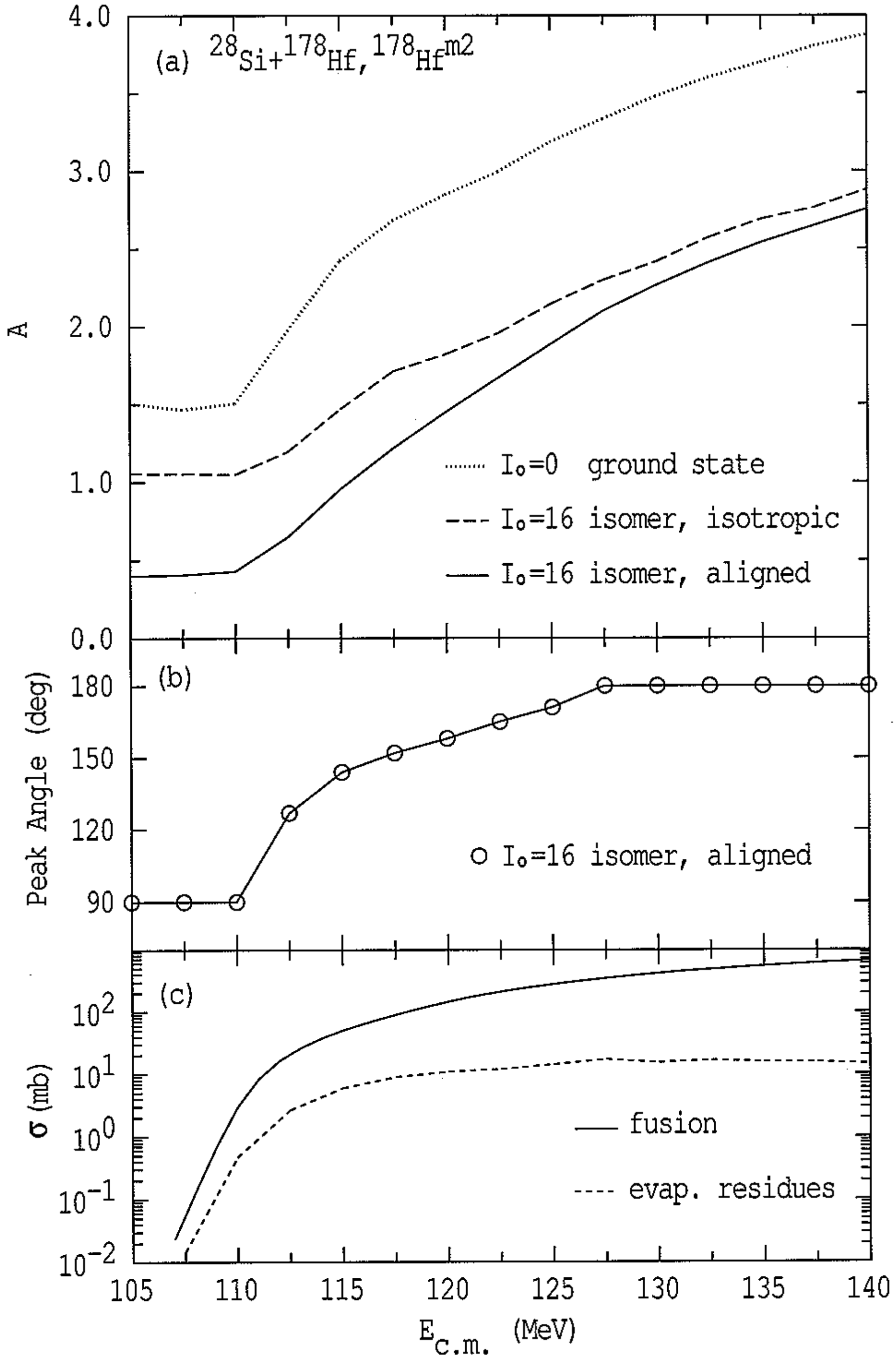

Figure 3.14: (a) The anisotropies predicted for ^{28}Si+^{178}Hf^{m2}, when deformation is included (solid line), excluded (dashed line), and for the reaction ^{28}Si+^{178}Hf (zero spin: dotted line). (b) The angle at which the fission fragment angular distribution peaks. (c) The calculated fusion and evaporation residue cross-sections for ^{28}Si+^{178}Hf^{m2}.

CHAPTER 4

Experiment and Analysis

All measurements reported in this thesis were performed using ANU's 14UD Pelletron Accelerator (Section 4.2.2) to provide a beam of charged particles, and the CUBE detector array (Section 4.2.3) to collect data.

4.1 Choice of Reactions

4.1.1 Fusion-Fission

In order to observe the effects of deformation-aligned ground-state spin on fission anisotropies, a strongly deformed prolate target nucleus with high ground-state spin is required, and a reaction with a significant fission cross-section at sub-barrier energies. These conditions are met in the reaction ^{31}P+^{176}Lu, where ^{176}Lu has a ground-state spin of 7 and a large prolate deformation. However, measurements on this reaction alone would not be conclusive, since it is not yet clear that anisotropies can be predicted a-priori with sufficient accuracy. Therefore measurements were also performed for the reaction ^{29}Si+^{178}Hf, which makes the same compound nucleus (^{207}Rn). In this reaction the target nucleus has zero spin and a prolate deformation almost identical to ^{176}Lu.

These two reactions are expected to have similar inelastic and transfer couplings influencing the fusion process, and the agreement between the calculated fusion cross-sections and the data (see Section 5.1) supports this. Because of the similar projectile masses, the compound nuclei will have similar angular momenta and probabilities for fission (and quasi-fission, if present). This allows the effect of the ground-state spin of ^{176}Lu to be isolated experimentally.

Compound Nucleus	Reaction	Ground-state spin	
		Projectile	Target
^{207}Rn	^{31}P+^{176}Lu	1/2	7
^{207}Rn	^{29}Si+^{178}Hf	1/2	0
^{206}Rn	^{31}P+^{175}Lu	1/2	7/2
^{206}Rn	^{28}Si+^{178}Hf	0	0

Table 4.1: Ground-state spins of the target and projectile for the four reactions studied.

The available ^{176}Lu target material had a low enrichment, the remainder being ^{175}Lu; thus it was necessary to make measurements on the reaction ^{31}P+^{175}Lu so that the contributions from the different isotopes could be disentangled. The ^{175}Lu nucleus has a ground-state spin of 7/2 and is thus intermediate between the zero-spin and spin 7 cases. For comparison with this reaction, the reaction ^{28}Si+^{178}Hf, which makes the same compound nucleus (^{206}Rn), was also studied. The ground-state spins for the projectile and target nuclei in the reactions studied are given in Table 4.1.

Both ^{28}Si and ^{178}Hf have zero spin in their ground states, and the 1/2 spin of ^{29}Si and ^{31}P may reasonably be considered negligible. It is then only the spins of the deformed Lu target nuclei which can have a measurable effect on the fission angular distributions, small for ^{175}Lu, but potentially large for ^{176}Lu, since its spin is comparable with the angular momentum brought in by the projectile at sub-barrier energies.

4.1.2 Quasi-fission

The choice of quasi-fission reactions to pursue was made in light of Lestone et al's work [LES97] on comparing the reactions ^{12}C+^{235,236,238}U. Lestone reported high fission-like fragment anisotropies for the zero-spin reactions ^{12}C+^{236,238}U, and markedly lower anisotropies for ^{12}C+^{235}U, where ^{235}U has a ground-state spin of 7/2, indicating that the ground-state spin had a substantial effect on the angular distribution of the fission-like fragments.

Similar cross-section and fission-like fragment anisotropy data, but with considerably better precision, were already available for the reaction ^{16}O+^{238}U [HIN96], and the observed anisotropies at below-barrier energies were appreciably higher than for the corresponding ^{12}C reaction, due partly to the increased angular momentum brought in by the heavier ^{16}O projectile, but also to an increased probability of quasi-fission, and/or a larger anisotropy for the quasi-fission itself. It was suggested that the reaction ^{16}O+^{235}U should show a similar or greater reduction in fission-like fragment anisotropies in the below-barrier region, compared to the ^{16}O+^{238}U, as was observed in the ^{12}C reactions. Therefore, obtaining high-precision anisotropy measurements for the ^{16}O+^{235}U reaction should allow more quantitative testing of whether or not the quasi-fission data could be explained by the model of ground-state spin already tested for fusion-fission.

4.2 Experimental Conditions

The fusion-fission experiments are described first, and then the quasi-fission experiments are covered.

All experimental data are recorded in event-by-event form; the analysis process involves sorting these event-by-event data, identifying the important quantities, calibrating or normalizing the measurement, and fitting the results to obtain the quantities of interest.

4.2.1 Targets

The ^{176}Lu targets were made from a sample of lutetium oxide enriched to 47.2% in ^{176}Lu, which was reduced to metal using thorium, and then sputtered onto a ~20 μg/cm^2 carbon backing to form targets of thickness 20–40 μg/cm^2. We made three targets from this sample. For two of these enriched targets, the thorium content was determined to ±0.3% using the Rutherford back-scattering (RBS) technique, with a beam of ^{31}P at 91.9 MeV. These targets had thorium concentrations of 22.3% and 22.5% respectively. Fitting the energy spectrum of the elastically scattered beam particles in the monitor detectors at 22.5° gave thorium concentrations consistent with RBS measurements within ±1%. The third target was only examined using elastically scattered beam-particles in the monitors; these revealed that the thorium concentration was 28%.

In order to account for fission events originating from reactions on ^{175}Lu, other targets were made using natural lutetium (97.4% ^{175}Lu). These targets did not have significant thorium content, as the ^{nat}Lu sample was large enough to be double-distilled to remove the thorium.

The ^{178}Hf targets consisted of $\approx$ 200 μg/cm^2 of metal evaporated onto $\approx$ 30 μg/cm^2 backing foils of aluminium.

The uranium targets required for the quasi-fission experiment comprised uranium nitrate or uranium metal evaporated onto 12 μg/cm^2 carbon foils. The ^{235}U target was a "recovered" target and the target layer, comprising 30 μg/cm^2 uranium nitrate (20 μg/cm^2 uranium), was sandwiched between two carbon foils. The enrichment of this target was >94%. The ^{238}U target was made from natural uranium metal, which is 99.274% ^{238}U, and was mounted with the uranium layer (100 μg/cm^2 thick) facing the oncoming beam, so as to avoid beam degradation in the carbon layer prior to interaction with the uranium.

4.2.2 Beam

Beams for the experiments were produced using the Australian National University 14UD tandem accelerator. In this accelerator, mass-selected ions with single negative charge are accelerated towards a large, positive potential. There, several electrons are stripped off, and the now positively charged ion is further accelerated away from the positive potential.

Ions with the desired charge-state and energy are selected using a 90-degree magnet with a very precise magnetic field setting. These may then be focussed onto a target foil in the detector array. The field is calibrated every few years using the 14.231 MeV resonance in the ^{12}C(p,α) reaction. Very consistent results have been obtained, indicating an absolute energy uncertainty of less than 10^{-3}.

The beam of ions is usually bunched and chopped into pulses about 1ns wide and some multiple of 106 ns apart. The same RF signal that controls this chopping is supplied to the data collection system for the purposes of time measurements. In the fusion-fission and quasi-fission measurements, the pulsed beam consisted of 1 ns long bursts separated by 106 ns. This allowed time-of-flight measurements for fission fragments to be made.

Fusion-fission measurements were performed over the course of five runs, each of 2–3 days duration. The 14UD provided beams with energies ranging from 135.0–165.0 MeV for ^{31}P, from 123.7–160.6 MeV for ^{28}Si, and from 126.6–159.1 MeV for ^{29}Si, as listed in Tables 5.1–5.4. The beam energies for the reactions on ^{178}Hf were chosen to give the same compound nucleus excitation energies as for the reactions on ^{175}Lu and ^{176}Lu.

Quasi-fission measurements were performed during a single run of 3 days duration. The 14UD provided a ^{16}O beam with energies in the range 78.0–114.0 MeV, as listed in Table 6.2.

4.2.3 Fission Fragment Detectors

Fission fragments were detected in the CUBE detector array [MOR95], consisting during these fission measurements of two large area position sensitive multi-wire proportional counters (MWPC), two monitor detectors, and a backward-angle silicon surface-barrier detector.

These MWPC detectors consist of several planes. The plane closest to the target is a window intended to separate 4 Torr of propane gas inside the detector from the high-level vacuum in which the beam of projectiles meets the target. This window is a sheet of 0.9 μm thick polyethylene terephthalete (PET) foil, with one side coated with ≈50 μgcm^{-2} copper, which reduces the leakage of propane gas from the detector and prevents charge build-up on the window. In front of the window (closer to the target) are three horizontal and four vertical wires of 0.45mm diameter, which serve to reduce the bowing of the window towards the target under the 4 Torr pressure. These wires have only a minor impact on coincidence analyses, but their effects have been included. A gas flow system is used to maintain the pressure and renew the gas, preventing buildup of contamination from out-gassing of the detectors or ionization-damaged molecules.

The propane gas within the detector is ionized by the passage of ions such as fission fragments and elastically scattered beam particles. The active part of the detector comprises three parallel electrode planes. A voltage is maintained between the central and outer planes, which accelerates the electrons created by the primary ionization, giving secondary ionization and considerable signal amplification.

The first plane comprises 284 wires strung vertically, spaced at intervals of 1mm, made of tungsten coated with gold, and 20 μm in diameter. These serve to detect the X-position at which the particle strikes the detector, by virtue of the 1 ns delay between each pair of wires. If the incoming particle passes close to one wire, a signal is induced in that wire by the movement of the electrons towards the wire. That signal then propagates in both directions along the delay line, and the difference in time between the emergence of the signal at one end of the line to the other shows which wire collected the signal.

The central foil is 3mm further behind that, at its closest being 180 mm from the target. This layer is the central foil cathode, which comprises a sheet of 0.9 μm (PET) foil with gold evaporated onto both sides with thickness 40 μgcm^{-2}, separated into four quadrants to reduce its capacitance and thus increase the signal size. The foil is maintained at a potential of approximately -500 V. The signal from this cathode provides energy loss and time information for each particle, which in conjunction with the pulsed beam gives the time of flight of the particle.

The fourth layer comprises 357 horizontally strung gold-coated tungsten wires, located 3 mm behind the central cathode. These detect the Y-position of the particle in the same manner as the X-position is detected.

The active area of each detector is 284 mm wide, and 357 mm high. The detectors are positioned opposite one another as illustrated in Figure 4.1, so as to detect both the fission fragments from a fission event. They cover laboratory angles from 95°–170° ("Back" or "upstream" detector), and 5°–80° ("Front" or "downstream" detector).

The front detector is exposed to a rate of elastically scattered beam particles too high to be accepted by the data acquisition system. Since the back detector is not subject to such a high rate, events are not recorded unless there is a signal in the back detector. This cuts the elastic scattering signal rate to acceptable values (typically 300 Hz). Since fission fragments separate in opposite directions, if a fission fragment is detected in the front detector its partner should also be detected in the back detector, subject to a few solid angle restrictions. For the fusion-fission experiments this "back detector" trigger suffices; for the quasi-fission experiments data is recorded only if events are detected in *both* the front and back detectors, as a more complex data analysis procedure is required to eliminate transfer-fission events.

Two monitor detectors were placed at ±22.5°, to monitor elastically scattered

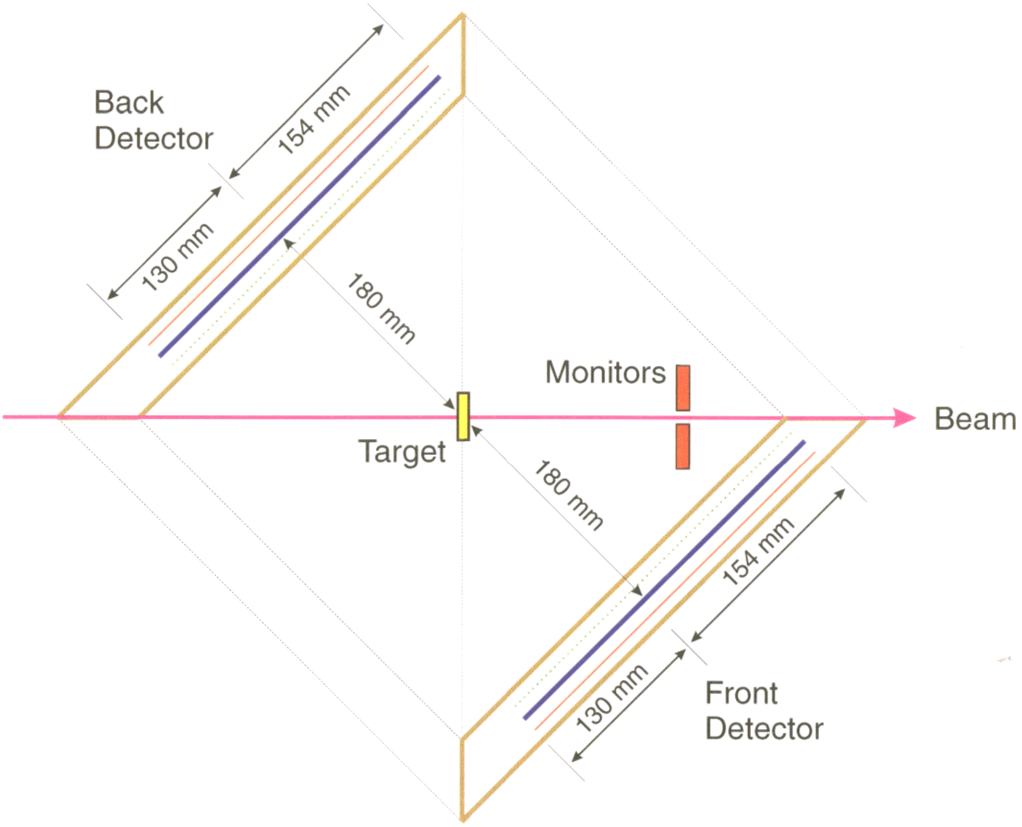

Figure 4.1: Plan view of the CUBE spectrometer. Diagram reproduced from [MOR95B].

beam particles. Since the Rutherford scattering cross-section is well known, use of these monitors allows cross-section determination. For some of the measurements, an annular silicon surface barrier detector (SBD) was placed at 174°, to measure target composition—this obscured the most backward angles, restricting the sensitive angular range of the MWPC to 95°–166°. For the ^{29}Si+^{178}Hf reaction, fission fragments were identified in the SBD, and contributed to the measured angular distributions. This detector was also used to detect alpha particles from evaporation residues (see Section 4.4 for details).

In order to obtain precise cross-sections and anisotropies, it was important to have accurate solid-angle information, and to take into account any non-linearities in the detector's position response function. This information was obtained by measuring Rutherford scattering of ^{31}P beams off a ^{197}Au target in the back fission detector at beam energies well below the fusion barrier. This calibration was repeated for each experimental run, and varied very little between runs.

4.3 Fission Event Identification and Analysis

4.3.1 Identifying Single Fragment Events

For the first part of the project, the reactions being studied were ^{28}Si+^{178}Hf, ^{29}Si+^{178}Hf, ^{31}P+^{175}Lu, and ^{31}P+^{176}Lu. All four of these reactions are similar in terms of nuclear deformations, excitation energy, angular momentum, and would be expected to have similar quasi-fission probability, if quasi-fission is present at all.

In all four of these reactions, fission events could be identified solely from the signals from the fission detector placed at backward angles. These comprised the energy loss signal ΔE in the detector and the time-of-flight to the detector. At most energies of interest, the fission and elastic events at all angles can be cleanly separated by one gate, as shown in Figure 4.2. However, at below-barrier beam energies, elastic events could appear in one area of the multi-wire proportional counter with similar energy and time-of-flight signals to fission events arriving in another area of the detector. However, for any given angle θ, the fission and elastic events may still be cleanly distinguished, and so for beam-energies below the Coulomb barrier, fissions were identified for each 5° bin individually.

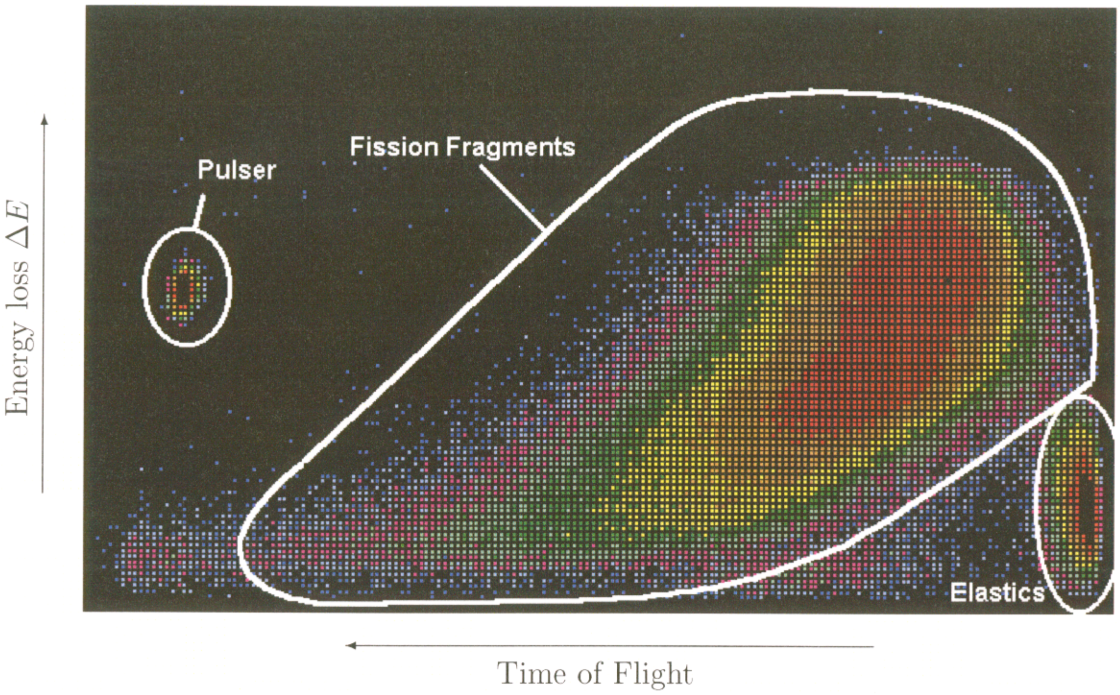

Figure 4.2: Detector events in the back MWPC, showing time of flight plotted against energy loss. The fission fragments are clearly distinguished from elastically scattered beam particles.

4.3.2 Identifying Coincidence Events

For the ^{16}O+^{235,238}U measurements, transfer-induced fission was present. In this case, it is necessary to distinguish fission following complete fusion by detecting both fission fragments in coincidence, and deducing the total linear momentum of the original fissioning system. With transfer-induced fission, the remainder of the projectile carries off significant momentum, imparting a recoil to the fissioning target-like nucleus, whereas complete fusion means the compound nucleus has the full momentum brought in by the projectile.

4.3.2.1 Kinematic Coincidence method

Fission fragments separate in opposite directions in the center of mass frame. However, due to momentum carried off by light particles emitted before or after fission, the center of mass velocity $\vec{v}_0$ may vary slightly from the $\vec{v}_{c.m.}$ deduced from the projectile velocity. For any given event we define the projection of the *actual* center of mass velocity $\vec{v}_0$ on the beam axis as $v_{0\|}$, and the projection in the plane perpendicular to the beam axis, normal to the fission direction, as $\vec{v}_{0\perp}$. For full

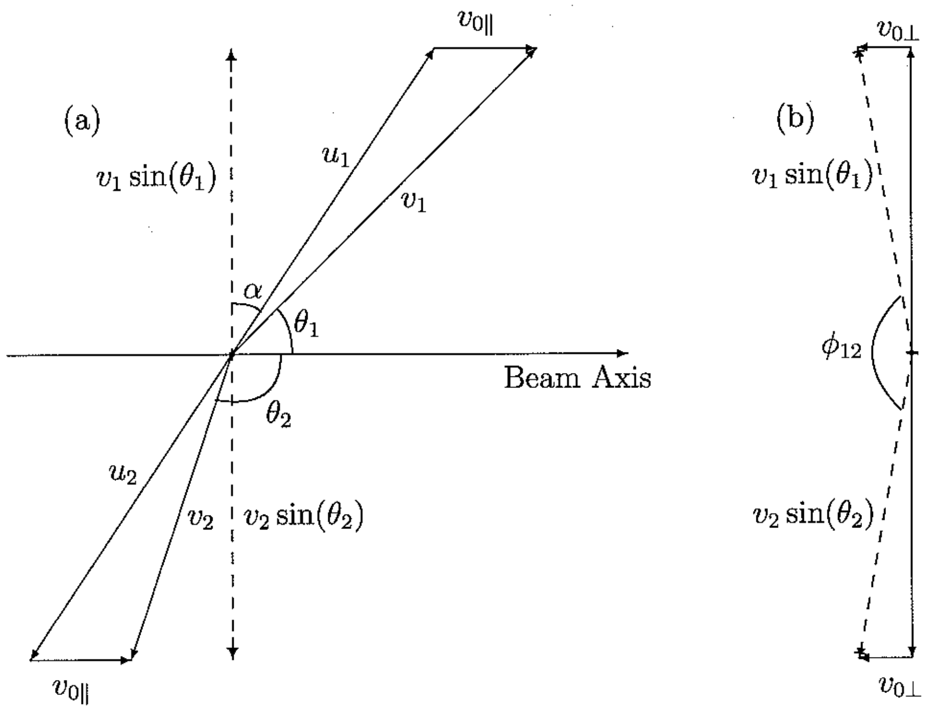

Figure 4.3: Sketches of the fission fragment velocities in (a) the plane including the beam axis and the fragment velocities, (b) the plane perpendicular to the beam axis. (u_1 and u_2 are collinear, despite optical illusions to the contrary!)

momentum transfer events, $v_{0\parallel}$ and $v_{0\perp}$ will differ very little from their expected values of $\vec{v}_{c.m.}$ and zero respectively.

It is necessary to determine the lab-frame fragment velocities $\vec{v}_1$ and $\vec{v}_2$ in order to evaluate $v_{0\parallel}$ and $v_{0\perp}$. The velocity of each fission fragment can be determined using the time-of-flight to the detector, and the position information. This requires calibration of the time-of-flight signal, to precisely identify the time at which the beam-pulse hit the target.

We assume $v_{0\perp}$ is negligible, which will only fail for events we were discarding anyway. Figure 4.3 defines the important quantities. The magnitudes of the center of mass velocities u_1 and u_2 may differ, according to the masses of the particles, but since the two are on average at opposite angles α:

$$\frac{u_1\cos(\alpha)}{u_1\sin(\alpha)} = \frac{u_2\cos(\alpha)}{u_2\sin(\alpha)}$$

We then note that $u_1\cos(\alpha) = v_1\sin(\theta_1)$ and $u_1\sin(\alpha) = v_1\cos(\theta_1) - v_{0\parallel}$. Solving the equation resulting from those substitutions for both fragments yields:

$$v_{0\parallel} = \frac{v_1 \sin(\theta_1) v_2 \cos(\theta_2) + v_2 \sin(\theta_2) v_1 \cos(\theta_1)}{v_1 \sin(\theta_1) + v_2 \sin(\theta_2)} \tag{4.1}$$

We define also the mass split A_1 as the fraction of the total mass carried away by fragment 1, and evaluate it using conservation of momentum considerations as:

$$A_1 = \frac{|u_2|}{|u_1| + |u_2|} \tag{4.2}$$

Once $v_{0\parallel}$ is determined, evaluation of $|u_1|$ and $|u_2|$ is trivial. However, it is assumed that $v_{0\parallel} = v_{c.m.}$ for the purposes of evaluating A_1 for full momentum transfer fission, to reduce sensitivity to experimental uncertainty.

Further trigonometry yields $v_{0\perp}$ [HIN96]:

$$v_{0\perp} = \frac{v_1 \sin(\theta_1) v_2 \sin(\theta_2) \sin \phi_{12}}{\sqrt{v_1^2 \sin^2(\theta_1) + v_2^2 \sin^2(\theta_2) + 2 v_1 \sin(\theta_1) v_2 \sin(\theta_2) \cos \phi_{12}}} \tag{4.3}$$

4.3.2.2 Calibrating the Time of Flight

Time of Flight information is derived from the central foil in the MWPCs. However, there are two of these foils (one in the front detector and one in the back) and each is divided into four quadrants, each with its own time-zero. The differences between quadrants, and between the front and back detectors, should be constant throughout the experiment, so these only need to be evaluated once. The overall time-zero, or precisely when the beam pulse hits the target, relative to the master oscillator pulses which generate the time structure of the beam, must be determined for each run individually. The time calibration per-channel is determined for the detector system using a calibration run where signals are input into the detector at precisely determined intervals, using an ORTEC time calibrator.

The time differences between signals from individual detector quadrants are ascertained by adjusting them until the fragment velocity v_1 or v_1 is a smooth function of θ or ϕ, for a narrow range of ϕ or θ intersecting two quadrants.

The difference in time-signals between front and back detectors Δt may not be precisely determined without also determining the overall time-zero T_z (also the time-zero for the back detector alone) for the particular run under consideration. This is carried out using an iterative procedure. Initially these parameters are determined approximately using an absolute calculation of lab-frame fission fragment

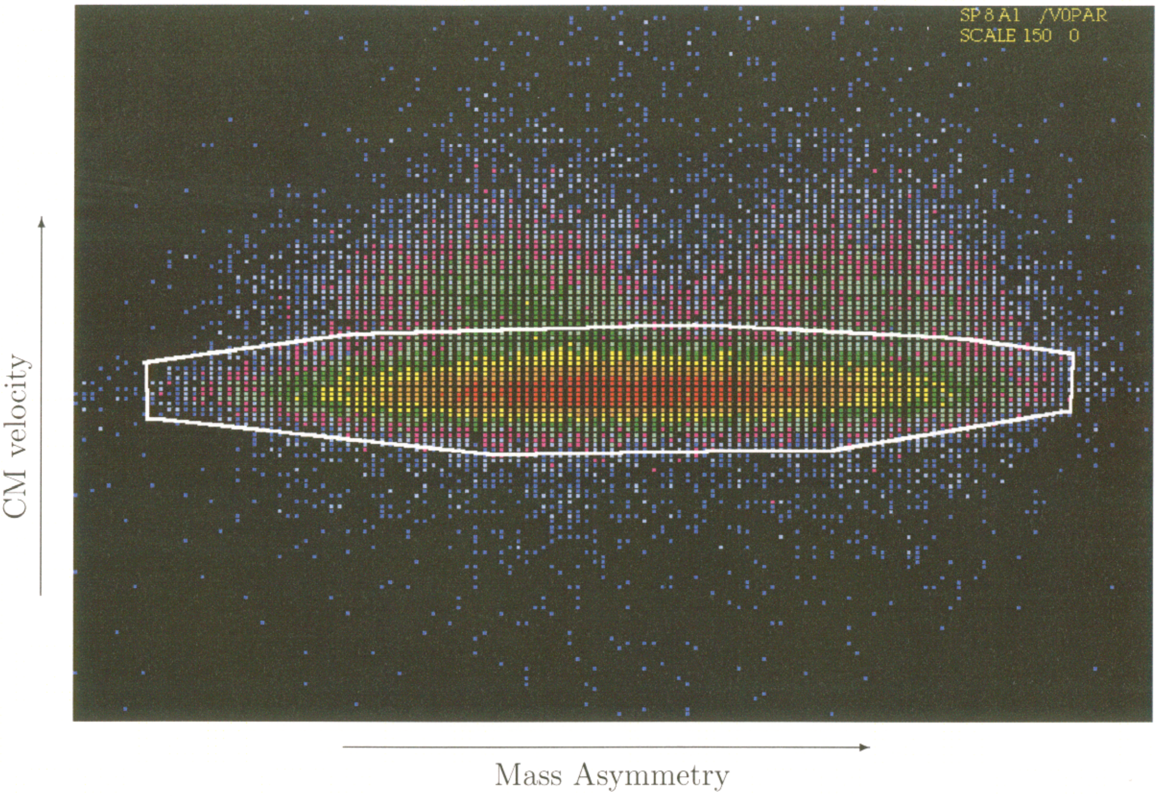

Figure 4.4: Coincidence events plotted according to the mass asymmetry and the apparent centre-of-mass velocity. The white polygon indicates the events used to measure the centroid, excluding the majority of the transfer fission events.

velocities, assuming Viola systematics. This involves comparing the observed time-of-flight of the fastest fragments (those at $\phi = 0°$ or $180°$, i.e. in the y=0 plane) at a given θ to the expected time-of-flight of the fission fragments to the detector.

Precise determination of Δt is performed using a reference reaction, for which the average fission-like fragment mass asymmetry A_1 is known (for reactions where only fusion-fission is present, this asymmetry will average 0.500) and the average $v_{0\|}$ is equal to $v_{c.m.}$. From experimental data for the reference reaction, we select only those events already identified as fissions according to ΔE and the time of flight, as per Figure 4.2, and calculate the average mass asymmetry and $v_{0\|}$ using the approximate values of Δt and T_z. We then make small adjustments to Δt and T_z until the reference values are reproduced. This calibration of Δt was performed for three different reference reactions, and the results obtained were in good agreement with one another.

To determine T_z for each beam energy, we hold Δt constant at the value determined above, and adjust T_z until the average $v_{0\parallel}$ is equal to $v_{c.m.}$. The majority of transfer fission events are excluded as indicated by the white line in Figure 4.4.

4.3.2.3 Separating out the events of interest

Transfer fission events can be distinguished from full momentum transfer fission events according to the deduced $v_{0\parallel}$ and $v_{0\perp}$. We make a cut in $v_{0\parallel}$, to reject mostly transfer events; this cut accepts FMT events with 98% efficiency, varying very little over the experimental energy range. With this cut, $v_{0\perp}$ is projected out for each angle θ, in 5° bins, for each beam energy, subtracting the transfer fission event background as shown in Figure 4.5, and determining the number of FMT events detected at that angle and that energy. Subsequent analysis may proceed precisely as for "singles" analysis, after correcting the solid-angle calibration for the losses due to the support wires for the front detector window, and the 2% efficiency loss from the front detector x-plane wires. These are both accounted for individually for each 5° bin in the back detector.

4.3.3 Fission Fragment Angular Distributions

The position information from the back angle MWPC was used to calculate the angle at which detected reaction products emerged from the target [HIN95]. Results were analysed using 5° intervals in the laboratory scattering angle θ. Within any given interval, fission fragments could be distinguished from elastically scattered particles according to the energy loss in the detector and the time of flight, as illustrated in Figure 4.6.

Measurements on the target enriched in ^{176}Lu contained contributions from thorium. In particular, the thorium content gave rise to additional elastically-scattered beam particles at slightly higher energies, which were detected in the monitor counters. These could be distinguished according to their energies by fitting the spectrum using the peak-fitting program FITEK (Section A.6.3), with an accuracy of 1%. However, since the Thorium concentration was known to 0.3% from a measurement using Rutherford back-scattering, the monitor counts were corrected numerically, as that gave higher precision. For the purposes of this work, the most important measurements are those at energies near or below the average fusion barrier (122.3 MeV, corresponding to E_{beam}=143.8 MeV). Due to the higher Z for ^{232}Th, fission events

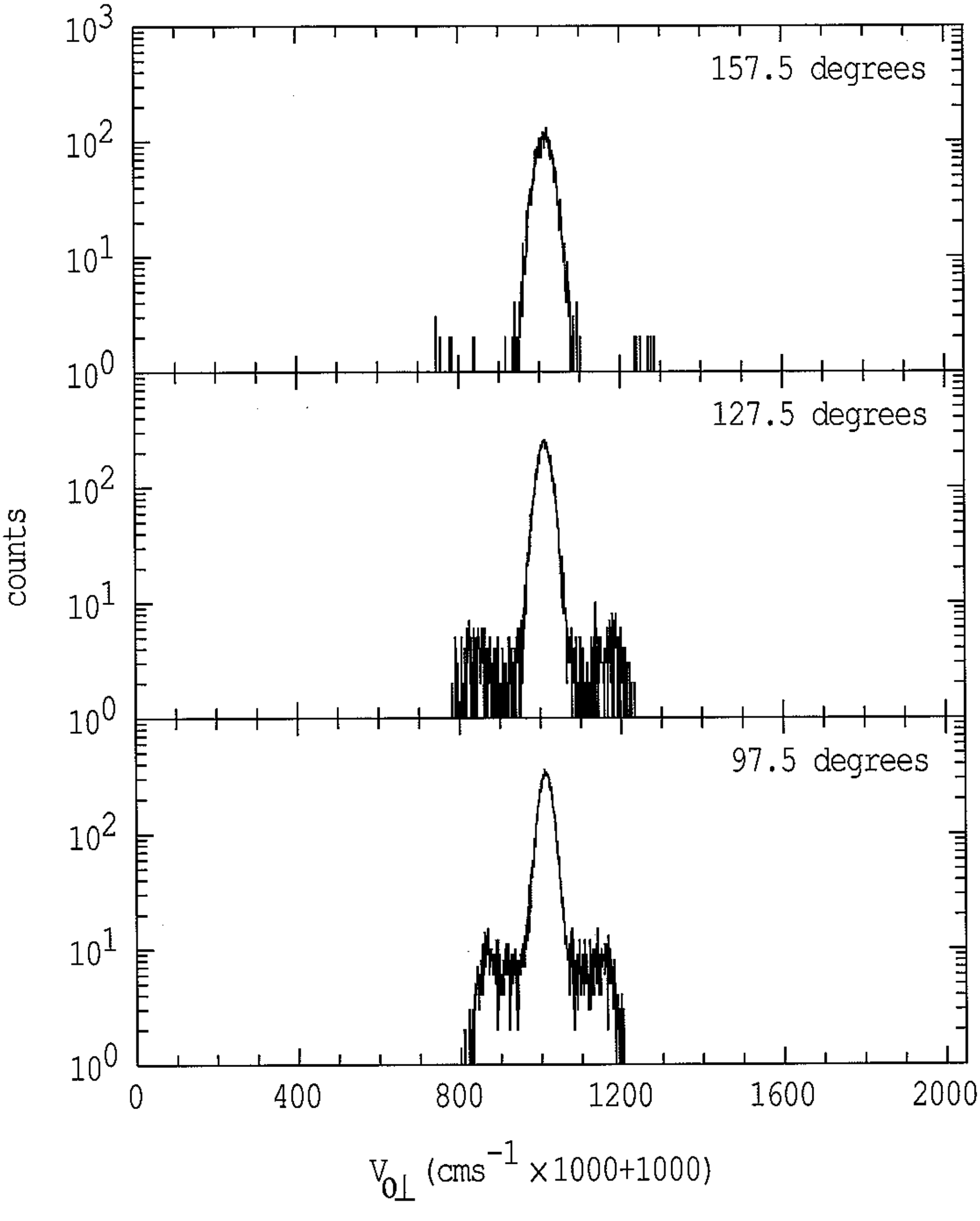

Figure 4.5: Fission events plotted as a function of $v_{0\perp}$ for the reaction ^{16}O+^{238}U at a beam energy of 100 MeV, for three different fragment angles θ. The transfer events are subtracted off according to the indicated background level.

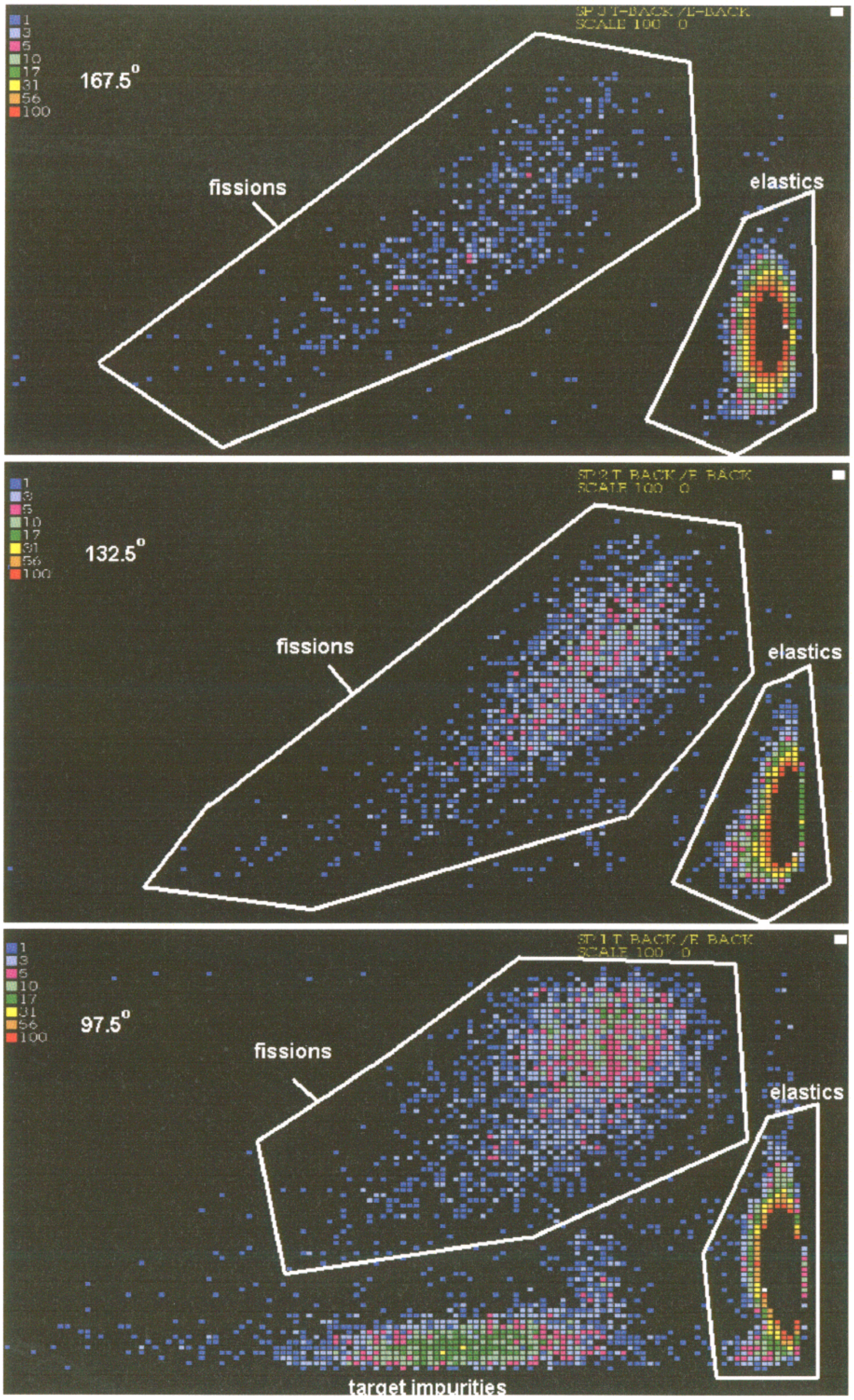

Figure 4.6: Detector events for 5° bins in the back MWPC, showing time of flight plotted against energy loss. At each angle, the fission fragments are clearly distinguished from elastically scattered beam particles.

from the reaction ^{31}P+^{232}Th constitute less than 1% of the detected fission events for beam energies lower than 157 MeV. This was estimated by scaling the fission excitation function measured for ^{32}S+^{232}Th [HINpriv] according to the Coulomb barrier energy for each reaction.

Where multiple measurements were made on the same target at the same energy, these were combined to improve statistics, after correction for any small variations in detector calibration between measurements.

Measurements made using the enriched and natural lutetium targets contained different contributions from reactions on ^{175}Lu and ^{176}Lu. In order to determine the fission differential cross-sections $\frac{d\sigma(\theta)}{d\Omega}$ for each isotope, in their respective centre of mass frames, it is necessary to eliminate the contributions from the other isotope. However, because the centre of mass frames differ depending on which isotope is involved in the reaction, the separation is performed in the laboratory reference frame, as follows. First $\frac{d\sigma(\theta)}{d\Omega}$ was determined for 5° bins in the laboratory frame, for each target and each beam energy, using the Rutherford-scattering calibration. Then we took the measurements made on enriched and natural targets at the same beam energy, and solved simultaneous equations using the known concentrations of the isotopes in the targets, to obtain $\frac{d\sigma(\theta)}{d\Omega}$ for each isotope, in the laboratory frame, at that beam energy. This was then converted into the centre of mass reference frame appropriate to the isotope.

For "singles" data, the resulting fission fragment angular distributions (FFAD) covered 15 angles (or 14 angles if the data were from a run where the annular silicon SBD obscured the most backward angles of the MWPC), from 102.5° to 167.5° (162.5°). For "coincidence" data (^{16}O+^{235,238}U), the coincidence requirement further restricted the useful range of the back detector, and a 13 angle distribution was used. For each reaction and each energy, the FFAD was converted to the centre of mass frame using fission total kinetic energies from systematics [VIO85] and fitted in the zero-spin limit [BAC85] to determine fission cross-sections and anisotropies. An iterative procedure was used, starting with a triangular angular momentum distribution, and thereafter using the angular momentum distributions from the coupled-channels calculation that reproduced the fusion excitation function. (The final coupled-channels calculations are described in Section 5.1 for the fission-fission reactions, and Section 6.4.1 for the quasi-fission reactions.) This iteration was performed because the shape of the l-distribution affects the shape of the corresponding family of FFADs, as illustrated in Section 2.2.2.4.

The χ^2 per degree of freedom from the best fit to each angular distribution was determined, and averaged over the distributions at all energies for a given reaction to estimate the dispersion parameter ϕ_d

$$\phi_d = \frac{\sum_{i=1}^{m} (\chi^2/n)_i}{m} \tag{4.4}$$

In the ideal case of appropriate theory fitting data with correctly estimated random errors, ϕ_d should be close to unity for a large data set. The average value of ϕ_d was determined for each reaction, and was found to be 1.0–1.4 for the reactions ^{28,29}Si+^{178}Hf, ^{31}P+^{175}Lu, and ^{16}O+^{235,238}U, and 4.2 for the reaction ^{31}P+^{176}Lu, where a large contribution from ^{175}Lu had been subtracted. A value of ϕ_d substantially larger than unity is referred to as "over-dispersion" [MCC89] and can occur when fitting experimental data, particularly where high precision data has been obtained. This over-dispersion may have three causes: either the theory is not appropriate for the data, a source of random error has been underestimated or neglected, and/or a source of error that has been treated as random is in fact systematic. An example of the last one is the uncertainty in the detector calibration, which is the same for all measurements in a given run. Inspection of the experimental angular distributions for ^{31}P+^{176}Lu shown in Figure 4.10 shows scatter, rather than theoretical mismatch.

The practical consequence of over-dispersion is that uncertainties in fitted quantities are underestimated by the normal statistical prescription, in which the standard deviation corresponds to an increase of the total χ^2 by unity [BEV92]. Instead, for cases with over-dispersion, the uncertainty in fitted quantities corresponds [MCC89] to an increase in the total χ^2 by ϕ_d. Thus for ^{31}P+^{176}Lu, the uncertainty in the anisotropies at each energy correspond to an increase in the total χ^2 for each fission fragment angular distribution by ϕ_d.

Final fits for the reactions ^{28,29}Si+^{178}Hf and ^{31}P+^{175,176}Lu are shown in Figures 4.7–4.10. For comparison, the fits to the raw data from the target with 47% ^{176}Lu are given in Figure 4.11. Final fits for the reactions ^{16}O+^{235,238}U are shown in Figures 6.3 and 6.4. The final fission cross-sections and anisotropies, with errors, are given in Tables 5.1–5.4, and Tables 6.2 and 6.1.

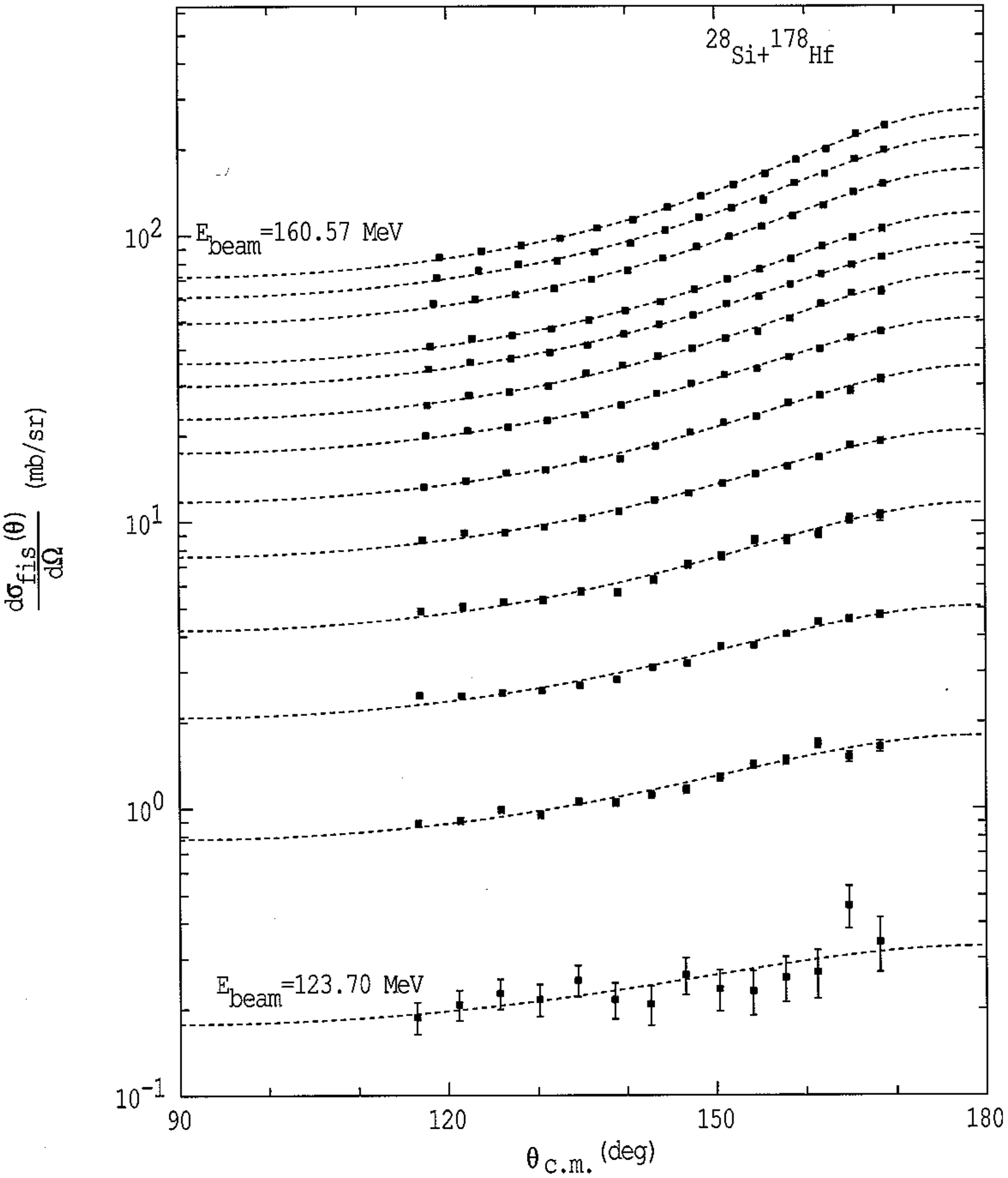

Figure 4.7: Fission fragment angular distributions, fitted using the zero-spin approximation, for ^{28}Si+^{178}Hf. Error bars are smaller than the point size except where visible.

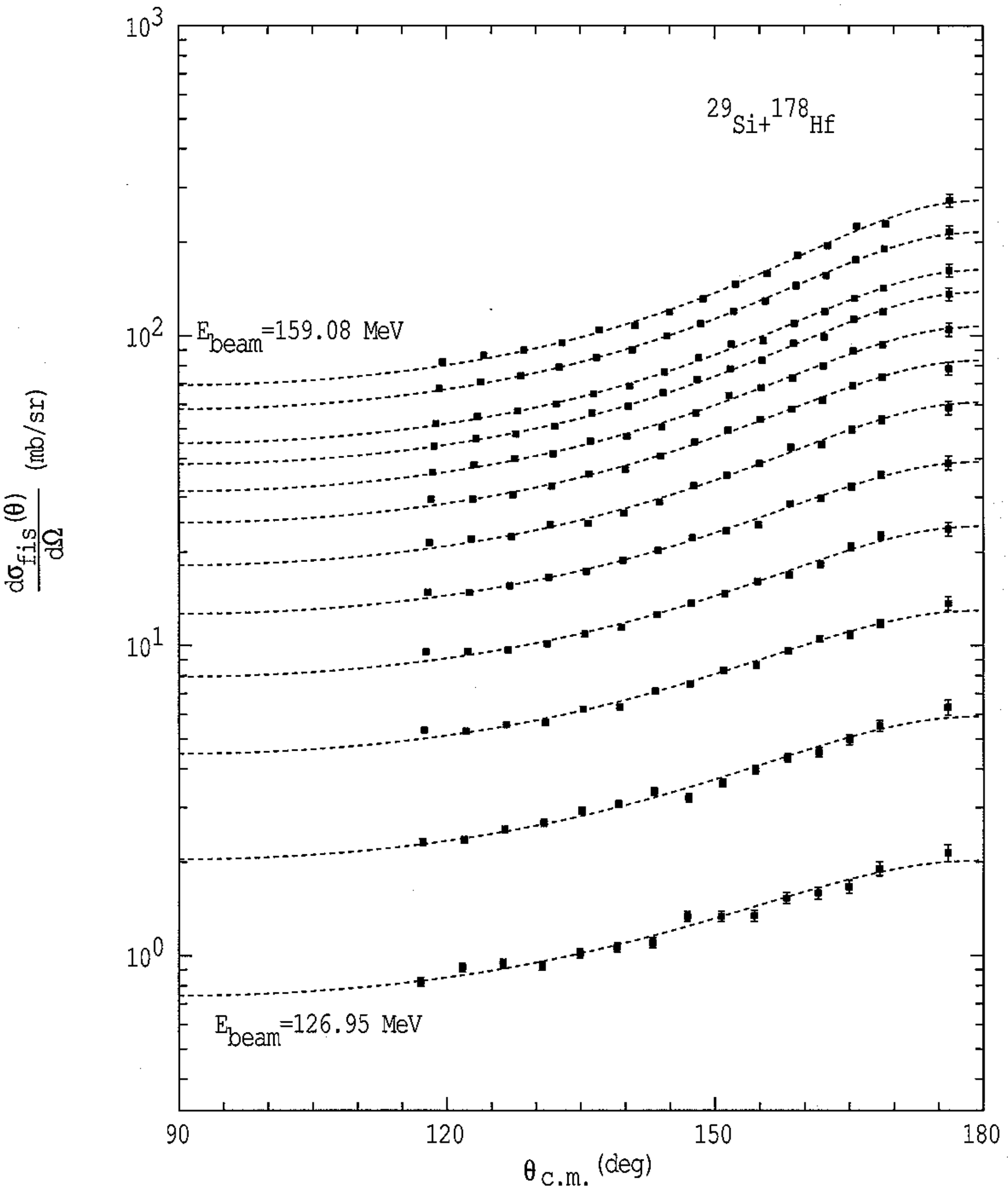

Figure 4.8: Fission fragment angular distributions, fitted using the zero-spin approximation, for ^{29}Si+^{178}Hf. Error bars are smaller than the point size except where visible. The data points at 174° are from a solid-state detector.

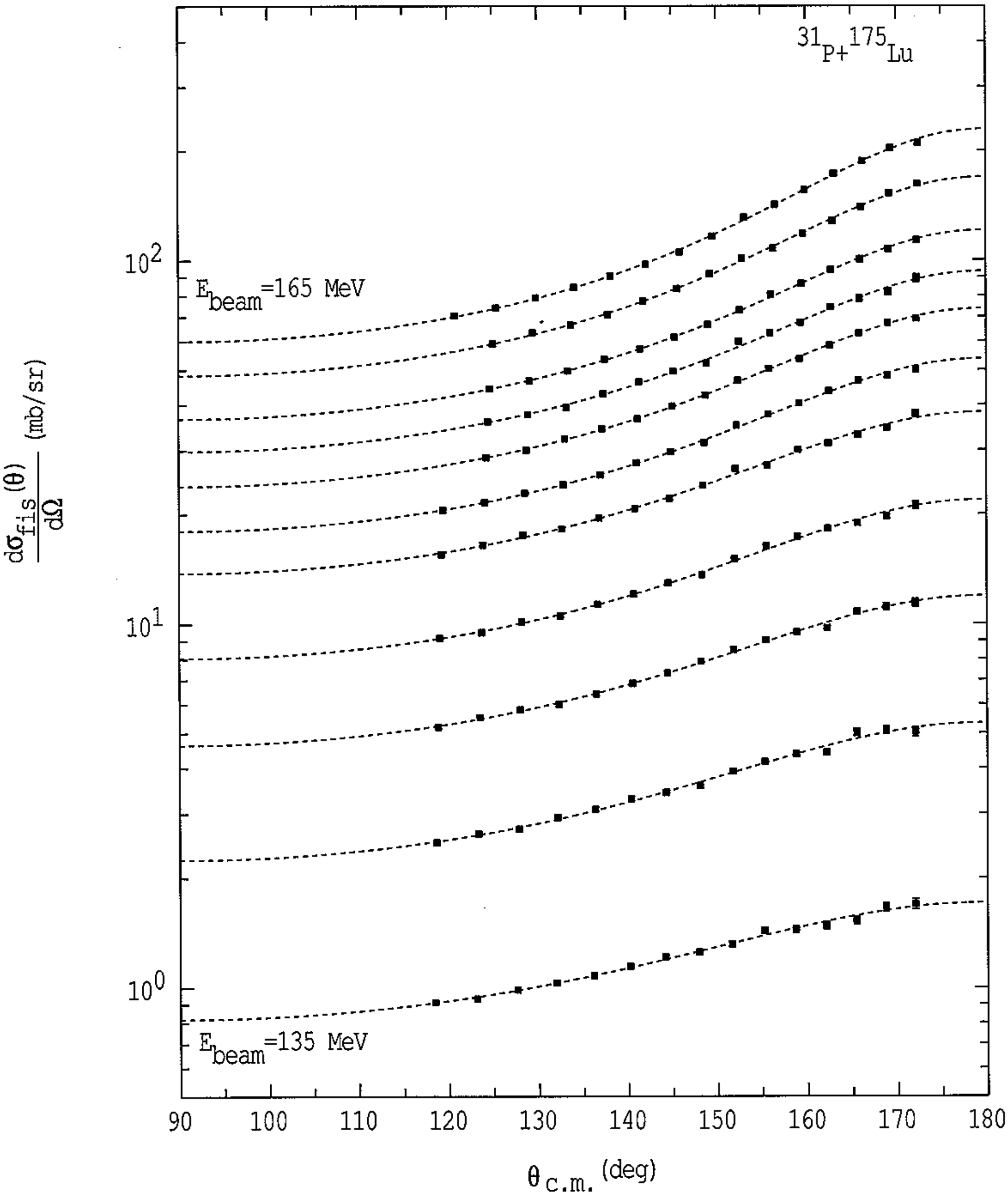

Figure 4.9: Fission fragment angular distributions, fitted using the zero-spin approximation, for ^{31}P+^{175}Lu. The contribution from the 2.59% of ^{176}Lu in the ^{NAT}Lu target has been removed. Error bars are smaller than the point size except where visible.

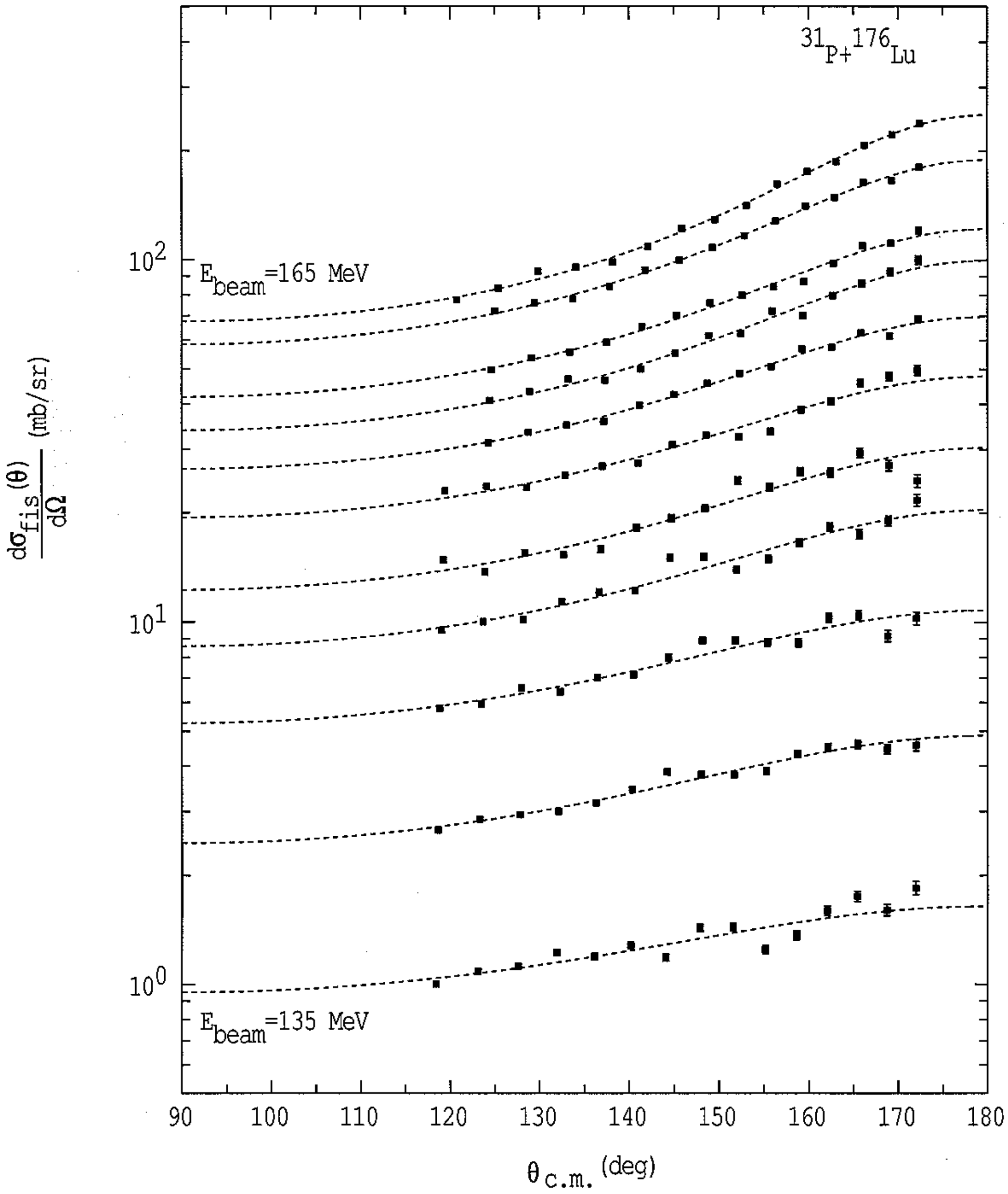

Figure 4.10: Fission fragment angular distributions, fitted using the zero-spin approximation, for ^{31}P+^{176}Lu. The contribution from the 52.8% of ^{175}Lu in the enriched target has been removed. Error bars are smaller than the point size except where visible.

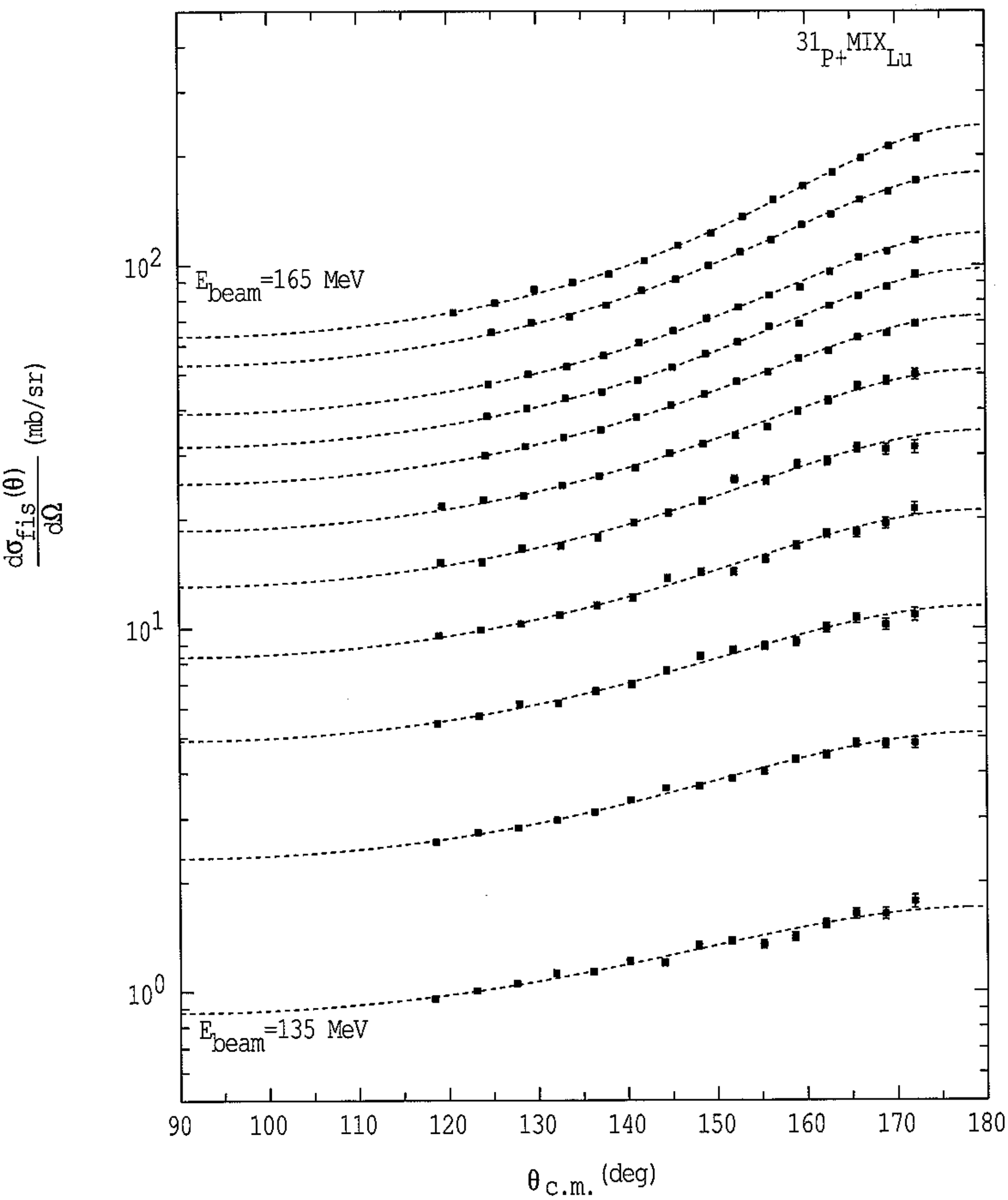

Figure 4.11: Fission fragment angular distributions, fitted using the zero-spin approximation, for ^{31}P+^{175,176}Lu, prior to subtraction of the 53% ^{175}Lu component. Error bars are smaller than the point size except where visible.

4.4 Evaporation Residue Identification and Analysis

Evaporation residue cross-sections were measured in a separate experiment. The residues were stopped in a 1.8 mg/cm^2 Al catcher foil at the target position. Alpha particles from their decay were detected in the annular silicon SBD placed at an average angle of 174° [MOR95, BER01]. The beam was chopped with 1 s on, 1 s off, and alpha particles detected between beam-bursts; alpha-particle lifetimes ranged from 3.5 s to 11.5 min. Individual evaporation residue channels were identified solely by alpha-particle energy. Measurements were made at five energies in the case of the reaction ^{28}Si+^{178}Hf, and at three energies for the reactions ^{29}Si+^{178}Hf and ^{31}P+^{175}Lu. The targets enriched in ^{176}Lu were too thin to allow ER measurements to be completed in a reasonable time, due to the small ER cross-sections.

Identification of surviving nuclei relied upon detection of the alpha particles emitted in their radioactive decay. The energy resolution was poor due to the deep implantation of the evaporation residues, and this precluded clean separation in energy of the alpha particles corresponding to each evaporation channel.

The energy calibration and resolution of the annular detector were determined from a control measurement (^{30}Si+^{186}W, for which the α peaks had a greater energy separation), and adjusted at each energy for the calculated change in the mean implantation depth of the evaporation residues. The relative energy separations and ratio of peak heights were fixed according to the known α energies and branching ratios [TOI96] for primary and daughter nuclei. The intensities of the primary peaks were then varied to obtain a good fit to the full alpha particle spectrum. An example of such a fit is shown in Figure 4.12. The cross-sections of the individual evaporation residues were calculated from the areas of the resulting peaks, taking into account branching ratios, lifetimes, and data collection cycles.

The total evaporation residue cross-section σ_{ER} was relatively insensitive to the detailed partition of the observed spectrum between the different channels, because the branching ratios and lifetimes are closely correlated with alpha-particle energy. The measured xn, pxn, and αxn cross-sections are as listed in Tables 4.2–4.4. For some channels, α-decays were observed from isomeric excited states of the surviving nucleus; these are denoted by a star (for example, ^{203}Rn*).

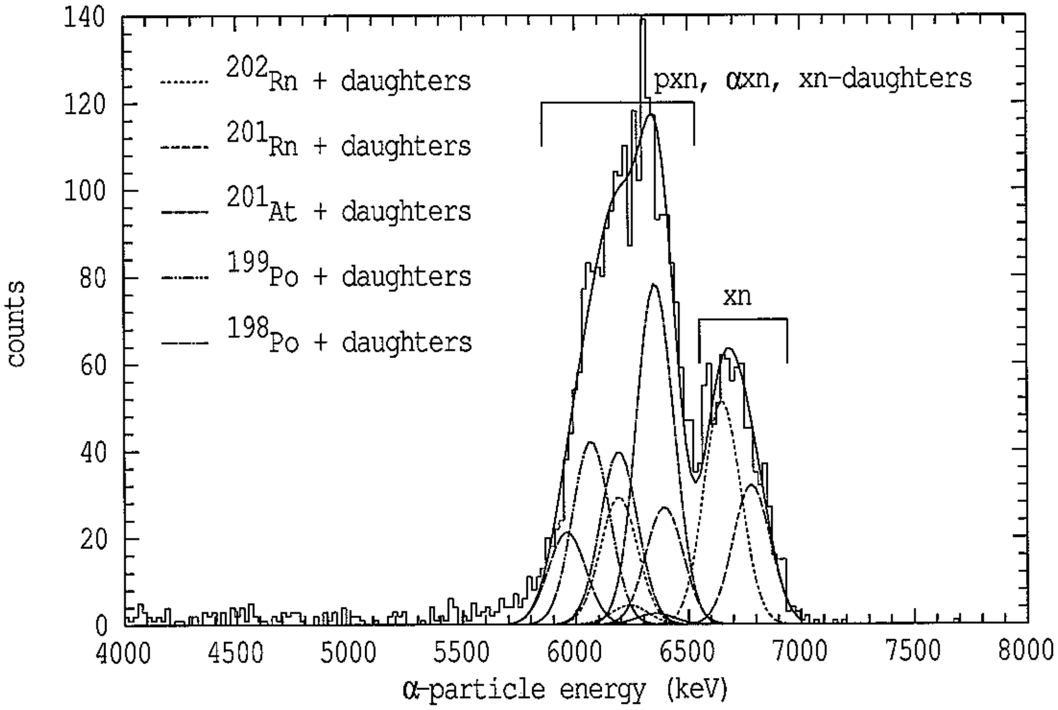

Figure 4.12: Energy distribution of alpha particles for the ^{28}Si+^{178}Hf reaction, detected in the annular silicon surface barrier detector, at the beam energy 145.82 MeV. At this energy, the largest yields are α3n (^{199}Po) and p3n (^{201}At), although 4n (^{202}Rn), 5n (^{201}Rn), and α4n (^{198}Po) are also present in appreciable quantity.

Table 4.2: Measured evaporation residue channel cross-sections for ^{28}Si+^{178}Hf → ^{206}Rn. Decay from isomeric states of the evaporation residue is denoted by an asterisk.

E_{beam} (MeV)	channel	Emitting nucleus	σ_{ER} (mb)
123.79	3n	^{203}Rn	0.096 ± 0.013
	3n	^{203}Rn*	0.033 ± 0.011
	4n	^{202}Rn	0.057 ± 0.010
		Total	0.187 ± 0.035
128.79	3n	^{203}Rn	0.257 ± 0.032
	3n	^{203}Rn*	0.378 ± 0.038
	4n	^{202}Rn	0.265 ± 0.018
	5n	^{201}Rn	0.076 ± 0.016
	α2n	^{200}Po	0.35 ± 0.14
		Total	1.32 ± 0.24
135.99	3n	^{203}Rn	0.211 ± 0.069
	3n	^{203}Rn*	0.566 ± 0.086
	4n	^{202}Rn	1.352 ± 0.075
	5n	^{201}Rn	0.260 ± 0.044
	α2n	^{200}Po	1.14 ± 0.38
		Total	3.53 ± 0.65
145.81	4n	^{202}Rn	0.688 ± 0.060
	5n	^{201}Rn*	0.415 ± 0.047
	p4n	^{201}At	1.24 ± 0.13
	α3n	^{199}Po	1.99 ± 0.38
	α3n	^{199}Po*	1.21 ± 0.20
	α4n	^{198}Po	0.78 ± 0.20
		Total	6.31 ± 0.99
160.57	4n	^{202}Rn	0.208 ± 0.067
	5n	^{201}Rn	0.047 ± 0.024
	5n	^{201}Rn*	0.021 ± 0.020
	p4n	^{201}At	2.03 ± 0.21
	p5n	^{200}At	1.72 ± 0.19
	α3n	^{199}Po	1.62 ± 0.44
	α3n	^{199}Po*	0.70 ± 0.25
	α4n	^{198}Po	1.60 ± 0.27
		Total	7.9 ± 1.5

Table 4.3: Measured evaporation residue channel cross-sections for ^{29}Si+^{178}Hf → ^{207}Rn. Decay from isomeric states of the evaporation residue is denoted by an asterisk.

E_{beam} (MeV)	channel	Emitting nucleus	σ_{ER} (mb)
131.87	3n	^{204}Rn	1.130 ± 0.072
	4n	^{203}Rn	1.25 ± 0.10
	4n	^{203}Rn*	1.233 ± 0.096
	5n	^{202}Rn	0.387 ± 0.045
		Total	4.00 ± 0.32
139.31	3n	^{204}Rn	1.01 ± 0.14
	4n	^{203}Rn	1.77 ± 0.10
	4n	^{203}Rn*	2.59 ± 0.12
	5n	^{202}Rn	1.227 ± 0.074
	p3n	^{203}At	0.24 ± 0.40
	α3n	^{200}Po	0.8 ± 1.2
		Total	7.6 ± 2.0
145.81	4n	^{203}Rn	0.517 ± 0.052
	4n	^{203}Rn*	0.876 ± 0.064
	5n	^{202}Rn	1.99 ± 0.11
	6n	^{201}Rn	0.218 ± 0.029
	6n	^{201}Rn*	0.196 ± 0.026
	p3n	^{202}At	0.75 ± 0.28
	α3n	^{200}Po	2.95 ± 0.41
	α4n	^{199}Po*	1.68 ± 0.39
		Total	9.2 ± 1.4

Table 4.4: Measured evaporation residue channel cross-sections for ^{31}P+^{175}Lu → ^{206}Rn. Decay from isomeric states of the evaporation residue is denoted by an asterisk.

E_{beam} (MeV)	channel	Emitting nucleus	σ_{ER} (mb)
137.50	3n	^{203}Rn	0.302 ± 0.042
	3n	^{203}Rn*	0.080 ± 0.034
	4n	^{202}Rn	0.254 ± 0.031
	α2n	^{200}Po	0.64 ± 0.32
		Total	1.27 ± 0.43
145.00	3n	^{203}Rn	0.080 ± 0.062
	3n	^{203}Rn*	0.436 ± 0.077
	4n	^{202}Rn	0.884 ± 0.062
	α2n	^{200}Po	1.46 ± 0.45
	α3n	^{199}Po*	0.15 ± 0.12
		Total	3.02 ± 0.77
155.00	4n	^{202}Rn	0.265 ± 0.076
	5n	^{201}Rn	0.222 ± 0.051
	5n	^{201}Rn*	0.200 ± 0.046
	p3n	^{202}At	0.92 ± 0.25
	p4n	^{201}At	0.52 ± 0.19
	α3n	^{199}Po	0.227 ± 0.079
	α3n	^{199}Po*	1.03 ± 0.12
		Total	3.38 ± 0.82

Since measurements were made at only a few energies, it was necessary to interpolate or extrapolate measured data to all other energies at which fission cross-sections were measured. The reduced cross-sections

$$\tilde{\sigma}_{ER}(E) = \sigma_{ER}(E)\frac{2\mu E}{\pi\hbar^2} \tag{4.5}$$

(where μ is the reduced mass of the system) were found to vary approximately linearly over the energy range of interest, as shown in Figure 4.13. The reduced cross-sections for the two reactions leading to the compound nucleus ^{206}Rn were found to be in agreement at matching excitation energies. Similar agreement can be expected for the reactions producing ^{207}Rn. A line was fitted to the reduced cross-sections for ^{206}Rn as a function of compound nucleus excitation energy using a weighted least squares procedure. This fit was then used to predict $\tilde{\sigma}_{ER}(E)$ and $\sigma_{ER}(E)$ at all other energies at which fission cross-sections were measured for those reactions, so that total fusion cross-sections σ_{fus} could be determined. The same technique, applied to the reaction ^{29}Si+^{178}Hf (leading to the compound nucleus ^{207}Rn) also allowed us to predict $\tilde{\sigma}_{ER}(E)$ for the reaction ^{31}P+^{176}Lu. The resulting fusion cross-sections for all reactions are given in Tables 5.1–5.4. Because the ER survival probabilities ranged from 10% at the lowest beam energies to 1% at the highest, even a large uncertainty in the extrapolated survival cross-section translates to only a small uncertainty in total fusion cross-section.

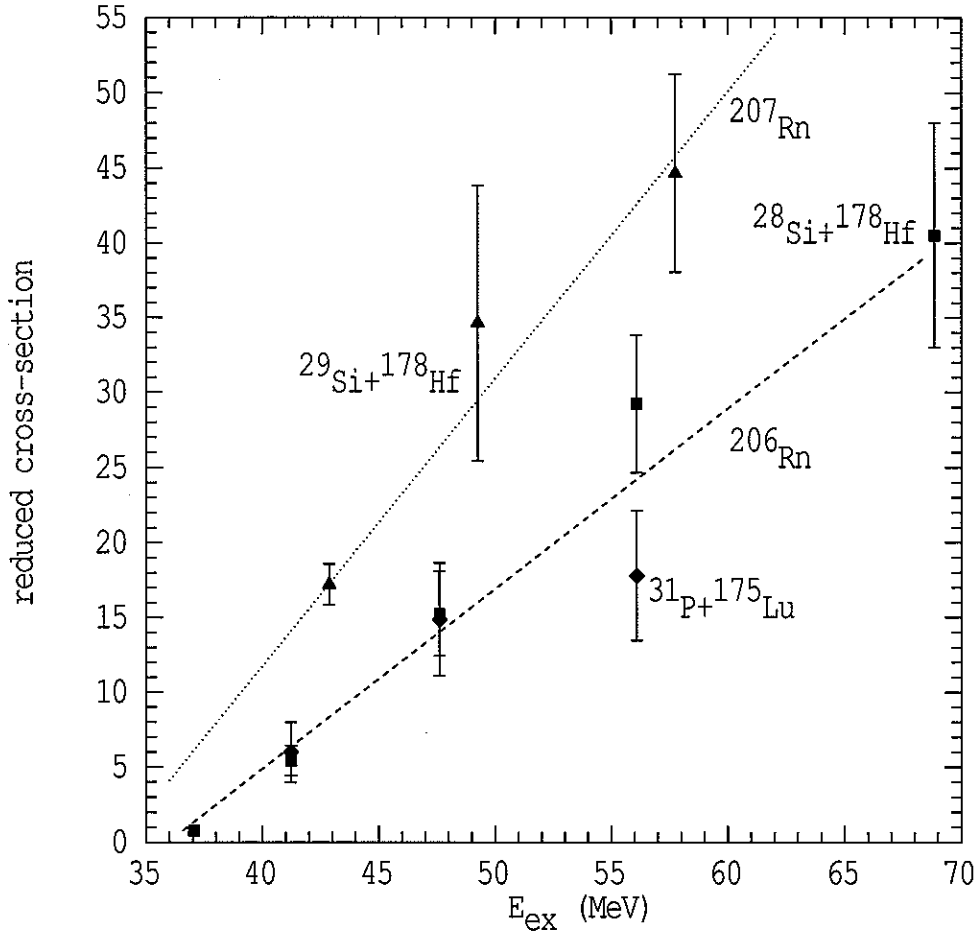

Figure 4.13: Reduced cross-sections, plotted as a function of compound nucleus excitation energy. The dashed and dotted lines show the results of the least-squares fits to these reduced cross-sections for ^{206}Rn and ^{207}Rn respectively.

CHAPTER 5

Experimental Anisotropies from a High-Spin Target

In this chapter we examine the results of experiments on the reactions ^{28}Si+^{178}Hf, ^{29}Si+^{178}Hf, ^{31}P+^{175}Lu, and ^{31}P+^{176}Lu, which are all expected to undergo fusion-fission, with some probability of survival to form evaporation residues. In particular we are interested in the fusion-fission anisotropies, because it is expected that the 7 units of spin of ^{176}Lu should have a strong effect on the fission fragment anisotropy.

The four reactions studied are expected to be very similar, both in terms of the mass and charge of the participating nuclei, and in terms of the number, nature, and strength of the significant coupled channels. Thus a model which accurately reproduces the anisotropies for the control reactions ^{28,29}Si+^{178}Hf should also accurately reproduce the anisotropies for the reactions ^{31}P+^{175,176}Lu, except in so far as the 7/2 spin of ^{175}Lu and the 7 spin of ^{176}Lu are significant.

The fusion angular momentum distribution at the energy of interest is a crucial quantity in the prediction of fission fragment angular distributions. It has been shown [ROW93, BAL96] that fusion angular momentum distributions are related to fusion excitation functions. Thus the angular momentum distribution can be calculated using a coupled-channels model which includes the major couplings, and reproduces accurately measured fusion excitation functions, and hence the barrier distributions.

5.1 Total Fusion Cross-sections

Experimental fusion cross-sections were determined by adding evaporation residue cross-sections obtained as described in Section 4.4, and fission cross-sections obtained as described in Section 4.3.3. These cross-sections, together with the fission fragment anisotropies determined simultaneously with the fission cross-sections, are listed in Tables 5.1–5.4.

Theoretical fusion cross-sections were obtained using the simplified coupled-channels code CCMOD [DAS92, DAS97]. The Woods-Saxon nuclear potential depth V_0 was taken as 100 MeV. The radius parameter r_0 and the diffuseness a_0 were simultaneously adjusted to reproduce the six highest energy data points for each of the three reactions ^{28}Si+^{178}Hf, ^{29}Si+^{178}Hf, and ^{31}P+^{175}Lu, as these high energy points should be insensitive to the couplings [LEI95]. Nevertheless, the couplings were included during the fitting process, for completeness. Based on the results of these fits, a_0 was fixed at 0.85 fm, and r_0 varied to fit these fusion cross-sections for each reaction, obtaining 1.115 fm, 1.116 fm, and 1.119 fm respectively.

The presence of ^{232}Th in the ^{176}Lu target (Section 4.2.1) gives rise to fission fragments from the reaction ^{31}P+^{232}Th. The fraction of the observed fission yield resulting from the reaction on thorium could not be accurately determined. However, it is expected to become appreciable above $E_{c.m.}$=130 MeV. Hence we discarded the highest energy measurements for the reaction ^{31}P+^{176}Lu (hollow points in Figure 5.4). These are not directly related to the main point of this work, and would only serve to determine the nuclear potential. The Woods-Saxon radius parameter r_0 was instead taken to be 1.119 fm, as found for the reaction on ^{175}Lu. The corresponding CCMOD input files for all four reactions are given in Appendix B.

The couplings included were the β_2 and β_4 deformations of the target nuclei, the lowest energy collective E2 excitation of the projectile nuclei, and positive Q-value transfer channels. Quadrupole deformations for ^{175,176}Lu were calculated from electromagnetic quadrupole moments using $r_0 = 1.2$ fm, obtaining $\beta_2 = 0.29$ for both nuclei [NDS93, NDS98]. The β_2 deformation of ^{178}Hf was taken as 0.28 [RAM87]. The β_4 deformations were taken as -0.03 for all three target nuclei, consistent with measurements collated in Ref. [RON77]. For each projectile, vibrational coupling to the first excited state was included. The energies and β_2 values for ^{28}Si were taken from Ref. [RAM87]. For the odd-mass projectiles they were determined by averaging

Table 5.1: Measured fission and evaporation residue cross-sections and adopted fusion cross-sections for the reaction ^{28}Si+^{178}Hf. Interpolated evaporation residue cross-sections are listed in italics. The values of $E_{c.m.}$ listed have also been corrected for the energy loss of the projectile before reaching the average interaction point in the target.

E_{beam} (MeV)	$E_{c.m.}$ (MeV)	σ_{fis} (mb)	Anisotropy	σ_{ER} (mb)	σ_{fus} (mb)
123.70	106.49	1.33±0.07	1.7±0.3	0.187 ± 0.020	1.52±0.07
126.15	108.61	6.21±0.09	2.23±0.08	*0.83 ± 0.14*	7.04±0.17
128.62	110.74	16.75±0.17	2.41±0.05	1.3 ± 0.3	18.1±0.4
131.07	112.87	34.7±0.3	2.69±0.09	*2.0 ± 0.4*	36.7±0.5
133.53	114.99	62.5±0.4	2.72±0.05	*2.6 ± 0.6*	65.1±0.7
135.99	117.12	98.3±0.7	2.93±0.07	3.5 ± 0.7	101.8±1.0
138.45	119.24	145.4±1.8	2.90±0.04	*3.7 ± 0.9*	149±2
140.91	121.37	194.5±1.1	3.19±0.07	*4.2 ± 1.0*	198.6±1.5
143.36	123.49	252.4±1.5	3.14±0.04	*4.7 ± 1.1*	257.1±1.9
145.82	125.62	306±2	3.32±0.07	6.3 ± 1.2	312±2
150.74	129.88	426±3	3.40±0.04	*6.0 ± 1.5*	432±3
155.97	134.40	532±4	3.61±0.05	*6.9 ± 1.7*	539±4
160.57	138.38	633±5	3.79±0.05	7.9 ± 1.9	641±6

Table 5.2: Measured fission and evaporation residue cross-sections and adopted fusion cross-sections for the reaction ^{29}Si+^{178}Hf. Interpolated evaporation residue cross-sections are listed in italics. The values of $E_{c.m.}$ listed have also been corrected for the energy loss of the projectile before reaching the average interaction point in the target.

E_{beam} (MeV)	$E_{c.m.}$ (MeV)	σ_{fis} (mb)	Anisotropy	σ_{ER} (mb)	σ_{fus} (mb)
126.65	108.50	6.13±0.12	2.64±0.11	*1.9 ± 0.3*	8.0±0.4
129.43	110.90	17.0±0.3	2.82±0.09	*3.0 ± 0.4*	12.0±0.5
131.89	113.02	37.3±0.6	2.86±0.07	4.0 ± 1.1	41.3±1.2
134.46	115.24	66.5±1.0	3.01±0.08	*4.8 ± 1.7*	71±2
136.84	117.27	106.2±1.6	3.06±0.07	*6 ± 2*	112±3
139.31	119.41	155.2±1.8	3.31±0.07	7.6 ± 2.8	163±3
141.78	121.53	213±2	3.31±0.06	*8 ± 3*	220±4
143.25	123.65	270±3	3.37±0.07	*8 ± 4*	278±5
146.72	125.79	333±3	3.56±0.06	*9 ± 4*	342±5
149.20	127.91	391±4	3.59±0.06	9 ± 5	400±6
154.14	132.17	507±4	3.70±0.06	*11 ± 6*	518±7
159.08	136.42	613±4	3.87±0.08	*12 ± 7*	625±8

Table 5.3: Measured fission and evaporation residue cross-sections and adopted fusion cross-sections for the reaction ^{31}P+^{175}Lu. Interpolated evaporation residue cross-sections are listed in italics. The values of $E_{c.m.}$ listed have also been corrected for the energy loss of the projectile before reaching the average interaction point in the target.

E_{beam} (MeV)	$E_{c.m.}$ (MeV)	σ_{fis} (mb)	Anisotropy	σ_{ER} (mb)	σ_{fus} (mb)
135.01	114.60	6.4±0.3	2.09±0.04	*0.83 ± 0.15*	7.2±0.3
137.50	116.72	18.0±0.6	2.38±0.04	1.3 ± 0.3	19.3±0.7
140.00	118.85	37.8±0.9	2.58±0.04	*1.9 ± 0.4*	39.7±1.0
142.50	120.97	66.4±1.5	2.72±0.04	*2.4 ± 0.5*	68.8±1.6
145.00	123.09	103.6±1.6	2.77±0.04	3.0 ± 0.7	106.6±1.7
147.50	125.22	151±2	2.98±0.04	*3.3 ± 0.7*	154±2
150.00	127.34	201±3	3.10±0.03	*3.7 ± 0.9*	205±3
152.50	129.47	251±3	3.14±0.06	*4.2 ± 1.0*	255±3
155.00	131.59	314±4	3.31±0.04	3.4 ± 1.1	317±4
160.00	135.84	420±4	3.51±0.04	*5.4 ± 1.3*	425±4
165.00	140.08	530±4	3.82±0.05	*6.1 ± 1.5*	536±4

Table 5.4: Measured fission cross-sections and adopted fusion cross-sections for the reaction ^{31}P+^{176}Lu. Interpolated evaporation residue cross-sections are listed in italics. The values of $E_{c.m.}$ listed have also been corrected for the energy loss of the projectile before reaching the average interaction point in the target.

E_{beam} (MeV)	$E_{c.m.}$ (MeV)	σ_{fis} (mb)	Anisotropy	σ_{ER} (mb)	σ_{fus} (mb)
135.00	114.70	7.0±0.3	1.73±0.04	*2.9 ± 0.5*	9.9±0.6
137.50	116.82	18.8±0.6	1.98±0.04	*3.7 ± 1.1*	22.5±1.2
140.00	118.95	40.8±0.9	2.05±0.05	*4.5 ± 1.6*	45.2±1.9
142.50	121.07	68.7±1.5	2.38±0.05	*5 ± 2*	74±3
145.00	123.20	110.7±1.6	2.47±0.06	*6 ± 3*	117±3
147.50	125.33	157±2	2.46±0.05	*7 ± 3*	163±4
150.00	127.45	216±3	2.64±0.03	*7 ± 4*	223±5
152.50	129.58	282±3	2.96±0.06	*8 ± 4*	290±5

the excitation energies and β_2 values from Ref. [RAM87] for the corresponding excitations in neighbouring even-even nuclei, giving β =0.3615 and E =2.0072 MeV for ^{29}Si, and β =0.312 and E =2.232 MeV for ^{31}P. For each reaction all ±1n, ±2n, ±1p, ±2p transfer channels were included that have net positive Q-values (accounting for changes in Coulomb energy). Transfer strength was uniformly taken as 1.0 MeV, as this resulted in good agreement between theoretical and experimental cross-sections at low energies.

Figures 5.1–5.4 compare both cross-sections and barrier distributions from these calculations with the data. Barrier distributions are a sensitive [DAS98] way to examine structure in the fusion cross-sections, and are therefore a useful way of comparing data with calculations. If the shape of the experimental barrier distribution is reproduced by a calculation, then it will also reproduce the shape of the angular momentum distribution, as the two depend on channel couplings in related fashion (Section 2.1.2.5).

The experimental barrier distributions were calculated by numerically double-differentiating the product $E_{c.m.}\sigma_{fus}$ with respect to $E_{c.m.}$ [LEI95] with a step length always close to 4.24 MeV. Theoretical barrier distributions were calculated using the same method, with a constant step length of 4.24 MeV. The dotted line in Figure 5.1 shows the corresponding calculations for no channel coupling, giving a single fusion barrier. In all four reactions, the agreement of the data with the simplified coupled channels calculations is excellent (Figures 5.1–5.4). As previously stated (Section 2.1.2.3), this agreement between data and calculations means that the associated fusion angular momentum distributions may be relied upon.

5.2 Comparison of measured anisotropies with predictions

Theoretical fission fragment anisotropies are calculated according to the method described in Section 3.2.7. The angular momentum distributions are generated using the same coupled channels calculations that reproduce the fusion cross-sections, as described above. The input files to the Monte Carlo statistical model code are as given in Appendix B.

The anisotropies from the ^{28,29}Si+^{178}Hf reactions are well reproduced by the

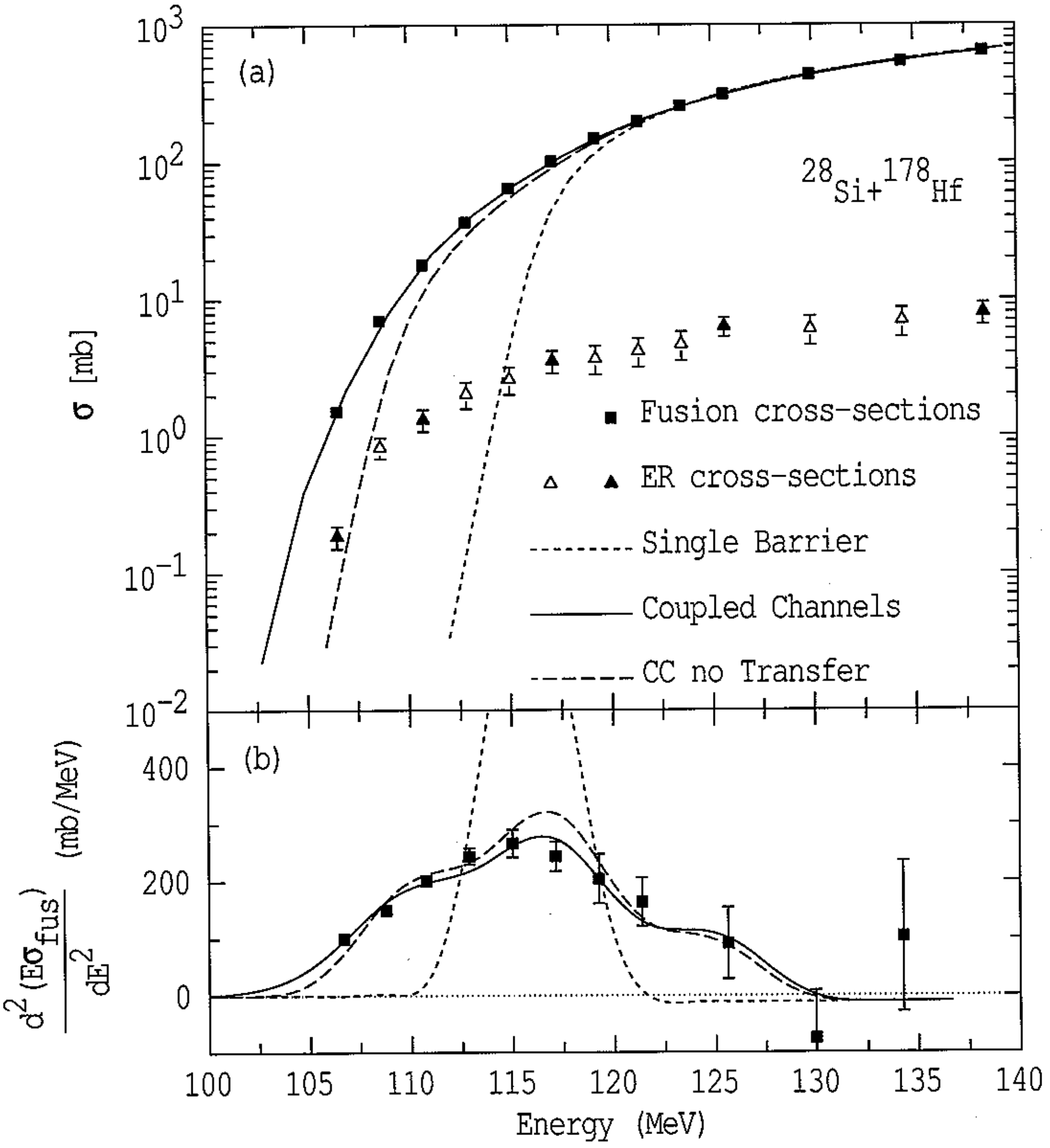

Figure 5.1: (a) Fusion cross-sections, and (b) fusion barrier distribution for the reaction ^{28}Si+^{178}Hf. In (a), the solid triangles show measured evaporation residue cross-sections, and the hollow triangles show interpolated evaporation residue cross-sections. The solid lines in (a) and (b) show the result of the CCMOD fusion calculations described in the text. The short-dashed line shows the corresponding calculations for a single fusion barrier. The long-dashed line shows the coupled-channels calculation which omits the transfer channels used for the solid line.

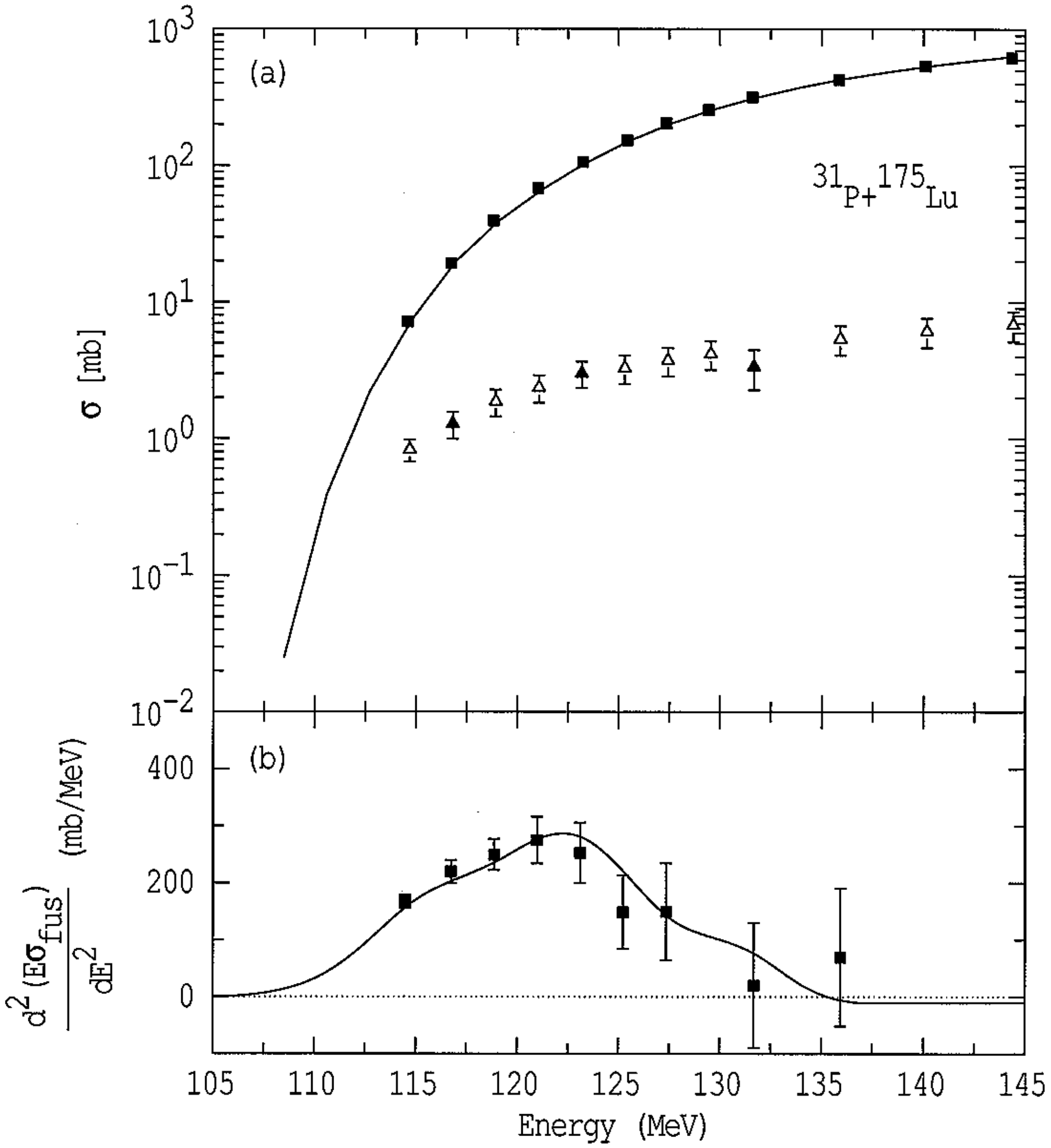

Figure 5.2: Measured and calculated (a) fusion cross-sections, and (b) fusion barrier distribution for the reaction ^{31}P+^{175}Lu. The solid line shows calculated values for the fusion cross-section and fusion barrier distribution.

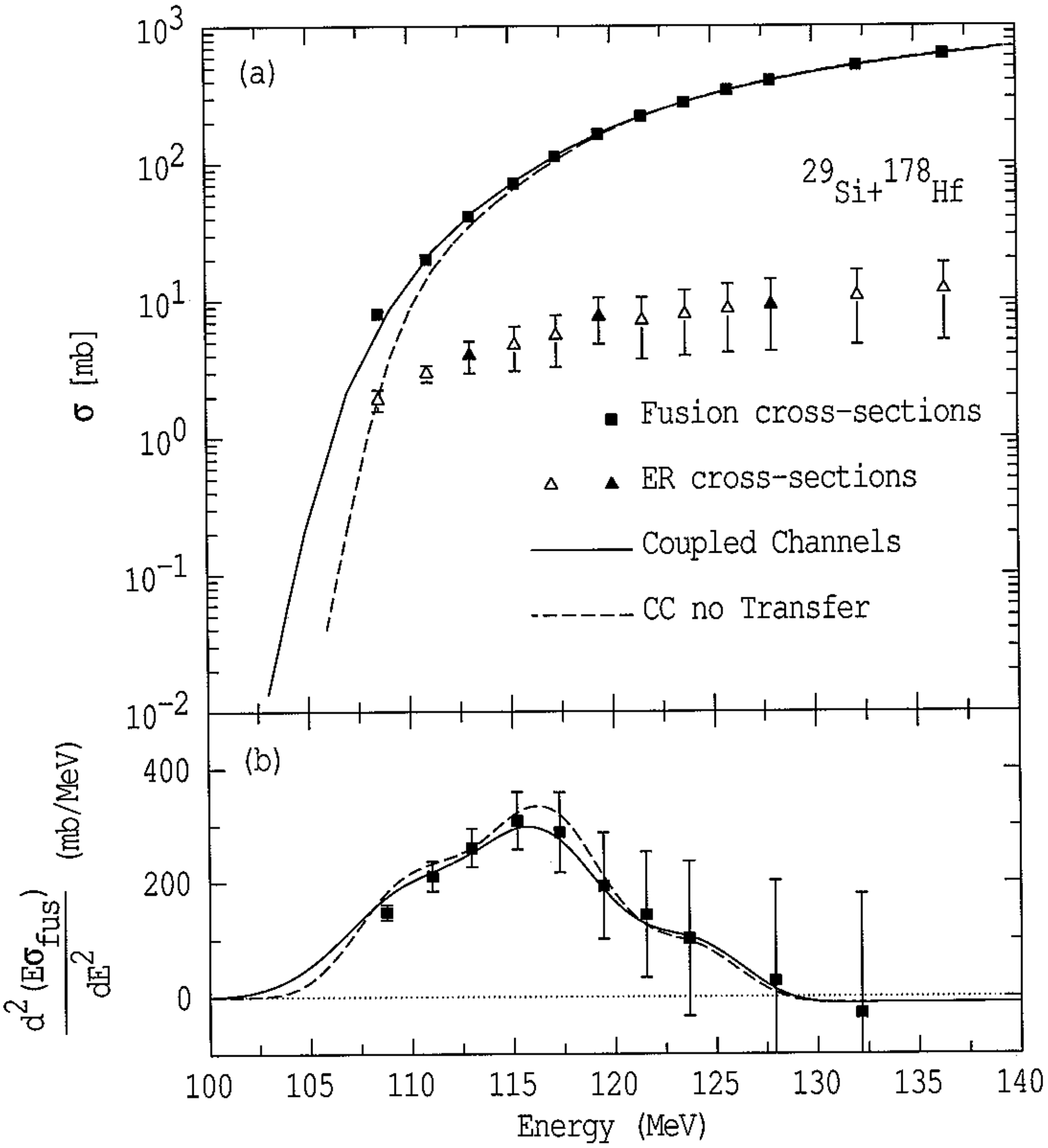

Figure 5.3: (a) Fusion cross-sections, and (b) fusion barrier distribution for the reaction ^{29}Si+^{178}Hf. The solid line in (a) and (b) shows the result of the CCMOD calculations as described in the text. The long-dashed line shows a coupled-channels calculation which omits the transfer channels used for the solid line.

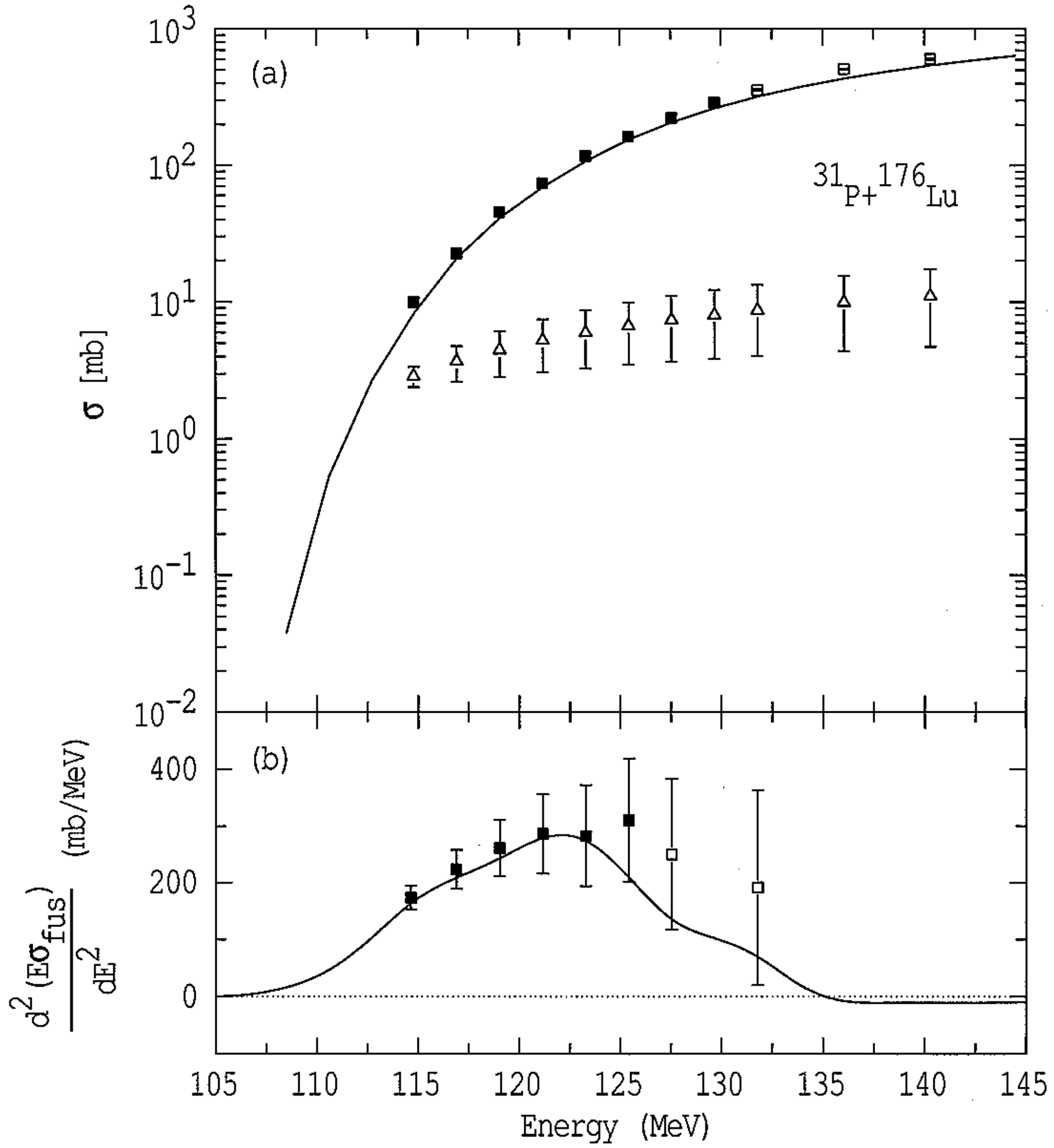

Figure 5.4: Measured and calculated (a) fusion cross-sections, and (b) fusion barrier distribution for the reaction ^{31}P+^{176}Lu. The solid line shows calculated values for the fusion cross-section and fusion barrier distribution. The hollow square points show those measurements which were discarded because of thorium contamination.

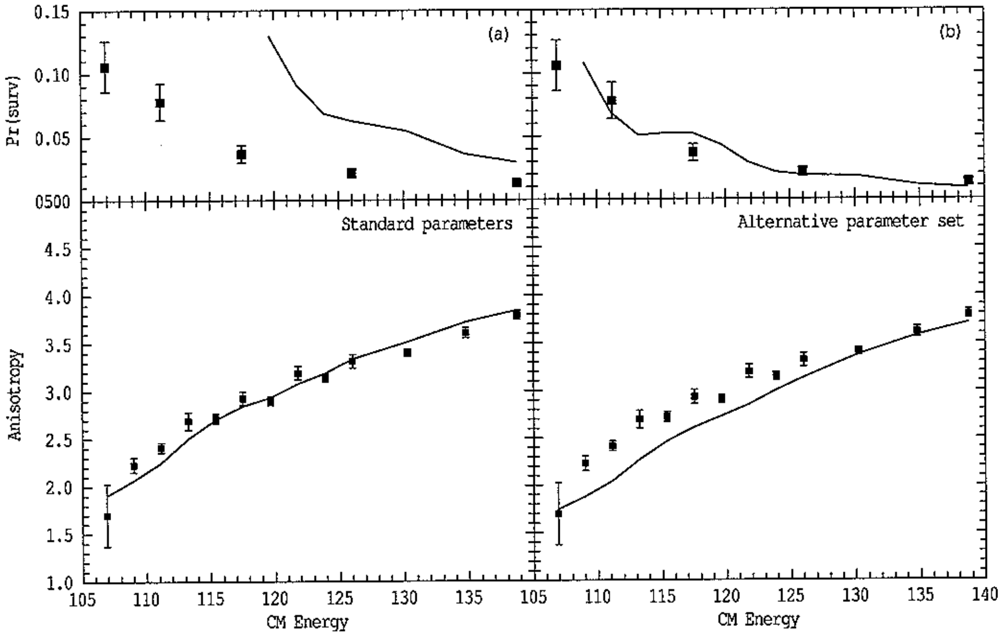

Figure 5.5: Survival Probability and Fission Fragment Anisotropy calculated using two different sets of input parameters to JOANNE, for the reaction ^{28}Si+^{178}Hf, where no ground-state spins are involved. (a) shows the standard calculation, and (b) shows the same calculation using a different set of parameters, adjusted so that the calculated survival probability (solid line) is in agreement with the measurements (points).

calculations with the above parameters, as shown in Figure 5.6 and Figure 5.8. However, the survival probabilities for the same reactions are not so well reproduced, as shown for ^{28}Si+^{178}Hf in Figure 5.5(a).

5.2.1 Relationship between survival and anisotropy

The same failure to simultaneously reproduce both anisotropies and survival probabilities for these reactions, was also found in Ref. [BER01C] for the reactions ^{16,18}O+^{192,194,196}Pt, ^{12}C+^{204}Pb, ^{19}F+^{197}Au, and ^{30}Si+^{186}W. Such simultaneous prediction has rarely been attempted, and the failure in this case may be due to physical effects not included in the calculations. For example, no dynamical effects were included in the calculations. Furthermore, it has been suggested [LES99] that the standard expression in statistical model codes for the fission width is inconsistent with the expressions for the angular distribution, and this can impact on simultaneous reproduction of different quantities.

Another consideration is the possibility that quasi-fission affects anisotropies and/or survival probabilities. Although quasi-fission is only expected for reactions with rather higher Z_1Z_2, recent experiments have shown subtler signs of quasi-fission effects at lower Z_1Z_2 [BER01, HIN02C], so this cannot be totally ruled out. Quasi-fission processes are still only qualitatively understood.

The sensitivity of the calculated anisotropies to the predicted survival cross-sections was investigated for these reactions. Even at the lowest energies, where the effect is greatest, adjusting statistical model parameters to reproduce ER cross-sections changes $\langle J'^2 \rangle$ by only 8%, and the mean nuclear temperature T' by 3%. The new parameters give anisotropies consistently reduced by ≈ 0.15, as illustrated in Figure 5.5(b). As these changes are similar for all four reactions, we chose to adjust the parameters of the calculations to reproduce the fission anisotropies for the ^{28,29}Si+^{178}Hf control reactions, to allow the clearest demonstration of the effect of ground-state spin and nuclear deformation. This gives an over-estimation of survival cross-sections by about a factor of two.

Any effects neglected in our analysis should be similar in all four reactions (Section 4.1.1). Since the existing calculations incorporate the known differences between the reactions, they can still be used as a reference in comparing the anisotropies for the four reactions, to demonstrate the effect of the correlation of ground-state spin and nuclear deformation on the fission anisotropies.

5.2.2 Demonstrating the Importance of Spin

Since the anisotropies for the reactions ^{28,29}Si+^{178}Hf can be well reproduced, as shown in Figures 5.6 and 5.8, the same model should be able to reproduce the anisotropies for the very similar reactions ^{31}P+^{175,176}Lu, except in so far as the spins of the lutetium target nuclei are important.

The experimental anisotropies (see Figure 5.7) for the reaction ^{31}P+^{175}Lu lie slightly below the predictions of simulations which ignore nuclear ground-state spin effects (solid line). If the 7/2 units of ground-state spin of ^{175}Lu and the 1/2 spin of ^{31}P are included in the calculations, but treated as isotropic, the calculated anisotropies are slightly reduced (dotted line). The calculated anisotropies are fur-

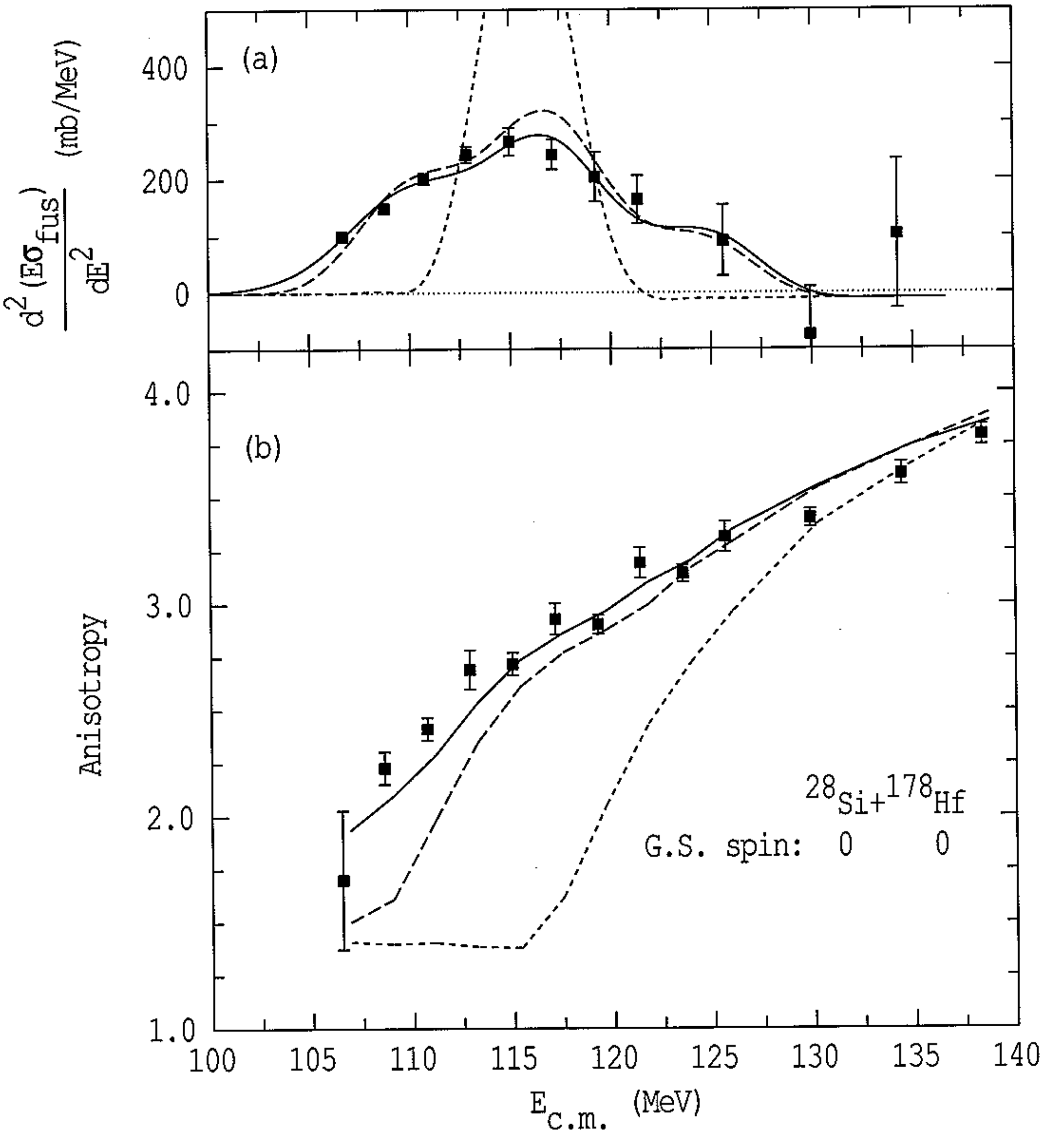

Figure 5.6: (a) Fusion barrier distribution and (b) fission fragment anisotropies for the reaction ^{28}Si+^{178}Hf, forming ^{206}Rn. The solid line in (a) shows the result of the CCMOD fusion calculations described in the text. The solid line in (b) shows the anisotropy calculated as described in Section 3.2.7. The short-dashed line shows the corresponding calculations for a single fusion barrier, while the long-dashed line corresponds to a coupled-channels fusion calculation neglecting transfer channels, which calculation does not reproduce the lowest energy cross-sections.

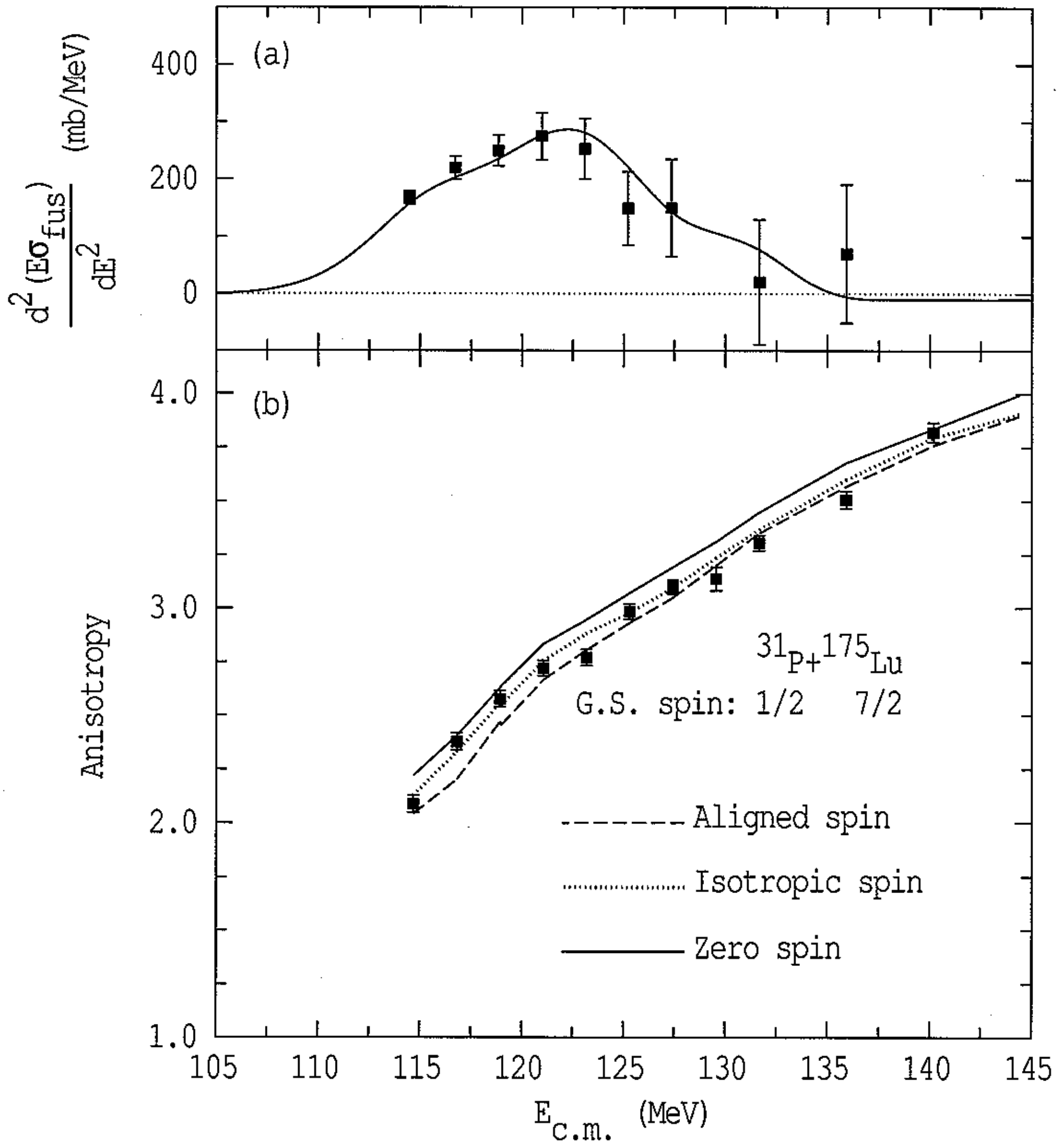

Figure 5.7: Measured and calculated (a) fusion barrier distributions, and (b) anisotropies, for the reaction $^{31}P+^{175}Lu$, forming ^{206}Rn. The solid line represents a zero-spin calculation of fusion barrier and anisotropy. The dotted line is a calculation incorporating the effects of the 7/2 ground-state spin of ^{175}Lu, isotropically oriented. The long-dashed line is a calculation incorporating the alignment of ground-state spin with nuclear deformation.

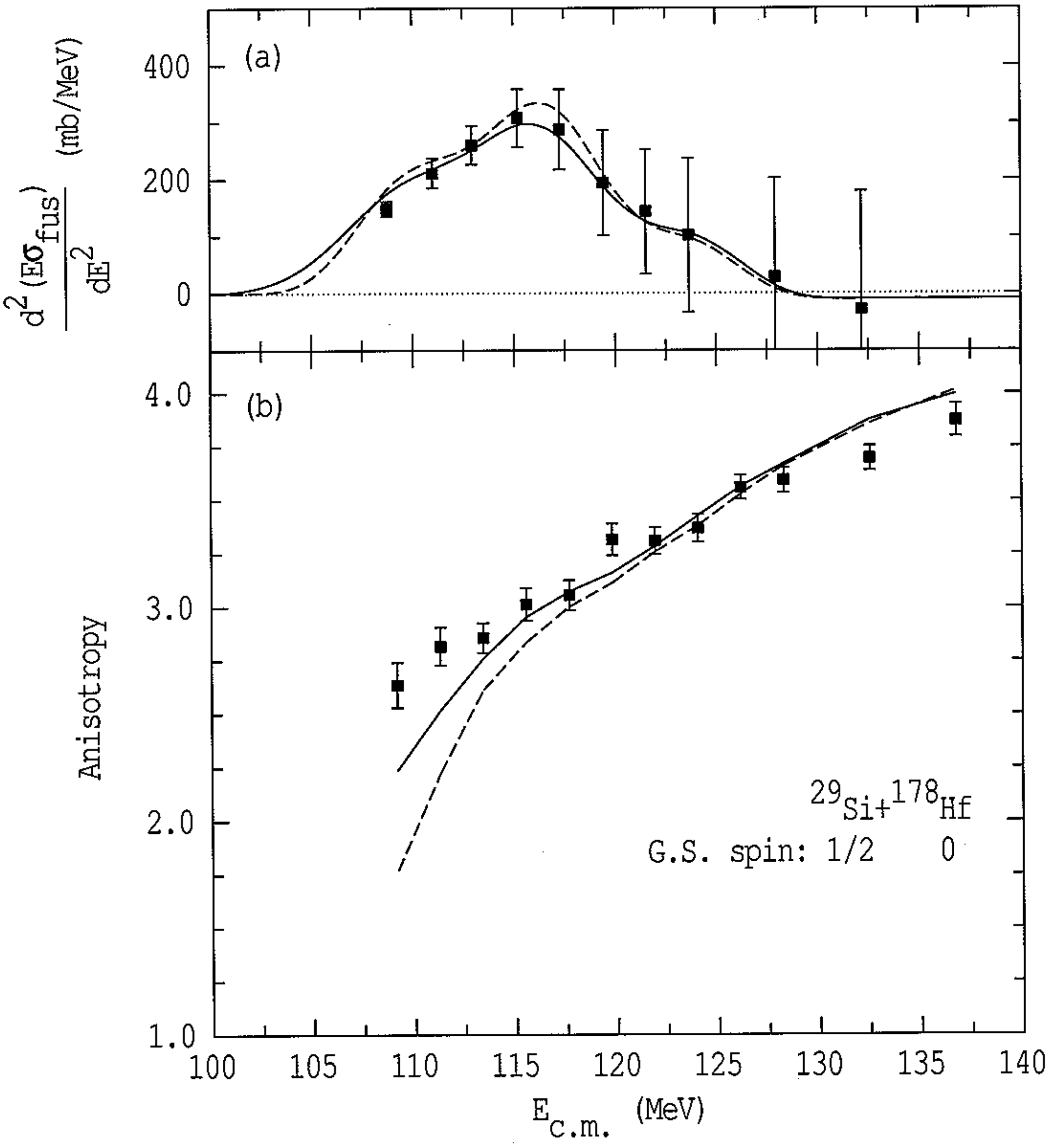

Figure 5.8: (a) Fusion barrier distributions, and (b) fission fragment anisotropies for the reaction ^{29}Si+^{178}Hf. The solid line in (a) shows the result of the CCMOD calculations as described in the text. The solid line in (b) shows the anisotropy calculated as described in Section 3.2.7. The long-dashed line corresponds to a coupled-channels fusion calculation neglecting transfer channels, which calculation does not reproduce the lowest energy cross-sections

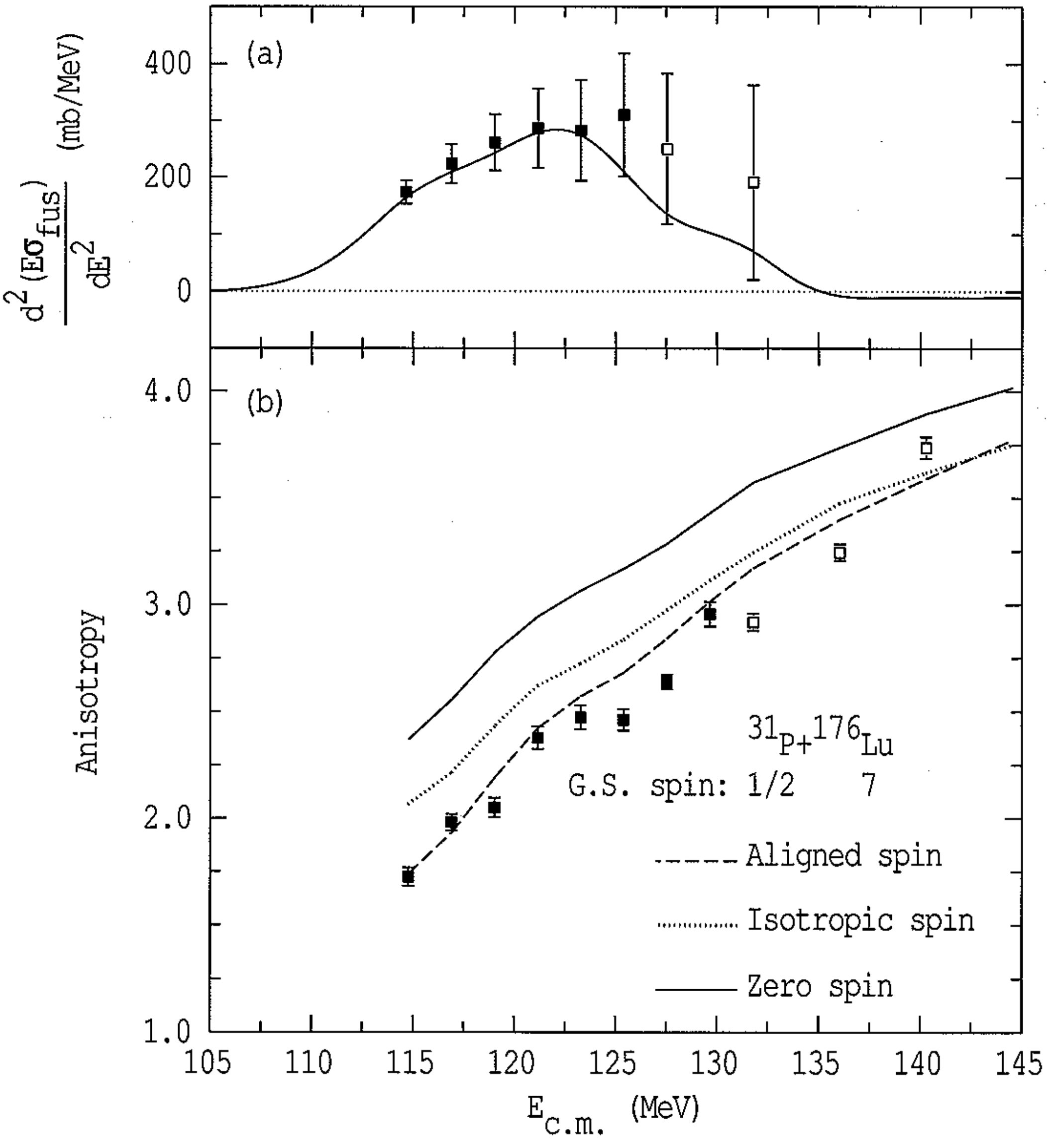

Figure 5.9: Measured and calculated (a) fusion barrier distributions, and (b) anisotropies, for the reaction ^{31}P+^{176}Lu. The solid line represents a zero-spin calculation of fusion barrier and anisotropy. The dotted line in (b) is a calculation incorporating the effect of the ground-state spin of 7, isotropically oriented. The dashed line includes the alignment of ground-state spin with nuclear deformation.

ther reduced when the spin alignment due to the nuclear deformation of ^{175}Lu is included as described in Section 3.2.7 (long-dashed line in Figure 5.7). The effect of the 7/2 spin is in either case rather small, and similar in magnitude to the deviations of the calculations from the data in the zero-spin control reaction (See Figure 5.6).

The effect of the ground-state spin of 7 for ^{176}Lu is however much more significant. The anisotropies for the reaction ^{31}P+^{176}Lu are significantly lower than the transition state model calculation which neglects spin and deformation effects, as shown in Figure 5.9 (solid line). Again, if ground-state spin is included, but treated as isotropic, the anisotropies are reduced (dotted line), this time substantially, due to the 7 units of ground-state spin of ^{176}Lu, but are still significantly higher than the experimental values. When the spin alignment due to nuclear deformation is included (long-dashed line), the predicted anisotropies are further reduced at low energies, with the effect of the alignment decreasing as the beam energy increases. From the excellent agreement of the long-dashed line with the data, it is clear that both ground-state spin and its alignment with the beam axis due to nuclear deformation are significant in this reaction, and that they have been correctly modelled by the procedure developed in Section 3.2.7.

CHAPTER 6

Quasi-fission and Target Spin

For some heavy ion reactions, typically those where both projectile and target have relatively high charges, studies of fusion-fission properties have revealed anomalous behaviour [BAC90, TOK84, TOK85]. In particular, at near-barrier beam energies, the observed fission fragment anisotropies were far higher than expected. Further, it has been observed that the cross-section for evaporation residue production is reduced in some of these reactions [HIN02C, BER01].

It has been concluded that these anomalies are not in fact due to true fusion-fission events, but rather to contributions from a different kind of reaction. We will discuss three of the qualitative descriptions that have been put forward for the new reaction(s). At present, these descriptions all fall well short of a quantitative understanding of the process(es) involved.

We will attempt semi-quantitative calculations with the "orientation-dependent" description of the quasi-fission process. We extend the calculations to include the effect of ground-state nuclear spin, and compare the results to experimental data collected as part of this work.

6.1 Context

There are a number of assumptions associated with the fusion-fission process. In particular, it is assumed that the target and projectile nuclei fuse and form a fully equilibrated compound nucleus. However, a necessary condition for compound nucleus formation is that the potential between the target and projectile nucleus must have a "pocket" - a local potential energy minimum, where the target "captures" the projectile and fusion occurs. This pocket disappears for high angular momentum l, and/or for high projectile and target charge Z_0Z_1.

The existence of the pocket is not sufficient to guarantee fusion-fission. It is possible for there to be a fusion pocket and yet there be zero barrier to fission, for systems with high enough total charge Z, and/or high enough angular momentum l. Further, if there is a fission barrier but it is only small, then when the target captures the projectile nucleus, the resulting compact system may fission before forming a fully equilibrated compound nucleus.

In either case, the system is outside the scope of fusion-fission models, and any events that look like fission must originate from wholly dynamical processes, where compound nucleus formation did not occur. Several questions then arise:

- What is the scope of the fusion-fission model; in what regions is it applicable?
- What is(are) the other process(es) that apply when the fusion-fission model does not?
- How do the other process(es) compete with fusion-fission in the intermediate regions?
- Can we develop an understanding of the other process(es)?

All the above speculation would be rather unimportant if the scope of the fusion-fission model covered all accessible reactions. However, experimental observations show that it does not. Some of the earliest observations of fission-like events were with highly fissile systems such as ^{58}Fe+^{238}U [TOK85]. For such reactions, fusion-fission models predict fragments of near equal mass, nearly isotropically distributed; but the observed fission-like fragment distributions have significant mass asymmetry and relatively high anisotropies. It is concluded that non-compound-nuclear processes have occurred.

Subsequent experiments on systems with lower fissilities observe more subtle effects. In these systems, such as ^{19}F+^{197}Au→^{216}Ra [BER01] and ^{40}Ar+^{180}Hf→^{220}Th [HIN02C], fusion does occur; compound nucleus "survival" is observed, in the sense that evaporation residues are detected. However, by comparing reduced survival cross-sections from these reactions with other reactions forming the same compound nuclei, it has been shown that the survival cross-sections in these reactions are suppressed [BER01, HIN02C]. It is then inferred that compound nucleus formation competes with other processes for these reactions.

There is, therefore, a wide variety of effects to study experimentally, and a wide variety of different reactions with which to study them. It is not even certain, at this stage, whether all the observations stem from variations on a single process, or if different non-compound-nuclear processes might dominate in different regions of the available parameter space.

6.2 Qualitative Considerations

When attempting to model a non-compound-nuclear (NCN) process, there are three major points to worry about. The first is simply the qualitative nature of the process itself. What is it? Some descriptions that have been put forward include:

Quasi-fission In this process, the target and projectile nuclei stick together for a while, converting their initial kinetic energy into internal excitation energy, and exchanging nucleons. The nucleons generally move from the larger nucleus to the smaller one, moving the system towards mass symmetry. The system never becomes spherical.

Fast-Fission Although the target and projectile fuse into a compact near-spherical system, this is unstable against fission because there is no fission barrier.

Pre-Equilibrium Fission In this picture, the target and projectile fuse into a spherical "compound nucleus". Most of the compound nucleus' degrees of freedom equilibrate rapidly, however the K-equilibration is postulated to be slower than the timescale of the fission process, and therefore some fission occurs before the K-quantum number equilibrates.

The second major issue is the probability of the process occurring. In practice this is usually discussed in terms of the probability of compound nucleus formation, P_{CN}, assuming that there is only one NCN process competing with compound nucleus formation. Addressing this question requires an understanding of the competition between the NCN process and compound nucleus formation.

The third major issue is, given that the process does occur, what actually happens? Where do the fragments go (anisotropy) and what is their mass asymmetry? This may be expected to be governed by the same quantities that govern P_{CN}. These quantities include:

Fissility The total charge of the system should affect the probability of both fission and quasi-fission, as it determines the shape of the potential energy surface.

Entrance Channel Mass Asymmetry The most asymmetric systems are more likely to fuse initially. More symmetric systems may evolve towards symmetry.

Elongation Systems with larger minimum elongations will probably scission with higher fragment anisotropies.

Temperature The higher the excitation energy of the system, the more rapidly various equilibrations occur.

Angular momentum The faster the system spins, the more it will resist compound nucleus formation. The orientation of the total angular momentum may also affect the spatial distribution of fission-like fragments.

Elongation axis Usually characterised by the projection K of the total angular momentum $\vec{J}$ on the elongation axis, the orientation of the elongation axis is important when determining the spatial distribution of fission-like fragments.

These parameters may in turn be influenced by the following quantities associated with the choice of target and projectile nuclei:

Charge and mass Z_0, Z_1, A_0, A_1 These determine the fissility and initial mass asymmetry, and affect the angular momentum and capture cross-section.

Centre of mass energy $E_{c.m.}$ This affects the capture cross-section, the angular momentum (depending on the nuclear deformation), and (accounting for nuclear binding energies) the temperature of the fused system.

Ground-state spins $\vec{I_0}$, $\vec{I_1}$ These affect $\vec{J}$ and the initial distribution of K.

Intrinsic deformation Quadrupole and hexadecapole moments of both nuclei, and maybe other moments, affect the angular momentum and capture cross-section sub-barrier. They also relate to the initial elongation of the system, depending on the **nuclear orientation** as specified by θ_0 and θ_1 for the target and projectile respectively.

The nuclear orientation θ plays a similar role in non-compound-nuclear reactions as in fusion-fission reactions. It is only meaningful if the reacting nuclei have appreciable static deformations, and is only well-defined if the amount of angular momentum involved is sufficiently large. It influences several different parameters simultaneously, and is itself influenced by $E_{c.m.}$, because (as with fusion-fission) the nuclear orientation changes the fusion barrier, with collisions with the tip of a prolate-deformed nucleus (small θ) being more likely than collisions with the sides. This means that the range of available orientations θ will depend on $E_{c.m.}$ at sub-barrier energies. The parameters influenced by θ are the orbital angular momentum l, the initial elongation of the system, and the orientation of the ground-state nuclear spin $\vec{I}$, which is aligned with the nuclear deformation axis.

Because the nuclear orientations θ_0 and θ_1 influence several different parameters simultaneously, the influenced parameters become correlated, and it may be very important to handle the correlations correctly. Several programs, described in Appendix A, have been developed to handle these effects. The ultimate objective would be to reproduce a wide range of experimental data using a dynamical simulation without free parameters. However, a dynamical simulation including all the above variables does not yet exist. For the non-compound-nuclear process(es), there are many unknowns; the process(es) are complex and it is not yet established which parameters are important (apart from the fissility and mass asymmetry), let alone the mechanisms by which they affect the experimental observables.

Experimental research in this field often involves guessing which parameters matter most, suggesting mechanisms by which they would influence observables, and then comparing the predictions with observables. However, at least some such studies have been flawed because they unknowingly varied more parameters than intended. In particular, the possible importance of nuclear deformation was not initially recognised in studies comparing reactions on ^{208}Pb with reactions on ^{238}U, and the possible importance of ground-state nuclear spin was not initially recognised when interpreting observed fission-like fragment anisotropies from reactions on ^{237}Np [RAM90, LES97B] (^{237}Np has spin 5/2).

6.3 Proposed Processes

Here we discuss three models which should be relevant to the reactions ^{16}O+^{235,238}U studied in this work. The reactions were studied at beam energies around the fusion barrier, thus the angular momenta introduced should be small enough that fast-fission (fission without barrier) should not be important.

In all these models, the fissility of the combined system and the mass asymmetry of the initiating reaction are most important in governing the probability of non-compound-nuclear processes. Other critical parameters of each model are described below.

6.3.1 Extra-push

The extra-push model [BJO81] focuses on E_{CM} as the main parameter governing the probability of quasi-fission or compound nucleus formation. It describes nuclear reactions in terms of three critical configurations:

Contact The two reacting nuclei touch; nucleon exchange becomes possible, and a "neck" is likely to form between them. This corresponds to deep-inelastic reactions.

Conditional Saddle The two nuclei overlap enough for there to be a barrier against their separating without exchanging nucleons. More precisely, in terms of the potential energy surface as a function of all the possible degrees of freedom of the system *except* the mass asymmetry, the conditional saddle is a saddle point at fixed mass asymmetry. This corresponds to quasi-fission reactions.

Unconditional Saddle The two nuclei overlap enough for there to be a barrier against their separation. In terms of the potential energy surface, for all degrees of freedom including the mass asymmetry, the system passes inside the saddle point. This corresponds to compound nucleus formation.

These configurations are also referred to in other models. They are not always equally significant. For a mass symmetric reaction, the conditional saddle at the initial mass asymmetry is the same as the unconditional saddle. For reactions involving relatively light nuclei the contact configuration is already inside the conditional saddle-point. For heavier systems it is not. The extra-push model states that the system will reach the conditional saddle point configuration, with probability unity, if it has sufficient extra radial injection velocity. For head-on ($l = 0$) collisions this translates to the requirement for a specific amount of additional energy, called the extra-push energy. The model explains this requirement in terms of the momentum of the incoming projectile and the nuclear friction effects, as well as any difference in the height of the potential energy surface between the contact and conditional saddle configurations.

For sufficiently heavy asymmetric systems, reaching the conditional saddle is not sufficient to reach the unconditional saddle. In this case the extra-push model states that still more radial injection velocity is required to get to the unconditional saddle point. In the $l = 0$ case, the extra energy required to get from the contact configuration to the unconditional saddle is called the extra-extra-push energy. The model assumes that if the extra energy is available, the probability of compound nucleus formation is unity.

The evolution of the combined system over the potential energy surface is described and illustrated in Ref. [TOK85, Figure 2].

6.3.1.1 Limitations of this model

One of the major implications of this model is that, for high enough excitation energies E^*, the reduced survival cross-sections for different reactions forming the same compound nucleus should be the same. Early measurements appeared to support this conclusion. However, subsequent measurements on more mass-asymmetric reactions showed convincingly that this conclusion is *not* supported [HIN02C]. The model also has other limitations. From the beginning, it was conceived as a simple dynamical model, so this is not surprising.

In particular, the model does not include any effect of nuclear deformation, which may be expected to be significant. At very least, within the model, collisions with the tip of a prolate-deformed target nucleus would experience more friction before reaching the unconditional saddle point than would collisions with the equator.

Further, the model only addresses the relative probabilities of fusion, quasi-fission, and deep-inelastic reactions, without addressing the outcomes of such reactions; what would the anisotropy of quasi-fission fragments be?

6.3.2 Pre-equilibrium Fission

The pre-equilibrium fission model assumes that a compound nucleus is formed, equilibrated in all degrees of freedom except for K (in other words, the angle of the elongation axis). Because the fission barrier is low, fission can occur on a timescale comparable with the K-equilibration time, assumed long in comparison to equilibration times for mass, temperature etc. As such, the dominant parameter is fissility, followed by the excitation energy E^*.

The initial form of this model, as proposed by Ramamurthy et al. [RAM85, RAM85B, RAM93], was essentially phenomenological. The anisotropies are high, therefore the K-distribution must be narrow. The question of K-equilibration time is addressed empirically, as is the issue of the non-equilibrated K-distribution.

It was postulated [RAM93] that a qualitative change in the fusion path leading to compound nucleus formation takes place as the mass asymmetry of the reaction is varied across the Businaro-Gallone critical asymmetry, giving rise to higher anisotropies being observed for more symmetric reactions. How this is a prediction of the pre-equilibrium fission model is, unfortunately, not made clear in accessible references, and is puzzling since the pre-equilibrium fission model appears to rely upon there being *no* qualitative change in the fusion processes.

6.3.2.1 Entrance-Channel-Dependent Pre-equilibrium Fission

Lestone et al. [LES97, LES97B] developed a more physical form of this model, with better predictive capability. They assumed that the initial K-distribution was significant, and proposed a method for calculating it, depending on the entrance channel nuclei and beam energy. This calculation, unlike the calculations of Ramamurthy et al [RAM85, RAM85B, RAM93], considered the effects of nuclear deformation, nuclear spin, and nuclear orientation, and incorporated the gradual equilibration of the K-distribution with time, rather than partitioning the fission cross-section into one uniformly non-equilibrated component and one fully equilibrated component.

6.3.2.2 Limitations of these models

The biggest single issue with the pre-equilibrium model in any form is the assumption of slow K-equilibration for a spherical or near-spherical compound nucleus. K is defined as the projection of the total angular momentum $\vec{J}$ along the elongation axis of the combined system. As such, when a spherical compound nucleus is formed, K is not defined. For a system with significant angular momentum, the compound nucleus will have non-zero deformation, so it is possible classically to define K; however, at small deformations it takes very little energy to change K significantly, so it may be expected to equilibrate rapidly. Thus, K is unlikely to be a good quantum number at the equilibrium deformation.

For example, consider the compound nucleus ^{227}Pa, in the case where it is formed with a total angular momentum $J = 60$. At the equilibrium deformation, increasing K from zero to 20 requires 0.3 MeV (compared to 1.2 MeV at the saddle point). In contrast, the fission barrier height is ≈ 1 MeV. Under these conditions, it would be very surprising if the K-equilibration time were greater than the fission time!

Ramamurthy et al say [RAM93]:

> "Direct evidence for the lethargic relaxation of the tilting mode in heavy-ion reactions has . . . come from measurements[10] of the angular distribution of charge-separated fission-like fragments though in this case the reaction involved is quasifission with the collision trajectory not leading the fused composite system inside the unconditional fission saddle point."

Lestone et al. [LES97] cite the theoretical work of Døssing and Randrup [DOS85] when doing their own K-equilibration calculations. However, the paper cited covers di-nuclear reactions rather than fusion reactions. In both this and Ramamurthy's source, then, the evidence for slow K-equilibration comes from situations where the elongation axis remains well-defined (and the elongation significant) throughout the reaction! Thus the physical basis of the model as applied to fusion-fission is not convincing.

Pre-equilibrium K-distributions may however be genuinely appropriate, even required, for modelling quasi-fission reactions, where the elongation remains significant. Combining this approach with a quasi-fission based model would be a worthwhile topic for future investigation.

6.3.3 Orientation-Dependent Quasi-fission

The main hypothesis of this model is that the probability of quasi-fission occurring depends on the elongation of the combined system at contact [HIN95, HIN95B, HIN96]. From this it is deduced that nuclear deformation β and the orientation θ of the reacting nuclei are important. In particular, if, for a large, strongly prolate deformed target nucleus, the nuclear deformation axis lies along the beam axis, then the projectile will make contact with the tip of the nucleus and the system is likely to undergo quasi-fission rather than fusion.

This hypothesis has the following consequences:

- Ground-state nuclear spin should have a strong influence on observed quasi-fission anisotropies, since where nuclei are prolate-deformed, the quasi-fission events are the same events where the nuclear spin lies along the beam axis, resulting in a total angular momentum $\vec{J}$ which is not orthogonal to the beam direction. This maximal de-alignment of $\vec{J}$ should, if the high anisotropies common to quasi-fission events derive from a sensitivity to $\vec{J}$, give rise to large reductions in the observed anisotropy.

- The relative probability of quasi-fission drops as the beam energy rises through the barrier region.

- Super-heavy element formation may be enhanced for collisions with the *equator* of a prolate-deformed target, in comparison to collisions with a spherical target of the same size.

6.3.3.1 Limitations of this model

There are a lot of unknowns associated with the model; it cannot yet make any quantitative predictions. In particular, it is not yet known how the initial elongation matters. If a small projectile strikes a large, prolate deformed target at an angle θ, at what θ does quasi-fission become likely, and is the transition smooth or abrupt? One would expect θ to vary with the choice of reaction.

Further, the model makes no predictions as to the behaviour of the quasi-fission events, e.g. the anisotropies with which the distribution of fission-like fragments should emerge.

6.4 Experiment

In order to investigate the effect of ground-state nuclear spin on quasi-fission fragment angular distributions, measurements of angular distributions and cross-sections were performed on the reaction $^{16}O+^{235}U$, at a range of energies spanning the Coulomb barrier. Measurements were also performed at some energies for $^{16}O+^{238}U$, for which the cross-section and angular distribution data was already available [HIN96].

The reactions are very similar in many respects; the target nuclei have very similar deformations, masses, etc. The main difference between the two reactions is that ^{235}U has a spin of 7/2, whereas the ground-state spin of ^{238}U is zero. This means that the reaction $^{16}O+^{238}U$ is an excellent control reaction for the purposes of determining the importance of ground-state spin in the reaction $^{16}O+^{235}U$. The experimental procedure and analysis are described in Chapter 4.

6.4.1 Fitting the Total Cross-section

For the purposes of comparing theoretical and experimental cross-sections, we work with the "capture" cross-section; this differs from the fusion cross-section in that it includes the quasi-fission cross-section. The simplified coupled-channels code CCMOD [DAS92, DAS97] generates the capture cross-section.

Theoretical fusion cross-sections were obtained, taking into account β_2 and β_4 deformations in the target, an E2 excitation in the projectile nucleus, and positive Q-value transfer channels. Quadrupole deformations for $^{235,238}U$ were taken from Ref. [RAM87], obtaining $\beta_2 = 0.2863$ for ^{238}U and $\beta_2 = 0.277$ for ^{235}U. The β_4 deformations were taken as 0.045 for both target nuclei. For each reaction all ±1n, ±2n, ±1p, transfer channels were included that have net positive Q-values (accounting for changes in Coulomb energy). Transfer strength was uniformly taken as 0.6 MeV, as this resulted in good agreement between theoretical and experimental cross-sections at low energies.

Coupling to the octupole excited state in ^{16}O was ignored, as it is expected only to give rise to a shift in the average barrier [HAG97]. This does have the practical consequence that the Woods-Saxon potential parameters must be adjusted to compensate.

The Woods-Saxon nuclear potential depth V_0 was taken as 100 MeV. The radius parameter r_0 and the diffuseness a_0 were simultaneously adjusted to reproduce all data points above 200mb for each reaction. For the reaction $^{16}O+^{238}U$, where there were 17 data points above 200 mb, a_0 was found to be 1.21 and r_0 was 1.020. For the reaction $^{16}O+^{235}U$, there were 10 points above 200mb, a_0 was 1.24, and r_0 was 1.010. The corresponding CCMOD input files for these reactions are given in Appendix B.

Figures 6.1 and 6.2 compare both cross-sections and barrier distributions from these calculations with the data. The barrier distributions are calculated with a step length around 2 MeV. The calculations are in good agreement with the experimental data.

The results are tabulated in Tables 6.1 and 6.2. Fitted fission fragment angular distributions are shown in Figures 6.3 and 6.4.

6.4.2 Comparison with the control reaction

Whatever the nature of the quasi-fission process, and its detailed dependencies, the two reactions $^{16}O+^{238}U$ and $^{16}O+^{235}U$ are so similar that one would expect the observed fission-like angular distributions to be very similar, excepting the effect of the ground-state spin of ^{235}U.

Figure 6.5 shows the fission-like fragment anisotropies obtained for the systems concerned. While there is some difference between the anisotropies measured in this work and those reported in Ref. [HIN96] for the reaction $^{16}O+^{238}U$, it is minor in comparison with the observed difference between the reactions $^{16}O+^{238}U$ and $^{16}O+^{235}U$. The anisotropies from the reaction $^{16}O+^{238}U$ rise as the beam energy decreases, whereas the anisotropies from the reaction $^{16}O+^{235}U$ decrease, so that at below-barrier energies the difference in measured anisotropies between the reactions is very large. This demonstrates clearly that the 7/2 units of ground-state spin of ^{235}U has a strong influence on the quasi-fission fragment angular distribution.

The decrease in $^{16}O+^{235}U$ anisotropy at below-barrier energies is remarkably rapid. It is very likely that exotic fission-like fragment angular distributions with anisotropies less than unity may be observable, if (a) the angular range can be extended closer to 180°, and/or (b) the measurements may be made at lower energies, and (c) the accuracy of the measured differential cross-sections can be improved.

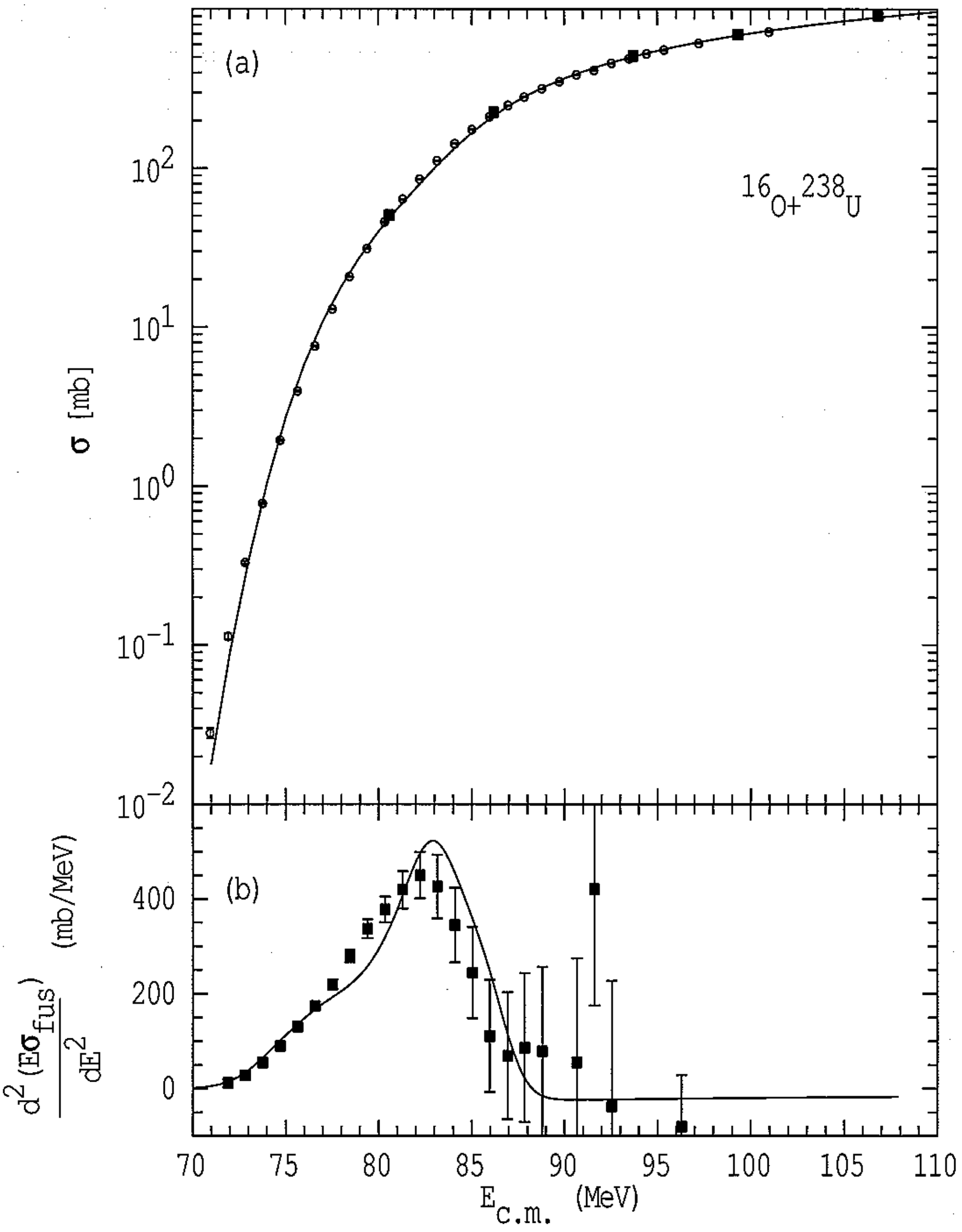

Figure 6.1: Measured and calculated (a) fusion cross-sections, and (b) fusion barrier distribution for the reaction $^{16}O+^{238}U$. The solid line shows calculated values for the fusion cross-section and fusion barrier distribution. In (a), large square points correspond to data from this work, and small points are from [HIN96]; the two data sets are in good agreement. All points in (b) are derived from [HIN96].

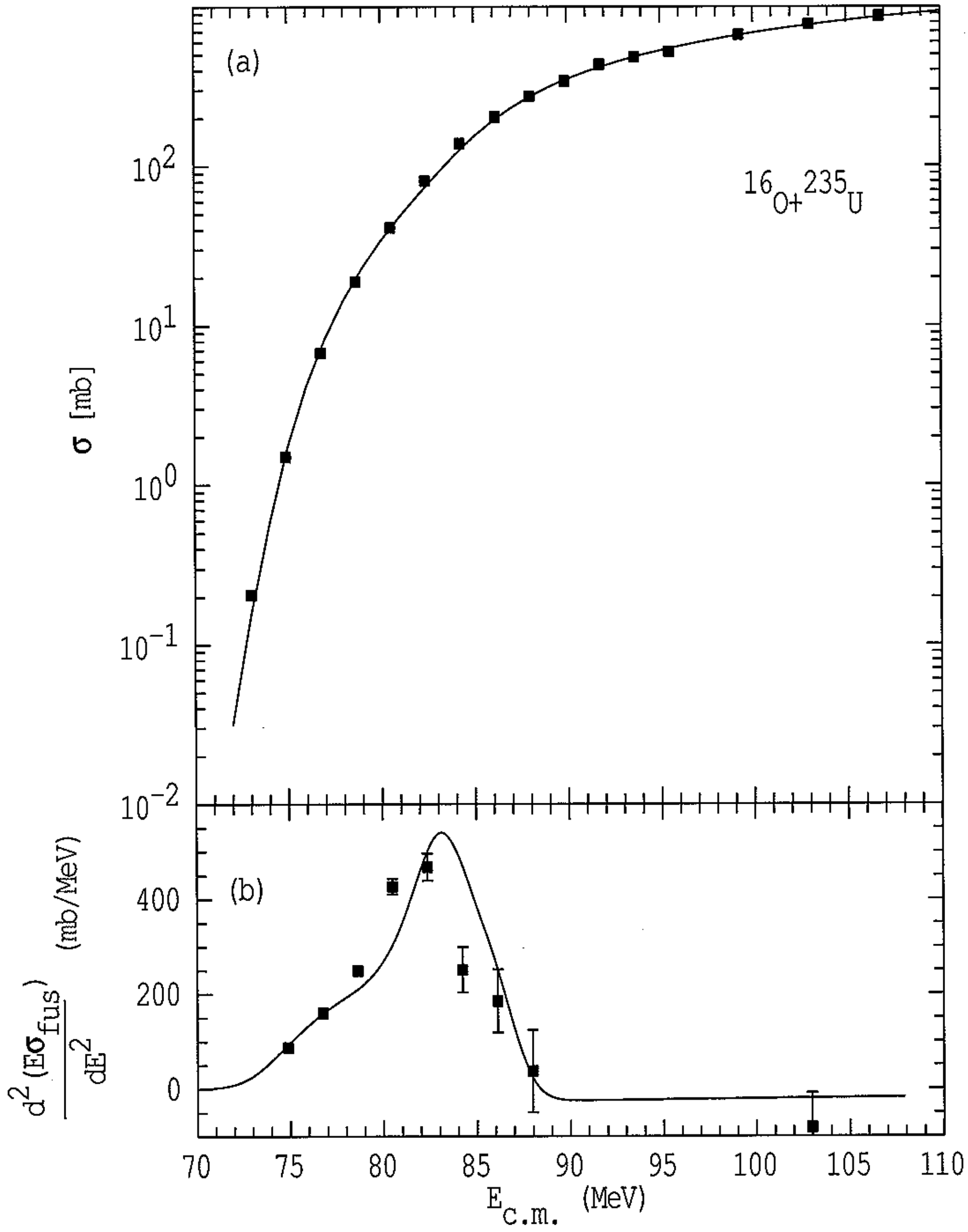

Figure 6.2: Measured and calculated (a) fusion cross-sections, and (b) fusion barrier distribution for the reaction $^{16}O+^{235}U$. The solid line shows calculated values for the fusion cross-section and fusion barrier distribution.

Table 6.1: Measured FMT fission cross-sections and anisotropies for the reaction ^{16}O+^{238}U. The values of $E_{c.m.}$ listed have also been corrected for the energy loss of the projectile before reaching the average interaction point in the target.

E_{beam} (MeV)	$E_{c.m.}$ (MeV)	σ_{fis} (mb)	Anisotropy
86.00	80.52	50.60±0.15	1.99±0.03
92.00	86.14	225.8±0.8	1.80±0.03
100.00	93.64	509.5±1.7	1.93±0.03
106.00	99.26	696±3	1.98±0.04
114.00	106.76	916±2	2.04±0.02

Table 6.2: Measured FMT fission cross-sections and anisotropies for the reaction ^{16}O+^{235}U. The values of $E_{c.m.}$ listed have also been corrected for the energy loss of the projectile before reaching the average interaction point in the target.

E_{beam} (MeV)	$E_{c.m.}$ (MeV)	σ_{fis} (mb)	Anisotropy
78.00	72.94	0.206±0.006	1.04±0.11
80.00	74.82	1.500±0.019	1.30±0.08
82.00	76.70	6.75±0.04	1.33±0.03
84.00	78.57	18.89±0.09	1.51±0.03
86.00	80.44	41.28±0.17	1.62±0.03
88.00	82.32	80.8±0.3	1.63±0.02
90.00	84.19	138.0±0.5	1.67±0.03
92.00	86.06	203.2±0.7	1.64±0.03
94.00	87.93	272.7±0.8	1.72±0.02
96.00	89.81	340.8±1.2	1.78±0.03
98.00	91.69	433.7±1.2	1.78±0.02
100.00	93.56	482.3±1.4	1.89±0.03
102.00	95.43	521.2±2.0	1.86±0.03
106.00	99.18	665.3±1.9	1.98±0.03
110.00	102.92	777±3	2.04±0.03
114.00	106.67	871±3	2.01±0.03

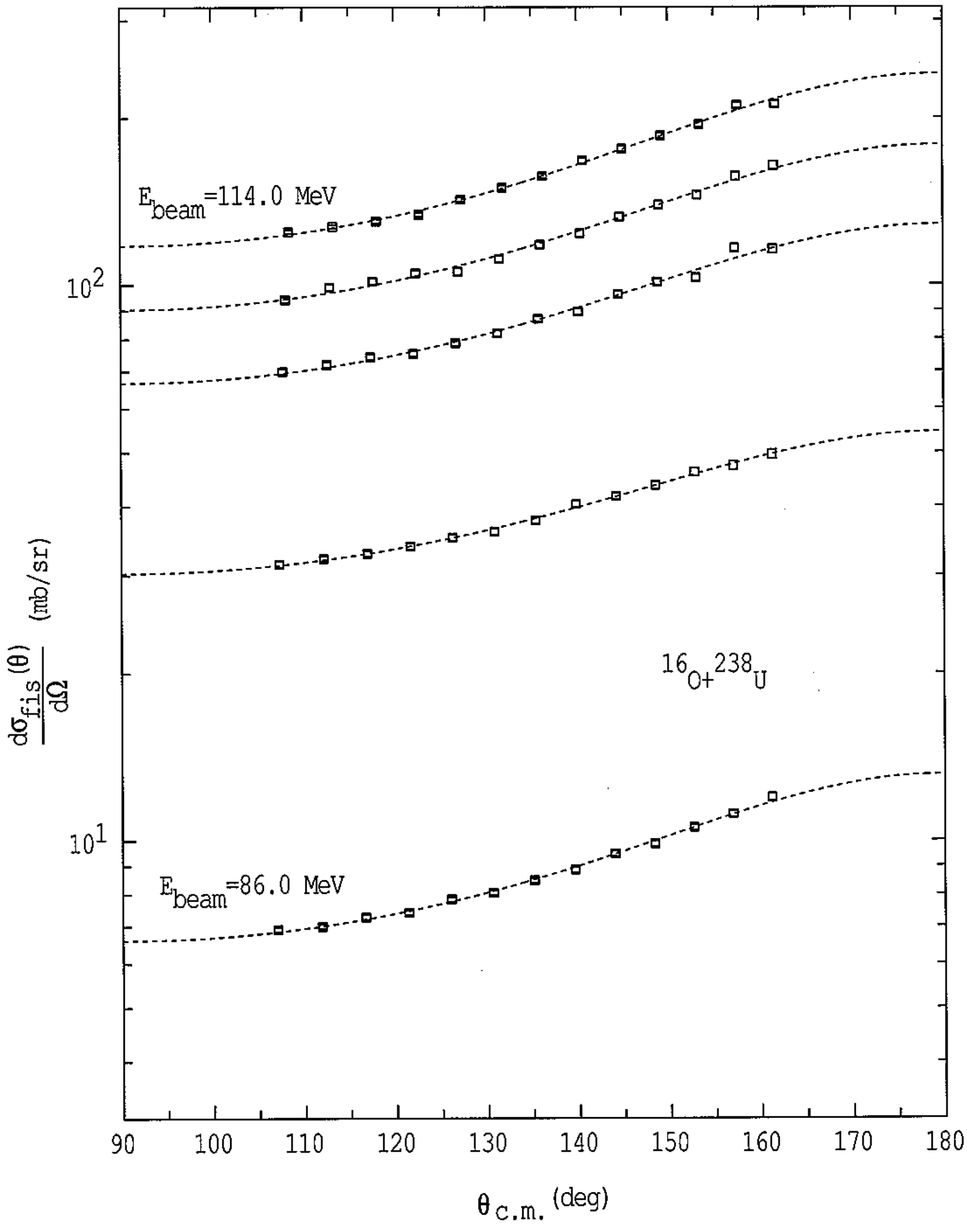

Figure 6.3: Fission-like fragment angular distributions, fitted using the zero-spin approximation, for ^{16}O+^{238}U. Error bars are smaller than the point size except where visible.

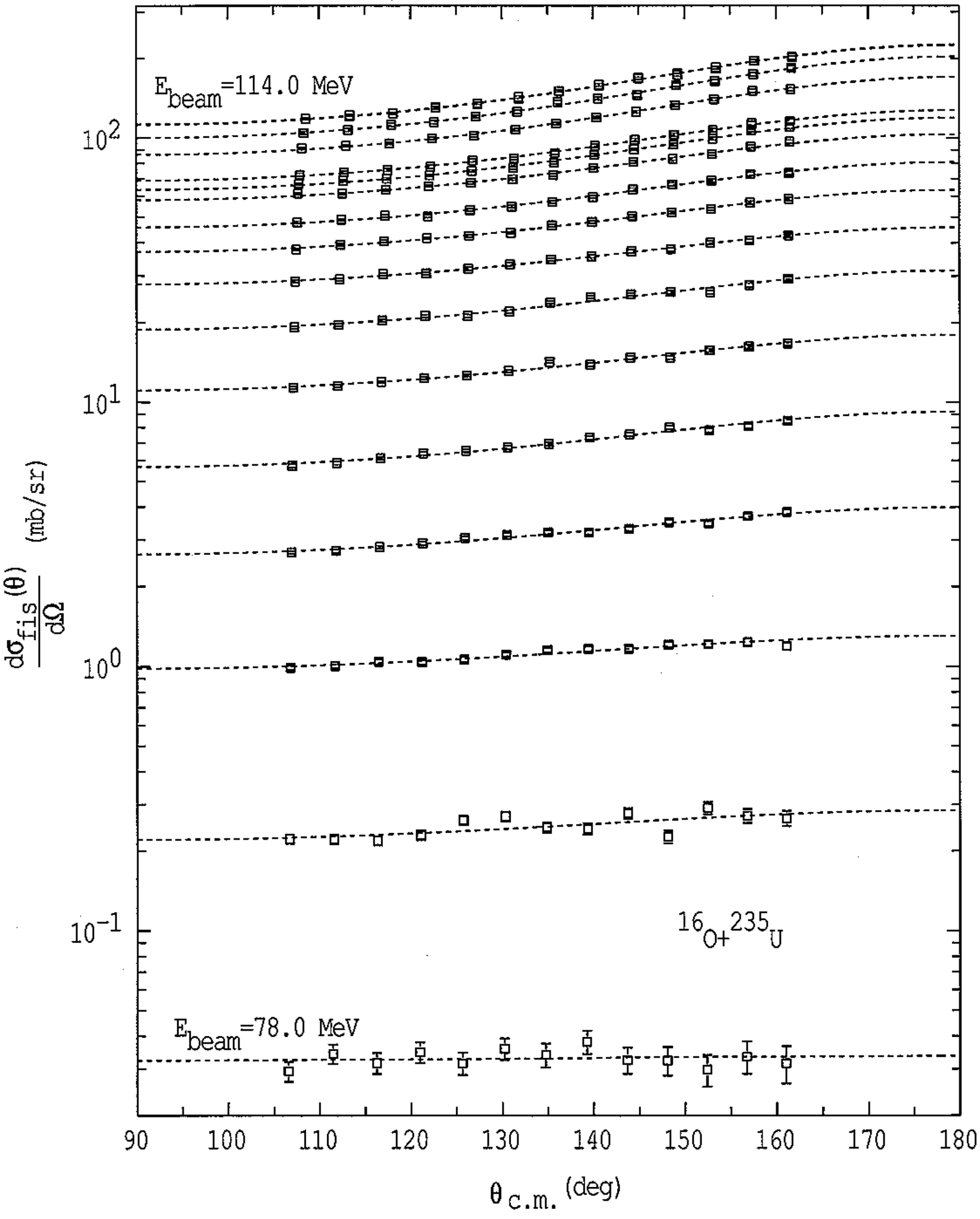

Figure 6.4: Fission-like fragment angular distributions, fitted using the zero-spin approximation, for $^{16}O+^{235}U$. Error bars are smaller than the point size except where visible.

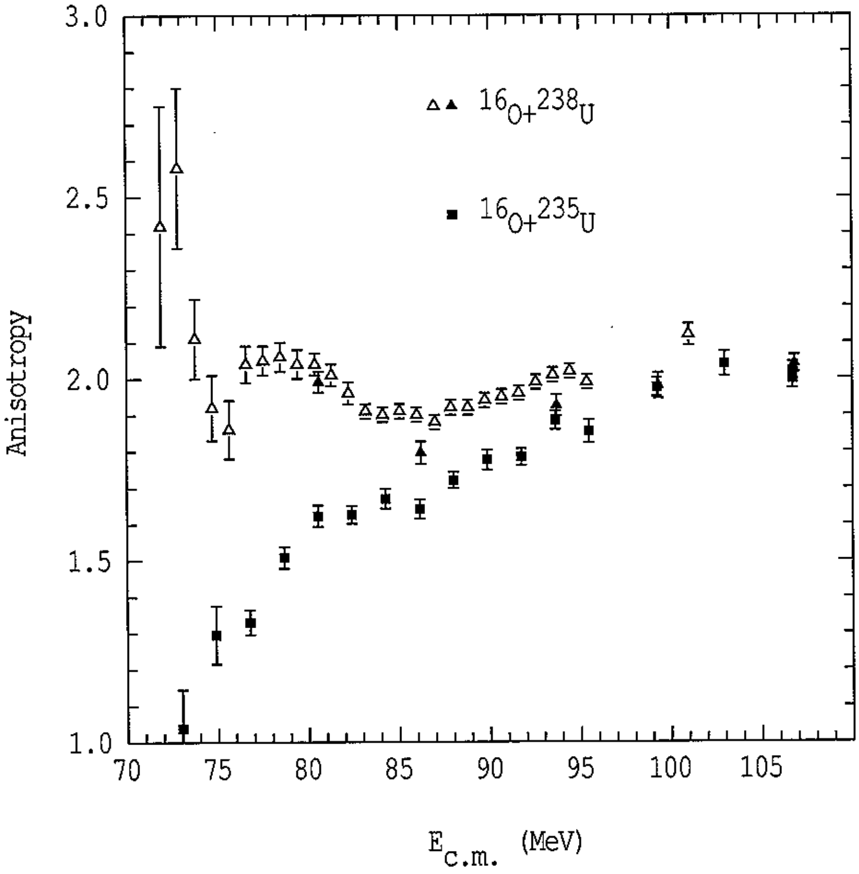

Figure 6.5: Fitted fission-like fragment anisotropies for the reactions ^{16}O+^{238}U (triangular points) and ^{16}O+^{235}U (square points), at a range of energies spanning the Coulomb barrier. Solid points represent measurements made as part of this work; open points come from Ref. [HIN96]; error bars reflect statistical uncertainty only. The large effect of the 7/2 spin of ^{235}U is clear.

6.5 Simulations

For the purposes of this study we perform our simulations with the orientation-dependent quasi-fission model. The source code is described in Section A.4.5 in the appendix, and is designed with future expansion in mind.

Using the orientation-dependent quasi-fission model, the dominant influence on the probability of quasi-fission is the quadrupole deformation (and therefore the orientation θ_0) of the target nucleus (assuming it has significantly more mass than the projectile nucleus). How the probability of quasi-fission depends on target orientation needs to be established. We investigated two different forms of this function; the sharp cutoff form:

$$\begin{aligned} P_{CN}(\theta_0) &= 0.0(\theta_0 < \theta_c) \\ P_{CN}(\theta_0) &= 1.0(\theta_0 \geq \theta_c) \end{aligned} \tag{6.1}$$

where the quantity θ_c is a parameter representing the angle at which quasi-fission cuts in, and the diffuse threshold form:

$$P_{CN}(\theta_0) = 1 - \frac{1}{1 + e^{\frac{\theta - \theta_c}{\Delta\theta}}} \tag{6.2}$$

where both the drop-off angle θ_c and the diffuseness $\Delta\theta$ need to be determined.

Total capture cross-sections were calculated using the simplified coupled-channels code CCMOD, which treats nuclear deformation and orientation classically. This permitted the extraction of partial cross-sections $\partial\sigma_c(l, \theta_0, \theta_1)$, which were then divided into $\partial\sigma_{CN}(l, \theta_0, \theta_1)$ and $\partial\sigma_{QF}(l, \theta_0, \theta_1)$, the compound nucleus formation and quasi-fission cross-sections respectively, according to Equation 6.1 or Equation 6.2. The partial cross-sections corresponding to compound nucleus formation were treated as described in Chapter 5. Since ^{16}O is spherical, all distributions $\partial\sigma$ are flat with respect to θ_1.

Calculating the quasi-fission fragment distributions was the next issue. If the system were fully equilibrated at the conditional saddle point, one could assume a gaussian K-distribution with width K_0 determined from the moment of inertia I_{eff} at the conditional saddle-point and the nuclear temperature. However, given that the system never reaches small elongations, and survives for a time short in comparison to fission times, assuming full K-equilibration may be inappropriate.

If the quasi-fissioning system does not equilibrate, then it is likely that the quasi-fission outcome depends on the initial condition; for example, a reaction between the tip of a large prolate-deformed target and a projectile, which is very likely to lead to quasi-fission, may lead to a very narrow K-distribution. If the same reaction occurs with the target at an angle where the probability of quasi-fission is reduced, the events that *do* quasi-fission may do so with a broader distribution; the di-nuclear system may have survived for longer, and/or gone to smaller elongations.

We approach the problem by assuming that the system quasi-fissions with a gaussian K-distribution, with width K_0 that may be dependent on the initial orientation θ_0 of the target nucleus. This K_0 is unknown. For simplicity we assume that K_0 (or the distribution $K_0(\theta_0)$) is constant at all beam energies (certainly for fission reactions K_0 often varies only slowly with beam energy).

The goal of this approach was to find a set of parameters that reproduced data from the control reaction ^{16}O+^{238}U, and then apply those parameters when performing calculations for the reaction ^{16}O+^{235}U, incorporating the effects of ground-state nuclear spin. However, it became clear that it was not possible to reproduce the anisotropies for both reactions within this model, as described in the next subsection.

6.5.1 Comparison of simulations with experiment

6.5.1.1 Zero ground-state spin

Consider a reaction where fusion-fission and quasi-fission are both present in similar quantities. In the angular distribution of fission-like fragments, the fusion-fission distribution will have rather a low anisotropy (due largely to the highly fissile nature of the compound nucleus, and therefore the small elongation of the saddle-point). In contrast, the quasi-fission component may have a very high anisotropy. This has significant consequences for the total distribution $W(\theta)$.

In particular, the anisotropy is no longer sufficient to entirely characterise the total distribution. Figure 6.6 illustrates this in the case of a relatively simple calculation at relatively high beam energies for the reaction ^{16}O+^{238}U. Most calculations of fission or fission-like anisotropies simply calculate $W(180°)/W(90°)$ directly. Some calculate $W(\theta)$ at a range of angles from 90° to 180°, assigning arbitrary errors and

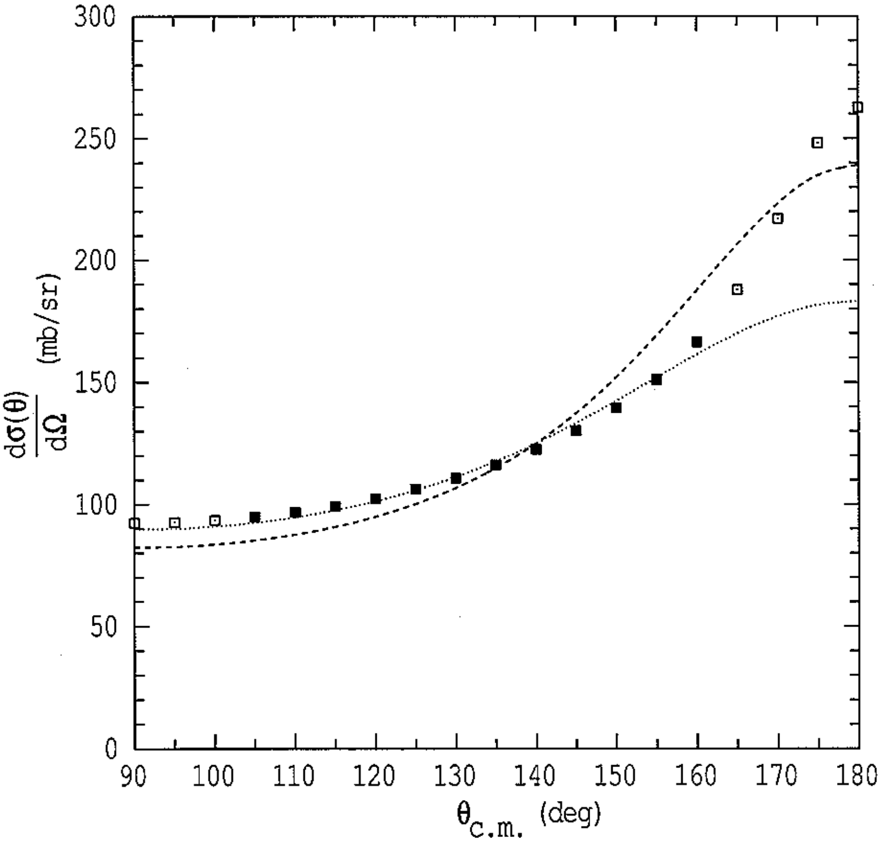

Figure 6.6: Fits to the fission-like fragment angular distribution calculated for $^{16}O+^{238}U$ at E_{CM}=100 MeV with $K_0 = 5.0$ and a quasi-fission threshold $\theta_c = 30°$, $\Delta\theta = 15°$. The calculated distribution $W(\theta)$ (square points) has an anisotropy $W(180°)/W(90°)$ of 2.84. The fit to the whole distribution (dashed line) in 5 degree steps has an anisotropy of 2.90, and a very high value of χ^2; if the fit is performed only on the (solid) points between 105° and 160° (inclusive; dotted line), corresponding to the range of angles measured in a coincidence experiment using the CUBE detectors, the fit returns an anisotropy of only 2.04, and a much lower χ^2. This shows that the anisotropy is not sufficient to characterise the fission-like angular distribution, and it is necessary to perform calculations using the same range of angles as are available in experimental fission-like angular distributions.

fitting the distribution in the same way that experimental data is fitted. However, for these two-component distributions which do *not* have the same kind of shape as a transition-state-model distribution, determining the anisotropy by fitting it with a TSM-like distribution will lead to results that vary according to the range of angles included in the fit.

This consideration applies wherever a distribution of fission or fission-like fragments contains two or more components with significantly different anisotropies. It has the following practical consequences:

- Care must be taken to ensure that theory and experiment are comparable; if either distribution shows signs of having two components, the theoretical distribution should be calculated and fitted using the same set of angles as the experimental distribution.
- Experiments performed on the same reaction using different equipment may yield different anisotropies simply because the detectors cover a different range of angles. The angles nearest 0° and 180° are most significant in this respect.

6.5.1.2 Systems with ground-state spin

Having predicted fission fragment angular distributions with anisotropy less than unity ([BUT02], Section 3.3, for the spin-16 target nucleus $^{178}\mathrm{Hf}^{m2}$) it would be interesting to see if quasi-fission distributions could also show anisotropy less than unity, for the much lower ground-state spin of ^{235}U of 7/2. Figure 6.7 shows distributions of quasi-fission fragments calculated for a range of possible K_0, at E_{CM}=73 MeV, for the reaction $^{16}\mathrm{O}+^{235}\mathrm{U}$. This is near the lowest measurable sub-barrier energy. The anisotropy is less than unity for those values of K_0 substantially smaller than the ground-state spin I_0.

The anisotropy $W(180°)/W(90°)$ *increases* with K_0 until K_0 is approximately equal to the ground-state nuclear spin I_0 of ^{235}U. At higher K_0 the ground-state spin has less impact and the anisotropy decreases with K_0 as with most systems.

This unusual behaviour is, however, mainly due to the behaviour of the distribution in the angular range 165–180°. At low K_0 the FFAD shape is more strongly influenced by the l-distribution brought in by the projectile than by the nuclear tilting. Figure 6.8 shows the result of fitting the $K_0 = 1.0$ distribution within the

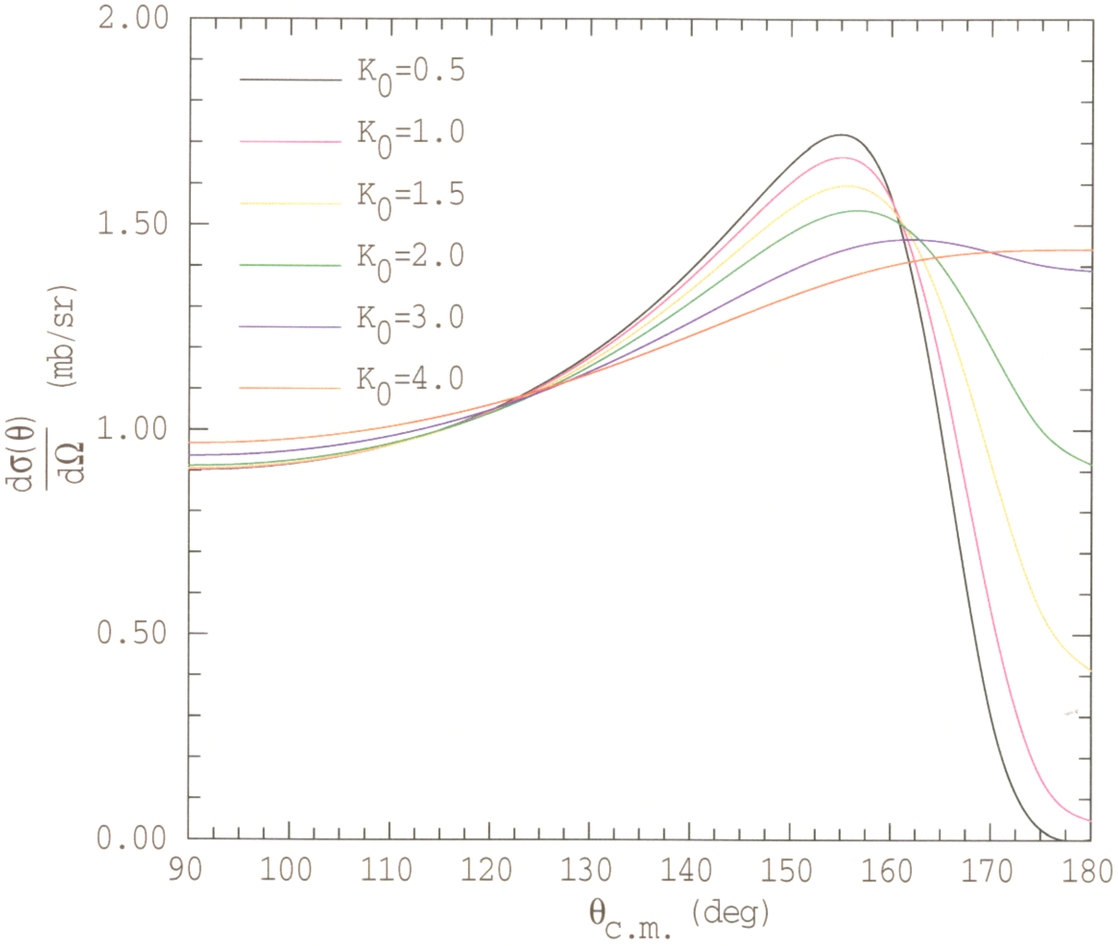

Figure 6.7: Quasi-fission fragment angular distributions calculated with K_0 taking the values 0.5, 1.0, 1.5, 2.0, 3.0, and 4.0, for I_0=7/2 (^{235}U).

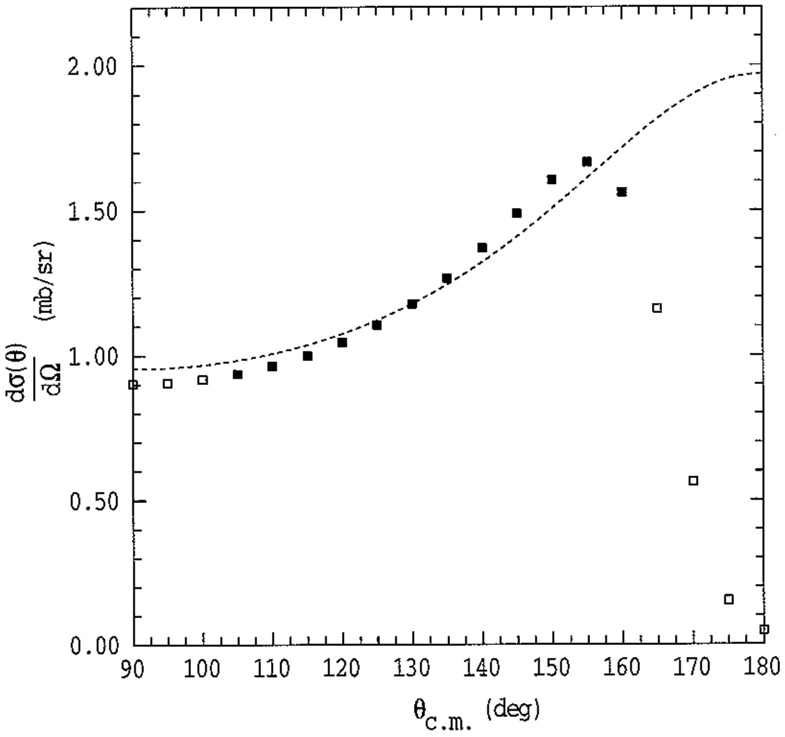

Figure 6.8: Pseudo-experimental fit to quasi-fission fragment angular distributions calculated with K_0 taking the value 1.0; fit uses solid points only.

range of angles roughly corresponding to experiment; the fitted anisotropy is far higher than the actual anisotropy. Further investigation of this kind reveals that, within this angle range, the apparent anisotropy increases as K_0 decreases, just as with normal fission fragment angular distributions. The rate of the increase is much lower, but the direction is the same.

This has unfortunate consequences when it comes to attempting to reproduce the anisotropies for both the reactions ^{16}O+^{235}U and ^{16}O+^{238}U. Figure 6.9 compares calculated anisotropies (using fits over the experimental angle range) for fission, quasi-fission, and the total fission-like distributions with the experimental data. They reproduce the anisotropies for ^{16}O+^{238}U well enough, although the agreement could be improved with finer parameter adjustment. However, the calculated anisotropies for ^{16}O+^{235}U are consistently too high, with these or other parameters.

To further investigate this situation, we focussed on reproducing the anisotropy of the lowest measured data point for the reaction ^{16}O+^{235}U. Given the "fit to experimental angle" constraints described above, however, we found that there were only two ways of doing this. Either the probability of quasi-fission is very low,

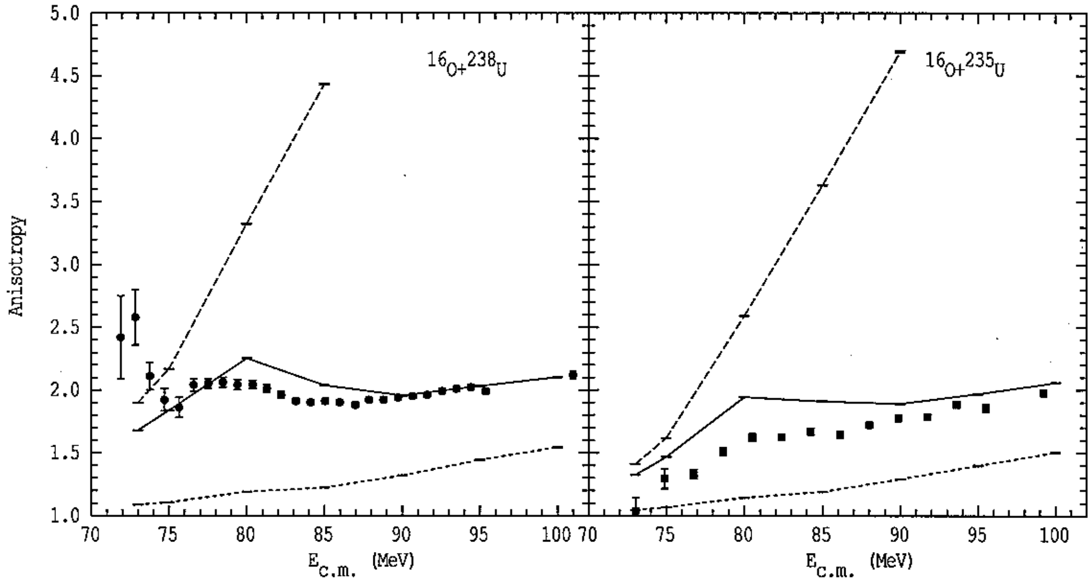

Figure 6.9: Comparison of experimental and calculated anisotropies (using fits over the experimental angle range) for fission (dotted line), quasi-fission (dashed line), and the total fission-like distributions (solid line, data points). Calculations were performed using K_0 constant at 5.0 and the quasi-fission probability parameters $\theta_c = 30$, $\Delta\theta = 15$.

and the reaction is fission-dominated (which runs contrary to reported measurements for similar reactions, e.g. ^{12}C+^{236,238}U [LES97]) or the effective K_0 for quasi-fission is fairly high. In either case this would require the corresponding fission-like anisotropies for the reaction ^{16}O+^{238}U to also be low; and this is not consistent with the data.

6.6 Summary

It is concluded that it is not possible to simultaneously reproduce the observed fission-like anisotropies, over the range of observed CM angles 108–162°, for both the reactions ^{16}O+^{235}U and ^{16}O+^{238}U, within the current model. The effect of the ground-state spin of ^{235}U is stronger even than the current model predicts. (This limitation would not be noticed if the model anisotropies were obtained directly from the calculated $W(180°)/W(90°)$, as such anisotropies may take on almost arbitrary values depending on the quasi-fission probability and the effective K_0. It is a result of the non-TSM-like shape of the distributions.)

6.7 Future work

We have established that the present model does not adequately describe the observed fission-like anisotropies. However, there is room to extend the model in ways that may allow ground-state nuclear spin to have a stronger effect.

One possibility is entrance-channel-dependent pre-equilibrium *quasi*-fission, as referred to in Section 6.3.2.2. Within a quasi-fission event, where the elongation remains significant and well defined throughout, the K-degree of freedom may well be very slow to equilibrate. Further, the initial K-distribution is affected; if the target nucleus has its elongation axis aligned with the beam direction, then when fusion occurs, the the initial elongation axis of the di-nucleus is also along the line of the beam direction, and the projection K of the total angular momentum J on this elongation axis is the same as M; i.e. the initial K-distribution has two peaks near $K = \pm I_0$, rather than one peak at $K = 0$ [LES97, LES97B]. This will also influence the total fragment distribution. The change in K-distribution may, however, reduce the significance of the de-alignment of $\vec{J}$, so the relative importance of this change needs to be investigated.

Another possibility is that the probability of the quasi-fissioning system scissioning before completing a full rotation may be significant. This is likely to depend on the relative fissility and mass asymmetry of the system, and the total angular momentum brought in by the projectile; for heavy compound nuclei and low angular momenta the rotation time may become comparable with the scission time, especially since a quasi-fission event involves a larger moment of inertia and a faster scission time than a fusion-fission event.

In this case the calculation of the quasi-fission fragment angular distribution is appreciably more complex. In particular, the assumption that fission-like fragments are isotropically distributed in the angles orthogonal to $\vec{J}$ breaks down; the rotation of the system about $\vec{J}$ from the initial collision configuration must be taken into account. If the system were to scission about half a rotation after it formed, a very high anisotropy would result; if the system were to scission after a quarter of a rotation, the fragments would be focussed near 90° and the anisotropy would be less than unity. In practice the distribution of J would give rise to a wide variation in the number of rotations for which the di-nucleus survives.

If partial rotations are significant, then calculations of the fragment angular

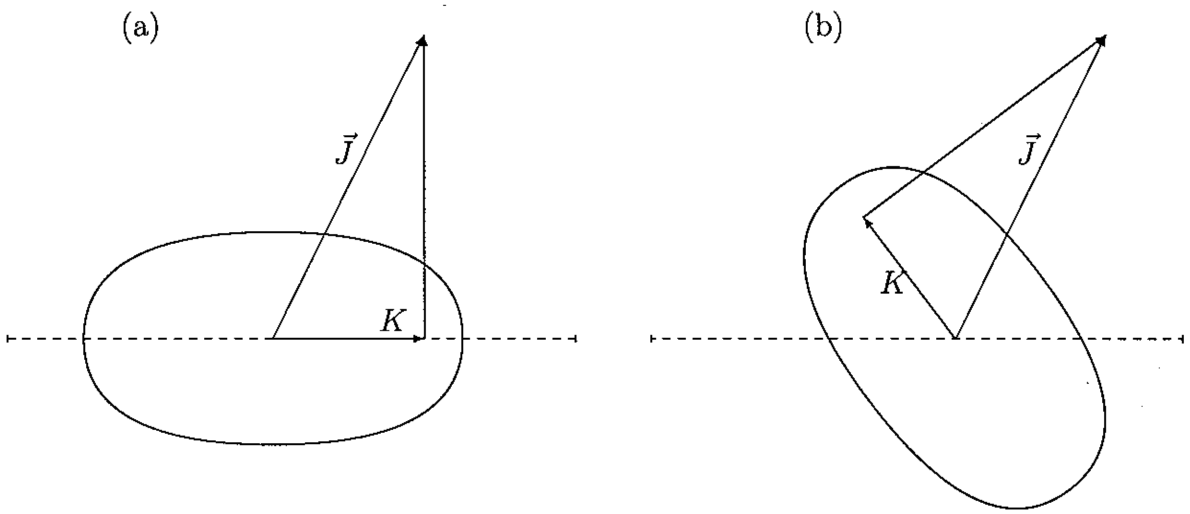

Figure 6.10: A di-nucleus rotates with constant K, about the angular momentum $\vec{J}$. (a) The di-nucleus as it was formed, along the beam axis. (b) The same di-nucleus half a rotation later.

distribution in the presence of ground-state spin are appreciably more complicated still, as the nuclear elongation axis traces out a cone centered on $\vec{J}$; if there is no ground-state spin I then K is zero and the cone becomes a plane, but if I is significant, then for below-barrier collisions with the tip of a prolate target, K is initially populated at $\pm I$ and the nuclear elongation axis changes plane rapidly. Figure 6.10 illustrates this in the case of a di-nucleus undergoing half a rotation.

CHAPTER 7

Conclusion

7.1 The Effect of Target Spin on Fission Anisotropy.

Fission fragment cross-sections and anisotropies for the four reactions ^{28}Si+^{178}Hf, ^{29}Si+^{178}Hf, ^{31}P+^{175}Lu, and ^{31}P+^{176}Lu have been measured at a range of energies spanning the average fusion barrier. Each target nucleus has essentially the same large prolate deformation, but the ground-state spin varies from 0 (^{178}Hf) through 7/2 (^{175}Lu) to 7 (^{176}Lu). Measurements of evaporation residue cross-sections at selected energies allowed total fusion cross-sections for all four reactions to be determined at all energies studied. These results enabled accurate calculation of the fusion angular momentum distributions for each reaction, which are essential to calculation of fission fragment anisotropies.

Using these distributions, statistical model calculations were made which accurately reproduced the anisotropies for the reactions ^{28}Si+^{178}Hf and ^{29}Si+^{178}Hf, involving the zero-spin target nucleus. For the reaction ^{31}P+^{175}Lu, the alignment of the 7/2 ground-state spin of ^{175}Lu only has a small effect on anisotropy. For the reaction ^{31}P+^{176}Lu, where ^{176}Lu has a large ground-state spin of 7, measured anisotropies are significantly lower than those for the other reactions. The transition state model calculations do not reproduce these data when the ground-state spin is ignored or assumed to be isotropically oriented. Only by including the alignment of the ground-state spin with the nuclear deformation axis can the experimental data be well reproduced.

These results demonstrate that ground-state spin can have a significant effect on fission fragment anisotropies. When the nucleus with spin also has a static deformation, because the spin is aligned with the nuclear deformation axis, the effect of the spin is enhanced.

7.2 The Effect of Target Spin on Quasi-fission Anisotropy.

For observations including significant quantities of both fission and quasi-fission, the combined angular distribution comprises two very different components, with very different anisotropies, and therefore the combined anisotropy is not adequate to characterise the combined distribution. It becomes important to simulate theoretical distributions over the same angular range as experimental data.

Full momentum transfer fission cross-sections and anisotropies have been measured at a range of energies spanning the fusion barrier for the reaction $^{16}O+^{235}U$, and compared with existing measurements for the reaction $^{16}O+^{238}U$. At beam energies below the average fusion barrier, the measured anisotropies for the ^{235}U reaction are drastically lower than those from the ^{238}U reaction, demonstrating clearly that the 7/2 ground-state spin of ^{235}U has a dramatic effect.

The trend of the measured anisotropies for $^{16}O+^{235}U$ indicates that it may be possible to observe a fission-like fragment angular distribution with anisotropy less than unity, by collecting data at a slightly lower beam energy and/or including experimental measurements at angles closer to 180°.

Since the fusion-fission process is well understood, and the effect of 7/2 units of spin for this reaction is negligible, the observed effect must arise from quasi-fission events. However, although existing quasi-fission models predict a strong effect from the spin of ^{235}U, the observed effect is appreciably stronger still in the experimental angular range. This should be an important tool in evaluating models of the quasi-fission process.

APPENDIX A

Computer Codes and Simulations

This chapter is devoted to the different computer programs used to perform experimental analyses and theoretical simulations during this project. The term simulations is here used to cover both Monte Carlo codes and the kind of code which simply evaluates the predictions of a model, since this often involves summations over a large number of possibilities. The general tasks are described, identifying the main programs used and the flow of data between them, and providing sample command files. In later sections each program and its significant variants are described in more detail.

The contents of this chapter will also be released as the ANU internal publication "A guide to selected fusion-fission analysis and simulation programs", ANU-P1541. This internal publication may be updated from time to time.

People from institutions outside the ANU wishing to use those of these programs developed at the ANU should contact Dr David Hinde (David.Hinde@anu.edu.au) for permission.

A.1 Program Usage

For the most part all programs are run using command-files. While this is not strictly necessary, it eliminates enormous amounts of tedium, various sources of error, and permits rapid re-performing of calculations, with perhaps minor variations, without much effort. This section describes the main sequence of program operation for a variety of tasks, and provides command files implementing that sequence. In some cases the development of these command files has reduced three days of entering commands to ten minutes of making or updating a command file.

We provide samples of several such command files here. Line numbers are shown for discussion purposes only; they are not present in practice. We provide flow-charts illustrating the main flow of data between programs; these charts are not exhaustive in that they do not show all inputs or outputs to all programs (that information is discussed in later sections), nor do the charts show all combinations of programs actually used during the work which underlies this thesis.

A.1.1 Data Analysis

We will not consider the intricacies of using DCP, the Data Collection and Processing program which is generally used to examine and analyse the raw event-by-event data. This section discusses only the analysis of data once usage of DCP is complete; at which point the user should have a set of files listing the fission counts in each 5° bin in the lab angle θ, together with the associated monitor and pulser counts for each run.

The goal of the subsequent analysis is to turn these fission counts into differential cross-sections in the centre of mass frame, and then to fit these differential cross-sections to obtain fission fragment anisotropies and cross-sections.

The analysis of evaporation residues, using the program FITEK, is not discussed in this section. The results from FITEK comprise counts from α-particle peaks at particular energies. The corresponding evaporation residue cross-sections are calculated using CROSSEC2.

A.1.1.1 Simple back-detector analysis

Physics The number of events N detected in a detector of solid angle Ω at an angle θ is given by:

$$N = \frac{d\sigma(\theta)}{d\Omega}\Omega N_{projectiles} N_{targets}/A_{beam} \tag{A.1}$$

where $N_{projectiles}$ is the number of incident particles in the beam, and $N_{targets}$ is the number of nuclei in the target in the area A_{beam} illuminated by the beam.

In practice, the exposure $N_{projectiles}N_{targets}/A_{beam}$ is not known, and Ω is not known precisely. N is measured experimentally, and the differential cross-section $\frac{d\sigma(\theta)}{d\Omega}$ is usually the quantity sought.

The exposure is eliminated by comparing measurements from two different detectors, taken simultaneously, where one of the detectors (the monitor detector) detects events with a well-established differential cross-section. In practice, the monitor invariably detects elastically scattered beam particles, where the Rutherford differential cross-section is given by:

$$\frac{d\sigma_R(\theta)}{d\Omega} = \frac{Z_0^2 Z_1^2 e^4}{16E_{beam}^2 \sin^4(\theta/2)}. \tag{A.2}$$

Then the ratio of the yield in the monitor to the yield in the back detector is given by:

$$\frac{N_{det}}{N_{mon}} = \frac{\Omega_{det}\frac{d\sigma(\theta_{det})}{d\Omega}}{\Omega_{mon}\frac{d\sigma_R(\theta_{mon})}{d\Omega}} \tag{A.3}$$

The quantity $\frac{\Omega_{det}}{\Omega_{mon}}$ may then be determined using a calibration run, in which both the monitor and the fission detector collect particles scattered with Rutherford cross-sections.

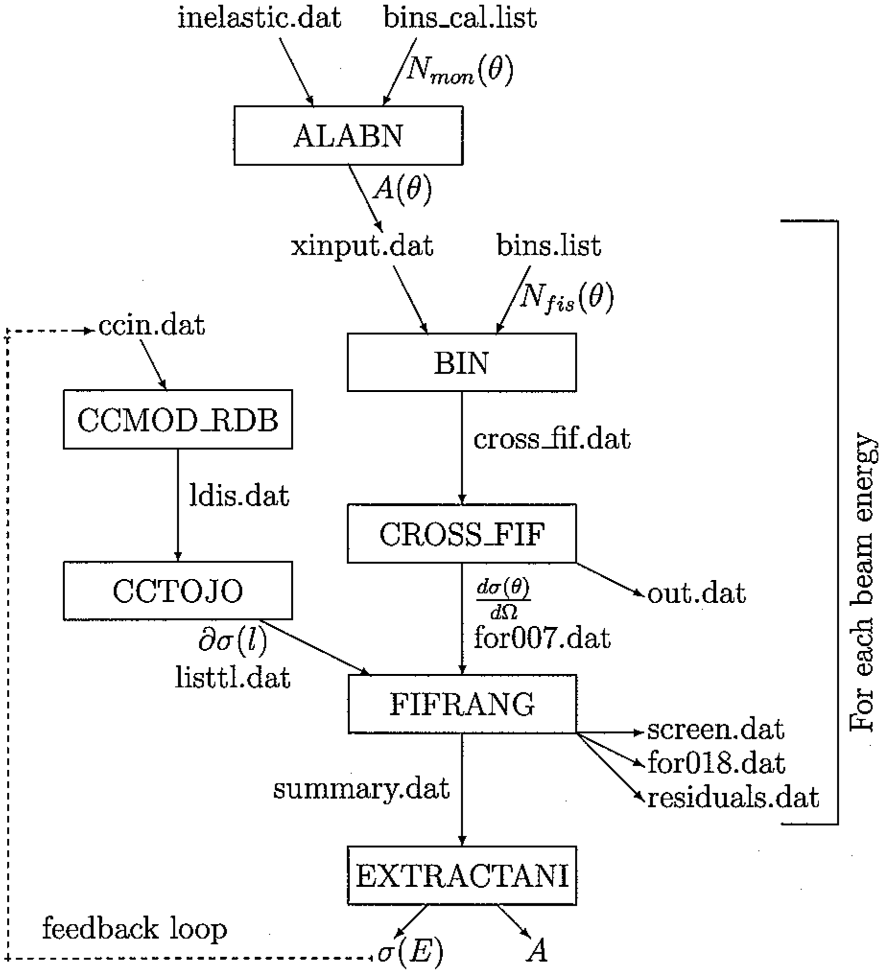

Figure A.1: Flow-chart for simple back-detector data analysis.

In practice, this ratio $\frac{\Omega_{det}}{\Omega_{mon}}$ is evaluated indirectly; for each detector bin at an angle θ_{det}, we determine a calibration coefficient $A(\theta_{det})$, using data solely from the calibration run [MOR95B]:

$$A(\theta_{det}) = \left(\frac{\sin(\theta_{det})\Delta\phi}{2\pi}\right)\frac{N_{mon}\frac{d\sigma_R(\theta_{det})}{d\Omega}}{N_{det}\frac{d\sigma_R(\theta_{mon})}{d\Omega}} \tag{A.4}$$

and the differential cross-section for the reaction of interest is determined using only $A(\theta)$ quantities from the experimental run according to [MOR95B]:

$$\frac{d\sigma(\theta_{det})}{d\Omega} = \frac{2\pi A(\theta_{det})}{\Delta\phi\sin(\theta_{det})}\frac{N_{fis}\frac{d\sigma_R(\theta_{mon})}{d\Omega}}{N_{mon}} \tag{A.5}$$

There are several practical consequences of this approach. Neither the specified nor the actual phi-cut $\Delta\phi$ affect the final differential cross-section $\frac{d\sigma(\theta_{det})}{d\Omega}$. Nor does the angle at which the monitor detectors are placed need to be correct, so long as neither the actual nor the stated monitor angle change between the calibration run and the experimental run. (In contrast, the fission detector angle θ_{det} *is* important, because events like fission fragment detection will not have the same angular dependence as Rutherford scattering.)

Calling patterns The quantities N_{fis} and N_{mon} are determined using DCP, and subsequently processed as indicated in Figure A.1.

ALABN is usually called manually, once. The resulting $A(\theta)$ are then copy-pasted into xinput files, together with the appropriate details of the calibration run. These xinput files are prepared for each experimental run, with monitor counts, beam energy, etc, entered manually. Once prepared, these files generally do not need any further attention.

The calculation and fitting of differential cross-sections, using some angular momentum distribution, is performed in one command-file (BCFFCF.COM), for all energies from a single reaction, in order. The file summary.dat should be empty before BCFFCF.COM is called, so that when the command file finishes, summary.dat contains results from precisely those energies processed in the command file. This may then be fed, together with an ordered list of the energies processed, to EXTRACTANI, which reformats the results for easy graphing.

The measured fusion cross-sections (the sum of the fission and evaporation resudie cross-sections) may be compared to CCMOD cross-section calculations, and the CCMOD input ccin.dat amended to better reproduce the observed cross-sections. This affects the angular momentum distributions $\partial\sigma(l)$ calculated using CCMOD, which in turn affects the FIFRANG fit; the anisotropies change slightly, the cross-sections barely at all (which reduces or eliminates the need for subsequent iterations).

Sample command-file: BCFFCF.COM

```
$ copy blank.dat summary.dat
$ copy xinput_002.dat xinput.dat
$ copy bins_002.list bins.list
$ run [fission.rdb103.progs]ccmod_rdb
ccin_31p175lu.dat
127.43 127.43 1.0
$ run [fission.rdb103.joanne]cctojo
ldis.dat
listtl.dat
$ DEF/LOG DATAFILE CROSSF_IN.DAT
$ R [FISSION.rdb103.progs]BIN
$ DEL OUT.DAT;*
$ DEL FOR007.DAT;*
$ PURGE FOR018.DAT
$ R [FISSION.rdb103.progs]CROSS_FIF
CROSSF_IN.DAT
OUT.DAT
$ DEF/LOG FILE$NAME FOR007.DAT
$ Run [fission.rdb103.progs]fifrang
100,-52,-20,9,2
$ copy out.dat out_002.dat
$ copy for007.dat for7_002.dat
$ copy for018.dat for18_002.dat
$ copy screen.dat fifa_002.out
... and a second energy ...
$ copy xinput_004.dat xinput.dat
$ copy bins_h004.list bins.list
$ run [fission.rdb103.progs]ccmod_rdb
ccin_31p175lu.dat
116.81 116.81 1.0
$ run [fission.rdb103.joanne]cctojo
ldis.dat
listtl.dat
$ DEF/LOG DATAFILE CROSSF_IN.DAT
$ R [FISSION.rdb103.progs]BIN
$ DEL OUT.DAT;*
$ DEL FOR007.DAT;*
$ PURGE FOR018.DAT
$ R [FISSION.rdb103.progs]CROSS_FIF
CROSSF_IN.DAT
OUT.DAT
$ DEF/LOG FILE$NAME FOR007.DAT
$ Run [fission.rdb103.progs]fifrang
100,-52,-20,9,2
$ copy out.dat out_h004.dat
$ copy for007.dat for7_h004.dat
$ copy for018.dat for18_h004.dat
$ copy screen.dat fifa_h004.out
```

```
... etc for more energies.
$ copy summary.dat summ_natlu.dat
```

Sample command-file: EXTRACTANI.COM

```
$ run [fission.rdb103.progs]extractani
summ_natlu.dat
elist_natlu.dat
31 175
```

A.1.1.2 Coincidence analysis

Physics With two detectors operating, and a coincidence requirement determining when event-by-event data gets written, some additional constraints are imposed upon the analysis process. For the most part this influences the analysis within DCP, as described in Section 4.3.2. The other considerations are as follows:

- Supporting wires on the front detector occasionally prevent coincidence events from being registered which should have been detected. These result in slightly suppressed detector efficiency in the back detector, at angles depending on the beam energy. The suppression factors are calculated using CALVINER and the correction is applied to the standard calibration factors $A(\theta)$ using HOBBES, which also corrects for uniform efficiency effects and assembles the xinput.dat files.

- Fission fragments reaching the most backward angles on the back detector have forward-moving partners that are extremely likely to miss the front detector altogether, meaning that the most backward angles on the backward detector aren't useful. These are then discarded, using CHOPPER, before fitting the fission fragment angular distribution.

Calling Patterns ALABN is run manually as for the simple, single-detector analysis procedure. Corrections to the resulting $A(\theta)$ are generated as the first part of the HOBBES.COM commandfile. The preparation of the xinput files is partly automated using HOBBES.COM, where the minimum necessary xinput data is entered into the second half of HOBBES.COM as command-line parameters for the program HOBBES.

Once the xinput files are prepared, the differential cross-sections can be computed and fitted with BCFFCF.COM as before, the main difference being the use of the tiny program CHOPPER to discard the angles rendered useless by coincidence failures. The resulting summary file may be processed with EXTRACTANI.COM precisely as before.

Sample Command File: HOBBES.COM

```
$ run [fission.rdb103.progs.fifrang]calviner
8 16 92 235
```

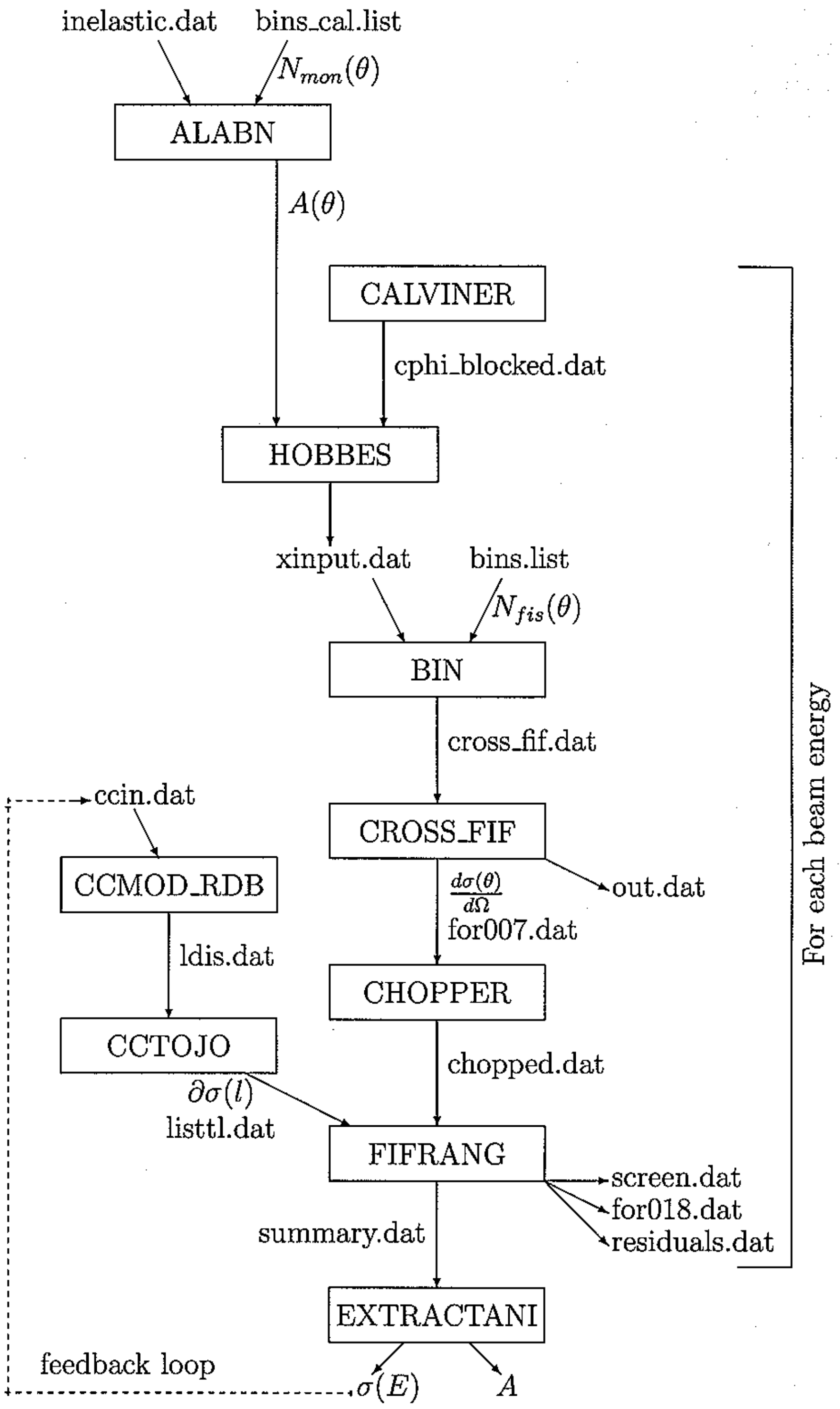

Figure A.2: Flow-chart for coincidence data analysis.

```
106.0
0.20
$ copy cphi_blocked.dat cphi_blocked_u235_106.dat
$ copy bd_coarse.dat bd_coarse_u235_106.dat
... repeat for lots of energies ...
$ run [fission.rdb103.progs.fifrang]calviner
8 16 92 235
102.0
0.20
$ copy cphi_blocked.dat cphi_blocked_u235_102.dat
$ copy bd_coarse.dat bd_coarse_u235_102.dat

$ run [fission.rdb103.progs.fifrang]hobbes
 28.      58.    79.    197.
 100.000      22.5
slot.dat
1.02
8 16 92 235
JAN01
... (that's the basic data, next the data for each energy)
106.0
001
56079.92 4374 4267
cphi_blocked_u235_106.dat
... repeat for all the above energies ...
102.0
022
34670.90 2576 2473
cphi_blocked_u235_102.dat
-1.0
(negative energy to finish).
```

Sample Command File: BCFFCF.COM

```
$ copy blank.dat summary.dat

$ copy xinput_001.dat xinput.dat
$ copy bins_H001.list bins.list
$ run [fission.rdb103.progs]ccmod_rdb
ccin_235.dat
99.243 99.243 1.0
$ run [fission.rdb103.joanne]cctojo
ldis.dat
listtl.dat
$ DEF/LOG DATAFILE CROSSF_IN.DAT
$ R [FISSION.rdb103.progs]BIN
$ DEL OUT.DAT;*
$ DEL FOR007.DAT;*
```

```
$ DEL chopped.DAT;*
$ PURGE FOR018.DAT
$ R [FISSION.rdb103.progs]CROSS_FIF
CROSSF_IN.DAT
OUT.DAT
$ run [fission.rdb103.progs.fifrang]chopper
FOR007.dat
13
$ DEF/LOG FILE$NAME chopped.DAT
$ Run [fission.rdb103.progs.fifrang]fifrang
100,-52,-20,9,2
$ copy out.dat out_H001.dat
$ copy chopped.dat for7_H001.dat
$ copy for018.dat for18_H001.dat
$ copy screen.dat fifa_H001.out
... repeat for all energies.
$ copy summary.dat summary_235.dat
```

A.1.2 Fusion-Fission simulations

A.1.2.1 Basic Simulations, in the absence of nuclear spin

Physics The simulation of a fusion-fission process is broken down according to the processes involved.

The initial stage is the formation of a compound nucleus via fusion. This is modelled using a coupled-channels calculation, as described in section 2.1.2.

The second stage is to model the decay of the compound nuclei, once formed. This involves determining the relative fission and particle evaporation probabilities, as described in Section 2.2.1, and we use a Monte Carlo calculation to obtain a distribution of excitation energies, angular momenta, number of evaporated particles, and whether or not the nucleus fissioned or survived, taking into account a variety of effects as described in Section 3.2.7.

The third stage is to model the fission fragment angular distribution. We start by taking the distribution of fissioning systems, and, for each energy and angular momentum, calculating the corresponding angular distribution. These components are then added up according to the weight of the initial state:

$$W(\theta) \propto \sum_{J'=0}^{\infty} \int_{K'_0} w'(J', K'_0) \sum_{K=-J'}^{J'} \frac{(2J'+1)|d^{J'}_{0,K'}(\theta)|^2 \exp(-K^2/2K_0'^2) dK'_0}{\sum_{K=-J'}^{J'} \exp(-K^2/2K_0'^2)} \tag{A.6}$$

Calling Patterns The flow-chart in Figure A.3 illustrates the logical flow of information between the different programs used.

The calls to SPTL, to calculate particle evaporation transmission coefficients, and MOMCALC, to calculate saddle-point effective moments of inertia, are done only once for a given reaction. Thus these programs are called by hand, and their output files saved with unique names.

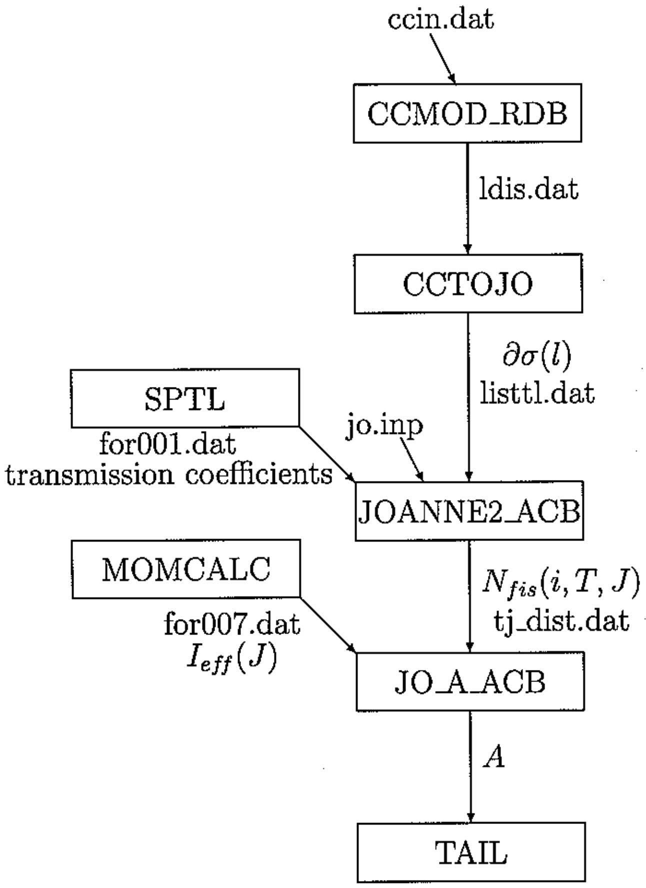

Figure A.3: Flow-chart for basic fusion-fission simulation.

The file of transmission coefficients is named in the input file for JOANNE; the file of $\mathcal{I}_{eff}$ is named in a VAX shell variable. The coupled-channels fusion calculation is performed with CCMOD_RDB. The decay of the compound nuclei is modelled by JOANNE2_ACB (or JO_SHELL, which requires a slightly different format for jo.inp but is otherwise functionally equivalent), and JO_A_ACB calculates the corresponding fission fragment angular distribution. All these calculations are performed in a single command-file.

Sample Command-File: JOANNE.COM

```
... initialize files
! 31P + 176Lu
! Running Joanne code as modified by ACB
! command file for series of E(cm)
!
$ del survive.dat;*
$ del sur_ex.dat;*
$ del fission.dat;*
$ del fis_ex.dat;*
$ del XNSUR.dat;*
$ del jo_a.out;*
$ del anisot.dat;*
$ del anisot00.dat;*
$ del anisot01.dat;*
$ del anisot02.dat;*
$ del anisot03.dat;*
$ del anisot04.dat;*
$ del anisot05.dat;*
$ del anisot06.dat;*
$ del anisot07.dat;*
$ del anisot08.dat;*
$ del anisot09.dat;*
$ del anisot10.dat;*
$ del ani_ex.dat;*
$ del ani00_ex.dat;*
$ del ani01_ex.dat;*
$ del ani02_ex.dat;*
$ del ani03_ex.dat;*
$ del ani04_ex.dat;*
$ del ani05_ex.dat;*
$ del ani06_ex.dat;*
$ del ani07_ex.dat;*
$ del ani08_ex.dat;*
$ del ani09_ex.dat;*
$ del ani10_ex.dat;*
$ DEF/LOG INPUT$FILE Plu.INP
$ SHOW LOGICAL INPUT$FILE
$ def/log datieff Rn207ieff.dat
```

```
!
! E(cm) = 114.783~MeV
!
$ run [fission.rdb103.progs]ccmod_rdb
ccin.dat
114.783 114.783 1.0
$ run [fission.rdb103.joanne]cctojo
ldis.dat
db2o_er114.ldis
$ DEF/LOG LDIS$FILE db2o_er114.ldis
$ RUN [FISSION.rdb103.PROGS.jomyd]JOANNE2_acb
114.783
$ RENAME/lo FOR001.DAT JO_plu_er114.OUT
$ RUN [fission.rdb103.progs.jomyd]JO_A_acb
114.783
!
! E(cm) = 116.920~MeV
... repeat for all desired energies.
Then sort resulting data for easy graphing.
$ r $USER2:[FISSION.ACB103.ALPHAPROG]tail
$ rename/lo survive.dat survive_plu.dat
$ rename ANISOT.DAT ANISOT_plu.dat
$ rename/lo sur_ex.dat jo_surv_plu.dat
$ rename ANI_ex.DAT jo_ANI_plu.dat
$ rename/lo XNSUR.dat xnsur_plu.dat
$ rename jo_a.out jo_a_plu.out
$ copy fission.dat fission_plu.dat
$ purge JO_CPB*.OUT
$ purge TJ_DIST.DAT
$ purge FOR007.DAT
$ purge TJ.DAT
$ EXIT
```

A.1.2.2 Fusion-fission calculations including nuclear spin

Physics The essence of the calculation with ground-state nuclear spin differs little from the calculation ignoring ground-state nuclear spin; but rather more information must be passed between the programs.

The main difference between the with-spin and without-spin calculations is the necessity for calculating a distribution $w(J, M)$, which is done by QMELANIE or MELANIE, from data generated during the coupled-channels calculations.

COLLETTE takes the distribution $N_{fis}(i, T, J, M)$ from JO_EVAP and calculates the fission fragment angular distribution according to:

$$W(\theta) \;\propto\; \sum_{J'=0}^{\infty} \sum_{M'=-J'}^{+J'} \sum_{i} \int_{K_0'} N_{fis}(i, T, J', M')$$

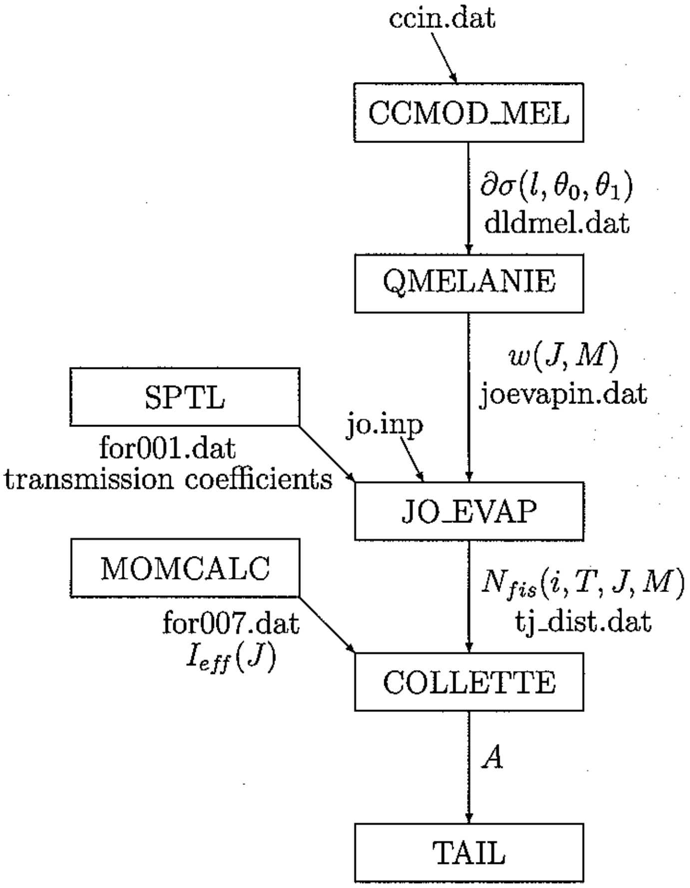

Figure A.4: Flow-chart for fusion-fission simulation including ground-state spin effects.

$$\times \sum_{K=-J'}^{J'} \frac{(2J'+1)|d^{J'}_{M',K'}(\theta)|^2 \exp(-K^2/2K_0'(T,J)^2)dK_0'}{\sum_{K=-J'}^{J'} \exp(-K^2/2K_0'(T,J)^2)} \tag{A.7}$$

where i denotes the number of evaporated neutrons.

Calling Patterns Because the programs are passing around more information, the programs for the ground-state spin calculations have different names, as shown in Figure A.4, although with the exception of QMELANIE they fulfil the same roles as the programs shown in Figure A.3. There are in fact multiple ways of performing fusion-fission calculations including ground-state spin, but we describe here the one that includes all the physical effects we were able to consider.

Sample Command-File: JO_EVAP.COM

```
    1    $ set default [fission.rdb103.joanne.31p176lu]
    2    ! 31P + 176Lu
    3    ! Running Joanne code as modified by ACB
    4    ! command file for series of E(cm)
    5    ! Uses Jo_evap!
    6    ! this command file does the initial CCMOD_mel call,
    7    ! followed by a call to MELANIE (m-distributions)
    8    ! before feeding all results for that energy to JOANNE.
    9    ! Final data is collated by COLLETTE.
   10    !
   11    $ copy [fission.rdb103.ccmod.31p176lu]ccin_paper.dat ccin.dat
   12    !
... (lines 13-42 of this file are identical to lines 5-34 of JOANNE.COM)
   43    $ DEF/LOG INPUT$FILE Plu_evap.INP
   44    !$ SHOW LOGICAL INPUT$FILE
   45    $ def/log datieff Rn207ieff.dat
   46    !
   47    ! E(cm) = 114.783~MeV
   48    !
   49    $ run [fission.rdb103.progs.joevap]ccmod_mel
   50    ccin.dat
   51    114.783 114.783 1.0
   52    $ run [fission.rdb103.progs.joevap]QMELANIE
   53    7.0 0.5
   54    dldmel.dat
   55    $ DEF/LOG LDIS$FILE joevapin.dat
   56    !$ SHOW LOGICAL LDIS$FILE
   57    $ copy joevapin.dat joevapin_qmel_p114.dat
   58    $ RUN [FISSION.rdb103.PROGS.joevap]JO_evap
   59    114.783
   60    $ RENAME/lo FOR001.DAT JOE_qlu_p114.OUT
   61    $ RUN [fission.rdb103.progs.joevap]COLLETTE
   62    114.783
```

```
... repeat for lots of energies ...
!
$ r $USER2:[FISSION.ACB103.ALPHAPROG]tail
$ rename survive.dat survive_qmel.dat
$ rename ANISOT.DAT ANISOT_qmel.dat
$ rename sur_ex.dat jo_surv_qmel.dat
$ rename ANI_ex.DAT jo_ANI_qmel.dat
$ rename XNSUR.dat xnsur_qmel.dat
$ rename jo_a.out jo_a_qmel.out
$ copy fission.dat fission_qmel.dat
$ purge/nolog TJ_DIST.DAT
$ purge/nolog FOR007.DAT
$ purge/nolog TJ.DAT
$ purge/nolog melcheckel.dat
$ purge/nolog pdws.dat
$ purge/nolog jkia.dat
$ purge/nolog joevapin.dat
$ purge/nolog dldmel.dat
$ EXIT
```

A.1.3 Quasi-Fission simulations

A.1.3.1 Simple Quasi-fission distribution

Physics The first stage of the calculation is to determine a "capture" cross-section, or distribution of partial cross-sections $\partial\sigma(l, \theta_0, \theta_1)$. This is done using a standard coupled-channels calculation, CCMOD_MEL, assuming that whenever a system passes inside the fusion barrier, capture occurs. (The assumption for reactions without quasi-fission is that whenever a system passes inside the fusion barrier, fusion occurs.)

The second stage is to decide what fraction of the partial cross-sections proceeds to fuse, and what part does not fuse properly and therefore undergoes quasi-fission. One of the DOM programs (Section A.4.1) calculates the probability of quasi-fission $Pr_{qfis}(l, \theta_0, \theta_1)$, getting the formatting from the output of CCMOD_MEL; PHILLIPA separates $\partial\sigma(l, \theta_0, \theta_1)$ into $\partial\sigma_{fis}(l, \theta_0, \theta_1)$ and $\partial\sigma_{qfis}(l, \theta_0, \theta_1)$ according to $Pr_{qfis}(l, \theta_0, \theta_1)$ from DOM.

At this point the simulation splits into two branches; one dealing with fusion, the other with quasi-fission. The goal is to generate fission-like fragment angular distributions for each branch, and then to combine them according to their relative cross-sections. The fusion-fission branch is processed as described in Section A.1.2.2.

The quasi-fission branch may be simulated via one of two methods. The conceptually simpler method is to generate a distribution $w(J, M)$, as with the fusion-fission branch, and then to assume that all nuclei quasi-fission with the same effective K_0, and generate the corresponding fragment angular distribution. This is the method illustrated in Figure A.5, using QMELANIE and MYDE_MELFED.

The second method is to assume that the quasi-fission fragment angular distribution depends on the same quantities that govern the probability of quasi-fission,

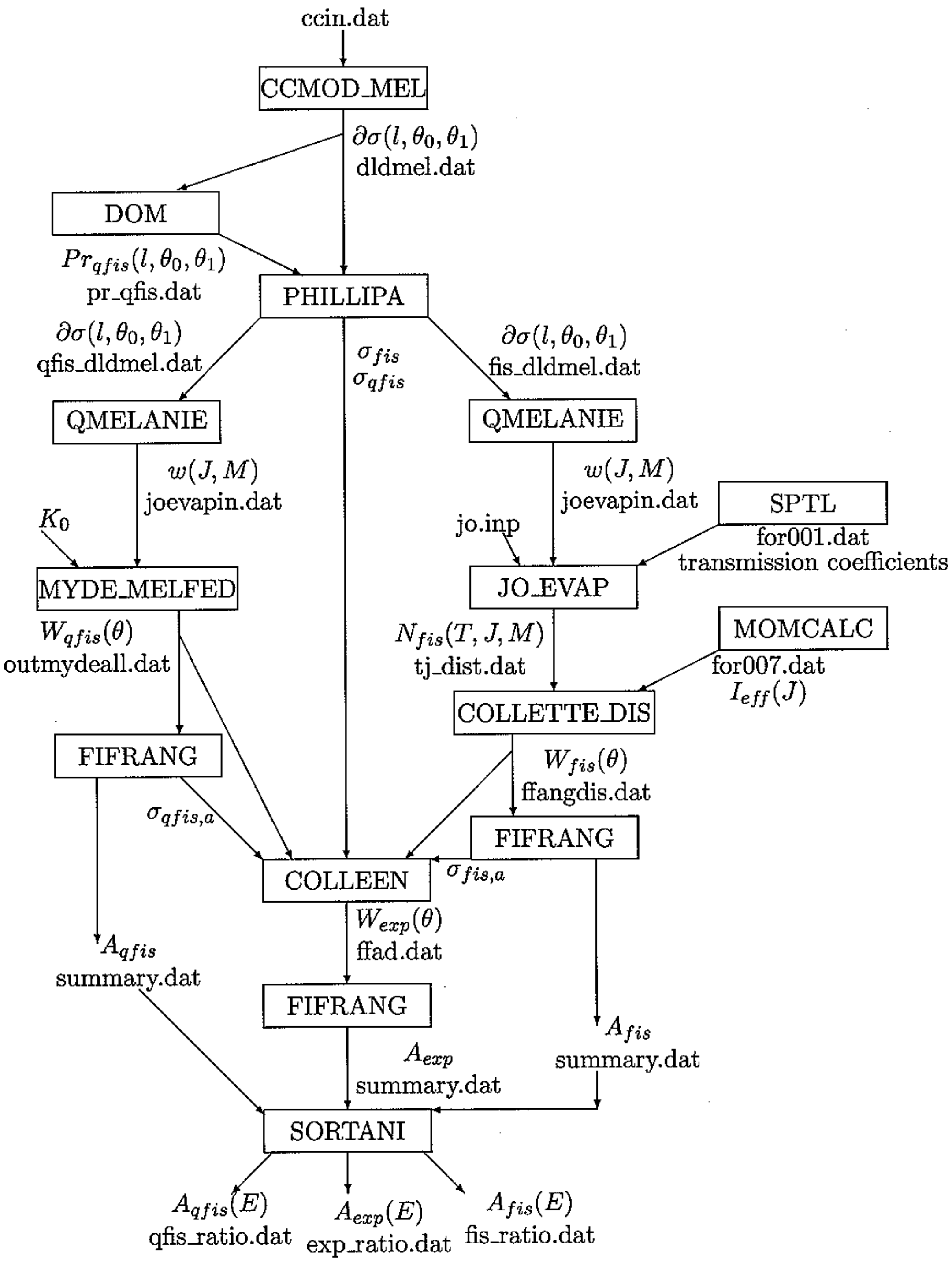

Figure A.5: Flow-chart for quasi-fission simulation including ground-state spin effects. The programs focussing on quasi-fission are on the left side of the diagram; on the right side a fusion-fission simulation proceeds much as in Figure A.4; in the center are shown the programs dealing with both fusion and quasi-fission. Note that several programs produce output files each used by more than one subsequent program. Note also that all instances of FIFRANG append their results to the same summary.dat file.

and therefore to generate fission-like fragment angular distributions for every possible set of quantum numbers (l, μ_0, μ_1, S, J) and small steps in classical quantities (θ_0, θ_1), and add all the distributions up with appropriate weightings. This is the approach taken by QMARY, which simply replaces the combination of QMELANIE and MYDE_MELFED.

The quasi-fission and fusion-fission fragment angular distributions are added in proportion to the initial cross-sections, yielding the pseudo-experimental distribution $W_{exp}(\theta)$. This is then fitted with FIFRANG to give the pseudo-experimental anisotropy A_{exp}.

SORTANI simply sorts out all the anisotropies for the fission, quasi-fission, and pseudo-experimental fragment angular distributions, using a supplied list of beam energies to generate several files ready for plotting with MULTIFIG.

Calling Patterns QMARY in particular can be extremely slow to run. For this reason, it is advisable that the command-files used be run in batch mode. Command-files may be run at low priority using commands like:

```
$ set process/priority=1
$ @GIRLSIM
```

However, low priority is most useful for jobs taking about an hour of computer time. For jobs taking several hours or days, batch mode is invoked using:

```
$ submit/queue=NUCZ03$BATCH/log=girlsim_238u.dat GIRLSIM.COM
```

There are a few things worth noting about batch mode.

- You can log out of the system altogether, and the batch file will keep running perfectly happily. You can check its status using:

  ```
  $ show queue NUCZ03$BATCH
  ```

  from any terminal.

- Batch mode actually makes slightly more efficient use of the CPU than a low-priority command file, while being more certain not to slow down other users of the machine.

- Invoking a batch file is a bit like starting a new terminal; importantly, the default directory goes back to your home directory, so that's where the log file is written, and you need to start your command-file with a command specifying the directory where all the working data files go, as per line 1 of the example below.

If the batch queue status is "stopped", first try:

```
$ set host 0
username: startq
```

but if that fails, the local IT administration may need to be involved.

Sample Command-File: GIRLSIM.COM

```
    1   $ set def [fission.rdb103.joanne.16o235u.altcalc]
    2   $ copy blank.dat summary.dat
    3   ! JOANNE initialisation
    4   !
... (lines 5-34 of this file are identical to lines 5-34 of JOANNE.COM)
   35
   36   $ DEF/LOG INPUT$FILE ou_evap.INP
   37   !$ SHOW LOGICAL INPUT$FILE
   38   $ def/log datieff fm253ieff.dat
   39
   40
   41   ! Functional Unit
   42   !
   43   ! E(cm) = 73.00~MeV
   44   !
   45   $ run [fission.rdb103.progs.joevap]ccmod_mel
   46   ccin.dat
   47   73.00 73.00 1.0
   48   $ run [fission.rdb103.progs.quasifission]tdom
   49   30
   50   15
   51   dldmel.dat
   52   $ run [fission.rdb103.progs.quasifission]phillipa
   53   dldmel.dat
   54   pr_qfis.dat
   55   ! quasi-fission stream
   56   $ run [fission.rdb103.progs.joevap]QMELANIE
   57   3.5 0.0
   58   qfis_dldmel.dat
   59   $ run [fission.rdb103.progs.quasifission]myde_melfed
   60   joevapin.dat
   61   5.0
   62   $ run [fission.rdb103.joanne]cctojo
   63   melcheckel.dat
   64   listtl.dat
   65   $ DEF/LOG FILE$NAME outmydeall.dat
   66   $ run [fission.rdb103.progs.fifrang]fifrang
   67   100 -42 -1 7 2
   68   $ copy for018.dat for18_qfis73.dat
   69   $ copy for028.dat qfis_sig.dat
   70   $ copy screen.dat ffa_qfis73.dat
   71   ! fusion-fission stream
   72   $ run [fission.rdb103.progs.joevap]QMELANIE
   73   3.5 0.0
   74   fis_dldmel.dat
   75   $ DEF/LOG LDIS$FILE joevapin.dat
```

```
$ copy joevapin.dat joevapin_er73.dat
$ RUN [FISSION.rdb103.PROGS.joevap]JO_evap
73.00
$ RENAME/lo FOR001.DAT JOE_sihf_er73.OUT
$ RUN [fission.rdb103.progs.joevap]COLLETTE_DIS
73.00
$ run [fission.rdb103.joanne]cctojo
melcheckel.dat
listtl.dat
$ DEF/LOG FILE$NAME ffangdis.dat
$ run [fission.rdb103.progs.fifrang]fifrang
100 -42 -1 7 2
$ copy for018.dat for18_fis73.dat
$ copy for028.dat fis_sig.dat
$ copy screen.dat ffa_fis73.dat
! merge streams
$ run [fission.rdb103.progs.quasifission]colleen
ffangdis.dat
outmydeall.dat

! we need an l-distribution for the whole lot;
! using melanie is overkill but anyway
$ run [fission.rdb103.progs.joevap]QMELANIE
3.5 0.0
dldmel.dat
$ run [fission.rdb103.joanne]cctojo
melcheckel.dat
listtl.dat
$ DEF/LOG FILE$NAME ffad.dat
$ run [fission.rdb103.progs.fifrang]fifrang
100 -42 -1 7 2
$ copy for018.dat for18_exp73.dat
$ copy screen.dat ffa_exp73.dat

! Functional Unit
!
! E(cm) = 75.00~MeV
... repeat for lots of energies ...
! Summarize data ...
!
$ run [fission.rdb103.progs.quasifission]sortani
summary.dat
elist.dat
$ purge
```

A.2 Data Analysis Programs

A.2.1 ALABN

Authorship Clyde Morton

Purpose Calculating detector calibration coefficients $A_{lab}(\theta)$ from Rutherford scattering measurements.

Variants ALABN2—different input and output file names.

References [MOR95B], section 3.2.3.

Language Fortran.

Size 114 lines

Standard input files inelastic.dat, bins.list

Standard output files alabf.dat, alabout.dat

A.2.1.1 Physics

ALABN calibrates the detector by determining, from a calibration run measuring Rutherford scattering, a calibration coefficient $A(\theta_{det})$ for each detector bin at an angle θ_{det} [MOR95B]:

$$A(\theta_{det}) = \left(\frac{\sin(\theta_{det})\Delta\phi}{2\pi}\right) \frac{N_{mon}\frac{d\sigma_R(\theta_{det})}{d\Omega}}{N_{det}\frac{d\sigma_R(\theta_{mon})}{d\Omega}} \tag{A.8}$$

For the purposes of easy handling, ALABN outputs $A(\theta) \times 10^6$, which was within 10% of 1000 for most of the constant ϕ-cut calculations in this thesis.

A.2.1.2 Calling patterns

The file inelastic.dat is prepared with the following data about the Rutherford scattering measurement:

- The beam energy E_{beam}, proton number Z_1 and nucleon number A_1 of the projectile, Z_0 and A_0 of the target nucleus;
- The angle θ_{mon} at which the monitor detectors are placed;
- The run in which the data is recorded (not used);
- The total pulser counts, and the number of pulser counts left after the same constraints are imposed on the pulser as on the elastic scattering events;
- The number of events detected in the monitor detectors. This may be either the average (as used throughout this thesis) or the sum for the two detectors, so long as the convention used is consistent between the calibration calculation here and the cross-section calculation later;

- A list of the average angles θ at which detector bins are centered. ALABN is hard-coded to expect 15 angles.

The file bins.list should contain a list of counts $N(\theta)$ of observed elastically scattered particles for each detector bin. $\Delta\phi$ is hard-coded into both ALABN and BINS.

ALABN is typically called once for a three-day experiment. It is called manually, and the important results are copied manually from alabf.dat to "xinput" files, where one xinput file describes one run (at a particular beam energy, projectile, target, etc). (There is room for increased automation of xinput file generation.)

A.2.2 CALVINER

Authorship Rachel Butt

Purpose Calculating variations to detector efficiency coefficients $A_{lab}(\theta)$ due to loss of coincident particles on detector support structure.

Variants CALVIN - inverse physics; where CALVINER takes a particle in the back detector and finds out where its partner hits the front detector, CALVIN takes the particle in the front detector and locates the backward-travelling particle.

Language Fortran.

Size 315 lines.

Standard input files command line or command file only.

Standard output files back_detector.dat, bd_coarse.dat, cphi_blocked.dat, cphi_flat.dat, vphi_blocked.dat, vphi_flat.dat, xback_counts.dat

A.2.2.1 Physics

CALVINER compensates for the presence of support wires in front of the front detector, as these have a position-dependent impact on the sensitivity of the back detector.

CALVINER operates in a roughly Monte Carlo fashion; for each 1 mm × 1 mm square in the back detector, it works out the corresponding lab angles θ_b and ϕ_b according to:

$$\cos(\theta_b) = \frac{z_b + x_b}{\sqrt{2(x_b^2 + y_b^2 + z_b^2)}} \tag{A.9}$$

$$\cos(\phi_b) = \frac{z_b - x_b}{\sqrt{2y_b^2 + (z_b - x_b)^2}} \tag{A.10}$$

where x_b and y_b are the coordinates in the plane of the detector, and z, the distance from the target to the detector, is reliably 180 mm. Then, for that θ_b and ϕ_b, the trajectories of 100 events are traced.

For each trajectory, a mass-split $\mathcal{A}$ is randomly assigned, using a gaussian distribution with width matching the experimental mass distribution, truncated for

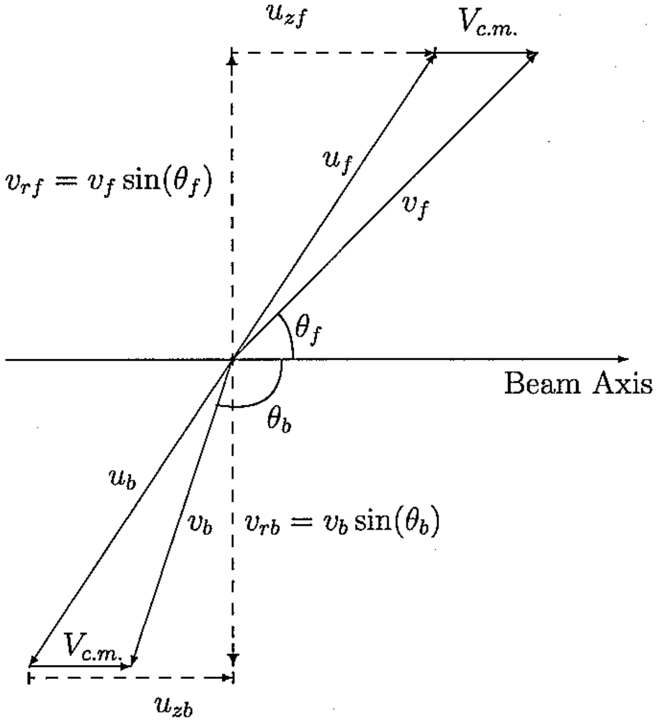

Figure A.6: Sketches of the fission fragment velocities in the plane including the beam axis and the fragment velocities.

mass splits equal to or more extreme than the initial target-projectile mass split. The total energy E_K divided between the fissioning fragments is determined from Viola systematics [VIO85]:

$$E_K = 0.1166\frac{(Z_0 + Z_1)^2}{(A_0 + A_1)^{1/3}} + 9.0 \text{ MeV} \tag{A.11}$$

and divided between the fission fragments according to their mass, to obtain the magnitude of the velocity (in the centre of mass frame) of the fragment detected in the back detector:

$$|u_b| = \sqrt{\frac{2E_K(1-\mathcal{A})}{\mathcal{A}(A_0 + A_1)}} \tag{A.12}$$

The angles θ_b and ϕ_b are appropriate to the lab frame. We know the centre of mass velocity:

$$V_{c.m.} = \sqrt{\frac{2E_{beam}A_1}{A_0 + A_1}} \tag{A.13}$$

Therefore, using the geometry illustrated in Figure A.6, we can determine the centre of mass velocities:

$$u_{zb} = V_{c.m.}\left(\sin^2(\theta_b) + \cos(\theta_b)\sqrt{(\frac{u_b^2}{V_{c.m.}^2 - \sin^2(\theta_b)})}\right) \tag{A.14}$$

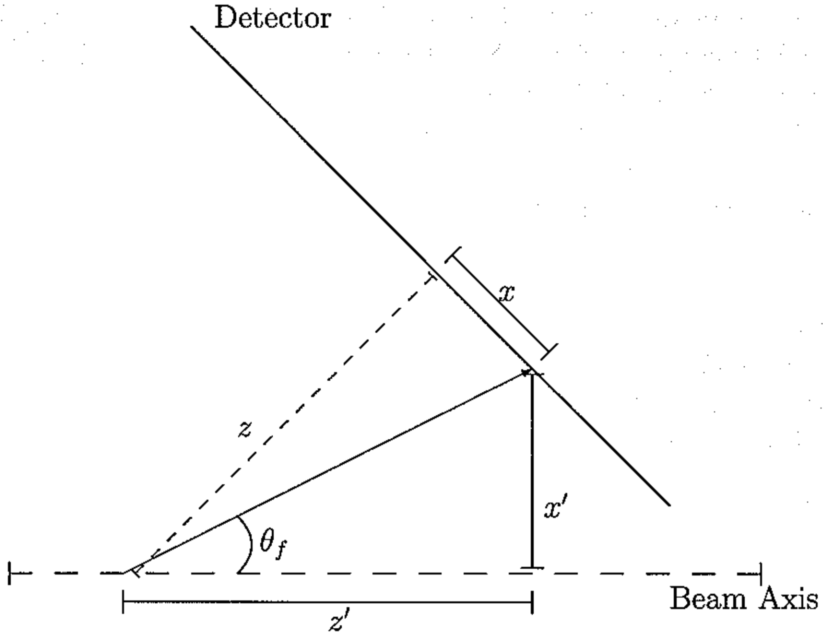

Figure A.7: The vector along which a particle approaches the front detector. The y axis is out of the plane of the page. The x axis is in the plane of the detector, z axis orthogonal to that plane, whereas the x' and z' axes are defined relative to the beam direction (the y' axis is the same as the y axis).

$$u_{rb} = (u_z b - V_{c.m.})\tan(\theta_b) \tag{A.15}$$

The velocities for the forward-moving particle are related to those of the backward-moving particle according to $\vec{v_f} = \frac{-\mathcal{A}}{1-\mathcal{A}}\vec{v_b}$. The effects of particle evaporation could be included at this stage, but have been assumed to be negligible.

It is then necessary to reverse the calculation to obtain the position at which the forward-moving particle would intersect the plane of the front detector. Like the back detector, the front detector is 180 mm from the target, at an angle of $-45°$ with the beam direction (whereas the back detector distance is shortest at an angle of $+135°$).

In the absence of particle evaporation, $\phi_f = \phi_b$. $\theta_f = \tan^{-1}(\frac{u_{rf}}{u_{zf}+V_{c.m.}})$. Then, using the coordinate system illustrated in Figure A.7, $\tan(\phi_f) = y/x'$ and $tan(\theta_f) = r/z'$ where $r = x'^2 + y^2$, so we deduce for the desired x:

$$x = z\left(\frac{1-\tan(\theta_f)\cos(\phi_f)}{1+\tan(\theta_f)\cos(\phi_f)}\right) \tag{A.16}$$

where z is known to be 180 mm and $y = \sqrt{1/2}(z-x)\tan(\phi_f)$.

From here, CALVINER determines (a) whether or not the forward fission fragment hits the forward fission detector, (b) if it hits the detector, whether or not it hits one of the support wires. From the counts $N(\theta_b)$ coming from within a particular range of θ_b that did hit the front detector and the subset $B(\theta)$ that hit a blocking wire, it constructs the calibration coefficient correction $N(\theta)/(N(\theta) - B(\theta))$; this is written out to vphi_blocked.dat. A similar calculation is performed with a constant cut on ϕ_b, written to cphi_blocked.dat.

CALVINER could be adapted to calculate the fall-off of efficiency in one detector due to the fact that the forward and backward detectors are not perfectly opposite one another in the *centre of mass* frame, which means that when a fission fragment is detected at the edge of one detector, its partner might miss the other detector. However, this has not currently been attempted, and the affected angles are simply discarded during later data analysis.

A.2.2.2 Calling patterns

Input is usually from command file. CALVINER prompts for the proton number Z_1 and nucleon number A_1 of the projectile, Z_0 and A_0 of the target nucleus; then the beam energy E_{beam}, and finally the Gaussian width of the fragment mass distribution. The positions and thicknesses of the detector obstructions are currently hard-coded into CALVINER.

CALVINER's output goes into several files; usually the only one of importance is cphi_blocked.dat, although vphi_blocked.dat should be substituted if no ϕ-cut has been used for experimental data. This output file is used by HOBBES in combination with the standard calibration coefficients from ALABN.

A.2.3 HOBBES

Authorship Rachel Butt

Purpose Assembles "xinput" files for coincidence analyses, using data from CALVINER and ALABN, among other data.

Language Fortran.

Size 82 lines.

Standard input files command line or command file, copies of cphi_blocked.dat and alabf.dat (edited).

Standard output files xinput_nnn.dat

A.2.3.1 Calling patterns

HOBBES assembles the xinput files for coincidence analyses for later processing. It is intended to be run once for a given reaction, assembling multiple xinput files for multiple beam energies. It can in theory be operated from the command line,

however it is intended to be run from command file, where the input numbers are saved for later verification and easy correction.
An example call to HOBBES is shown in Section A.1.1.2. Initially HOBBES prompts for elastic scattering calibration data:

- The proton number Z_1 and nucleon number A_1 of the projectile, Z_0 and A_0 of the target nucleus;
- The beam energy E_{beam}, and the angle θ_{mon} at which the monitor detectors are placed;
- The file in which the back-detector calibration coefficients are recorded (edited output of ALABN);
- A uniform scaler to compensate for losses such as ions directly striking x-position wires (2% loss to this effect means the scaler input is 1.02).

Then the reaction under study should be described: the proton number Z_1 and nucleon number A_1 of the projectile, Z_0 and A_0 of the target nucleus; and a five letter keyword identifying the run (used only in comment line in xinput files).

Then each individual energy should be described, in repeating blocks, terminating with a negative energy, as follows:

- The beam energy at which the experiment is performed.
- A three character run identifier, usually the same run number as the event-by-event data is stored under.
- The monitor counts, calculated in the same fashion as used for ALABN, and the total pulser counts, and the number of pulser counts left after the same data analysis constraints are imposed on the pulser as on the elastic scattering events;
- The name (and location, if another directory) of the file in which the CALVINER corrections for this reaction at this energy are stored.

HOBBES is hard-coded for fifteen angles, like ALABN, and CALVINER which preceed it, and BIN and CROSS which follow it. HOBBES does not currently verify that the angles at which CALVINER data is calculated match the angles at which ALABN coefficients are supplied.

A.2.4 BIN

Authorship Clyde Morton

Purpose Combine xinput and bins data in a nice format for input to CROSS_F or CROSS_FIF

Language Fortran.

Size 50 lines.

Standard input files xinput.dat, bins.list

Standard output files crossf_in.dat

A.2.4.1 Calling patterns

The file xinput.dat is prepared with the following data:
For the Rutherford scattering calibration measurement:

- The beam energy E_{beam}, proton number Z_1 and nucleon number A_1 of the projectile, Z_0 and A_0 of the target nucleus;
- The angle θ_{mon} at which the monitor detectors are placed (assumed to be the same for the experimental run, later);

For the experimental run of interest:

- The run in which the data is recorded (not used);
- The proton number Z_1 and nucleon number A_1 of the projectile, Z_0 and A_0 of the target nucleus;
- The energy of the projectiles in the lab frame (in MeV);
- The total pulser counts, and the number of pulser counts left after the same constraints are imposed on the pulser as on the elastic scattering events;
- The number of events detected in the monitor detectors. This may be either the average (as used throughout this thesis) or the sum for the two detectors, so long as the convention used is consistent between the cross-section calculation here and the calibration calculation earlier;
- A list of the average angles θ at which detector bins are centered, together with the coefficients $A(\theta)$ (and errors $\Delta A(\theta)$) calculated for those angles (usually using ALABN). Any "pointcode" on these lines will be ignored.

The file Bins.list should contain a list of counts $N_{det}(\theta)$ of observed fission fragments for each detector bin.

A.2.5 CROSS

Program Name CROSS_FIF

Authorship Clyde Morton

Purpose Calculate differential cross-sections $\frac{d\sigma(\theta)}{d\Omega}$ from fission data.

Modifications Code carrying out a cubic-spline fit to the data was removed from CROSS_F by Rachel Butt to generate CROSS_FIF, as the cubic-spline fits were no longer used, and interfered with recompilation of the code on different platforms by referring to libraries not available on all platforms.

Language Fortran.

Size 153 lines.

Standard input files crossf_in.dat

Standard output files for007.dat, for004.dat, out.dat

A.2.5.1 Physics

The energy and nucleon numbers for the elastic scattering calibration measurement are included in the input for this program for purely historical reasons; they are not used by the program.

The differential cross-sections are calculated according to:

$$\frac{d\sigma(\theta)}{d\Omega} = \frac{2\pi A(\theta)}{\Delta\phi \sin(\theta)} \frac{N_{det}(\theta)\frac{d\sigma_R(\theta_{mon})}{d\Omega}}{N_{mon}} \tag{A.17}$$

CROSS_FIF outputs $\frac{d\sigma(\theta)}{d\Omega}$ as calculated in the lab frame (for004.dat), and the centre of mass frame (for007.dat). (The file out.dat tabulates various different quantities and errors therein, but is not used in routine analysis.)

A.2.5.2 Calling patterns

CROSS_FIF is invariably called immediately after BIN, with the output of BIN as the sole required input. BIN and CROSS_FIF could be replaced with a single program, since BIN contributes little of particular use. This has not been done, simply because the existing methods work, and—given the available command-files—do not take noticeably more or less time than a single program would.

A.2.6 BINCROSS

Authorship Rachel Butt

Purpose Calculates differential cross-sections $\frac{d\sigma(\theta)}{d\Omega}$ from fission data for two different measurements, separating contributions from different isotopes present in different proportions in the different measurements.

Language Fortran.

Size 466 lines.

Standard input files bcin.dat, two xinput.dat files, two bins.list files.

Standard output files summary.dat, cross_fif.out, cross_fif2.dat

A.2.6.1 Physics

The initial phase of BINCROSS calculations involves disentangling the contributions of two different isotopes. We assume a "main" run, with specified percentages of each isotope, and an "other" run, with significantly different isotope percentages. (It is also assumed that the main run has a higher percentage of isotope 1 than the other run.) In order to make the runs comparable, we have to (a) correct both sets of counts for dead-time, (b) correct for beam "exposure" (via monitor counts; $X = N_{mon}/\frac{d\sigma_R(\theta_{mon})}{d\Omega}$), and (c) correct for differences in calibration coefficients $A(\theta)$. We work in the lab frame because the centre of mass frame differs for the two isotopes.

The separation of contributions from isotope 1 and 2 then involves solving two simultaneous equations:

$$\frac{d\sigma}{d\Omega}_{main,meas} = \%_{main,1}\frac{d\sigma}{d\Omega}_1 + \%_{main,2}\frac{d\sigma}{d\Omega}_2 \tag{A.18}$$

$$\frac{d\sigma}{d\Omega}_{other,meas} = \%_{other,1}\frac{d\sigma}{d\Omega}_1 + \%_{other,2}\frac{d\sigma}{d\Omega}_2 \tag{A.19}$$

In practice we assume $\%_{main,1} + \%_{main,2} = 1$ and $\%_{other,1} + \%_{other,2} = 1$, and the separation is implemented by constructing an angle-dependent correction factor $C(\theta)$:

$$C(\theta) = \frac{N_{mon,main}\frac{d\sigma_{R,mon,other}}{d\Omega}A_{other}(\theta)\%_{main,2}}{N_{mon,other}\frac{d\sigma_{R,mon,main}}{d\Omega}A_{main}(\theta)\%_{other,2}} \tag{A.20}$$

to give separated fission counts (after the dead-time corrections have been applied):

$$N_{fis,1}(\theta) = N_{fis,main}(\theta) - N_{fis,other}(\theta)C(\theta) \tag{A.21}$$

and increased statistical uncertainties in the fission counts $N_{fis,1}(\theta)$ (this quantity is calculated *prior* to dead-time corrections, although this usually makes less than 2% difference):

$$\frac{\Delta N_{fis,1}(\theta)}{N_{fis,1}(\theta)} = \sqrt{\frac{1}{N_{fis,main}(\theta)} + \frac{C(\theta)}{N_{fis,other}(\theta)}} \tag{A.22}$$

Monitor counts must be corrected to match:

$$N_{mon,1} = N_{mon,main}\frac{(\%_{main,1} - \%_{other,1})\%_{main,2}}{\%_{other,2}} \tag{A.23}$$

BINCROSS then proceeds to calculate the differential fission cross-sections in the centre of mass frame according to:

$$\frac{d\sigma(\theta)}{d\Omega} = \frac{2\pi A(\theta)}{\Delta\phi\sin(\theta)}\frac{N_{fis,1}(\theta)\frac{d\sigma_R(\theta_{mon})}{d\Omega}}{N_{mon,corr}} \tag{A.24}$$

and writes these results to cross_fif.out.

A.2.6.2 Calling patterns

BINCROSS initially reads in data from bcin.dat as follows:

- The percentages of the two isotopes in the first experimental run;
- The xinput file name and location for the first experimental run;
- The bins.list data file name and location for the first experimental run;
- The same data for the second experimental run.

BINCROSS then opens the four specified data files, which have formats as described in Section A.2.4.1. BINCROSS will write the deconvoluted differential fission cross-sections to cross_fif.out (for isotope 1) and cross_fif2.out (for isotope 2).

A.2.7 FIFRANG

Program Name FIFRANG

Authorship David Hinde, Rachel Butt

Purpose To fit fission fragment angular distributions $\frac{d\sigma(\theta)}{d\Omega}$, yielding (among other things) the fission fragment anisotropy and the total fission cross-section.

Modifications The original program (FIFANG) has been commented, partitioned into re-usable library functions, and made markedly more robust, by Rachel Butt.

Variants FIFRANK, FIFRANGMYD, FIFRANG_MELFED.

References [BAC85]

Language Fortran.

Size 241 lines.

Standard input files `file$name`, listtl.dat

Standard output files for018.dat, screen.dat, residuals.dat, summary.dat, for028.dat

A.2.7.1 Physics

FIFRANG fits experimental fission fragment angular distributions by calculating angular distribution curves using a lookup table from [BAC85] for three evenly spaced values of K_0. These curves are normalised to the same cross-section as the experimental data. The χ^2 measure of fit quality is evaluated for each K_0 in turn. FIFRANG then fits a parabola to that to estimate the K_0 corresponding to the best possible fit, and repeats the process with a smaller K_0 spacing centred on the new K_0.

This algorithm, which is used in the original FIFANG and all its variants, has an important limitation which arises simply because the program is searching for a

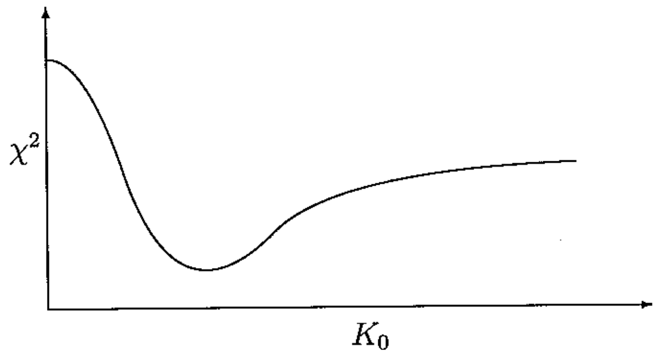

Figure A.8: Shape of χ^2 curve; schematic. If FIFANG relies on the assumption that χ^2 is parabolic with respect to K_0, and K_0 is in the wrong region, the algorithm will fail. We exploit the fact that the χ^2 curve has only one minimum to help us center K_0 in the right region.

parabolic minimum on a function which has widely varying curvature, as illustrated in Figure A.8. If the starting K_0 values are too far from the true minimum, FIFANG may get lost, or simply crash. The algorithm works properly so long as its fitted parabola has both positive curvature and a minimum in the range spanned by the three starting K_0 values. The "robust" codes described here all detect the failure of either of these conditions, stop, and evaluate χ^2 at ten different K_0 spaced over a wider range, repeating as required. They resume when they have found a set of K_0 values spanning the only minimum in the χ^2 function. (The codes will still fail if all three K_0 values are equal. This can occur when attempting to fit oddly shaped theoretically generated curves with very small stated errors; i.e. when the total χ^2 is extreme.)

FIFRANK differs from FIFRANG solely in its handling of errors. FIFRANK prompts for a parameter ϕ_d, describing the "over-dispersion" or degree to which the statistical errors supplied for the data are inaccurate. The errors in anisotropy and K_0 are increased by approximately $\sqrt{\phi_d}$. This approach was developed in consultation with John Maindonald of the ANU Statistical Consulting Unit, and relevant theory is described in Ref. [MCC89].

Fitting experimental distributions using data from the lookup table in WFIS.DAT is fast and practical. However, there are occasions where it is worthwhile going to a more demanding calculation. The lookup data is only available in 5° steps, and linear interpolation must be performed to estimate the theoretical distribution at the angles for which data is available. Moreover, the lookup data is appropriate for M=0 reactions, and becomes less accurate when target and projectile nuclei possess non-zero intrinsic spin in their ground states. The lookup data also loses quality at very high anisotropies. It is therefore sometimes appropriate to calculate fission fragment angular distributions from scratch at precisely the desired angles. FIFRANGMYD and FIFRANG_MELFED perform this calculation in different ways.

FIFRANGMYD's calculation of fission fragment angular distributions is precisely as described in Section 3.2.3, Equation 3.4:

$$\begin{aligned} W(\theta) \; &\propto \; \sum_{J=0}^{\infty} \sum_{M=-(I_0+I_1)}^{+I_0+I_1} \left\{ \sum_{l=0}^{\infty} \sum_{S=|I_0-I_1|}^{I_0+I_1} \sum_{\mu_0=-I_0}^{+I_0} \frac{\partial\sigma(M)(2l+1)T_l|C^{S,l,J}_{M,0,M}|^2|C^{I_0,I_1,S}_{\mu_0,M-\mu_0,M}|^2}{\sum_{l=0}^{\infty}(2l+1)T_l\sum_{M=-(I_0+I_1)}^{+I_0+I_1}\partial\sigma(M)} \right\} \\ &\times \left[\sum_{K=-J}^{J} \frac{(2J+1)|d^J_{M,K}(\theta)|^2\exp(-K^2/2K_0^2)}{\sum_{K=-J}^{J}\exp(-K^2/2K_0^2)} \right] \end{aligned} \tag{A.25}$$

where I_0 is the spin of the target nucleus, and μ_0 its projection upon a space-fixed axis (in experiments, the beam axis). The channel spin S is the vector sum of I_0 and I_1, where I_1 is the spin of the projectile nucleus. The orbital angular momentum l, together with S, determines $\vec{J}=\vec{l}+\vec{S}$, the total angular momentum of the fissioning nucleus. M is the projection of J onto the space-fixed axis. K_0^2 characterizes the width of the distribution of K, the projection of J on the nuclear elongation axis, and is given by [HAL58]:

$$K_0^2 = T\mathcal{I}_{eff}/\hbar^2 \tag{A.26}$$

where T is the nuclear temperature and $\mathcal{I}_{eff}$ is the effective moment of inertia at the saddle-point.

$C^{S,l,J}_{M,0,M}$ and $C^{I_0,I_1,S}_{\mu_0,M-\mu_0,M}$ are Clebsch-Gordan coefficients. T_l is the fusion transmission coefficient for a given orbital angular momentum l. The function $d^J_{M,K}(\theta)$ is the well known d-function [VAN73, ROS61]:

$$\begin{aligned} d^J_{M,K}(\theta) \; &= \; \{(J+M)!(J-M)!(J+K)!(J-K)!\}^{1/2} \\ &\times \sum_X \frac{(-1)^X[\sin(\theta/2)]^{K-M+2X}[\cos(\theta/2)]^{2J-K+M-2X}}{(J-K-X)!(J+M-X)!(X+K-M)!X!} \end{aligned} \tag{A.27}$$

where the summation is performed over all integer values of X where all factorial arguments are non-negative.

The quantity in curly brackets in Equation A.25 is $w(J,M)$, the weighting for each possible fission channel (J,M). The quantity in square brackets in Equation A.25 specifies the fission fragment angular distribution $\rho(J,M,\theta)$ for a given channel (J,M).

The M-distribution $\partial\sigma(M)$ may be calculated semi-classically using CCTOMDIS.

FIFRANG_MELFED calculates fission fragment angular distributions using a correlated distribution $w(J,M)$:

$$W(\theta) \; \propto \; \sum_{J=0}^{\infty} \sum_{M=-(I_0+I_1)}^{+I_0+I_1} w(J,M) \times \left[\sum_{K=-J}^{J} \frac{(2J+1)|d^J_{M,K}(\theta)|^2\exp(-K^2/2K_0^2)}{\sum_{K=-J}^{J}\exp(-K^2/2K_0^2)} \right] \tag{A.28}$$

This correlated distribution $w(J,M)$ may be calculated semi-classically, as in Section 3.2.4 (using MELANIE), or quantum-mechanically, as in Section 3.2.5 (using QMELANIE).

A.2.7.2 Calling patterns

FIFRANG prompts for a list of parameters, from the command line:

- The energy of the projectile (which is ignored, as it is only there for historical reasons),
- the plotting point-code it should pass to MULTIFIG,
- the average angular momentum l it should calculate the angular distributions with,
- the initial value for the curve-characterising parameter K_0, and
- the initial step ΔK_0.

If a negative value is specified for the angular momentum l, FIFRANG will look in the file listtl.dat for an angular momentum distribution, specified by a list of partial cross-sections, one for each l, one number per line, terminated with a zero.

FIFRANG looks for the differential cross-sections in the file specified by the VAX shell variable `file$name`. It expects these to be specified by angle, differential cross-section, error, point-code (a real number specifying the size and shape of the dot with which the program MULTIFIG would plot the datapoint ... FIFRANG ignores the value, but it expects a value to be present).

The variant FIFRANGMYD will request the intrinsic ground-state spins for the target and projectile nuclei, at the command-line (or in the command-file). It will expect to find M-distribution information in MDIST.DAT; this may be generated using the combination of CCMOD_RDB and CCTOMDIS, or manually under some circumstances.

The variant FIFRANG_MELFED will prompt for the name of a data-file containing the distribution $w(J, M)$, headed by the maximum range of spins $(I_0 + I_1)$. This file is usually generated using MELANIE or QMELANIE.

FIFRANGMYD and FIFRANG_MELFED are not exhaustively tested and may not be fully integrated in the generalized fashion that FIFRANG now enjoys. They are also markedly slower to actually run.

FIFRANG (but not, currently, any other variant) writes the fitted cross-section σ to for028.dat. This is used by COLLEEN.

A.2.8 EXTRACTANI

Program Name EXTRACTANI

Authorship Rachel Butt

Purpose To pull cross-section and anisotropy data from summary files as written by FIFRANG during command file operation, and format the data for easy graphing with MULTIFIG.

Variants EXTRACTCONVANI—extracts and separates similar data from summary files produced during isotope disentanglement calculations (using BINCROSS). SORTANI—extracts and separates similar data produced during quasi-fission simulations.

Language Fortran.

Size 103 lines.

Standard input files summary.dat, elist.dat

Standard output files sigmacm.dat, ratiocm.dat, sigma.dat, ratio.dat, Esigma.dat, chisqppt.dat

A.2.8.1 Calling patterns

EXTRACTANI prompts for the name of the summary.dat file where the FIFRANG output is, and the name of the file listing the beam energies corresponding to the reactions fitted by FIFRANG. (Note that different versions of FIFRANG may require different FORMAT statements within EXTRACTANI.) It then prompts for the masses of the projectile and target nuclei respectively.

EXTRACTANI writes out, in MULTIFIG format, the anisotropies and cross-sections as functions of beam energy or centre of mass energy. It also lists the χ^2, for averaging to determine the input ϕ_d for FIFRANK, and makes a file of $E\sigma$ vs. E.

EXTRACTCONVANI differs from EXTRACTANI in that it interprets the summary files produced by BINCROSS-based calculations, where alternating lines come from different isotopes at the same energy, and EXTRACTCONVANI writes out sigma1.dat and sigma2.dat, etc.

SORTANI interprets the summary files produced by GIRLSIM calculations, separating the simulated fission, quasi-fission, and experimental anisotropies into three different files, ready for graphing.

A.3 Fusion-Fission Simulation Programs

A.3.1 CCMOD

Authorship Carlos Dasso, substantially rewritten by Mahananda Dasgupta

Purpose Coupled-channels calculations of fusion cross-sections, barrier distributions, and angular momentum distributions.

Variants CCMOD_RDB, CCMOD_MEL, CCMOD_CHI

References Section 2.1.2.2, [DAS97]

Language Fortran.

Size 788 lines.

Standard input files ccin.dat

Standard output files ccotm.dat, ldis.dat, xsecplot.dat, deriv.dat, pacein.dat

A.3.1.1 Physics

The physics behind CCMOD is described in Section 2.1.2, with CCMOD specifics given in section 2.1.2.2.

A.3.1.2 Calling patterns

CCMOD is modified from the original CCDEF by Mahananda Dasgupta.
Ref. [DAS97] provides an explanation of its number-by-number input and output.
For fission purposes, CCMOD is often used as follows:

- Look up nuclear deformations. Include these in the input file. For the time being, turn off all inelastic and transfer reactions.

- Adjust the potential parameters V_0, a_0, r_0 until CCMOD's output is in good agreement with cross-section measurements high above the fusion barrier. The program CCMOD_FINPAR will perform a FIFRANG-style search for the best values of a_0 and r_0

- Now look up inelastic excitations, seeking *collective* nuclear excitations. If nuclear deformation effects are in place already, do *not* include rotational states in the inelastic excitations; they have already been taken into account. Vibrational states must be considered in any case.

- Also look up transfer reactions (run [fission.programs.exe]transfer, on any VAX). Typical strengths range between 0.6 and 1.0 MeV for 1-particle transfers; smaller for two-particle transfers; they are free parameters, unfortunately. Only positive Q-values are expected to affect the cross-sections substantially.

- Apply these "coupled channels" so that CCMOD predicts cross-sections accurately at energies below and around the Coulomb barrier.

The resulting parameter file, which should generate accurate cross-sections at *all* energies, is then the one you want to use for all angular momentum calculations. The angular momentum distribution information $\partial\sigma(l)$ will come out in the file ldis.dat. CCTOJO reformats this file for use by JOANNE or FIFRANG.

CCMOD_RDB uses the same input file as CCMOD, but it ignores the contents of the line on projectile energy, and prompts for the same data from the command-line. It is intended to make generating angular momentum distributions easier: in your command-file, put the requested data (E_{min}, E_{max}, ΔE). (For an l-distribution calculation, give the desired *centre of mass* Energy twice, then a third real number which will be ignored.) See lines 3–5 of the sample command-file given in Section A.1.1.1. CCMOD_RDB also outputs the partial cross-sections $\partial\sigma(\theta_0, \theta_1)$ to dldm.dat, which is used by CCTOMDIS.

CCMOD_MEL differs from CCMOD_RDB only in that it collects and reports more nuclear orientation information from the CCMOD calculation process. This information relies on the semiclassical approach used by CCMOD for calculating nuclear deformation effects. The output ($\partial\sigma(l, \theta_0, \theta_1)$, in dldmel.dat) is needed by MELANIE and QMELANIE for nuclear intrinsic spin calculations, which in turn are needed by JO_EVAP, a variant of JOANNE.

A.3.2 CCTOJO

Authorship Rachel Butt

Purpose Convert ldis.dat files from CCMOD to the format used for FIFRANG input.

Language PASCAL.

Size 36 lines.

Standard input files ldis.dat

Standard output files listtl.dat

A.3.2.1 Calling patterns

CCTOJO prompts for the name of the file where CCMOD wrote the l-distribution, then for the name of the file to which the reformatted l-distribution should be written. (CCMOD's output is formatted for MULTIFIG plotting, whereas CCTOJO lists $\partial\sigma(l)$ as one value per line.)

A.3.3 CCMOD_FINPAR

Authorship Rachel Butt

Purpose Locates optimal Woods-Saxon parameters a_0 and r_0 for given V_0 by calculating the χ^2 measure of goodness of fit for CCMOD calculations of cross-section and experimental cross-section measurements high above the fusion barrier.

Variants CCMOD_FINPAR_SUPPRESS

Language Fortran.

Size 594 lines.

Standard input files ccin.dat, expt.dat

Standard output files ccin_fitted.dat, finparout.dat

A.3.3.1 Physics

CCMOD_FINPAR uses the same robustified χ^2 search algorithm as FIFRANG. However, CCMOD_FINPAR is searching over two variables, not one. This is accomplished by finding, for each value of a_0, the r_0 that minimizes the total χ^2, then calculating which a_0 to try next based on those minimized χ^2.

The dependence of high energy cross-sections on a_0, given that r_0 is found for each a_0, is fairly weak. Since high energy cross-section calculations also have a slight dependence on coupled-channels, the minimum a_0 appears fairly sensitive to included coupled-channels.

The variant CCMOD_FINPAR_SUPPRESS does searches over a third parameter, s, finding the a_0 giving minimum χ^2 for each s and then searching for the s giving the minimum overall χ^2. The parameter s is a constant cross-section suppression factor, which could arise for example from a detector with un-identified losses, or from particle breakup before fusion. However, a_0 is very sensitive to s, and the changes in a_0 largely compensate for the effects of s, so that the χ^2 curve as a function of s is very shallow and little useful information may be obtained in this way.

A.3.3.2 Calling patterns

CCMOD_FINPAR prompts for an input file in CCMOD format, and a file listing energies, cross-sections and errors in the cross-sections for measurements made at well-above-barrier energies (usually cross-sections above 200 mb). It then prompts for initial steps Δa_0 and Δr_0. (CCMOD_FINPAR_SUPPRESS first prompts for s and Δs.) It outputs a comparison between the measured and calculated datapoints for its final parameter set, together with the final values for a_0 and r_0, and a CCMOD input file with the new parameters.

A.3.4 CCTOMDIS

Authorship Rachel Butt

Purpose CCTOMDIS calculates M-distributions $\partial\sigma(M)$ from $\partial\sigma(\theta_0, \theta_1)$ using a semi-classical method.

Language Fortran.

Size 560 lines.

Standard input files dldm.dat

Standard output files tgtline.dat, prjline.dat, sigmatrix.dat, totline.dat, jomydata.dat, mdistr.dat

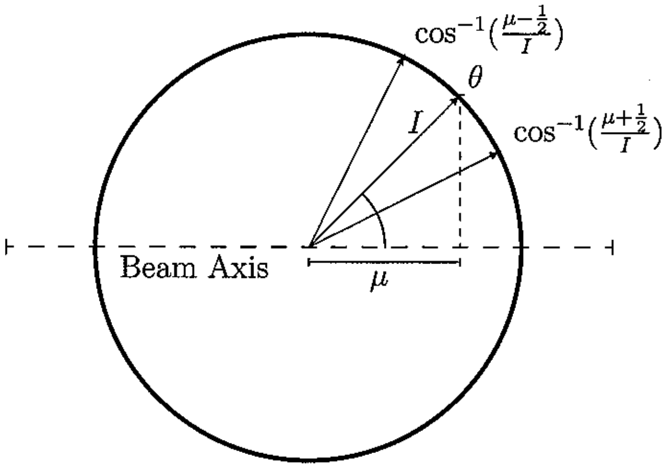

Figure A.9: If the nuclear spin I makes an angle θ with the beam axis, the classical projection of I on the beam axis is taken as μ if $\mu - \frac{1}{2} < I\cos(\theta) < \mu + \frac{1}{2}$.

A.3.4.1 Physics

CCTOMDIS assigns $\partial\sigma(\theta_0, \theta_1)$ to $\partial\sigma(M)$:

$$\partial\sigma(M) = \sum_{\mu_0=\max(-I_0,M-I_1)}^{\min(I_0,M+I_1)} \int_{\theta_0=\cos^{-1}\left(\frac{\mu_0+\frac{1}{2}}{I_0}\right)}^{\cos^{-1}\left(\frac{\mu_0-\frac{1}{2}}{I_0}\right)} \int_{\theta_1=\cos^{-1}\left(\frac{M-\mu_0+\frac{1}{2}}{I_1}\right)}^{\cos^{-1}\left(\frac{M-\mu_0-\frac{1}{2}}{I_1}\right)} \partial\sigma(\theta_0, \theta_1) d\theta_0 d\theta_1 \tag{A.29}$$

where the limits of the integrals are assigned according to the projections of the target and projectile nuclei on the beam axis, as illustrated in Figure A.9. In practice, the integrals are evaluated numerically in 1° steps, using linear interpolation at the boundaries.

A.3.4.2 Calling patterns

CCTOMDIS requires $\partial\sigma(\theta_0, \theta_1)$ to be supplied in a file like dldm.dat, which is generated by CCMOD_RDB. The desired M-distribution is written to mdistr.dat.

A.3.5 MELANIE

Authorship Rachel Butt

Purpose MELANIE performs a semi-classical calculation of $w(J, M)$ based on the data $\partial\sigma(l, \theta_0, \theta_1)$ supplied by CCMOD_MEL.†

References Section 3.2.4

Language Fortran.

---

†MELANIE calculates M,L distributions; thus "Mel".

Size 586 lines.

Standard input files dldmel.dat, pdws.dat

Standard output files joevapin.dat, melcheckel.dat, mmdist.dat, mmdistl.dat

A.3.5.1 Physics

To evaluate $\partial\sigma(l, \mu_0, \mu_1)$ we use a semi-classical coupled-channels calculation as described for CCTOMDIS, extracting the distribution $\partial\sigma(l, \theta_0, \theta_1)$ and calculating $\partial\sigma(l, \mu_0, \mu_1)$ according to:

$$\partial\sigma(l, \mu_0, \mu_1) = \int_{\theta_0=\cos^{-1}\left(\frac{\mu_0+\frac{1}{2}}{I_0}\right)}^{\cos^{-1}\left(\frac{\mu_0-\frac{1}{2}}{I_0}\right)} \int_{\theta_1=\cos^{-1}\left(\frac{\mu_1+\frac{1}{2}}{I_1}\right)}^{\cos^{-1}\left(\frac{\mu_1-\frac{1}{2}}{I_1}\right)} \partial\sigma(l, \theta_0, \theta_1) d\theta_0 d\theta_1 \qquad \text{(A.30)}$$

using the same classical partitioning of θ into μ as illustrated in Figure A.9.

We can then perform an angular momentum addition using the three angular momenta $\vec{l}$, $\vec{I_0}$, $\vec{I_1}$:

$$w(J, M) = \left\{ \sum_{l=0}^{\infty} \sum_{S=|I_0-I_1|}^{I_0+I_1} \sum_{\mu_0=-I_0}^{+I_0} \frac{\partial\sigma(l, \mu_0, M-\mu_0)|C_{M,0,M}^{S,l,J}|^2 |C_{\mu_0,M-\mu_0,M}^{I_0,I_1,S}|^2}{\sum_{l=0}^{\infty} \sum_{\mu_0=-I_0}^{+I_0} \sum_{\mu_1=-I_1}^{I_1} \partial\sigma(l, \mu_0, \mu_1)} \right\} \qquad \text{(A.31)}$$

where $\vec{S} = \vec{I_0} + \vec{I_1}$ and $\vec{J} = \vec{I_0} + \vec{I_1} + \vec{l}$.

MELANIE is, in practice, superseded by QMELANIE.

A.3.5.2 Calling patterns

MELANIE prompts for the target and projectile spins I_0 and I_1. It then prompts for a file such as dldmel.dat from which it can take $\partial\sigma(l, \theta_0, \theta_1)$. This file is generated by CCMOD_MEL. MELANIE silently reads from pdws.dat a factor which CCMOD_MEL uses to correct its cross-sections, so that MELANIE can apply this correction to the partial cross-sections $\partial\sigma(l, \theta_0, \theta_1)$, which are, by necessity, written to file before the correction factor is calculated. The correction is close to unity and arises from geometric considerations.

MELANIE writes the total spin $I_0 + I_1$ to joevapin.dat, followed by the matrix $w(J, M)$ in the format J, trunc(M), $w(J, M)$, for $0 \leq M \leq I_0 + I_1$. MELANIE writes the distribution $w(J) = \sum_M w(J, M)$ to melcheckel.dat and the distribution $w(M) = \sum_J w(J, M)$, for $-(I_0 + I_1) \leq M \leq I_0 + I_1$, to mmdist.dat, and to mmdistl.dat in the format M, $w(M)$.

A.3.6 QMELANIE

Authorship Rachel Butt

Purpose QMELANIE performs a quantum-mechanical calculation of $w(J, M)$ based on the data $\partial\sigma(l, \theta_0, \theta_1)$ supplied by CCMOD_MEL.

Variants QMELANIE_HIGHTGT, QMELANIE8.

References [BUT02], Section 3.2.5

Language Fortran.

Size 427 lines.

Standard input files dldmel.dat, pdws.dat

Standard output files joevapin.dat, melcheckel.dat, qmdist.dat, qmdistl.dat

A.3.6.1 Physics

The semi-classical program MELANIE depends upon the classical assumption that the ground-state nuclear spin is perfectly aligned with the nuclear deformation axis. However, quantum-mechanically, this cannot be the case; the direction of an angular momentum vector is never perfectly determined. QMELANIE takes account of this inherent uncertainty.

Given a spin I with projection κ on the nuclear deformation axis, what projection μ does I have on the beam axis? In other words, how does angular momentum transform under rotation? We assume an angle θ between the two axes. Rose [ROS61] shows that the angular momentum eigenfunction $|I, \kappa\rangle$, expressed in terms of the basis of eigenfunctions $|I, \mu\rangle$ relative to the beam axis, is as follows:

$$|I, \kappa\rangle = \sum_{\mu} d^{I}_{\mu,\kappa}(\theta)|I, \mu\rangle \tag{A.32}$$

Hence, to obtain the partial cross-sections $\partial\sigma(l, \mu_0, \mu_1)$, we must invert the above using the partial cross-sections $\partial\sigma(l, \theta_0, \theta_1)$. CCMOD has calculated this distribution in one-degree steps. The inversion is as follows:

$$\partial\sigma(l, \mu_0, \mu_1) = \sum_{\theta_0, \theta_1} |d^{I_0}_{\kappa_0=I_0,\mu_0}(\theta_0)|^2 |d^{I_1}_{\kappa_1=I_1,\mu_1}(\theta_1)|^2 \partial\sigma(l, \theta_0, \theta_1) \sin\theta_0 \sin\theta_1. \tag{A.33}$$

From $\partial\sigma(l, \mu_0, \mu_1)$ we determine $w(J, M)$ precisely as given in Equation A.31; that is to say, we add the three angular momenta from ground-state target spin, ground-state projectile spin, and collision-induced angular momentum, according to the Clebsch-Gordan coefficients.

A.3.6.2 Calling patterns

QMELANIE calling patterns are essentially identical to those for MELANIE.

QMELANIE_HIGHTGT accepts target spins greater than $10\hbar$; thus it is the appropriate program to use when modelling isomers such as $^{178}\mathrm{Hf}^{m2}$ ($16\hbar$). Capacity for high projectile spins is not provided, partly because no need has yet arisen, and partly because if QMELANIE_HIGHTGT also accepted high projectile spins, it would exceed current quotas for how much memory one program can use!

QMELANIE8 uses double-precision variables where QMELANIE uses quadruple precision variables. This does not have much effect on the output, but it does reduce the time required for the program to run.

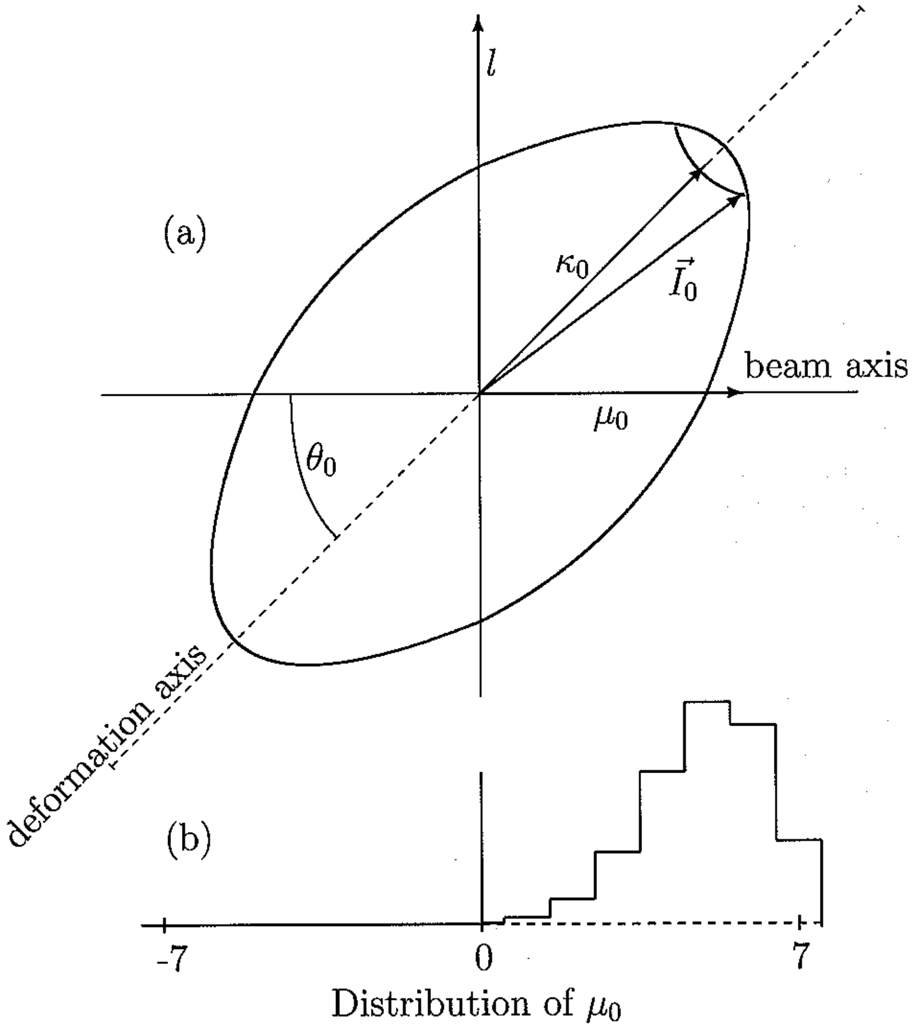

Figure A.10: (a) A schematic diagram of a deformed nucleus with ground-state spin. Because the ground-state nuclear spin $\vec{I}_0$ cannot be perfectly aligned with the nuclear deformation axis, μ_0 may take a range of values. (b) The calculated distribution of μ_0 is illustrated for the case $I_0 = 7$, $\kappa_0 = 7$, $\theta_0 = 45°$.

A.3.7 PSEUDO_MELDIS

Authorship Rachel Butt

Purpose To take an l-distribution and combine it with an M-distribution, producing an "uncorrelated" (separable) distribution $w(J, M)$ for comparison with correlated $w(J, M)$ distributions from MELANIE or QMELANIE and calculations thereon.

Language Fortran.

Size 110 lines.

Standard input files joevapin.dat, mdist.dat

Standard output files joevapin_def.dat

A.3.7.1 Calling patterns

PSEUDO_MELDIS gets its l-distribution $w(l)$ from a file joevapin.dat generated by MELANIE or QMELANIE with input of zero spin. It gets its M-distribution $w'(M)$ from a file mmdist.dat normally generated by MELANIE or QMELANIE when the input spin was non-zero. PSEUDO_MELDIS outputs the product distribution $w(l, M) = w(l)w'(M)$ to joevapin_def.dat.

In the command-files, this is carried out by replacing the normal MELANIE call:

```
$ run [fission.rdb103.progs.joevap]MELANIE
7.0 0.5
dldmel.dat
$ copy mmdist.dat mdis_er114.dat
$ DEF/LOG LDIS$FILE joevapin.dat
```

with:

```
$ run [fission.rdb103.progs.joevap]MELANIE
0.0 0.0
dldmel.dat
$ run [fission.rdb103.progs.joevap]pseudo_meldis
7.0 0.5
joevapin.dat
mdis_er114.dat
$ DEF/LOG LDIS$FILE joevapin_def.dat
```

Note that this example uses an M-distribution saved from a MELANIE call including nuclear spin.

A.3.7.2 DLDMEL_FLATTENER

DLDMEL_FLATTENER is similar in purpose to PSEUDO_MELDIS, but operates rather differently. DLDMEL_FLATTENER prompts for the name of a file like joevapin.dat, which contains a distribution $w(J, M)$, and calculates

$$w'(J, M') = \frac{\sum_{M=-I}^{+I} w(J, M)}{2I + 1} \tag{A.34}$$

prompting for the name of the file to which it should write the new distribution.

A.3.8 JOANNE

Program Name JO_EVAP

Authorship John Lestone

Purpose To model particle evaporation, compound nuclear survival and nth-chance fission events, using a Monte Carlo approach.†

Modifications Annette Berriman incorporated nuclear shell effects into the calculation. Rachel Butt added the facility to track changes to the projection M of the total nuclear spin J along the beam axis.

Variants JO_SHELL, JOANNE2

References [LES90B, BER01C]

Language Fortran.

Size 3992 lines.

Standard input files reaction.inp, reaction_tc.dat, listtl.dat or joevapin.dat.

Standard output files tj_dist.dat, for001.dat survive.dat, fission.dat, sur_ex.dat, fis_ex.dat, er_red.dat, xn_red.dat, xnsur.dat.

JOANNE is the core of realistic fusion-fission simulations that predict fission probabilities, anisotropies etc.

JOANNE comes in quite a number of variants with appreciably different calling patterns. We have only described the principal variants here. The versions available at ANU are all descended from "JOANNE2". The original author, John Lestone, further developed JOANNE, refining it, rearranging the code in line with substantially better programming practice, and introducing some new physics. However, that new physics is sufficiently controversial that our own new physics has *not* been added to "JOANNE4", and we work solely with the "JOANNE2" branch.

[†] JOANNE is named for the original author's wife.

A.3.8.1 Physics

JOANNE is a reasonably large and complex program, and we will not describe all the physics in detail here.

Broadly, all JOANNE variants follow the following steps:

1. Select J (and M, if appropriate) randomly (weighted by cross-section).
2. Calculate widths (probabilities) for particle emission, for neutrons, protons and α-particles, for a range of possible changes in angular momenta ΔJ and a range of possible changes of excitation energy ΔE for the daughter nucleus.
3. Calculate the fission width.
4. Select one of the possibilities randomly, based on the calculated probabilities. Record the emission. (JO_EVAP selects a ΔM at this point.)
5. Repeat the calculation of widths and selection of possibilities, based on the new excitation energy, angular momentum, charge and mass, until either the nucleus fissions or the nucleus cannot emit any more particles.
6. Under certain circumstances, calculate post-scission particle emissions.
7. Record details of the decay chain and ultimate outcome.
8. Repeat for many of decay chains ("cascades").
9. Write out aggregate data.

The equations used to calculate the fission and particle emission widths are given in John Lestone's PhD thesis [LES90B], section 2.3.2. Annette Berriman covers the same material in her thesis [BER01C], sections 2.2.4 and 2.5.4, including specific coverage of the JO_SHELL extensions in 2.5.4.2. We reproduce the fission and particle emission widths in this thesis in Equations 2.32 and 2.36.

The JO_EVAP extensions have a number of aspects. Firstly, the program is extended to accept and handle half-integer spins. So as to minimize interference with existing input and output for the program, this is done using a Boolean variable recording whether or not the current angular momentum J is integer or half-integer. Secondly, the intrinsic spin of evaporated neutrons and protons (half a unit) is also tracked. Thirdly, the input angular momentum distribution is $w(J, M)$, not $\partial\sigma(l)$; this has several physical consequences. The effect of the correlation of J and M may be studied after including any changes in J or M due to pre-fission particle emission, and (more importantly) the changes in the J-distribution due to low-J compound nuclear survival. The increase in the average J due to the addition of ground-state nuclear spins I is included and marginally increases the fission probability. And it becomes appropriate to track the changes in the projection M of the total spin J on the beam axis, due to angular momentum carried off by evaporated particles. The relative probability that the change takes the value ΔM is given by:

$$Pr(\Delta M) = \Omega \left| C^{J_p, \Delta J, J_d}_{M_p, \Delta M, M_d} \right|^2 \tag{A.35}$$

where subscript p denotes the parent nucleus, and d the daughter; and the corresponding solid angle Ω takes the values:

$$\Omega = \begin{array}{ll} \frac{4\pi}{\sqrt{\Delta J(\Delta J+1)}} & \Delta M = 0 \\ \frac{2\pi}{\sqrt{\Delta J(\Delta J+1)}} & 0 < \Delta M < \Delta J \\ 2\pi\left(1 - \frac{\Delta J-1/2}{\sqrt{\Delta J(\Delta J+1)}}\right) & \Delta M = \Delta J \end{array} \tag{A.36}$$

These two equations may not be perfectly rigorous. However, the effect they predict is extremely small, as shown in Section 3.2.7.

A.3.8.2 Calling patterns

JOANNE gets most of its information from an input file (e.g. reaction.inp) which should be specified in the VAX shell variable `INPUT$FILE`. A sample is given in Section B.2.1; it is largely self-explanatory. This input file should name the file containing the particle evaporation transmission coefficients (e.g. reaction_tc.dat).

JOANNE requires an angular momentum distribution $w(l)$, which it reads from a file (e.g. listtl.dat) specified in the shell variable `LDIS$FILE`. (JO_EVAP reads in $w(J, M)$ from this file, usually named joevapin.dat or something similar.)

JOANNE silently reads from gsmass.tab, vgsld.tab, and frldm.tab, in the same directory as the program's source code. Users should not have to worry about this.

JOANNE writes out $N_{fis}(i, T, J)$ to tj_dist.dat, where i is the number of neutron emissions that have occurred prior to fission (i is set to 10 if a proton or α-particle is evaporated). (JO_EVAP writes out $N_{fis}(i, T, J, M)$ instead.) Collated information on a wide variety of quantities is written to the various output files; particularly for001.dat.

A.3.9 COLLETTE

Authorship John Lestone, Annette Berriman, Rachel Butt

Purpose To take the distribution of fission fragments from JOANNE and generate the appropriate fission fragment angular distribution.[†]

Variants JO_A_FFAD, JO_A_ACB, JO_MYD, COLLETTE_DIS

Language Fortran.

Size 348 lines.

Standard input files reaction_ieff.dat, reaction.inp, tj_dist.dat

Standard output files ieff.dat, jo_a.out, jkia.dat, anisot.dat, anisotnn.dat, ani_ex.dat, aninn_ex.dat

---

[†] COLLETTE "collects" data.

A.3.9.1 Physics

COLLETTE and related programs calculate fission fragment angular distributions from distributions generated by JOANNE or related programs. Most forms of the program also calculate partial fission fragment angular distributions for each i, where i denotes the number of evaporated neutrons. (If a proton or α-particle was evaporated, i is set to 10.) These "nth chance fission" anisotropies are often interesting in themselves.

JO_A_FFAD and JO_A_ACB differ very little in their physics; the latter has slightly more error checking and records a little more information. They read in the matrix $N_{fis}(i, T, J)$ (assuming $J = l$) and calculate the fragment angular distribution:

$$\begin{aligned} W(\theta) &\propto \sum_i \sum_J \sum_T N_{fis}(i,T,J) \\ &\quad \times \sum_{K=-J}^{J} \frac{(2J+1)|d^J_{0,K}(\theta)|^2 \exp(-K^2/2K_0(J,T)^2)}{\sum_{K=-J}^{J} \exp(-K^2/2K_0(J,T)^2)} \end{aligned} \tag{A.37}$$

JO_MYD incorporates the ground-state nuclear spin into the simulation, by reading in $N_{fis}(i, T, l)$ (which ignored ground-state spin) and then assuming that the distribution $\partial\sigma(M)$ is appropriate to all T and J, calculating:

$$\begin{aligned} W(\theta,i,T,l) &\propto \sum_{J=|l-(I_0+I_1)|}^{l+I_0+I_1} \sum_{M=-(I_0+I_1)}^{+I_0+I_1} N_{fis}(i,T,l) \\ &\quad \left\{ \sum_{l=0}^{\infty} \sum_{S=|I_0-I_1|}^{I_0+I_1} \sum_{\mu_0=-I_0}^{+I_0} \frac{\partial\sigma(M) |C^{S,l,J}_{M,0,M}|^2 |C^{I_0,I_1,S}_{\mu_0,M-\mu_0,M}|^2}{\sum_{M=-(I_0+I_1)}^{+I_0+I_1} \partial\sigma(M)} \right\} \\ &\quad \times \left[\sum_{K=-J}^{J} \frac{(2J+1)|d^J_{M,K}(\theta)|^2 \exp(-K^2/2K_0(J,T)^2)}{\sum_{K=-J}^{J} \exp(-K^2/2K_0(J,T)^2)} \right] \end{aligned} \tag{A.38}$$

and from that, calculating $W(\theta) \propto \sum_i \sum_T \sum_l W(\theta, i, T, l)$. JO_MYD is the first attempt at including the effects of nuclear ground-state spin in full fusion-fission simulations. The above equation has the wrong lower limit for J for the case where both I_0 and I_1 are significant and $l < I_0 + I_1$. JO_MYD is superseded by COLLETTE.

COLLETTE reads in $N_{fis}(i, T, J, M)$, calculating:

$$W(\theta,i,T,J,M) \propto N_{fis}(i,T,J,M) \left[\sum_{K=-J}^{J} \frac{(2J+1)|d^J_{M,K}(\theta)|^2 \exp(-K^2/2K_0(J,T)^2)}{\sum_{K=-J}^{J} \exp(-K^2/2K_0(J,T)^2)} \right] \tag{A.39}$$

and subsequently $W(\theta) \propto \sum_i \sum_T \sum_J \sum_M W(\theta, i, T, J, M)$. COLLETTE_DIS differs from COLLETTE only in that it calculates $W(\theta)$ at a range of angles specified in thetalist.dat, and writes $W(\theta)$ to ffangdis.dat.

A.3.9.2 Calling patterns

All forms of this program look in the shell variable `INPUT$FILE` for the name of a file describing the reaction (the same file JOANNE used for its input; e.g. reaction.inp). They also look in the shell variable `DATIEFF` for the name of the file containing the $\mathcal{I}_{eff}(J)$ information (e.g. reaction_ieff.dat). The distribution $N_{fis}(i, T, J)$ or $N_{fis}(i, T, J, M)$ is read from tj_dist.dat. (Note that the slight dependence of $\mathcal{I}_{eff}$ on i is not considered!)

JO_MYD looks in jomydata.dat for target and projectile spins, and the associated M-distribution. This file is usually prepared with CCTOMDIS.

Quite a bit of information is written out to various files. Usually the most interesting is anisot.dat, where the calculated anisotropies are written.

A.3.10 TAIL

Authorship Annette Berriman

Purpose Organise data from JOANNE simulations for easy graphing.

Language Fortran.

Size 72 lines.

Standard input files anisot.dat, anisotnn.dat, ani_ex.dat, aninn_ex.dat

Standard output files anisot.dat, ani_ex.dat

A.3.10.1 Calling patterns

TAIL is called at the end of a command-file executing a JOANNE simulation. TAIL examines the various files which are written during the JOANNE simulations, collating all the data in the files anisot.dat and ani_ex.dat, with suitable MULTIFIG lift-pen and change-line-style commands.

A.4 Quasi-Fission Simulation Programs

A.4.1 DOM

Program Name FDOM, SDOM, TDOM

Authorship Rachel Butt

Purpose To generate a matrix $P_{CN}(l, \theta_0, \theta_1)$ specifying what fraction of each element of the matrix $\partial\sigma(l, \theta_0, \theta_1)$ proceeds to fuse, and what fraction undergoes quasi-fission without fusing.[†]

Language Fortran.

[†] DOM stands for "Division Of Matrix".

Size 100 lines.

Standard input files dldmel.dat

Standard output files pr_qfis.dat

A.4.1.1 Physics

Each variant of the program uses a different method for specifying the division of "capture" events between fusion (compound nucleus formation) and quasi-fission.

FDOM uses a constant fraction. Whatever the angles θ_0, θ_1, and the angular momentum l, still we assume that x% proceeds to quasi-fission and (1-x)% to fusion.

SDOM uses a square cut in θ_0. For angles less than θ_c, the system quasi-fissions; for angles larger, the system fuses.

TDOM uses a threshold cut:

$$P_{CN}(\theta_0) = 1 - \frac{1}{1 + e^{\frac{\theta - \theta_c}{\Delta\theta}}} \tag{A.40}$$

A.4.1.2 Calling patterns

The DOM programs use dldmel.dat from CCMOD_MEL, simply as a template; something to give the range and spacing of θ_0, θ_1, and l appropriate to the reaction (since sometimes dldmel.dat only covers θ_0, with θ_1 taking only one value). The programs could in theory also do the next stage, of calculating $P_{CN}(l, \theta_0, \theta_1)\partial\sigma(l, \theta_0, \theta_1)$, but this way $P_{CN}(l, \theta_0, \theta_1)$ and $\partial\sigma(l, \theta_0, \theta_1)$ may be recalculated separately. The output $P_{qfis} = 1 - P_{CN}$ of any DOM program goes in pr_qfis.dat to PHILLIPA, which performs the division of $\partial\sigma(l, \theta_0, \theta_1)$ between fusing and quasi-fissioning components.

A.4.2 PHILLIPA

Authorship Rachel Butt

Purpose To separate the fission and quasi-fission components of $\partial\sigma(l, \theta_0, \theta_1)$ according to an input matrix $P_{qfis}(l, \theta_0, \theta_1)$.[†]

Language Fortran.

Size 111 lines.

Standard input files dldmel.dat, pr_qfis.dat

Standard output files fis_dldmel.dat, qfis_dldmel.dat, sig_fis.dat, sig_qfis.dat

---

[†] PHILLIPA "filters" a distribution.

A.4.2.1 Calling patterns

PHILLIPA reads $P_{qfis}(l, \theta_0, \theta_1) = 1 - P_{CN}(l, \theta_0, \theta_1)$ from pr_qfis.dat (as calculated by a DOM program) and $\partial\sigma(l, \theta_0, \theta_1)$ from dldmel.dat. It generates $\partial\sigma_{fus}(l, \theta_0, \theta_1) = P_{CN}(l, \theta_0, \theta_1)\partial\sigma(l, \theta_0, \theta_1)$ (which goes to fis_dldmel.dat), $\sigma_{fus} = \sum_{l,\theta_0,\theta_1} \partial\sigma_{fus}(l, \theta_0, \theta_1)$, which goes to sig_fis.dat, and their quasi-fission equivalents.

The two $\partial\sigma$ files will proceed through different calculations, one appropriate to fusion-fission, the other appropriate to quasi-fission, until COLLEEN combines the two resulting fragment angular distributions according to the total cross-sections σ_{fus}, σ_{qfis}. (Note that COLLEEN's result will be slightly off according to the survival probability of the fused system; however, if quasi-fission is significant, survival cross-sections are usually negligible! This may have to be corrected for particular cases not covered in this thesis.)

A.4.3 PATRICIA

Authorship Rachel Butt

Purpose To compress the input $\partial\sigma_{qfis}(l, \theta_0, \theta_1)$ to QMARY, so that QMARY finishes calculations faster.[†]

Language Fortran.

Size 87 lines.

Standard input files qfis_dldmel.dat

Standard output files qfis_dldmel_c.dat

A.4.3.1 Calling patterns

PATRICIA assumes that the contents of qfis_dldmel.dat are $\partial\sigma_{qfis}(l, \theta_0, \theta_1)$, where θ_0 comes in one degree steps and there is no iteration over θ_1. (If the projectile nucleus is significantly deformed, and there is iteration over θ_1, a new, 2D PATRICIA will be urgently needed!) PATRICIA calculates and writes out $\partial\sigma_{qfis}(l, \theta_0, \theta_1)$ where θ_0 comes in larger steps, the size of the steps depending on the integer read in from command-file.

A.4.4 MYDE

Program Name MYDE_LDIS

Authorship Rachel Butt

Purpose To generate fission fragment angular distributions for given K_0, $\partial\sigma(l)$, $\partial\sigma(M)$.

[†] PATRICIA re-"partitions" a matrix.

Variants MYDE_MELFED, MYDE_II

References [VAN73, BUT02], Sections 3.2.4, 3.2.3

Language Fortran.

Size 533 lines.

Standard input files listtl.dat, thetalist.dat, mdist.dat

Standard output files outmyde.dat, outmydeall.dat, summary.dat

A.4.4.1 Physics

MYDE generates fragment angular distributions for constant K_0 (in contrast to COLLETTE and related programs, where K_0 varies, depending on J (via $\mathcal{I}_{eff}$ and evaporated particles (via T)). Nothing in MYDE is specific to quasi-fission.

MYDE_LDIS evaluates the fission fragment angular distribution according to [VAN73]:

$$W(\theta) \propto \sum_{J=0}^{\infty} \sum_{M=-(I_0+I_1)}^{+I_0+I_1} \left\{ \sum_{l=0}^{\infty} \sum_{S=|I_0-I_1|}^{I_0+I_1} \sum_{\mu_0=-I_0}^{+I_0} \frac{\partial\sigma(M)(2l+1)T_l |C^{S,l,J}_{M,0,M}|^2 |C^{I_0,I_1,S}_{\mu_0,M-\mu_0,M}|^2}{\sum_{l=0}^{\infty}(2l+1)T_l \sum_{M=-(I_0+I_1)}^{+I_0+I_1} \partial\sigma(M)} \right\}$$
$$\times \left[\sum_{K=-J}^{J} \frac{(2J+1)|d^J_{M,K}(\theta)|^2 \exp(-K^2/2K_0^2)}{\sum_{K=-J}^{J} \exp(-K^2/2K_0^2)} \right] \tag{A.41}$$

Here, I_0 is the spin of the target nucleus, and μ_0 its projection upon a space-fixed axis (in experiments, the beam axis). The channel spin S is the vector sum of I_0 and I_1, where I_1 is the spin of the projectile nucleus. The orbital angular momentum l, together with S, determines $\vec{J} = \vec{l} + \vec{S}$, the total angular momentum of the fissioning nucleus. M is the projection of J onto the space-fixed axis. K_0^2 is as defined in Section 2.2.2. $C^{S,l,J}_{M,0,M}$ and $C^{I_0,I_1,S}_{\mu_0,M-\mu_0,M}$ are Clebsch-Gordan coefficients. The function $d^J_{M,K}(\theta)$ is the well known d-function, as defined in Equation A.27. T_l is the fusion transmission coefficient for a given orbital angular momentum l. The M-distribution $\partial\sigma(M)$ is the weighting of each value of M, assumed to be independent of l.

The quantity in curly brackets in Equation 3.1 is $w(J, M)$, the weighting for each possible fission channel (J, M). The quantity in square brackets in Equation 3.1 specifies the fission fragment angular distribution $\rho(J, M, \theta)$ for a given channel (J, M).

MYDE_II arranges the equation slightly differently, with an eye to efficiency for single-l calculations.

MYDE_MELFED shifts a higher proportion of the calculation to its parent program, demanding the correlated distribution $w(J, M)$ as input, and calculating the fission fragment angular distribution according to:

$$W(\theta) \propto \sum_{J=0}^{\infty} \sum_{M=-J}^{J} w(J,M) \sum_{K=-J}^{J} \frac{(2J+1)|d^J_{M,K}(\theta)|^2 \exp(-K^2/2K_0^2)}{\sum_{K=-J}^{J} \exp(-K^2/2K_0^2)} \tag{A.42}$$

A.4.4.2 Calling patterns

There are various minor differences between versions of MYDE, depending on whether or not they read in their selection of angles θ from thetalist.dat or take 90°–180° in 5° steps, whether they include the angles 90° and 180° as well as the angles read in from thetalist.dat, whether they take a fixed number of angles from thetalist.dat or just whatever is there, how they assign errors to their calculated angular distributions (since that is arbitrary), and what angles they write out to the result files outmyde.dat and outmydeall.dat. To determine which code does which, look at the source code, and make minor amendments and recompile if there isn't already something that does precisely what you want.

MYDE prompts for an angular momentum l, and (if the value is negative) then prompts for the name of a file containing the l-distribution. It prompts for the value of K_0, and the target and projectile spins. It takes character input for whether to use a single value of M (which it would prompt for; this is mainly of theoretical interest) or an M-distribution, whereupon MYDE will prompt for the filename.

MYDE_MELFED simply prompts for the name of the file containing the distribution $w(J, M)$ (usually joevapin.dat) and the value of K_0 to use.

All programs write the calculated fragment angular distribution $\theta, W(\theta)$ to outmyde.dat, and the basic input of the calculation to summary.dat. If the angles 90° and 180° are added to the list of angles used, the program also writes those to outmydeall.dat, and calculates an anisotropy $W(180°)/W(90°)$ which is written to summary.dat.

A.4.4.3 COMGEN

Under some circumstances MYDE has been used in surveys of large ranges of input values. To facilitate this, the program COMGEN was written to generate appropriate command-files, which could call MYDE a thousand times. (Note that each iteration generates fresh versions of some files, and VAX version numbers are limited to just over 32 thousand.) COMGEN prompts for files containing the list of K_0 values, I_0 values, and I_1 values the command-file is to cover.

The MKGRAPH programs are then used to analyse the resulting summary files, picking the relevant data from the summary files, and writing subsets of it to new files, which could then be sorted, possibly further manipulated (eg SORTRIP, which sorts on and then strips off the first number on each line, or GRAPHIKI, which manipulates the results into a form suited for 3D plots with MATHEMATICA), and then graphed. This is how Figure 3.2 was generated. Fortran is not intrinsically suited to string manipulation, unlike Perl, and MKGRAPH may be sensitive to which versions of FIFRANG and MYDE are being used. As with MYDE it is easier to look at the source and change it as needed than to list which file uses which formats.

A.4.5 QMARY

Authorship Rachel Butt

Purpose To calculate quasi-fission fragment angular distributions $W(\theta)$, given $\partial\sigma_{qfis}(l,\theta_0,\theta_1)$, allowing K_0 to vary with θ_0.[†]

Language Fortran.

Size 556 lines.

Standard input files thetalist.dat, ccin.dat (currently ignored), qfis_dldmel.dat, pdws.dat

Standard output files qf_ffad.dat, joevapin.dat, melcheckel.dat, qmdist.dat, qmdistl.dat

A.4.5.1 Physics

QMARY calculates quasi-fission fragment angular distributions where K_0 is not constant. The input is $\partial\sigma_{qfis}(l,\theta_0,\theta_1)$. QMARY basically breaks each element of this matrix down into substantially tinier pieces, each with unique values of μ_0, μ_1, $\vec{S}=\vec{I}_0+\vec{I}_1$, and $\vec{J}=\vec{l}+\vec{S}$. The weighting of each component is assigned according to:

$$w(l,\theta_0,\theta_1,\mu_0,\mu_1,S,J)=\partial\sigma_{qfis}(l,\theta_0,\theta_1)\left|d^{I_0}_{I_0,\mu_0}(\theta_0)\right|^2\left|d^{I_1}_{I_1,\mu_1}(\theta_1)\right|^2\left|C^{I_0,I_1,S}_{\mu_0,mu_1,M}\right|^2\left|C^{l,S,J}_{0,M,M}\right|^2 \tag{A.43}$$

where $M=\mu_0+\mu_1$, and the total fission-like fragment angular distribution is assigned according to:

$$W(\theta)\propto\sum_{\theta_0}\sum_{\theta_1}\sum_{l}\sum_{\mu_0}\sum_{\mu_1}\sum_{\vec{S}}\sum_{\vec{J}}\rho(J,M,K_0,\theta)w(l,\theta_0,\theta_1,\mu_0,\mu_1,S,J) \tag{A.44}$$

where K_0 has been determined using any or all of the available parameters, and $\rho(J,M,K_0,\theta)$ describes where the fission fragments go for those parameters.

This is something of a brute force approach; the input information is broken down as finely as we can sensibly imagine, and calculating millions of distributions ρ and adding them all back up again is computationally demanding. On the other hand, by changing the way K_0 is determined and possibly even the nature of the microscopic angular distribution ρ, we can try out almost anything. Since we are still trying out plausible possibilities for quasi-fission fragment angular distributions, this flexibility is important.

The selection of K_0 and corresponding calculation of a fission-like fragment angular distribution is performed in a pair of sub-routines in a library file (currently KO_TGTTHETA.FOR, 164 lines), which may readily be replaced.

The existing subroutine update_ffad chooses a K_0 according to:

$$K_0 = \begin{array}{cc} x_2 & \theta_0 < x_3 \\ \frac{x_2-x_1}{x_3}\theta_0+x_1 & \theta_0 \geq x_3 \end{array} \tag{A.45}$$

[†] Quasi-fission counterpart to QMELANIE. By the time QMARY was written, the "Girls" theme for program names was well entrenched.

where x_1, x_2, and x_3 are parameters read in from the command-line or command-file. Update_ffad then gets a fragment angular distribution using that K_0 from subroutine get_incremental_ffad, and adds it, appropriately weighted, to the fission-like fragment angular distribution already computed.

The subroutine get_incremental_ffad expects to be passed J, M, K_0, and a list of angles θ; it returns:

$$\rho(J, M, K_0, \theta) = \sum_{K=-J}^{J} \frac{(2J+1)\left|d^J_{M,K}(\theta)\right|^2 e^{-K^2/2K_0^2}}{\sum_{K=-J}^{J} e^{-K^2/2K_0^2}} \tag{A.46}$$

This could be replaced if, for example, the time it takes the compound nucleus or di-nucleus to rotate once is comparable to or longer than the time it takes to scission.

A.4.5.2 Calling patterns

QMARY reads in thetalist.dat to find out what angles to calculate the quasi-fission fragment distribution at; it is important, if the results are to be compared with experiment, that these angles match the experimental angles, as discussed in Section 6.5.1.1.

QMARY writes out files like QMELANIE, partly so that these files may be examined as a bug-preventative. When simulating fragment angular distributions, the only file of interest is qf_ffad.dat.

QMARY, running in quad-precision and input spin of 7/2, can take two full days to calculate an ffad for one beam energy. Using QMARY8 speeds this considerably (at least a factor of 4) without detectable loss of precision in the results. Using PATRICIA compression of 3-5 cuts QMARY run times by the same factor; detectable loss of precision in the results appears around PATRICIA compression of 10.

Because QMARY takes so long to run, it is advisable to run command files calling QMARY in "batch mode".

A.4.6 COLLEEN

Authorship Rachel Butt

Purpose COLLEEN takes the fission and quasi-fission fragment angular distributions, and adds them in proportion to supplied cross-sections.[†]

Language Fortran.

Size 102 lines.

Standard input files thetalist.dat, qf_ffad.dat, outmydeall.dat, sig_fis.dat, sig_qfis.dat, fis_sig.dat, qfis_sig.dat

Standard output files ffad.dat

[†] Like COLLETTE, COLLEEN collects data.

A.4.6.1 Calling patterns

COLLEEN reads the list of angles θ at which fission-like fragment angular distributions have been calculated from thetalist.dat. The cross-sections σ_{fis} and σ_{qfis} that the input distributions *ought* to have are read in from sig_fis.dat and sig_qfis.dat respectively. The cross-sections $\sigma_{fis,a}$ and $\sigma_{qfis,a}$ that the data actually show are read in from fis_sig.dat and qfis_sig.dat respectively. These may differ from earlier cross-sections because, since the shape of the angular distribution is more important than the cross-section, some programs which calculate FFADs do not attempt to conserve cross-section. The subroutine ANGCROSS can be used to measure cross-sections or re-scale distributions, but it does not return good results for irregularly distributed angles; hence COLLEEN reads cross-sections from files, where the files may be written by FIFRANG (for028.dat) after fitting each angular distribution.

COLLEEN prompts for the file containing the fission angular distribution $W_{fis}(\theta)$, and then for the file containing the quasi-fission angular distribution $W_{qfis}(\theta)$, and calculates the combined FFAD according to:

$$W(\theta) = W_{fis}(\theta)\frac{\sigma_{fis}}{\sigma_{fis,a}} + W_{qfis}(\theta)\frac{\sigma_{qfis}}{\sigma_{qfis,a}} \tag{A.47}$$

writing the result to ffad.dat.

A.5 Libraries

The following are not programs in themselves, but are libraries written in simple FORTRAN that have been used in many of the existing programs, and are documented here because they should be useful for future programs. While there are more sophisticated standard libraries available on the VAX and Alpha, the different machines require linking against different libraries, and from a user's perspective it is difficult to locate the desired library.

A.5.1 ANGCROSS

Authorship Rachel Butt

Purpose Returns the cross-section of the supplied angular distribution or returns the supplied angular distribution scaled to the supplied cross-section.

Language Fortran.

Size 255 lines.

ANGCROSS works out what order the supplied angles go in, then calculates the observed cross-section according to:

$$\begin{aligned} \sigma_o &= (\theta_1 - 90^\circ)\sin(\theta_1)W(\theta_1) \\ &\quad + \sum_{i=2}^{n-1}(\theta_{i+1} - \theta_{i-1})/2\sin(\theta_i)W(\theta_i) \\ &\quad + (180^\circ - \theta_n)/2\sin(\theta_n)W(\theta_n) \end{aligned} \tag{A.48}$$

If the supplied cross-section σ_s is negative, ANGCROSS sets it to the observed cross-section; if it is positive, ANGCROSS scales the angular distribution by σ_s/σ_o.

ANGCROSS takes real numbers for $W(\theta_i)$. ANGCROSS_DBLPREC takes double-precision, and ANGCROSS_HIGHPREC takes quad-precision.

A.5.2 CHIDIFF

Authorship Rachel Butt

Purpose Returns the χ^2 measure of fit quality between a supplied set of theoretical values and the corresponding data.

Language Fortran.

Size 24 lines.

If the theoretical points are given by $T(i)$, the data by $E(i)$ and the errors by $\Delta E(i)$, then CHIDIFF returns:

$$\chi^2 = \sum_{i=1}^{n} \frac{(E(i) - T(i))^2}{\Delta E(i)^2} \tag{A.49}$$

A.5.3 CHIFIF

Authorship Rachel Butt

Purpose FIFRANG library functions, GETANGDIST, CHIDIFF, SAMPLEINTERVAL

Language Fortran.

Size 193 lines.

The abstraction of these library functions from FIFRANG is not complete, in that these functions basically cannot be used in other programs without at least a little modification, and other functions cannot be substituted for these without also modifying FIFRANG a little (e.g. FIFRANGMYD). However, they do improve things.

GETANGDIST returns a theoretical angular distribution for a particular K_0, using a supplied l-distribution and scaling the total cross-section to match the supplied experimental angular distribution. It gets the basic distribution, in 5° steps, by calling FANGDIS in the library FANG; this distribution is linearly interpolated to the angles at which the experimental data is available, and then scaled to the same total cross-section.

CHIDIFF matches the function in the library of the same name.

SAMPLEINTERVAL implements the robustification of FIFRANG's parabolic search algorithm. It takes a set of three evenly spaced K_0 values x_1, x_2, x_3, and uses them as a starting point for a search for three K_0 values spanning the only minimum in the χ^2 function. The initial search is over eleven evenly spaced points from $(2x_1 - x_2)$ (or zero, if that is negative) to $(2x_3 - x_2)$. If one of the middle points returns the lowest χ^2, SAMPLEINTERVAL will return that point and the two either side of it, for FIFRANG to use in its search; if not, SAMPLEINTERVAL will try sampling eleven points over a new interval, and repeat until a result is obtained. If the previous limits were x_{max} and x_{min}, then if the lowest point has the lowest χ^2, then the new interval runs from $3/2x_{min} - 1/2x_{max}$ or zero to $(x_{max} + x_{min})/2$; if the highest point has the lowest χ^2, the new interval has double the old step-size and runs from the middle of the old interval.

A.5.4 CLEBSCH

Authorship Rachel Butt

Purpose CLEBSCH returns a Clebsch-Gordan coefficient for the supplied angular momenta. LITLDE returns the "*d*-function".

Variants CLEBSCH8

Language Fortran.

Size 219 lines.

CLEBSCH is a straight-forward calculation of Clebsch-Gordan coefficients using quad-precision variables:

$$\begin{aligned} C^{j_1,j_2,j_3}_{m_1,m_2,m_3} &= \delta_{m_3,(m_1+m_2)} \\ &\times \left[(2j_3+1)\frac{(j_3+j_1-j_2)!(j_3-j_1+j_2)!(j_1+j_2-j_3)!(j_3+m_3)!(j_3-m_3)!}{(j_1+j_2+j_3+1)!(j_1-m_1)!(j_1+m_1)!(j_2-m_2)!(j_2+m_2)!}\right]^{1/2} \\ &\times \sum_\nu \frac{(-)^{\nu+j_2+m_2}(j_2+j_3+m_1-\nu)!(j_1-m_1+\nu)!}{\nu!(j_3-j_1+j_2-\nu)!(j_3+m_3-\nu)!(\nu+j_1-j_2-m_3)!} \end{aligned} \tag{A.50}$$

where the summation is carried out over all ν such that all arguments involving ν are non-negative. This uses the FACTRL function in this library, which must be initialized using the subroutine MKFACT, and which can return $n!$ for $n \leq 300$.

These libraries also contain the function LITLDE, which evaluates [VAN73, ROS61]:

$$\begin{aligned} d^J_{M,K}(\theta) &= \{(J+M)!(J-M)!(J+K)!(J-K)!\}^{1/2} \\ &\times \sum_X \frac{(-1)^X[\sin(\theta/2)]^{K-M+2X}[\cos(\theta/2)]^{2J-K+M-2X}}{(J-K-X)!(J+M-X)!(X+K-M)!X!} \end{aligned} \tag{A.51}$$

where the summation is performed over all integer values of X where all factorial arguments are non-negative.

CLEBSCH8 uses only double-precision variables. It still copes with spins in excess of $100\hbar$, which is not straightforward using double-precision variables, by dint of separating the factorials into their exponent and mantissa, and performing calculations using both.

In any program using this, the array of factorials should be initialized using "CALL MKFACT" or "CALL MKFACTEM" for CLEBSCH or CLEBSCH8 respectively.

A.5.5 FANG

Authorship Birger Back

Purpose Returns a component of a fission fragment angular distribution.

References [BAC85]

Language Fortran.

Size 76 lines.

The FANG library contains two subroutines; FANG and FANGDIS. FANG expects an angular momentum I, K_0, and the angle θ (specified as the integer $(\theta^\circ - 85)/5$, since the function only works in 5° steps), and returns:

$$F(I, K_0, \theta) = \sum_{K=-I}^{I} \frac{G(I, K, \theta) e^{-K^2/2K_0^2}}{\sum_{K=-I}^{I} e^{-K^2/2K_0^2}} \tag{A.52}$$

where $G(I, K, \theta)$ is retrieved from the lookup table in wfis.dat, and should be equal to $(2I + 1)|d^I_{0,K}(\theta)|^2$.

FANGDIS expects an angular momentum distribution $\partial\sigma(l)$ and the parameter K_0, and returns the distribution $W(\theta)$, evaluated in 5° steps:

$$W(\theta) = \sum_l F(l, K_0, \theta)\partial\sigma(l) \tag{A.53}$$

A.5.6 GAUSS

Authorship Rachel Butt

Purpose Returns a number selected randomly from a Gaussian distribution with average zero and standard deviation 1.

References [BEV92, pgs 84–88]

Language Fortran.

Size 92 lines.

For integers x_i selected randomly from the interval 0–1, the sum $\sum_{i=0}^{n} x_i$ approaches Gaussian form as n increases, with the average $n/2$ and the standard deviation $\sqrt{n/12}$. The function RANGAUSS12 returns such a result, calculated with n=12, scaled to have average zero and standard deviation 1; The function RANGAUSS48 uses n=48 for higher precision.

A.5.7 PARMIN

Authorship Rachel Butt

Purpose Returns the coefficients of a parabola passing through the three supplied points.

Language Fortran.

Size 87 lines.

PARMIN expects the arrays $x(1:3)$ and $y(1:3)$, and returns a, b, and c for the equation $y = a(x-b)^2 + c$. b is evaluated according to:

$$b = \frac{\frac{y_3-y_2}{y_2-y_1}(x_1^2 - x_2^2) + (x_3^2 - x_2^2)}{2(x_1 - x_2)\frac{y_3-y_2}{y_2-y_1} + 2(x_3 - x_2)} \tag{A.54}$$

whereupon a is evaluated according to:

$$a = \frac{y_2 - y_1}{(x_2 - b)^2 - (x_1 - b)^2} \tag{A.55}$$

and c according to $c = y_3 - a(x_3 - b)^2$.

If a is negative, or if b is outside the range x_1–x_3, PARMIN sets the sign of b to be negative as an error signal. (This assumes, naturally, that b *should* be positive; which is true for FIFRANG, at present the main program using PARMIN.) PARMIN will also report errors if two or more of the supplied x-values are identical, but this functionality is not yet as good as it could be.

A.6 Major External Programs

A.6.1 DCP

Authorship Gordon Foote

Purpose To collect and analyse data from any of the ANU detector systems.

DCP is an integral part of the data collection process. During operation of the 14UD accelerator and almost any associated detector system, the data is collected and recorded in event-by-event form, and initial examination and analysis is carried out, using DCP.

Much more of the user's time is spent doing subsequent data analysis with DCP, using the saved event-by-event data. DCP will sort the data into one-dimensional and two dimensional spectra, selecting subsets of the data by applying any number of "gates" constraining the data to be within specified one-dimensional or two-dimensional regions of any variable. The preparation, display, manipulation of, and extracting numbers from these spectra constitutes the greater part of DCP's usage. Among the program's advantages is the facility to manipulate recorded data to generate derived quantities which may then be displayed or used to set gates.

A.6.2 MULTIFIG

Authorship Bernhard Fabricius

Purpose To prepare graphs of data from a wide range of sources.

References ANU-P/1124

Most of the graphs in this thesis are generated using MULTIFIG. MULTIFIG can take data directly from spectrum files written by DCP or from plain-text data files, in a variety of formats. (The DCPv035 format, available only on the Alphas, requires the version of MULTIFIG that runs only on the Alphas.) The most commonly used plain-text format specifies the X coordinate, the Y coordinate, the error in the Y coordinate, and the point-code specifying the symbol or other information regarding how to plot the indicated point. MULTIFIG graphs may be improved with the use of label files.

MULTIFIG has reasonably complete online help, which is reproduced in the manual ANU-P/1124.

A.6.3 FITEK

Original Author Wolfgang Stoeffl, Lawrence Livermore Laboratory

Purpose To fit peaks or lifetimes in saved (DCP) spectra.

Modifications Adapted to the ANU VAX system and extended by Aidan Byrne, Paul Davidson and Tibor Kibedi.

References ANU-P/1226

FITEK analyses spectrum files as output by DCP, fitting overlapping peaks at fixed or free widths, positions, relative height restrictions, etc. The capacity to fit lifetimes, including multiple lifetimes and prompt components, appears something of an afterthought, and is a little less easy to use, but still works ok. FITEK is usually used when analysing α-particle or γ-ray spectra.

There is an extensive FITEK Manual, ANU-P1226, edited by Tibor Kibedi. It omits two useful commands, however: EXFT, which extracts the fit in MULTIFIG format; and EXDT, which extracts the data. The behaviour of EXFT is altered by the "plot individual peak functions" choice in the menu of options.

APPENDIX B

Data Files

B.1 CCMOD Input

B.1.1 ^{28}Si+^{178}Hf

```
************
File $USER2:[FISSION.RDB103.JOANNE.28SI178HF]CCIN_PAPER.DAT;6
    1      100.0000      0.8500000       1.114759
    2      28.0 14.0 -178.0 72.0 20.0  1.0   0.407   0.0 0.280   -0.03
    3          90.00   140.88      2.120
    4        1  4       1.20
    5        0.407  -2   -1.779
    6      1.00 0.848
    7      1.00 0.433
    8      1.00 5.074
    9      1.00 5.774
   10
   11   4.240
************
```

B.1.2 ^{29}Si+^{178}Hf

```
************
File $USER2:[FISSION.RDB103.JOANNE.29SI178HF]CCIN_PAPER.DAT;6
    1      100.0000      0.8500000       1.115754
    2      29.0 14.0 -178.0 72.0 20.0  1.0   0.0    0.0  0.280  -0.03
    3          90.00   151.48      2.120
    4        1  3  1.200
    5        0.3615 -2 -2.0072
    6      1.0 2.984
    7      1.0 3.189
    8      1.0 3.687
    9
   10
   11   4.240
************
```

B.1.3 ^{31}P+^{175}Lu

```
************
File $USER2:[FISSION.RDB103.JOANNE.31P175LU]CCIN_PAPER.DAT;5
    1      100.0000      0.8500000       1.118549
    2      31.0 15.0 -175.0 71.0 20.0  1.0   0.0   0.0  0.29  -.03
    3         100.00   150.88      2.120
    4        1  4  1.20
    5       0.312 -2 -2.232
    6      1.0 0.267
    7      1.0 5.926
    8      1.0 3.609
    9      1.0 3.617
   10
   11   4.240
************
```

B.1.4 ^{31}P+^{176}Lu

```
************
File $USER2:[FISSION.RDB103.JOANNE.31P176LU]CCIN_PAPER.DAT;4
    1      100.0000      0.8500000       1.118549
    2    31.0 15.0 -176.0 71.0 20.0  1.0   0.0   0.0  0.29  -.03
    3       100.00   150.88      2.120
    4      1  4  1.20
    5       0.312 -2 -2.232
    6    1.0 1.644
    7    1.0 6.009
    8    1.0 4.078
    9    1.0 4.179
   10
   11   4.240
************
```

B.1.5 ^{16}O+^{238}U

```
************
File $USER2:[FISSION.RDB103.JOANNE.16O238U]CCIN_THESIS.DAT;1
    1      100.0000       1.206820       1.019798
    2    16.0  8.0 -238.0 92.0 20.0  1.0   0.1   0.0  0.2863  .045
    3        65.00   110.00      1.000
    4      1  2  1.200
    5       0.0865 3 -0.7320
    6      0.600 2.910
    7      0.600 0.909
    8
    9    2.000
************
```

B.1.6 ^{16}O+^{235}U

```
************
File $USER2:[FISSION.RDB103.JOANNE.160235U]CCIN_THESIS.DAT;1
    1      100.0000        1.243270        1.010314
    2     16.0   8.0 -235.0 92.0 20.0  1.0   0.1   0.0  0.277  .045
    3         65.00   110.00      1.000
    4       1  2  1.200
    5        0.080 3 -0.800
    6       0.600 2.427
    7       0.600 0.047
    8
    9     2.000
************
```

B.2 JOANNE input

These data files are for JO_SHELL or JO_EVAP; data files for JOANNE2_ACB require an extra line, after the line specifying A and Z of the reacting nuclei, specifying a centre of mass energy for the reaction (which is ignored in JOANNE2_ACB, though not in earlier versions of JOANNE2), and the Q-value of the reaction. An example of this additional line is shown on line 29 of the first input file. All forms of JOANNE ignore everything below line 14, and the commentary is retained unchanged in different files.

B.2.1 ^{28}Si+^{178}Hf

```
************
File $USER2:[FISSION.RDB103.JOANNE.28SI178HF]SIHF_EVAP.INP;1
    1   20000                  : Number of cascades.
    2   28 14 178 72           : A,Z of the projectile, then target.
    3   8.6   1.00  8.6        : apar,arot and assc (inverse level density parameters).
    4   0.94  1.0              : Fis. bar. and Kramers scaling factors.
    5   0  0  0    (SSC T=0)   : Change in the SSC n,p and a binding energies (MeV).
    6   0                      : SSC deformation energy (MeV).
    7   2                      : SSC moment of inertia (spherical units)
    8   0                      : Fission transient delay time (s*E-21)
    9   0                      : SSC delay time (s*E-21)
   10   0 0     "LDIS$FILE"    : Fusion XS(mb) and spin diffuseness(hbar)
   11   Rn206TL.DAT            : File containing the ground state transmission coeff's.
   12   Rn206TL.DAT            : File containing the SSC transmission coeff's.
   13   4   0              : SHELLPP OPTION, Level density param. option
   14
   15   Note:
   16   If the fusion XS is equal to zero then the fusion XS spin distribution will
   17   be read in from the file "fusion_sd.dat". The n(th) line of "fusion_sd.dat"
   18   should contain the fusion cross in mb at angular moment n(hbar). A partial
   19   XS of zero will terminate the spin distribution.
   20
   21   Note:
```

```
Use command file to run this program -
eg [fission.rdb103.joanne.31p175lu]ccjoevap.com

Jo_shell/Jo_evap calculate Q-values for you, once beam energy is read in
from commandfile.  Various model parameters are also calculated for you
(description below).

115.0 -69.91         : C.M. energy and reaction Q value (MeV).

So there's one line missing from the above, that earlier Joanne versions
required, and there's an additional line at the bottom for switching jo_shell
effects on and off with.

apar=0 Calculated Value
arot=0 Calculated Value
arot=1 fission and particle level density parameters the same
assc=0 SSC and particle level density parameters the same
8.72  1.00 8.6       : apar,arot and assc (inverse level density parameters).
0  0  0          : apar,arot and assc (inverse level density parameters).

If the fusion XS is equal to zero then the fusion XS spin distribution will
be read in from the file defined as "LDIS$FILE".
    The n(th) line of this l distribution file should contain
    the fusion cross in mb at angular moment n(hbar). A partial
    XS of zero will terminate the spin distribution.

       SHELLPP OPTION  = 0 only ground state properties calculated
                       = 1 shell no pairing  corrections
                       = 2 pairing no shell corrections
                       = 3 shell+pairing included in masses and energy
       LD_option =0    LEVEL DENSITY PARAMETER
                       - TOKE ET AL. NUC PHYS A372 (1981) 141
       LD_option =1    ASYMPTOTIC LEVEL DENSITY PARAMETER
                       - JUNGHANS ET AL. NUC PHYS A629 (1998) 635
```

****

B.2.2 ^{29}Si+^{178}Hf

****

```
File $USER2:[FISSION.RDB103.JOANNE.29SI178HF]SIHF_EVAP.INP;2
20000                : Number of cascades.
29 14 178 72         : A,Z of the projectile, then target.
8.6   1.00  8.6      : apar,arot and assc (inverse level density parameters).
0.94  1.0            : Fis. bar. and Kramers scaling factors.
0  0  0    (SSC T=0) : Change in the SSC n,p and a binding energies (MeV).
0                    : SSC deformation energy (MeV).
2                    : SSC moment of inertia (spherical units)
0                    : Fission transient delay time (s*E-21)
0                    : SSC delay time (s*E-21)
0 0     "LDIS$FILE"  : Fusion XS(mb) and spin diffuseness(hbar)
Rn207TL.DAT          : File containing the ground state transmission coeff's.
Rn207TL.DAT          : File containing the SSC transmission coeff's.
4   0            : SHELLPP OPTION, Level density param. option
... comments snipped
```

```
************
```

B.2.3 ^{31}P+^{175}Lu

```
************
File $USER2:[FISSION.RDB103.JOANNE.31P175LU]PLU_EVAP.INP;7
    1   20000                  : Number of cascades.
    2   31 15 175 71           : A,Z of the projectile, then target.
    3   8.6   1.00  8.6        : apar,arot and assc (inverse level density parameters).
    4   0.94  1.0              : Fis. bar. and Kramers scaling factors.
    5   0  0  0     (SSC T=0)  : Change in the SSC n,p and a binding energies (MeV).
    6   0                      : SSC deformation energy (MeV).
    7   2                      : SSC moment of inertia (spherical units)
    8   0                      : Fission transient delay time (s*E-21)
    9   0                      : SSC delay time (s*E-21)
   10   0 0     "LDIS$FILE"    : Fusion XS(mb) and spin diffuseness(hbar)
   11   Rn206TL.DAT            : File containing the ground state transmission coeff's.
   12   Rn206TL.DAT            : File containing the SSC transmission coeff's.
   13   4   0              : SHELLPP OPTION, Level density param. option
... comments snipped
************
```

B.2.4 ^{31}P+^{176}Lu

```
************
File $USER2:[FISSION.RDB103.JOANNE.31P176LU]PLU_EVAP.INP;7
    1   20000                  : Number of cascades.
    2   31 15 176 71           : A,Z of the projectile, then target.
    3   8.6   1.00  8.6        : apar,arot and assc (inverse level density parameters).
    4   0.94  1.0              : Fis. bar. and Kramers scaling factors.
    5   0  0  0     (SSC T=0)  : Change in the SSC n,p and a binding energies (MeV).
    6   0                      : SSC deformation energy (MeV).
    7   2                      : SSC moment of inertia (spherical units)
    8   0                      : Fission transient delay time (s*E-21)
    9   0                      : SSC delay time (s*E-21)
   10   0 0     "LDIS$FILE"    : Fusion XS(mb) and spin diffuseness(hbar)
   11   Rn207TL.DAT            : File containing the ground state transmission coeff's.
   12   Rn207TL.DAT            : File containing the SSC transmission coeff's.
   13   4   0              : SHELLPP OPTION, Level density param. option
... comments snipped
************
```

B.2.5 ^{16}O+^{238}U

```
************
File $USER2:[FISSION.RDB103.JOANNE.16O238U]OU_EVAP.INP;2
    1   20000                  : Number of cascades.
    2   16  8 238 92           : A,Z of the projectile, then target.
    3   8.6   1.00  8.6        : apar,arot and assc (inverse level density parameters).
    4   0.94  1.0              : Fis. bar. and Kramers scaling factors.
    5   0  0  0     (SSC T=0)  : Change in the SSC n,p and a binding energies (MeV).
    6   0                      : SSC deformation energy (MeV).
    7   2                      : SSC moment of inertia (spherical units)
```

```
    8   0                       : Fission transient delay time (s*E-21)
    9   0                       : SSC delay time (s*E-21)
   10   0 0     "LDIS$FILE"     : Fusion XS(mb) and spin diffuseness(hbar)
   11   FM256TL.DAT             : File containing the ground state transmission coeff's.
   12   FM256TL.DAT             : File containing the SSC transmission coeff's.
   13   4   0               : SHELLPP OPTION, Level density param. option
... comments snipped
************
```

B.2.6 $^{16}O+^{235}U$

```
************
File $USER2:[FISSION.RDB103.JOANNE.160235U]OU_EVAP.INP;3
    1   20000                   : Number of cascades.
    2   16  8 235 92            : A,Z of the projectile, then target.
    3   8.6   1.00  8.6         : apar,arot and assc (inverse level density parameters).
    4   0.94  1.0               : Fis. bar. and Kramers scaling factors.
    5   0  0  0     (SSC T=0)   : Change in the SSC n,p and a binding energies (MeV).
    6   0                       : SSC deformation energy (MeV).
    7   2                       : SSC moment of inertia (spherical units)
    8   0                       : Fission transient delay time (s*E-21)
    9   0                       : SSC delay time (s*E-21)
   10   0 0     "LDIS$FILE"     : Fusion XS(mb) and spin diffuseness(hbar)
   11   FM253TL.DAT             : File containing the ground state transmission coeff's.
   12   FM253TL.DAT             : File containing the SSC transmission coeff's.
   13   4   0               : SHELLPP OPTION, Level density param. option
... comments snipped
************
```

B.3 Other programs

These files are examples only.

B.3.1 inelastic.dat

```
************
File $USER2:[FISSION.RDB103.CUBE.JAN01.CAL]INELASTIC.DAT;50
    1     100.000    28.      58.     82.     206.
    2        22.5
    3     JAN0037.DAT
    4           7541     7249
    5           138095.8
    6
    7      97.5
    8     102.5
    9     107.5
   10     112.5
   11     117.5
   12     122.5
   13     127.5
```

```
   14     132.5
   15     137.5
   16     142.5
   17     147.5
   18     152.5
   19     157.5
   20     162.5
   21     167.5
************
```

B.3.2 xinput.dat

```
************
File $USER2:[FISSION.RDB103.CUBE.MAR00.THETABINS]XINPUT.DAT;648
    1       96.088               15          31          79         197
    2       22.5
    3    MAR0027.DAT
    4             15          31          71         176
    5     135.000
    6           10104     9892
    7           95170.87
    8
    9        97.50    989.39      4.28  33.
   10       102.50    995.33      4.51  33.
   11       107.50    995.22      4.73  33.
   12       112.50   1000.84      5.01  33.
   13       117.50   1009.50      5.34  33.
   14       122.50   1023.90      5.75  33.
   15       127.50   1055.75      6.35  33.
   16       132.50   1061.85      6.80  33.
   17       137.50   1010.99      6.77  33.
   18       142.50   1009.57      7.25  33.
   19       147.50    996.83      7.69  33.
   20       152.50   1010.12      8.54  33.
   21       157.50   1040.79      9.88  33.
   22       162.50   1001.17     10.58  33.
   23       167.50   1029.78     13.00  33.
************
```

APPENDIX C

References

[BAC90] B. B. Back, S. Bjørnholm, T. Døssing, W. Q. Shen, K. D. Hildenbrand, A. Gobbi, S. P. Sørensen, *Relaxation of angular momentum in fission and quasi-fission reactions*, Phys. Rev. C **41**, 1495–1511 (1990).

[BAC85] B. B. Back, R. R. Betts, J. E. Gindler, B. D. Wilkins, S. Saini, M. B. Tsang, C. K. Gelbke, W. G. Lynch, M. A. McMahan and P. A. Baisden, *Angular distributions in heavy-ion-induced fission*, Phys. Rev. C **32**, 195 (1985).

[BAL96] A. B. Balantekin, A. J. DeWeerd, S. Kuyucak, *Relations between fusion cross-sections and average angular momenta*, Phys. Rev. C **54**, 1853 (1996).

[BER01] A. C. Berriman, D. J. Hinde, M. Dasgupta, C. R. Morton, R. D. Butt, J. O. Newton, *Unexpected inhibition of fusion in nucleus-nucleus collisions*, Nature **413**, 144 (2001).

[BER01C] A. C. Berriman, *Investigating Entrance Channel Effects in Fusion-Fission Dynamics*, **PhD Thesis**, Australian National University, 2001.

[BEV92] P. R. Bevington, D. K. Robinson, *Data Reduction and Error Analysis for the Physical Sciences*, (McGraw-Hill, New York, 1992) 144.

[BJO81] S. Bjørnholm, W. J. Swiatecki, *Dynamical aspects of nucleus-nucleus collisions*, Nucl. Phys. **A391**, 471–504 (1982).

[BOH36] Niels Bohr, *Neutron Capture and Nuclear Constitution*, Nature **137**, 344–351 (1936).

[BUT02] R. D. Butt, M. Dasgupta, I. Gontchar, D. J. Hinde, A. Mukherjee, A. C. Berriman, C. R. Morton, J. O. Newton, A. E. Stuchbery, J. P. Lestone, *Effects of finite ground-state spin on fission fragment angular distributions following collisions with spherical or deformed nuclei*, Phys. Rev. C **65**, 044606 (2002).

[BUT02B] R. D. Butt, D. J. Hinde, M. Dasgupta, A. C. Berriman, A. Mukherjee, C. R. Morton, J. O. Newton, *Measurement of the effect of large deformation-aligned ground-state spin on fission fragment anisotropies*, Phys. Rev. C, **66** 044601 (2002).

[DAS98] M. Dasgupta, D. J. Hinde, N. Rowley, A. M. Stefanini, *Measuring barriers to fusion*, Annu. Rev. Nucl. Part. Sci. **48**, 401 (1998).

[DAS97] M. Dasgupta, *CCMOD and CCMPH*, Australian National University Internal Publication, ANU-P/1333 (1997).

[DAS92] M. Dasgupta, A. Navin, Y. K. Agarwal, C. V. K. Baba, H. C. Jain, M. L. Jhingan, and A. Roy, *Fusion of* $^{28}Si+^{68}Zn$, $^{32}S+^{64}Ni$, $^{37}Cl+^{59}Co$ *and* $^{45}Sc+^{51}V$ *in the vicinity of the fusion barrier*, Nucl. Phys. **A539**, 351 (1992).

[DAS83] C. H. Dasso, S. Landowne, A. Winther, *Channel-Coupling Effects in Heavy-Ion Fusion Reactions*, Nucl. Phys. **A405**, 381–396 (1983).

[DAS83b] C. H. Dasso, S. Landowne, A. Winther, *A study of Q-value effects on barrier penetration*, Nucl. Phys. **A407**, 221–232 (1983).

[DES90] A. deShalit, H. Fesbach, *Theoretical Nuclear Physics Volume 1: Nuclear Structure*, (John Wiley & Sons, New York 1990).

[DOS85] T. Døssing, J. Randrup, *Dynamical evolution of angular momentum in damped nuclear reactions; (I) Accumulation of angular momentum by nucleon transfer*, Nucl. Phys. **A433**, 215–279 (1985).

[ESB87] H. Esbensen, S. Landowne, C.Price, *High-spin excitations in the rotating frame and sudden approximations*, Phys. Rev. C **36**, 2359–2364 (1987).

[HAG97] K. Hagino, N. Takigawa, M. Dasgupta, D. J. Hinde, J. R. Leigh, *Adiabatic Quantum Tunnelling in Heavy-Ion Sub-barrier Fusion*, Phys. Rev. Lett. **79**, 2014–2017 (1997).

[HAG97B] K. Hagino, N. Takigawa, M. Dasgupta, D. J. Hinde, J. R. Leigh, *Validity of the linear coupling approximation in heavy-ion fusion reactions at sub-barrier energies*, Phys. Rev. C **55**, 276–284 (1997).

[HAL58] I. Halpern and V. M. Strutinsky, *Angular Distributions in Particle-Induced Fission at Medium Energies*, in *Proceedings of the 2nd United Nations Conference on the Peaceful Uses of Atomic Energy* **15**, 408 (1958).

[HIN02C] D. J. Hinde, M. Dasgupta, A. Mukherjee, *Severe inhibition of fusion by quasi-fission in reactions forming* ^{220}Th, Phys. Rev. Lett. **89**, 282701 (2002).

[HIN96] D. J. Hinde, M. Dasgupta, J. R. Leigh, J. C. Mein, C. R. Morton, J. O. Newton, H. Timmers, *Conclusive evidence for the influence of nuclear orientation on quasifission*, Phys. Rev. C. **53**, 1290 (1996).

[HIN95] D. J. Hinde, C. R. Morton, M. Dasgupta, J. R. Leigh, J. C. Mein, H. Timmers, *Competition between fusion-fission and quasi-fission in the reaction* $^{28}Si+^{208}Pb$, Nucl. Phys. **A592**, 271 (1995).

[HIN95B] D. J. Hinde, M. Dasgupta, J. R. Leigh, J. C. Mein, C. R. Morton, J. O. Newton, H. Timmers, *Fusion-Fission versus Quasifission: Effect of Nuclear Orientation*, Phys. Rev. Lett. **74**, 1295–1298 (1995).

[HINpriv] D. J. Hinde, private communication.

[HUI69] J. R. Huizenga, A. N. Behkami and L. G. Moretto, *Note on Interpretation of Fission-Fragment Angular Distributions at Moderate Excitation Energies*, Phys. Rev. **177**, 1826 (1969).

[KAI94] S. Kailas, P. Singh, *Influence of pre-fission neutron emission on fission fragment angular distribution for the system* $^{209}Bi+^{16}O$, Z. Phys. A **347**, 267 (1994).

[KRU93] A. T. Kruppa, P. Romain, M. A. Nagarajan, N. Rowley, *Effect of multi-phonon coupling on heavy-ion fusion*, Nucl. Phys. **A560**, 845–862 (1993).

[LEI95] J. R. Leigh, M. Dasgupta, D. J. Hinde, J. C. Mein, C. R. Morton, R. C. Lemmon, J. P. Lestone, J. O. Newton, H. Timmers, J. X. Wei, N. Rowley, *Barrier distributions from the fusion of oxygen ions with* $^{144,148,154}Sm$ *and* ^{186}W, Phys. Rev. C **52**, 3151 (1995).

[LES99] J. P. Lestone, *Calculating fission rates at high spin: Incorporation of rotational degrees of freedom in thermodynamically fluctuating axially symmetric systems*, Phys. Rev. C **59**, 1540 (1999).

[LES97] J. P. Lestone, A. A. Sonzogni, M. P. Kelly and R. Vandenbosch, *Influence of the ground state spin of target nuclei on the anomalous behavior of fission fragment anisotropies*, Phys. Rev. C **56**, R2907 (1997).

[LES97B] J. P. Lestone, A. A. Sonzogni, M. P. Kelly, R. Vandenbosch, *Near- and sub-barrier fission fragment anisotropies and the failure of the statistical theory of fission decay rates*, J. Phys. G., **23**, 1349–1357 (1997).

[LES93] J. P. Lestone, J. R. Leigh, J. O. Newton, J. X. Wei, J. W. Chen, S. Elfström, M. Zielinska-Pfabé, *Pre-scission charged-particle multiplicities following the reactions* $^{164,167,170}Er+^{28}Si$, Nucl. Phys. **A559**, 277 (1994).

[LES90] J. P. Lestone, J. R. Leigh, J. O. Newton, J. X. Wei, *Fission fragment angular distributions following transfer reactions for* $^{232}Th+^{16}O$, Nucl. Phys. **A509**, 178–194 (1990).

[LES90B] J. P. Lestone, *Light Charged Particle Production in Heavy-Ion Induced Fusion-Fission Reactions*, **PhD Thesis**, Australian National University, 1990

[MCC89] P. McCullagh, J. A. Nelder, *Generalised Linear Models* (Chapman and Hall, London, 1989) 126.

[MOR01] C. R. Morton, A. C. Berriman, R. D. Butt, M. Dasgupta, D. J. Hinde, A. Godley, J. O. Newton, *Influence of higher order deformations in the* ^{34}S+^{168}Er *fusion reaction*, Phys. Rev. C **64**, 034604 (2001).

[MOR95] C. R. Morton, D. J. Hinde, J. R. Leigh, J. P. Lestone, M. Dasgupta, J. C. Mein, J. O. Newton, H. Timmers, *Resolution of the anomalous fission fragment anisotropies for the* ^{16}O+^{208}Pb *reaction*, Phys. Rev. C **52**, 243 (1995).

[MOR95B] C. R. Morton, *Fusion Barrier Distributions and Fission Fragment Anisotropies in Heavy-Ion Fusion Reactions*, **PhD Thesis**, Australian National University, 1995.

[MUL97] S. M. Mullins, G. D. Dracoulis, T. R. McGoram, S. Bayer, W. A. Seale, F. G. Kondev, *Rotational band on the 31 yr* 16^+ *isomer in* ^{178}Hf, Phys. Lett. B **393**, 279 (1997).

[NAG86] M. A. Nagarajan, A. B. Balantekin, N. Takigawa, *Geometric interpretation of the adiabatic model for heavy ion fusion*, Phys. Rev. C, **34** 894–898 (1986).

[NAY00] B. K. Nayak, R. G. Thomas, R. K. Choudhury, A. Saxena, P. K. Sahu, S. S. Kapoor, Raghav Varma, D. Umakanth, *Effect of projectile ground state spin on fission fragment anisotropies in* ^{10}B, ^{11}B+^{232}Th *reactions*, Phys. Rev. C **62**, 031601(R) (2000).

[NDS98] E. Browne and Huo Junde, *Nuclear Data Sheets for A=176*, Nuclear Data Sheets **84**, 357 (1998).

[NDS93] A. O. Macchiavelli, E. Browne, *Nuclear Data Sheets for A=175*, Nuclear Data Sheets **69**, 930 (1993).

[NIL95] S. G. Nilsson and I. Ragnarsson, *Shapes and Shells in Nuclear Structure*, (Cambridge University Press, Cambridge, 1995).

[OGA99] Yu. Ts. Oganessian, A. V. Yeremin, A. G. Popeko, S. L. Bogomolov, G. V. Buklanov, M. L. Chelnokov, V. I. Chepigin, B. N. Gikal, V. A. Gorshkov, G. G. Gulbekin, M. G. Itkis, A. P. Kabachenko, A. Yu. Lavrentev, O. N. Malyshev, J. Rohac, R. N. Sagaidak, S. Hofmann, S. Saro, G. Giardina, K. Morita, *Synthesis of nuclei of the superheavy element 114 in reactions induced by* ^{48}Ca, Nature, **400** 242–245 (1999).

[OGA92] Yu. Ts. Oganessian, S. A. Karamian, Y. P. Gangski, B. Gorsk, B. N. Markov, Z. Szeglowski, Ch. Briançon, D. Ledu, R. Meunier, M. Hussonnois, O. Constantinescu, and M. I. Subbotin, *Production, chemical and isotopic separations of the long-lived isomer* $^{178}Hf^{m2}$ *(*$T_{1/2}$*=31 years)*, J. Phys. G **18**, 393 (1992).

[POL83] G. Pollarolo, R. A. Broglia, A. Winther, *Calculation of the imaginary part of the heavy ion potential*, Nucl. Phys. **A406**, 369–389 (1983).

[RAM01] S. Raman, C. W. Nestor, Jr., P. Tikkanen, *Transition probability from the ground to the first-excited* 2^+ *state of even-even nuclides*, Atomic Data and Nuclear Data Tables **78**, 1–128 (2001).

[RAM93] V. S. Ramamurthy, S. S. Kapoor, *Determination of extra-push energies for fusion from differential fission cross-section measurements*, Phys. Rev. C **47**, 1311–1312 (1993).

[RAM90] V. S. Ramamurthy, S. S. Kapoor, R. K. Choudhury, A. Saxena, D. M. Nadkarni, A. K. Mohanty, B. K. Nayak, S. V. Sastry, S. Kailas, A. Chatterjee, P. Singh, A. Navin, *Entrance-channel dependence of fission-fragment anisotropies: a direct experimental signature of fission before equilibration*, Phys. Rev. Lett. **65**, 25–28 (1990).

[RAM89] S. Raman C. W. Nestor, Jr., S. Kahane, K. H. Bhatt, *Predictions of* $B(E2;0_1^+ \rightarrow 2_1^+)$ *values for even-even nuclei*, Atomic Data and Nuclear Data Tables **42**, 1–54 (1989).

[RAM87] S. Raman, C. H. Malarkey, W. T. Milner, C. W. Nestor, Jr., P. H. Stelson, *Transition probability* $B(E2)\uparrow$ *from the ground to the first excited* 2^+ *state of even-even nuclides*, Atomic Data and Nuclear Data Tables **36**, 1–96 (1987).

[RAM85] V. S. Ramamurthy, S. S. Kapoor, *Interpretation of fission-fragment angular distributions in heavy-ion reactions*, Phys. Rev. Lett. **54**, 178–181 (1985).

[RAM85B] V. S. Ramamurthy, S. S. Kapoor, *Effect of fission following incomplete fusion on the interpretation of fission fragment angular distributions in heavy ion reactions*, Phys. Rev. C **32**, 2182–2184 (1985).

[RON77] R. M. Ronningen, J. H. Hamilton, L. Varnell, J. Lange, A. V. Ramayya, G. Garcia-Bermudez, W. Lourens, L. L. Riedinger, F. K. McGowan, P. H. Stelson, R. L. Robinson, J. L. C. Ford, Jr., $E2$ *and* $E4$ *reduced matrix elements of* $^{154,156,158,160}Gd$ *and* $^{176,178,180}Hf$, Phys. Rev. C **16**, 2208 (1977).

[ROS61] M. E. Rose, *Elementary Theory of Angular Momentum* (Wiley, New York, 1961).

[ROW93] N. Rowley, J. R. Leigh, J. X. Wei, R. Lindsay *Obtaining average angular momenta from fusion excitation functions near the Coulomb barrier*, Phys. Lett. B **314** 179–184 (1993).

[ROW91] N. Rowley, G. R. Satchler, P. H. Stelson, *On the "distribution of barriers" interpretation of heavy ion fusion*, Phys. Lett. B **254**, 25–29 (1991).

[STO85] R. G. Stokstad, *The Use of Statistical Models in Heavy-Ion Reaction Studies*, Treatise on Heavy Ion Science, vol 3, edited by D. Allan Bromley (Plenum Press, New York, 1985).

[STO80] R. G. Stokstad, Y. Eisen, S. Kaplanis, D. Pelte, U. Smilansky, I. Tserruya, *Fusion of* ^{16}O+$^{148,150,152,154}Sm$ *at sub-barrier energies*, Phys. Rev. C, **21**, 2427–2435 (1980).

[THO85] K. T. R. Davies and A. J. Sierk, *Conditional saddle-point configurations*, Phys. Rev. C, **31**, 915–922 (1985).

[TOK85] J. Tōke, R. Bock, G. X. Dai, A. Gobbi, K. D. Hildenbrand, J. Kuzminski, W. F. J. Müller, A. Olmi, H. Stelzer, B. B. Back, S. Bjørnholm, *Quasi-fission—the mass drift mode in heavy-ion reactions*, Nucl. Phys. **A440**, 327–365 (1985).

[TOK84] J. Toke, R. Bock, Dai Guang-xi, A. Gobbi, S. Gralla, K. D. Hildenbrand, J. Kuzminski, W. F. J. Müller, A. Olmi, W. Reisdorf, S. Bjørnholm, B. B. Back, *Compound nucleus fission and quasifission in reactions of* ^{238}U *with* ^{16}O *and* ^{27}Al, Phys. Lett. B **142**, 258–262 (1984).

[TOI96] Table of Isotopes, 8th edition, Richard B. Firestone and Virginia S Shirley (editor) (Wiley, New York, 1996).

[VAN73] R. Vandenbosch and J. R. Huizenga, *Nuclear Fission* (Academic, New York, 1973).

[VIO85] V. E. Viola, K. Kwiatkowski, M. Walker, *Systematics of fission fragment total kinetic energy release*, Phys. Rev. C **31**, 1550 (1985).

[VOR95] D. Vorkapič and B. Ivaniševič, *Anomalous anisotropies of fission fragments for sub-barrier fusion-fission reactions*, Phys. Rev. C **52**, 1980–1985 (1995).